

Lawrence Berkeley National Laboratory

Recent Work

Title

OXYGEN REDUCTION IN FUEL CELL ELECTROLYTES

Permalink

<https://escholarship.org/uc/item/3bw497cf>

Authors

Striebel, K.A.
McLarnon, F.R.
Cairns, E.J.

Publication Date

1987-12-01

2



Lawrence Berkeley Laboratory

UNIVERSITY OF CALIFORNIA

APPLIED SCIENCE DIVISION

RECEIVED
LAWRENCE
BERKELEY LABORATORY

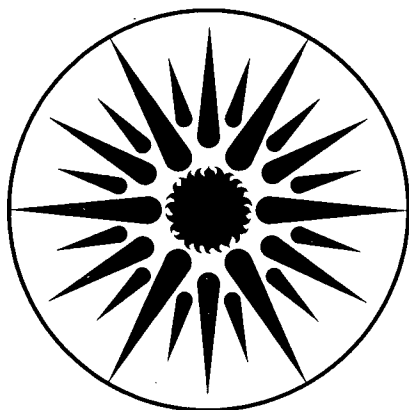
MAY 10 1988

LIBRARY AND
DOCUMENTS SECTION

Oxygen Reduction in Fuel Cell Electrolytes

K.A. Striebel,* F.R. McLarnon, and E.J. Cairns
(*Ph.D. Thesis)

December 1987



APPLIED SCIENCE
DIVISION

LBL-24340
2

DISCLAIMER

This document was prepared as an account of work sponsored by the United States Government. While this document is believed to contain correct information, neither the United States Government nor any agency thereof, nor the Regents of the University of California, nor any of their employees, makes any warranty, express or implied, or assumes any legal responsibility for the accuracy, completeness, or usefulness of any information, apparatus, product, or process disclosed, or represents that its use would not infringe privately owned rights. Reference herein to any specific commercial product, process, or service by its trade name, trademark, manufacturer, or otherwise, does not necessarily constitute or imply its endorsement, recommendation, or favoring by the United States Government or any agency thereof, or the Regents of the University of California. The views and opinions of authors expressed herein do not necessarily state or reflect those of the United States Government or any agency thereof or the Regents of the University of California.

LBL-24340

OXYGEN REDUCTION IN FUEL CELL ELECTROLYTES

by

Kathryn A. Striebel, Frank R. McLarnon and Elton J. Cairns

December 1987

Applied Science Division
Lawrence Berkeley Laboratory
University of California
Berkeley, California 94720

This work was supported by the Assistant Secretary for Conservation and Renewable Energy, Office of Energy Storage and Distribution of the U.S. Department of Energy under Contract No. DE-AC03-76SF00098.

The United States Department of Energy has the right to use this thesis for any purpose whatsoever including the right to reproduce all or any part thereof.

Oxygen Reduction in Fuel Cell Electrolytes

Copyright 1987

Kathryn Ann Striebel

Oxygen Reduction in Fuel Cell Electrolytes

Kathryn Ann Striebel

Abstract

Voltage losses in the O_2 cathode represent the major inefficiency in aqueous fuel cells for transportation or stationary applications. Experimental and theoretical studies of oxygen reduction (OR) in novel acid and alkaline electrolytes on smooth and supported Pt have been carried out.

Similar kinetically limited rates for OR were measured in the "super-acid" electrolytes trifluoromethane sulfonic acid (TFMSA) and tetrafluoroethane-1,2-disulfonic acid (TFEDSA), with the rotating disk electrode (RDE) technique at 23 °C and pH=1. A first-order dependence on O_2 pressure was measured, contrary to previously-reported results for TFMSA.

The mechanism for OR on Pt in alkaline electrolytes is complicated by the concurrent oxidation and reduction of Pt. Rotating ring-disk electrode (RRDE) studies carried out with anodic and cathodic potential sweeps in 0.1 to 6.9 M KOH and 0.1 to 4.0 M K_2CO_3 revealed similar currents when corrected for O_2 solubility differences. In dilute electrolytes, OR proceeds primarily through the 4-electron pathway to water, independent of pH. In KOH, the mechanism for Pt oxidation changes and the fraction of current yielding a peroxide product increases at 2 to 3 M. These changes were not observed in K_2CO_3 .

Porous gas diffusion electrodes (GDE) with supported Pt catalyst were studied in a special cell with low uncompensated solution resistance. Cyclic voltammograms yielded measurements of the wetted areas of carbon and Pt and the local electrolyte composition. GDE galvanostatic steady-state performance with 100% O_2 was measured in 2 to 11 M KOH and 2 to 5.5 M K_2CO_3 . Comparisons with kinetic results suggest that OR on carbon contributes to the high currents in 6.9 M KOH at high overpotentials. In K_2CO_3 , lower wetted areas and slow OH^- ion transport are responsible for the poor performance when compared with KOH.

Models for the steady-state operation of porous GDE's were developed. These models account for the diffusion and reaction of O_2 and ionic transport in KOH and K_2CO_3 . Performance data showed good agreement with the model, using reasonable values for the electrode structural parameters. The non-kinetic Tafel slope and the half-order dependence on O_2 pressure, observed with K_2CO_3 , were predicted without using adjustable parameters. The results suggest that modifications of the GDE structure will be necessary to obtain good performance with aqueous carbonate electrolytes.

Acknowledgements

I would like to express my gratitude to Professor Elton Cairns who has guided me throughout my stay at Berkeley and during the preparation of this thesis. Drs. Frank McLarnon and Philip Ross provided many valuable suggestions and support.

I would also like to thank Steve Rothway for constructing the electrodes and electrochemical cells and Lee Johnson for advice on how to do just about everything. I must also recognize Panos Andricacos for introducing me to the field of oxygen reduction and Phil Lessner for his indirect guidance in the modeling work.

I would like to thank Ms. Susan Lauer for her continued confidence and help in the preparation of the manuscript and figures. Special acknowledgement for their encouragement goes to Rick, Jesse, Pam, Lori, Barbie, Carol, Rick, Rain Brian, Dave, and my cat Kitty. And finally, this would not have happened without the inspiration of my mother Charlotte or my loving partnership with Mark.

This work was supported by the Assistant Secretary for Conservation and Renewable Energy, Office of Energy Storage and Distribution of the U.S. Department of Energy under Contract No. DE-AC03-76SF00098.

Table of Contents

Chapter 1 Introduction	1
1.1 Fuel Cells for Electric Vehicles	1
1.2 Oxygen Cathodes in Aqueous Electrolytes	3
1.3 Organization of this Thesis	5
Chapter 2 Oxygen Reduction on Platinum in Aqueous Electrolytes	7
2.0 Introduction	7
2.1 Platinum Oxidation and Reduction	8
2.2 Rotating Electrode Studies of Oxygen Reduction	13
2.3 Oxygen Reduction in Dilute Electrolytes	18
2.3.1 Acidic Electrolytes	19
2.3.2 Alkaline Electrolytes	21
2.3.3 Effect of Temperature	27
2.4 Dependence of Oxygen Reduction Kinetics on Oxide Coverage	28
2.5 Oxygen Reduction in Concentrated Alkaline Electrolytes	31
Chapter 3 Oxygen Reduction on Platinum in TFMSA and TFEDSA	33
3.0 Introduction	33
3.1 Experimental Procedure	33
3.2 Results	36
3.3 Conclusions	45
Chapter 4 Kinetic Studies of Oxygen Reduction on Pt in Alkaline Electrolytes	47
4.0 Introduction	47
4.1 Platinum/Electrolyte Interactions	48

4.1.1 Hydrogen Region	52
4.1.2 Platinum Oxidation Region	53
4.1.3 Surface Coverage of Oxide during OR Sweep Experiments	59
4.1.4 Summary	62
4.2.1 Experimental Equipment and Procedures	65
4.2.2 Electronics	65
4.2.3 Analysis of RRDE data in Dilute Electrolytes	65
4.2.4 General Results for Dilute Alkaline Electrolytes	69
4.2.5 Series 1: Carbonate Addition to Hydroxide	72
4.2.6 Series 2: Effect of CO_3^{2-} Concentration at Constant Ionic Strength	74
4.2.7 Series 3: Effects of Carbonate Concentration and pH	76
4.2.8 Summary of Anion Effects	78
4.3 Oxygen Reduction in Concentrated Alkaline Electrolytes	78
4.3.1 Experimental Equipment and Procedures	78
4.3.2 Subtraction of Background Currents	80
4.3.3 Analysis of RRDE and RDE Data with Multiple Reactions	83
4.3.4 General Results for Concentrated Electrolytes	84
4.3.5 OR Dependence on KOH Concentration at 23 °C	88
4.3.6 OR Rate Dependence on K_2CO_3 Concentration at 23 °C	95
4.3.7 KOH versus K_2CO_3 at 23 °C	97
4.3.8 Temperature Dependence of Oxygen Reduction in Concentrated Alkaline Electrolytes	99
4.4 Conclusions	103
Chapter 5 Fuel Cell Cathode Studies in Alkaline Electrolytes	105

5.0 Introduction	105
5.1 Previous Work	106
5.1.1 Performance and Electrode Structure	107
5.1.2 Platinum Particle Size Effects	108
5.1.3 Catalyst Support Activity and Interactions	109
5.1.4 The $\text{CO}_2/\text{HCO}_3^-/\text{CO}_3^{2-}$ System	110
5.2 Experimental Apparatus and Procedures	112
5.2.1 Cell Design	112
5.2.2 Electrolytes and Gases	115
5.2.3 Electrodes	115
5.2.4 Electronics	119
5.2.5 Experiment Design	119
5.3 Cyclic Voltammetry in Supported-Pt Gas-Diffusion Electrodes	120
5.3.1 Electrode Activation and Wetting	125
5.3.2 Local Electrolyte Composition in Electrode Pores	127
5.4. Cathode Performance in KOH Electrolytes	130
5.4.1 Smooth versus Supported Platinum	133
5.4.2 Electrolyte Concentration Effects	135
5.5 Cathode Performance in K_2CO_3 Electrolytes	136
5.6. Summary and Recommendations	145
Chapter 6 Modeling of the Aqueous Carbonate Fuel Cell Cathode	147
6.0 Introduction	147
6.1 Previous Work	148
6.2 Oxygen Cathode with Concentrated KOH Electrolyte	150

6.2.1 Model Development	150
6.2.2 Parameter Estimation	157
6.2.3 Results and Implications for Carbonate Model	159
6.3 Concentrated K_2CO_3 Cathode Model	162
6.3.1 Model Development	162
6.3.2 Parameter Estimation	164
6.3.3 Results and Discussion	164
6.4 Conclusions and Recommendations	168
Nomenclature	170
References	176
Appendix A Thermodynamic Properties of KOH and K_2CO_3	188
Appendix B Steady-State Flooded Agglomerate Model for the Gas-Diffusion Electrode in KOH and K_2CO_3	192
B.1 Introduction	192
B.2 Dimensionless Equations and Solution Technique	192
B.3 General Model Behavior	197
B.4 Computer Code	202

List of Figures

1-1 Flooded agglomerate model of the PTFE-bonded porous gas-diffusion electrode	4
2-1 Window-opening voltammogram in 2M KOH on platinum, 100mV/sec, 23 °C.	10
2-2 General lumped-parameter mechanism for oxygen reduction	15
3-1 Electrochemical cell	35
3-2 First-sweep cyclic voltammogram in TFEDSA, pH = 1, 25 °C, Ar atm.	37
3-3 First-sweep cyclic voltammogram in TFMSA recorded after pretreatment, pH =1, 25 °C, Argon atmosphere	38
3-4 Current-potential sweeps for oxygen reduction at a Pt RDE in TFEDSA, pH = 1, 25 °C	39
3-5 Levich Plots for TFEDSA and TFMSA at various oxygen partial pressures	41
3-6 Levich Slopes from Figure 3-5	42
3-7 Kinetic current dependence on oxygen pressure in TFEDSA and TFMSA	43
3-8 Kinetic current densities for oxygen reduction in "super-acid" electrolytes at 1 atm. oxygen, pH = 1.0 and 25 °C	45
4-1 Cyclic voltammograms in dilute alkaline electrolytes ($I_s = 0.7M$)	49
4-2 Cyclic voltammograms in KOH electrolytes	50
4-3 Cyclic voltammograms in alkali carbonate electrolytes	51
4-4 Oxide Coverage in KOH electrolytes	55
4-5 Oxide coverage in K_2CO_3 electrolytes	56
4-6 Oxide coverage dependence on KOH concentration	57
4-7 Temperature dependence of oxide coverage in KOH electrolyte	58
4-8 Potential profiles for measurement of oxide surface charge existent during on oxy- gen reduction experiment	60

4-9 Oxide coverage during oxygen reduction experiment	61
4-10 Potential profiles for oxygen reduction experiments	64
4-11 RRDE data in Ionic 2A for the three potential profiles of Figure 4-10 at a rotation speed of 1600 rpm	66
4-12 Data analysis plots at several potentials for experiment Ionic 2A	68
4-13 Kinetic current density for various electrode pretreatments in 0.1M KOH + 0.6M KF (Ionic 2A)	70
4-14 3-Step Model Rate Constants for 0.1M KOH + 0.6M KF (Ionic 2A)	71
4-15 Kinetic current density for Series 1 electrolytes	73
4-16 Kinetic Current Density for Series 2 Electrolytes, pH 13	75
4-17 Kinetic Current Density for Series 3 Electrolytes	76
4-18 All-PTFE rotating ring-disk electrode test cell	79
4-19 "Background" platinum oxidation currents in 5.4M KOH	82
4-20 RRDE data in 5.4M KOH, before and after the subtraction of "background" currents	83
4-21 Concentration dependence of Levich slope in alkaline electrolytes	85
4-22 Comparison of calculation techniques for oxygen reduction kinetic current density in 5.4M KOH, 23 °C	87
4-23 Concentration dependence of kinetic current density in KOH electrolytes	89
4-24 Concentration-dependence of i_k^* and i_k^{*o} , in KOH electrolytes, 25 °C	91
4-25 Hydroxide activity dependence of normalized current density in KOH electrolytes, 25 °C	92
4-26 Percentage of kinetic current proceeding through the 2-electron pathway on platinum in 5.4M KOH, 23 °C	93
4-27 J-Plots in KOH Electrolytes	94

4-28 Concentration dependence of kinetic current density in K_2CO_3 electrolytes, 23 °C	96
4-29 Concentration dependence of normalized current density in K_2CO_3 electrolytes, 23 °C	97
4-30 Comparison of mass-transfer-corrected current density in KOH and K_2CO_3 elec- trolytes, at 900mV vs. RHE, 23 °C	99
4-31 Temperature dependence of the Levich slope for oxygen reduction in alkaline elec- trolytes	100
4-32 Temperature dependence of kinetic current density in alkaline electrolytes	101
5-1 pH and water activity of KOH and K_2CO_3 solutions at 25 °C	112
5-2 Diagram of fuel cell electrode test cell	113
5-3 Fuel cell polarization study test setup	114
5-4 Optical micrograph of Prototech electrode	117
5-5 SEM of active layer of new Prototech electrode at 20kV	118
5-6 Cyclic voltammograms in 6.9M KOH at 23 °C	122
5-7 Platinum oxide coverage in 6.9M KOH, 23 °C	123
5-8 Cyclic voltammograms in 2.0M K_2CO_3 at 23 °C	124
5-9 Wetting progression in different fuel-cell electrodes	126
5-10 Cyclic voltammograms before and after O_2 polarization in 6.9M KOH at 23 °C, 50mV/sec	128
5-11 Cyclic Voltammograms before and after oxygen polarization measurement in car- bonate electrolytes, 50mV/sec, 23 °C	129
5-12 Oxygen reduction polarization measurements in 6.9M KOH corrected to current density per area wetted Pt, 23 °C	131
5-13 O_2 partial pressure dependence of polarization in 6.9M KOH, corrected to current	

density per area wetted Pt, 23 °C	132
5-14 Comparison between oxygen reduction on smooth Pt and Pt-on-C GDE, 23 °C	134
5-15 Specific current densities for oxygen reduction on a Prototech electrode in KOH electrolytes, 23 °C	136
5-16 Specific current densities for oxygen reduction on smooth Pt and Prototech porous GDE in K_2CO_3 electrolytes, 23 °C	138
5-17 Polarization behavior in 4.0M K_2CO_3 at various O_2 partial pressures, 23 °C	139
5-18 Dependence of current density on O_2 pressure at constant potential in 4.0 K_2CO_3 , 23 °C	140
5-19 O_2 polarization behavior in carbonates electrolytes at various conditions	141
5-20 "Cycling" polarization measurements in alkaline electrolytes 23 °C	143
5-21 The effect of CO_2 addition on O_2 cycling polarization measurements in 5.5M K_2CO_3 , 23 °C	144
6-1 Flooded agglomerate model of the fuel cell GDE	151
6-2 Effect of partial agglomerate wetting on the O_2 diffusion/reaction function	155
6-3 Prototech electrode P23 with 30% KOH and 100% O_2 23 °C	160
6-4 Predicted current density and electrolyte concentration profiles from KOH model for 30% KOH with $\epsilon_s = 0.5$	162
6-5 Comparison between steady-state model and observed performance behavior for a Prototech electrode K_2CO_3 with 100% O_2	165
6-6 Predicted current density profiles from K_2CO_3 model	166
6-7 Ionic concentration profiles from model for 2M K_2CO_3 100% O_2	168
A-1 Measured densities for K_2CO_3 solutions at 23 °C	190
A-2 Calculated apparent dissociation constants for K_2CO_3 solutions at 23 °C	191

x

B-1 Predicted results for 2M K_2CO_3 dimensionless parameter variation	198
B-2 Predicted results for 2M K_2CO_3 , finite mass-transfer rate boundary condition	199
B-3 Predicted results for 2M K_2CO_3 dependence on oxygen pressure	201

List of Tables

2-1 Diagnostic criteria reported for O ₂ reduction on Pt in dilute alkaline electrolytes	23
4-1 Voltammetric peak potentials in alkaline electrolytes	52
4-2 Summary of dilute electrolyte results	63
4-3 Henry's law coefficients	69
4-4 Three-step model rate constants dilute electrolytes	77
4-5 Experimental and predicted Levich slopes	87
4-6 Kinetic parameters in KOH electrolytes	88
4-7 Kinetic parameters in K ₂ CO ₃ electrolytes	95
4-8 Summary of variable-temperature experiments	103
5-1 Gas Diffusion electrode characteristics	116
6-1 Parameters for GDE models	158
B-1 Definitions	193
B-2 Dimensionless equations for KOH problem	194
B-3 Dimensionless equations for K ₂ CO ₃ problem	195
B-4 Dimensionless parameters for GDE model in 2M K ₂ CO ₃	197

Chapter 1

Introduction

1.1. Fuel Cells for Electric Vehicles

Fuel cells offer high theoretical efficiencies for converting hydrocarbon fuels to electricity with environmentally benign exhaust products, low noise and modular construction. Several types of hydrogen/oxygen fuel cell systems, which utilize hydrogen from reformed organic fuels, are in different stages of development for electric utility and electric vehicle (EV) applications (1). This thesis reports on some experimental and theoretical studies of the oxygen electrode in novel electrolytes for the alkaline fuel cell (AFC) and the phosphoric acid fuel cell (PAFC).

Battery-powered electric vehicles were invented and popularized early this century only to be abandoned in favor of the longer-range, higher-powered internal combustion engine vehicle (ICEV) by 1930. Renewed interest in EVs as a market for off-peak electricity has been expressed by public utilities, and several fleets of commercial vehicles powered by advanced lead-acid batteries will soon be in operation. While a number of advanced batteries will meet the stringent specific power requirements of the EV, they will have limited range and require hours for recharge. Fuel-cell-powered vehicles are limited in range only by the size of the fuel tank and require only minutes for refueling.

Modern fuel cells have been under development for transportation and stationary applications since their success in the space program in the early sixties. The low- to medium-temperature aqueous and solid-polymer-electrolyte systems are most practical for an EV application due to weight and start-up considerations. In 1967, Kordesch built and operated an electric vehicle powered by a 6kW Union Carbide alkaline compressed hydrogen/air fuel cell (2). This was a hybrid system including a lead acid battery for start-up and acceleration. It included an electrolyte circulation loop to prevent carbonate build-up, which occurs by reaction of carbon

dioxide from air with hydroxide ion (2). However, only limited attempts to consider the application of state-of-the-art fuel cells, developed for stationary applications, to vehicle propulsion have been made.

The phosphoric acid fuel cell (PAFC) is the most mature fuel cell technology today (within a few years of commercialization for stationary power generation in both utilities and on-site applications) largely because of its ability to reject carbon dioxide. This tolerance allows the use of reformed hydrocarbons, such as methanol, as sources of hydrogen avoiding the need for hydrogen storage and electrolyte circulation. PAFC's for utility applications operate with unscrubbed air and light hydrocarbons or natural gas, which are desulfurized, steam reformed and shifted to H_2 with $\sim 25\%CO_2$. Both electrodes contain Pt catalyst supported on high-specific-area carbon and bonded with polytetrafluoroethylene (PTFE). The concentrated H_3PO_4 (85-95 wt%) displays most of the physical properties desirable in a fuel cell electrolyte such as low volatility, low wettability of PTFE, acceptable conductivity, good stability and low cost. Even with platinum catalyst however, typical cell performance is 0.65 volts at 250 mA/cm^2 , 190°C and 3.4 bars, with the cathode responsible for most of the loss. The poor oxygen reduction kinetics in this electrolyte have been attributed to phosphate anion adsorption onto the platinum, which slows the kinetics for oxygen reduction (63). Considerable attention has been focused on fluorinated sulfonic acids as non-adsorbing alternatives to phosphoric acid. This thesis includes some kinetic studies of two of these new acid electrolytes.

Solid polymer electrolyte fuel cells (SPEFC) are also being developed for the EV application. This fuel cell employs acidic cation-exchange membranes such as Nafion (fluorinated ionomer) for the electrolyte. They have many potential advantages over the PAFC but still require very large amounts of platinum (0.75 mg/cm^2). Work with this system is covered in a recent review (1) and will not be discussed further here.

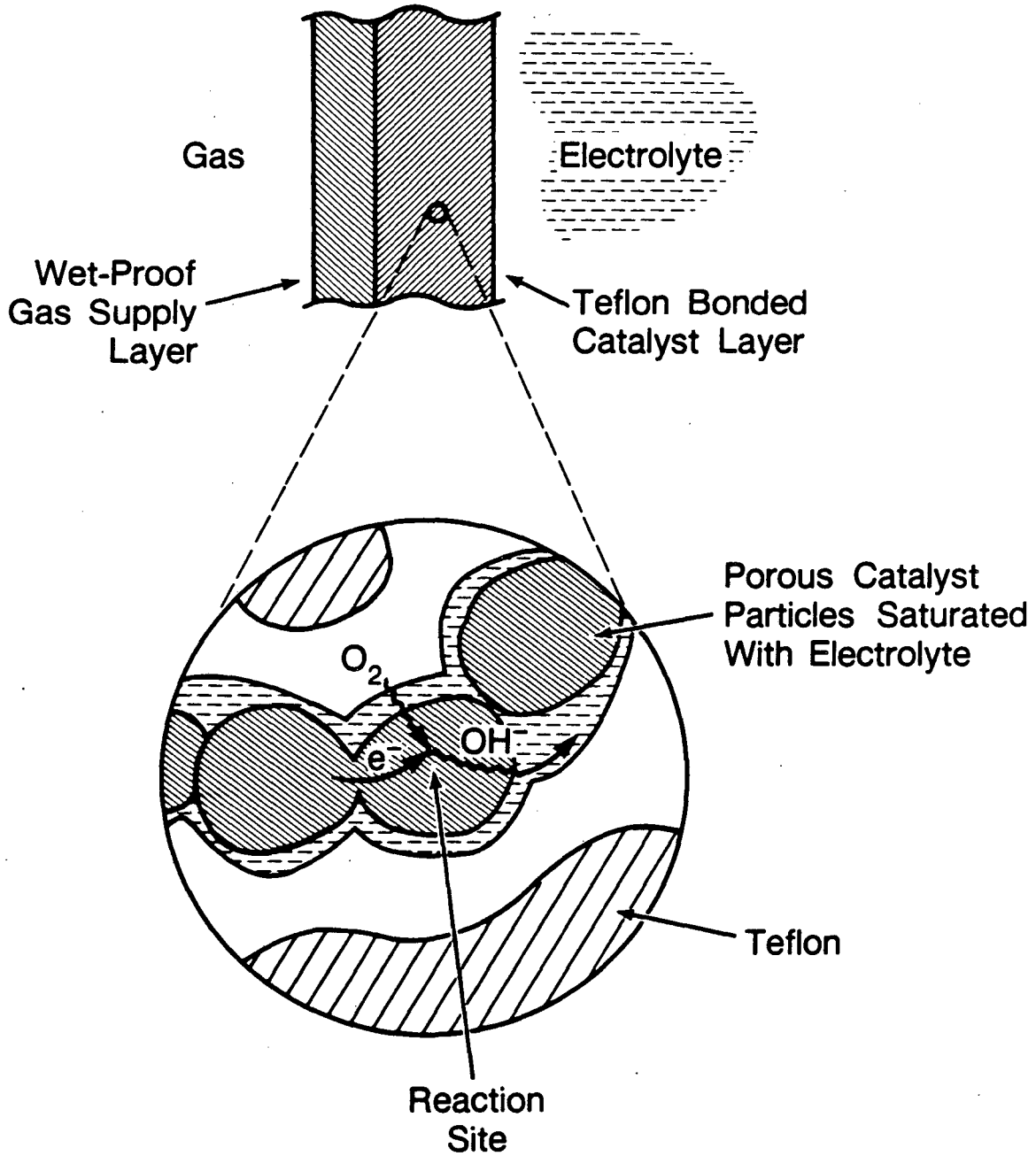
AFCs were developed for the Apollo space program because of the better reliability and operating characteristics generally observed in these systems. Alkaline electrolytes also offer the

best promise for the use of non-noble metal catalysts. As mentioned above, however, these systems must be operated with pure hydrogen and oxygen or include electrolyte circulation systems to remove carbonate ions. Concentrated carbonate electrolytes were suggested as CO₂-rejecting alternatives to KOH in the alkaline fuel cell by Cairns and Bartosik in 1964 (3). They studied a methanol/oxygen fuel cell with concentrated Cs₂CO₃ electrolyte. This early work demonstrated complete oxidation of the methanol to CO₂ and water at reasonable cell voltages without changes in the electrolyte composition. Such a system would allow the use of the preferred fuel, methanol, avoid the need for electrolyte circulation, and have better corrosion and stability characteristics because of the lower pH. A carbonate electrolyte should also facilitate good oxygen electrode kinetics and the possibility of non-noble electrocatalysts, as with alkaline systems in general. Several aspects of an alkaline fuel cell with concentrated carbonate electrolyte were investigated in this research to determine if this system warrants a concerted effort.

1.2. Oxygen Cathodes in Aqueous Electrolytes

The oxygen cathode is the major limiting factor in several fuel-cell and battery systems. At any given temperature and pressure, oxygen cathode performance depends on the electrocatalyst identity and physical structure, the electrolyte properties and the interaction between the two. The extreme irreversibility and low exchange current densities observed for oxygen reduction reaction require an electrode with highly dispersed catalyst on a suitably conductive support material, usually graphitic carbon. Because oxygen reduction is necessarily a three-phase reaction these supported catalyst particles are bound into a hydrophobic structure with PTFE, creating a three-dimensional reaction zone.

An idealized diagram of the structure of a PTFE-bonded platinum-on-carbon electrode such as used in this work is shown in Figure 1-1. The gaseous reactant, oxygen, must first diffuse through the hydrophobic gas pores created by the PTFE. It then dissolves in the electrolyte and diffuses through a flooded (PTFE-free) portion of porous catalyst to a platinum crystallite where it reacts through a number of fundamental steps (mechanism to be discussed later). The overall



XBL 8610-3869 A

Figure 1-1: Flooded agglomerate model of the PTFE-bonded porous gas-diffusion electrode.

reaction can be written



for acid and alkaline electrolytes respectively. Products must then diffuse away from the reaction zone toward the anode or gas chamber exhaust. Ions migrate and/or diffuse through the liquid phase carrying the ionic current balanced by electrons migrating through the solid matrix to the current collector.

The rate-limiting factor of all of these processes is the slow kinetics of the electrochemical reaction in many cases. Platinum is generally regarded as the most active electrocatalyst for this reaction. In alkaline media, the platinoid elements, silver, various transition metal oxides and carbon show significant activity. Several new electrocatalysts such as transition metal macrocyclic complexes and oxides are under development and are covered in a recent review (4). Since our work focused on electrolyte effects in the cathode, we studied only one electrocatalyst, platinum.

1.3. Organization of this Thesis

Chapter 2 provides an overview of previous research concerning oxygen reduction kinetics on Pt in aqueous media. The first part covers some of the lumped-parameter mechanisms proposed for the parallel pathways often observed in oxygen reduction. This is followed by a discussion of the proposed rate-limiting reaction steps and their dependences on surface oxidation state, pH and electrolyte composition.

Chapter 3 discusses the the measurement of kinetic currents using a rotating disk electrode in dilute electrolytes and presents the results of kinetic studies of oxygen reduction carried out in two "super-acid" electrolytes, trifluoromethanesulfonic acid (TFMSA) and tetrafluoroethane-1,2-disulfonic acid (TFEDSA). It has been suggested by other workers that the reaction order with respect to oxygen concentration is less than unity in these "superacid" electrolytes because of the

failure of data obtained very close to the limiting currents to follow adequately the first-order model for the rotating disk electrode (RDE) (26). We measured the reaction order directly by varying the concentration of oxygen in the electrolyte.

Chapter 4 presents the results of voltammetric and kinetic studies for oxygen reduction on Pt in alkaline electrolytes. The rotating ring-disk electrode (RRDE) technique was used to measure kinetic currents and rate constants for a three-step model where possible. Kinetic results for KOH and K_2CO_3 are compared at concentrations up to 6.9M and 4.0M, respectively. The dependence of measured parameters on electrode pretreatment is also discussed.

Chapter 5 reports the results of performance studies carried out with porous gas-diffusion electrodes in potassium carbonate and potassium hydroxide electrolytes. We were able to identify electrode kinetics as the limiting process in these electrodes with high-pH electrolytes over a wide performance range by direct comparison with smooth-electrode data. Hydroxide ion build-up in the porous electrode was identified as a serious issue for the development of a practical electrode with medium-concentration carbonate electrolyte. Our attempts at overcoming this hydroxide build-up by the addition of small quantities of CO_2 to the oxygen stream are also reported.

Chapter 6 covers the development of a mathematical model of our experimental carbonate cathode system. The model is based on the flooded agglomerate structure of the PTFE-bonded gas-diffusion electrode and takes into account the relatively complex chemistry occurring in the carbonate-containing cathode. Model results are compared with the experimental results of Chapter 5. Recommendations for further work in the development of a CO_2 -rejecting alkaline electrolyte suitable for electric-vehicle fuel cells are discussed.

Chapter 2

Oxygen Reduction on Platinum in Aqueous Electrolytes

2.0. Introduction

At roughly 200 mA/cm², 70% of the overpotential losses occurring in the most efficient hydrogen/air aqueous fuel cells can be attributed to the oxygen reduction reaction. A very large number of fundamental steps may be involved, due to the large number of electrons being transferred (4) and the fact that this is a surface reaction where adsorption and desorption of oxygen and the intermediate, hydrogen peroxide, may play major roles. Several approaches in the study of this reaction have been taken and will be reviewed here.

The first step in the determination of a mechanism is the measurement of the dependence of current-potential behavior and production rates of any intermediate species on reaction conditions. Based on such diagnostic criteria, one can write an expression for the observed kinetic current for a cathodic reaction far from equilibrium, such as

$$i_k = nFk_c^0 \left(\prod_i a_i^{s_i} \right) \exp\left(\frac{-\alpha FV}{RT} \right) \quad (2-1)$$

where s_i are the effective reaction orders with respect to activities a_i of species in solution or on the surface, α and k_c^0 are the transfer coefficient and the potential-independent part of the rate constant for the multistep cathodic reaction, respectively, and V is the electrostatic potential Φ_s of the solid relative to the pH-independent standard hydrogen reference electrode (SHE), just outside the double layer (5). An alternate form of Equation 2-1 in terms of a pH-dependent reference electrode, such as the reversible hydrogen electrode at the electrolyte pH (RHE), can also be written

$$i_k = nFk_c^0 \left(\prod_i a_i^{s_i} \right) a_{H^+}^{-\alpha} \exp\left(\frac{-\alpha FE}{RT} \right) \quad (2-2)$$

since

$$V = \Phi_S - E_{SHE} \quad , \quad E = \Phi_S - E_{RHE} \quad \text{and} \quad E_{RHE} - E_{SHE} = \frac{RT}{F} \ln a_{H^+}. \quad (2-3)$$

Diagnostic criteria give mechanistic information for regarding the nature of the reaction steps up to the rate-determining step (rds). When the mechanisms for the forward and reverse reactions are identical, diagnostic criteria for the reverse reaction shed light on the remaining reaction steps. The mechanism for oxygen reduction (OR) on platinum, however, is complicated by several factors. First, the oxidation and reduction processes occur at such widely separated potentials that the surface conditions differ and the oxidation and reduction pathways are probably not complementary. This is because the platinum surface itself is oxidized over the same potential range as that over which the OR reaction occurs. Second, two competing pathways may exist: the direct 4-electron reduction to water and the 2-electron reduction to peroxide which, may or may not be further reduced. When the rate of intermediate H_2O_2 production is measured, the rate constants for a more-detailed, lumped-parameter type of expression can be determined.

After a brief review of the oxidation and reduction of platinum, previous studies of OR in dilute electrolytes with the rotating ring-disk electrode (RRDE) will be discussed along with some of the lumped-parameter models that have been proposed for this mechanism on the basis of such investigations. The literature will then be evaluated to determine if there exists a consensus on the the effects of oxygen pressure, temperature, and pH on this reaction. The dependence of the reported diagnostics on the oxidation state of the platinum will then be reviewed. Finally, OR studies in concentrated electrolytes will be reviewed.

2.1. Platinum Oxidation and Reduction

There is still much disagreement over the nature of the oxidation product that forms on platinum in aqueous solutions; it has been postulated to be PtO , PtO_2 , $PtOH$, and $Pt(OH)_2$. It

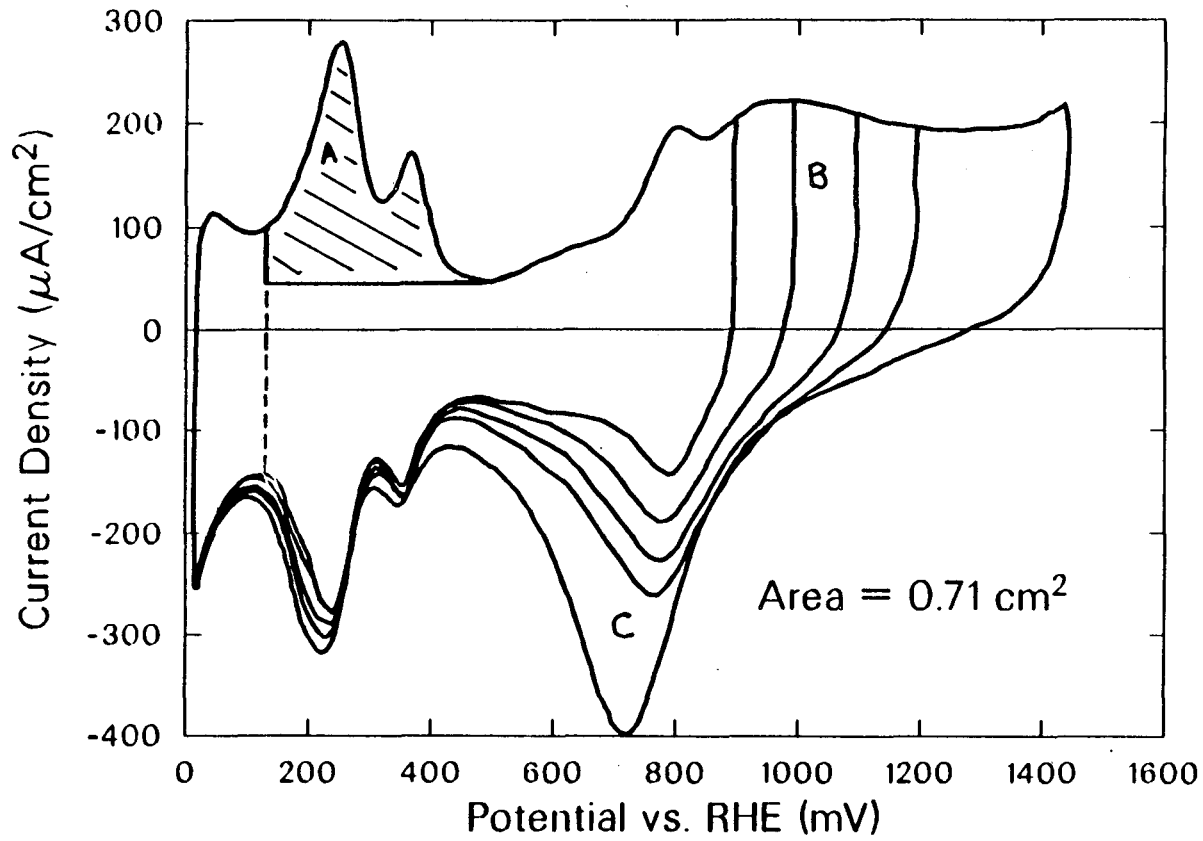
will be referred to as an "oxide" here, except when referring to specific works. The observed effects of the "oxide" on the electrocatalytic properties of platinum toward dissolved oxygen will be discussed in the next section.

The cyclic voltammogram shown in Figure 2-1 can be interpreted as a fingerprint for the electrochemical interaction between an aqueous electrolyte (2 M KOH in this figure) and smooth platinum. In sufficiently pure electrolytes, the sizes of the peaks should be directly proportional to sweep rate and independent of stirring rate, as expected for surface reactions. The degree of symmetry of the current peaks about the potential axis is an indication of the reversibility of the process. The platinum oxidation process begins at about 0.5 V in alkaline solutions (and at about 0.75 V in sufficiently pure acid solutions). In Figure 2-1, the reversibility of this process can be seen to be a function of the anodic turnaround potential. When cycling to potentials greater than 1.1 V, a significant amount of oxide is formed which is not reduced until well into the cathodic hydrogen region. This phenomenon is most prevalent in alkaline electrolytes and renders studies of the oxidation and reduction of platinum difficult. Conway (6) referred to the irreversibility of platinum oxidation as an "intrinsic irreversibility" involving different species or states.

The "coverage" of oxide is often defined by

$$\theta_{ox} = \frac{Q_{ox}}{2Q_h} \quad (2-4)$$

where Q_{ox} is the charge required to reduce the oxide and Q_h is the charge associated with the hydrogen desorption region, which is proportional to the active surface area of platinum (7) (see Figure 2-1, area marked A). Bagotsky and Tarasevich (8) found θ_{ox} to depend in a complex way on both potential and time at a given potential. For a constant oxidation potential, $E_{ox} < 0.9$ V, the formation and removal of the oxide appears to be completely reversible. For $0.9 < E_{ox} < 1.1$ V, the oxide appears to "age" or require more charge and lower potentials to be reduced. At oxidation potentials greater than about 1.1 V, the coverage has been observed to increase indefinitely with the logarithm of time, and the oxide becomes more irreversibly reduced (9).



- XBL 8710-4338 -

Figure 2-1: Window-opening voltammogram in 2M KOH on platinum, 100mV/sec, 23 °C.
A, Hydrogen desorption region; B, Platinum oxidation region; C, Platinum reduction region.

There are two schools of thought on the cause of this behavior. The logarithmic growth behavior is consistent with a bulk oxide phase formation (10-12). This is said to occur by a place-exchange mechanism whereby oxygen penetrates or is absorbed into the platinum lattice (10). This type of mechanism can account for the extremes in irreversibility but has difficulty explaining the different peaks that are frequently observed. Ross found no evidence of oxygen below the surface of a highly oxidized platinum electrode using Auger spectroscopy (detection limit 0.1 atomic %) and argued in favor of a strictly surface process (13). The irreversibility is then explained by the continual formation of more stable species adsorbed on the surface (14). Any number of possible oxidized platinum species can be proposed to account for the peaks observed in a voltammogram such as Figure 2-1.

Bagotsky et al. (15) found oxygen absorption to depend strongly on the degree of cycling to which an electrode had been subjected. For well-annealed platinum, they measured **steady-state** oxide coverages at potentials as high as 1.7 volts after only a few seconds. They suggested that there are two distinct "aging" mechanisms occurring in the oxidation of well-cycled polycrystalline platinum electrodes: oxygen absorption into the platinum as well as a change in the oxygenated species adsorbed on the surface. The peaks observed in a voltammogram such as Figure 2-1 are then due to surface processes, and the flattening sometimes observed is caused by oxygen absorption. They studied the surface aging, independent of absorption, by using well-annealed platinum and applying their cathodic measuring sweeps to only 0.4 V (assuming that all adsorbed oxide is reduced at more anodic potentials and all absorbed oxide is reduced at more cathodic potentials). Their "steady-state" results agree with those of many authors (12,16) in that θ varies essentially linearly with potential and the potential for a given coverage shifts 60 mV for each unit of pH according to the relation

$$\theta_{ox}^{eq} = a + \frac{f}{fRT} E \quad (2-5)$$

where f is a heterogeneity factor which depends on the assumed stoichiometry of the oxidation product. This form is consistent with a coverage-dependent adsorption energy,

$$\Delta G_{\theta} = \Delta G_{\theta}^{\circ} - fRT\theta_{ox} \quad (2-6)$$

Bagotsky et al. found $f = 15$ for PtOH formed at low potentials in alkaline electrolytes (15).

Bagotsky et al. (15) made extensive studies of the kinetics of the formation and reduction of the "oxide." One technique involved the measurement of the dependence of peak potential (E_p) and peak current (i_p) versus sweep rate (v) during a linear potential sweep experiment. For a surface reaction, this experiment can be analyzed as a thin-layer process or an adsorption process, yielding the diagnostic relations (17)

$$E_p = E^{\circ} + \frac{RT}{\alpha nF} \ln \left(\frac{A^{\circ} k^{\circ} RT}{\alpha nFv} \right) \quad (2-7)$$

and

$$i_{pc} \propto \frac{\alpha nF^2 C^{\infty}}{RT} v \quad (2-8)$$

written for a cathodic process, where α and k° are the transfer coefficient and rate constant for the process and A° is a geometric factor. The peak current, i_{pc} , depends linearly on sweep rate, and the peak potential depends linearly on $\log v$. A slope of 120 mV/decade for the latter can be interpreted as a one-electron process with $\alpha = \frac{1}{2}$. In 1.0 M KOH, they observed two types of oxide species formed in the intermediate-potential region (0.9-1.1 V) at short times, as evidenced by two reduction peaks. As the holding time or potential is increased, these peaks tend to merge into one at an intermediate potential. They concluded that at 0.9 V, in 1.0 M KOH and 0.1 M perchloric acid, a monolayer of PtOH is formed reversibly on the surface. Between 0.9 and 1.2 V, a third peak appears which corresponds to the one-electron oxidation of PtOH to Pt(OH)₂. The mechanism of surface aging in this potential range is not clear but might be attributable to a "dehydration" of Pt(OH)₂ to PtO.

In well-cycled systems, both oxide adsorption and absorption will be observed. The identity and the bond strength of the adsorbed surface species should play an important role in determining the electrocatalytic activity of the surface. The identification of two mechanisms for "aging"

should aid in the interpretation of the effect of oxide "coverage" on other reactions such as OR. Increased coverage is usually thought to decrease the electrocatalytic activity of platinum toward OR. Some authors have observed, however, that aging of a platinum surface (at constant coverage) increases the rate of the 2-electron pathway for oxygen reduction through the intermediate peroxide. This will be discussed further in Section 2-4.

2.2. Rotating Electrode Studies of Oxygen Reduction

The kinetics of OR are most frequently studied with controlled-mass-transfer techniques, such as the rotating disk electrode (RDE). The mass-transfer-limited current to an RDE depends on the rotation speed and solution properties according to the Levich equation which is expressed in a number of convenient forms:

$$i_L = 0.62nFC_i^\infty D_i^{2/3} \nu^{-1/6} \omega^{1/2} = B\omega^{1/2} = nFC_i^\infty \xi_i \omega^{1/2} = nFk_d C_i^\infty \quad (2-9)$$

Further details of this technique are covered elsewhere (18). Mueller and Nekarsov (19) were the first to detect quantitatively the intermediate product, H_2O_2 in the OR reaction, with a RRDE. With this technique, the reduction of oxygen is carried out on the disk while the ring is held at a potential in the limiting-current regime for peroxide oxidation ($E > 1.1$ V). The amount of peroxide that can be detected as it is swept past the ring is governed by geometry (18).

Equations for correcting rotating disk currents for mass transfer are derived by balancing the diffusion of oxygen to the surface with the consumption of oxygen through N reactions at the surface of the disk

$$\xi_{O_2} \omega^{1/2} (C_{O_2}^\infty - C_{O_2}^*) = \sum_{j=1}^N \frac{i_j}{n_j F} \quad (2-10)$$

where ξ_{O_2} is defined above, and $C_{O_2}^*$ and $C_{O_2}^\infty$ are the concentrations of oxygen at the electrode surface and in the bulk, respectively. For a single reaction, which is first-order with respect to O_2 , Equation 2-1 can be used to derive

$$\frac{C_{O_2}^*}{C_{O_2}^\infty} = \frac{i_d}{i_k} \quad (2-11)$$

where i_d is the measured disk current, and i_k is the mass-transfer-corrected current or "kinetic current." Substitution into Equation 2-10 and rearrangement gives the classical expression

$$\frac{1}{i_d} = \frac{1}{i_k} + \frac{1}{i_L} \quad (2-12)$$

When there are parallel reactions with possibly different values of n , which consume the diffusing species, the expression becomes more complex. Since only the current due to the sum of the reactions can be measured, it is necessary to propose a reaction sequence or lumped-parameter mechanism before data can be corrected for mass transfer effects.

The most general lumped-parameter mechanism for OR was proposed by Bagotsky, Tarasevich and Filinovski in 1972 (20) and is shown in Figure 2-2. Reactions 1-3 correspond to multistep electrochemical reactions (with the potential-dependent rate constants, k_1 , k_2 and k_3). Step 4 is the surface catalyzed chemical decomposition of H_2O_2 . Reactions 5 and 6 correspond to the adsorption/desorption of HO_2^- and O_2 , respectively. Hsueh, Chin and Srinivasan (21) reviewed several simplifications of this mechanism and discussed their relative applicabilities to OR in dilute sulfuric acid. The three mechanisms most applicable to OR on platinum in alkaline electrolytes will be discussed here.

The simplest and therefore most popular dual-path mechanism was originally proposed by Damjanovic et al. in 1966 (22). They considered steps 1-3 in the forward direction only, with the first-order rate constants k_1 , k_2 and k_3 . The current measured at the disk, i_d , can be written

$$i_d = i_1 + i_2 + i_3 = 2FC_{O_2}^*(2k_1 + k_2) + 2Fk_3C_{H_2O_2}^* \quad (2-13)$$

and that measured at the ring, i_r

$$i_r = \frac{2F\zeta_{H_2O_2}\omega^{3/4}C_{H_2O_2}^*}{N_c} \quad (2-14)$$

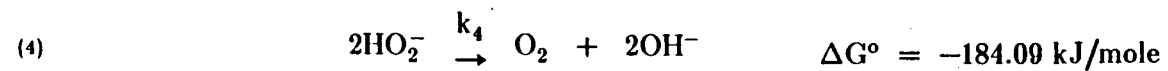
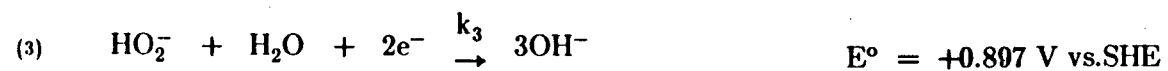
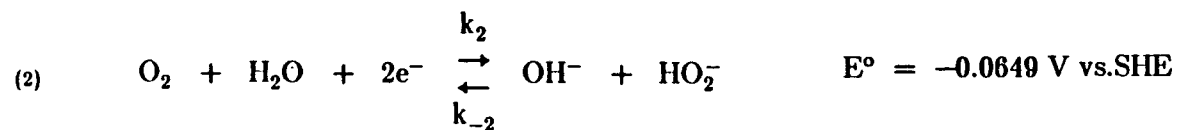
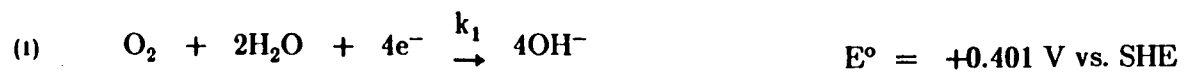
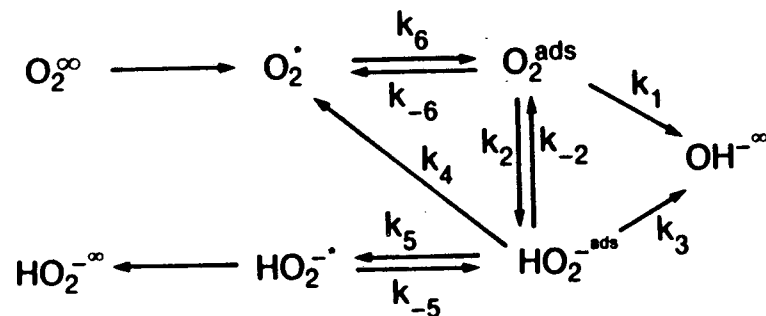


Figure 2-2: General lumped-parameter mechanism for oxygen reduction (20).

XBL 879-11195

where N_c is the collection efficiency. The mass balance on oxygen at the surface, Equation 2-10, for this reaction sequence, becomes

$$\frac{C_{O_2}^*}{C_{O_2}^\infty} = \frac{\xi_{O_2}\omega^{1/2}}{\xi_{O_2}\omega^{1/2} + k_1 + k_2} \quad (2-15)$$

and a similar relation, assuming $C_{H_2O_2}^\infty = 0$ can be written for peroxide

$$C_{H_2O_2}^* = \frac{k_2 C_{O_2}^*}{k_3 + \xi_{H_2O_2}\omega^{1/2}} \quad (2-16)$$

These four expressions (Equations 2-13 through 2-16) can be rearranged, eliminating surface concentrations, to give the following expressions of diagnostic value

$$\frac{1}{i_d^*} = \frac{N_c}{N_c i_d + i_r} = \frac{1}{4FC_{O_2}^\infty \xi_{O_2}\omega^{1/2}} + \frac{1}{4FC_{O_2}^\infty (k_1 + k_2)} \quad (2-17)$$

and

$$\frac{N_c i_d}{i_r} = \frac{2k_3}{\xi_{H_2O_2}\omega^{1/2}} \left(\frac{k_1}{k_2} + 1 \right) + \left(\frac{2k_1}{k_2} + 1 \right) \quad (2-18)$$

where i_d^* will be called a "corrected disk current." All three rate constants can be determined from the slopes and intercepts of plots of the left side of these expressions against $1/\omega^{1/2}$ at a given potential.

The precursor to the model shown in Figure 2-2, also developed by Bagotsky et al., included the reverse of reaction 2 (add step -2) and the catalytic decomposition of peroxide on the surface (step 4). However, their analysis did not account for the fact that the O_2 produced in step 4 will affect the rate of diffusion of O_2 to the surface. They considered step 4 to be first-order and obtained

$$\frac{(i_L^o - i_d)N_c}{i_r} = 1 + 2 \left(\frac{\xi_{O_2}}{\xi_{HO_2^-}} \right) \frac{k_{-2} + k_3 + k_4}{k_2} + \frac{2\xi_{O_2}\omega^{1/2}}{k_2} \quad (2-19)$$

and

$$N_c \frac{i_d}{i_r} = \frac{1}{\xi_{H_2O_2} \omega^{1/2}} \left[(k_{-2} + k_3 + k_4) \left(2 \frac{k_1}{k_2} + 1 \right) + (k_3 - k_{-2}) \right] + \left(2 \frac{k_1}{k_2} + 1 \right) \quad (2-20)$$

where i_r^0 is the limiting current assuming $n = 4$. Plots of the left sides of these equations against $1/\omega^{1/2}$ should also be linear for a given potential. However, only four of the five rate constants can be calculated in this manner.

Appleby and Savy (23) included in their analysis the possibility that H_2O_2 adsorption may be slow. They also accounted for the change in O_2 diffusion rate with "recycling." The analysis of recycling at a RDE was originally carried out by McIntyre (24) and involves summing over the geometric series obtained by following one mole of oxygen arriving at the surface of the disk. Using the above terminology, Appleby and Savy's results take the following form for a first-order recycling reaction and reaction 2 irreversible

$$\frac{N_c i_d}{i_r} = \frac{1}{\xi_{H_2O_2} \omega^{1/2}} \left[\frac{k_{-5}}{k_5} (k_3 + k_4) \left(2 \frac{k_1}{k_2} + \tau \right) \right] + \left(2 \frac{k_1}{k_2} + \tau \right) \left(\frac{k_3 + k_4 + k_5}{k_{-5}} \right) \quad (2-21)$$

where

$$\tau = \frac{2[(k_1 + k_2)(2k_3 + k_4 + k_{d_2}) + k_1 k_4]}{2k_1(k_3 + k_4 + k_{d_2}) + k_2(2k_3 + k_4 + 2k_{d_2})} \quad (2-22)$$

The value of τ is 1 in the absence of recycling and 2 with complete recycling and $k_{d_2} = \xi_{H_2O_2} \omega^{1/2}$. Appleby and Savy discussed many limiting cases for which different sets of rate constants could be calculated. Most notably, when the ratio of the slope to the intercept of this plot is a logarithmic function of potential then $k_3 > k_4$ and $k_5 \gg k_3 + k_4$ implying that desorption and catalytic recycling of peroxide are not extremely important and the mechanism approaches the simple three-step model above.

Bagotsky et al., Appleby and Savy and others extended their analyses to the case where the solution contains peroxide instead of oxygen. Similar systems of linear equations can be derived which allow the calculation of more constants. However, relatively few experimental studies have been carried out with enough accuracy to verify all of the rate constants.

Hsueh et al. (21) suggested that the constants for these more complex models can be calculated by fitting data to non-linear functions. A more sophisticated approach along this line was taken very recently by Adanuvor and White (25). They created a numerical model of the reaction scheme in Figure 2-2 (without the adsorption and desorption steps) and calculated expected RDE curves for different values of the rate constants, for OR in 0.1 M NaOH. However, they did not compare their theoretical results with any experiments, and the work was limited to the RDE. They were able to generate RDE curves which show a maximum current as a function of potential for the parallel reaction scheme with and without the consideration of step 4. This point is made because this type of behavior is unexpected in RDE experiments but has been reported in the literature (19).

2.3. Oxygen Reduction in Dilute Electrolytes

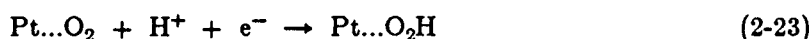
Kinetic studies of OR are usually carried out in dilute electrolytes even though practical fuel cells operate with concentrated electrolytes. Dilute electrolytes are favored due to higher solubilities of oxygen and the extreme sensitivity of catalytic activity to the presence of impurities. In this section, literature studies of dilute electrolytes will be reviewed in part as a basis for understanding OR kinetic behavior in the more-useful concentrated electrolytes.

Most authors agree that in most electrolytes, the reaction order with respect to oxygen pressure above the electrolyte is one. One exception to this was reported by Hsueh et al. (26) for TFMSA. In the present work, we measured a reaction order of one for this electrolyte as well. This matter is covered in Chapter 3.

The other points of agreement in the literature are that at least two regions of potential dependence are observed in all electrolytes and that higher coverages of oxide generally slow the rate of the direct 4-electron reduction to water. The remaining points such as the dependence of the rates of the two pathways on pH, temperature and platinum "oxide" coverage or age remain open to debate even after some 30 years of modern research.

2.3.1. Acid Electrolytes

The \log_{10} current-potential behavior of oxygen reduction on platinum in acid electrolytes usually exhibits two linear regions with slopes of $2F/2.3RT$ and $F/2.3RT$ ($\alpha = 1/2$ and 1 according to Equation 2-1). Damjanovic, Genshaw, and Bockris (27,28) detected no peroxide during RRDE experiments in sufficiently pure acid electrolytes, concluding that OR on platinum proceeds only through the direct 4-electron transfer to water. This behavior is consistent with a mechanism wherein the rate-determining step (rds) is the transfer of the first electron to an adsorbed oxygen molecule which, in acid electrolyte, is accompanied by protonation:



For this rate-limiting step, the relation

$$i_k = nFk_c a_{\text{H}^+} \theta_{\text{O}_2} \exp\left(\frac{-\beta_e FV}{RT}\right) \quad (2-24)$$

shows the same form as Equation 2-1 where a_{H^+} is the hydrogen ion activity, θ_{O_2} the coverage of adsorbed molecular oxygen and β_e is the symmetry factor for the electron-transfer process. θ_{O_2} is dependent on oxygen pressure, potential, pH and the coverage of other species. The two observed slopes are attributed to a change in the adsorption mechanism with the change from a bare platinum surface (Langmuir adsorption) to an oxidized surface (Tempkin adsorption).

The Langmuir adsorption isotherm can be approximated as

$$\theta_{\text{O}_2} = A' p_{\text{O}_2} \exp\left(\frac{-\Delta G_f^\ddagger}{RT}\right) \quad (2-25)$$

where ΔG_f^\ddagger is the activation energy for adsorption which depends on the energies of adsorption of both reactants and products in the rds. Substituting Equation 2-25 into 2-24 we get

$$i_k = nFk_c a_{\text{H}^+} A' p_{\text{O}_2} \exp\left(\frac{-\beta_e FV}{RT}\right) \exp\left(\frac{-\Delta G_f^\ddagger}{RT}\right) \quad (2-26)$$

which reduces to

$$i_k = nFk_c' a_{H^+} P_{O_2} \exp\left(\frac{-FV}{2RT}\right) \quad (2-27)$$

for low coverages when ΔG_j^\ddagger is constant and $\beta_e = \frac{1}{2}$.

At intermediate coverages of oxide species, the activation energy for adsorption is assumed to be proportional to coverage as is the adsorption energy (see Equation 2-6). This is expressed as follows with the addition of a symmetry factor for the adsorption process, β_a (28)

$$\Delta G_j^\ddagger(\theta) = \Delta G_j^\ddagger - \beta_a r RT \theta_{ox} \quad (2-28)$$

where r is the proportionality constant. Substituting Equations 2-5 and 2-28 into Equations 2-25 and then 2-24, we find

$$i_k = nFk_c' a_{H^+} P_{O_2} \exp\left(\frac{-\beta_e FV}{RT}\right) \exp\left(\frac{-\beta_a r FE}{fRT}\right) \quad (2-29)$$

Assuming for convenience that r from Equation 2-28 equals f from Equation 2-6, the symmetry factors β_e and β_a are both equal to $\frac{1}{2}$, and using the relation

$$V = E + \frac{RT}{F} \ln a_{H^+} \quad (2-30)$$

the following expression is obtained

$$i_k = nFk_c' a_{H^+}^{3/2} P_{O_2} \exp\left(\frac{-FV}{RT}\right) \quad (2-31)$$

This analysis supports the pH and potential dependence reported by these authors

$$s_{H^+} = 3/2 \quad \text{and} \quad \alpha = 1/2 \quad \text{for high current densities} \quad (2-32)$$

and

$$s_{H^+} = 1 \quad \text{and} \quad \alpha = 1 \quad \text{for low current densities} \quad (2-33)$$

Yeager (29), and Fischer and Heitbaum (30) have suggested that in acid electrolytes, dissolved molecular oxygen adsorbs to one platinum site with the O-O bond parallel to the surface (Griffith model). The first electron transfer breaks this bond in the rds, followed later by proto-

nation and eventually the formation of water. This is supported by the results of Ghoneim et al. (31), who observed no isotope effects in studies of OR kinetics in 85% D_3PO_4/D_2O and 85% H_3PO_4/H_2O , concluding that the proton is not involved in the rds. The expressions for current according to this mechanism will have the same Tafel slopes and oxygen reaction orders as above, but $s_{H^+} = 0$ and $\frac{1}{2}$ for high and low current densities, respectively. In the presence of adsorbed surface impurities, or highly oxidized surfaces, steric or energy considerations may lead to end-on adsorption of oxygen leading to an adsorbed peroxide species. This peroxide may eventually desorb (and be detectable with an RRDE) or it may be further reduced to water.

2.3.2. Alkaline Electrolytes

The main difference between OR on platinum in acid and alkaline electrolytes is the amount of peroxide product generated. Within the alkaline regime, the dependence of peroxide production on pH is less obvious. Authors have reported anywhere from 2 (32) to 100% (30) of the current going through the peroxide intermediate in 1N KOH depending on the electrochemical pretreatment of the platinum. Log current-potential plots usually exhibit at least two linear regions, as with acid electrolytes, but the slopes reported for these regions vary considerably. The reaction order with respect to hydrogen ion for OR kinetics continues to be the subject of controversy and confusion in the literature (33). Much of the confusion comes from the expression used to define the current (Equations 2-1 or 2-2), and specifically whether or not one is using a pH-dependent reference electrode. The strict definition of the reaction order with respect to hydrogen ion activity is obtained from Equation 2-1 as (34)

$$\left[\frac{\partial \log i_k}{\partial \log a_{H^+}} \right]_V = s_{H^+} \quad (2-34)$$

When one is comparing the relative merits of fuel cell electrolytes, a more appropriate expression is the current as a function of potential versus a pH-dependent reference electrode (E) such as Equation 2-2, since the counter electrode in a fuel cell (the hydrogen electrode) has the same

thermodynamic dependence on pH as the oxygen electrode. The expression

$$\left[\frac{\partial \log i_k}{\partial \log a_{\text{H}^+}} \right]_{\text{E}} = s_{\text{H}^+} - \alpha = q_{\text{H}^+} \quad (2-35)$$

follows from Equation 2-2, where q_{H^+} is a strictly kinetic reaction order (ie. without the effect of thermodynamics). Some of the reaction orders and transfer coefficients that have been reported are shown in Table 2-1. These are based on Equation 2-1 since s_{H^+} is usually reported. The following conversions to a hydroxide reaction order will be useful for comparison with the results in Chapter 4.

$$s_{\text{OH}^-} = -s_{\text{H}^+} \quad \text{and} \quad q_{\text{OH}^-} = s_{\text{OH}^-} - \alpha \quad (2-36)$$

Damjanovic, Genshaw and Bockris (35) examined the role of peroxide in the kinetics of OR in 0.1N KOH on platinum with the RRDE technique. They were the first to report that measured kinetic parameters for OR in alkaline electrolytes were **not** sensitive to impurities, as is the case for acids. They compared steady-state current measurements (as opposed to slow potential sweeps) on platinum surfaces that had been prerduced with a cathodic pulse with those that had not been so treated. Their data were analyzed according to Damjanovic's three-step model for the dual-path mechanism, already discussed in Section 2-2. They found the reaction to occur by both pathways at comparable rates on "prerduced" platinum, with about 23% of the current generated via the 2-electron pathway for potentials greater than 0.6 V vs. RHE. The rate constants k_1 and k_2 exhibited two Tafel regions (the symmetry coefficients are shown in Table 2-1). For their "not prerduced" electrode they found similar results for k_2 . However, they observed only one Tafel region for the 4-electron-path rate constant k_1 , with significantly lower values than for the reduced electrode. They suggested that the first part of the reaction sequence for the 2-electron path included the following steps:

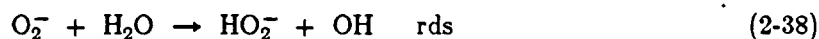


Table 2-1: Diagnostic Criteria Reported for Oxygen Reduction in Alkaline Electrolytes

Author (ref)	Platinum Oxidation State	Type of Experiment	Global Process				4-electron path				2-electron path			
			high cd		low cd		high cd		low cd		high cd		low cd	
			α	s_{H^+}	α	s_{H^+}	α	s_{H^+}	α	s_{H^+}	α	s_{H^+}	α	s_{H^+}
Damjanovic et al.(35)	Red.	SS	< 1/2	-	1	-	2/5	-	< 1	-	< 1/2	-	< 1	-
	lt. Oxid.	SS	< 1/2	-	< 1	-	< 1	-	< 1	-	2/5	-	< 1	-
Sepa et al.(28)	Red.	SS	1/2	0	1	1/2	-	-	-	-	-	-	-	-
Appel & Appleby (36)	Red.	SW	-	-	> 1	1	-	-	1	1	-	-	3/2	1
Bowen & Urbach (37)	lt.Oxid.	SW	-	-	?	?	-	-	-	-	-	-	3/2	1
Park et.al. (38)	lt.Oxid.	SW	0.18	-	< 1	-	2/5	-	-	-	-	-	-	-
Bagotski et al.(32)	lt. Oxid.	SS	-	-	-	-	1/2	1/2	1	1	-	-	-	-
	mod.Oxid.	SS	-	-	-	-	<< 1/2	-	.6-.43	?	<< 1/2	-	.64	-
Tarasevich (39)	Red.	SS	-	-	.85-1	1	-	-	-	-	-	-	-	-
	hi.Oxid.	SS	-	-	1.75-2	.875-1	-	-	-	-	-	-	2	1
Bagotski et al. (40)	hi.Oxid.†	SW	-	-	.66	.66	-	-	-	-	-	-	-	-
	hi.Oxid.†	SW	-	-	.75	.75	-	-	-	-	-	-	-	-
	Red.	SW	-	-	.75	.76	-	-	-	-	-	-	-	-
Fischer & Heitbaum(30)	?	SW	< 1/2	-	-	-	-	-	-	-	-	-	-	

SS: Steady state measurement

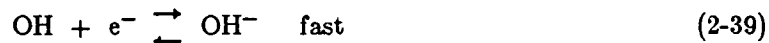
SW: Slow linear potential sweep measurement

Lightly Oxidized: $E_{ox} < 1.1V$

Moderately Oxidized: $1.1 < E_{ox} < 1.7V$

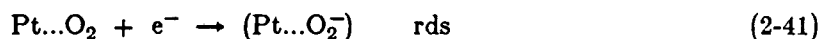
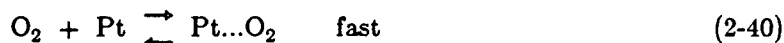
Highly Oxidized: $E_{ox} > 1.7V$

† Thermally Oxidized in O_2 at $500^\circ C$



with hydrogenation of an electroadsorbed oxygen molecule as the rds. This was based on the observed Tafel slopes and diagnostic criteria borrowed from oxygen evolution work. Such criteria refer necessarily to a highly-oxidized platinum surface and are really not applicable to OR at low oxide coverages. For the 4-electron path, they listed several possibilities with the rds dependent on current density.

In later work, Sepa, Vojnovic and Damjanovic (16,28) measured steady-state polarization curves with a prerduced platinum RDE, but this time they ignored the possibility of peroxide generation. They cited the work just discussed (35) as proving that both paths have the same rate-limiting step, depend on surface state in the same way, and can therefore be treated as one reaction. As for acid electrolytes, they proposed that the rds was the first electron transfer to a chemically adsorbed oxygen molecule at all current densities:



For this rds, the kinetic current is expressed as

$$i_k = nFk'_c a_{\text{O}_2} \exp\left(\frac{-\beta_c FV}{RT}\right) \quad (2-42)$$

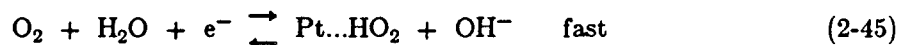
Following the procedure as outlined above for the acid electrolytes, Sepa et al. obtained the following expressions for the current density in the high-current-density (low-oxide-coverage) region and low-current-density (high-oxide-coverage) regions, respectively:

$$i_k = nFk'_c p_{\text{O}_2} \exp\left(\frac{-FV}{2RT}\right) \quad (2-43)$$

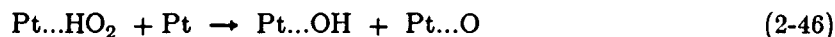
$$i_k = nFk'_c a_{\text{OH}^-}^{-1/2} p_{\text{O}_2} \exp\left(\frac{-FV}{RT}\right) \quad (2-44)$$

Appel and Appleby (36) studied this reaction as a function of pH in mixtures of KOH, K₂CO₃, and K₂SO₄, holding the concentration of K⁺ ion constant, with the RRDE technique.

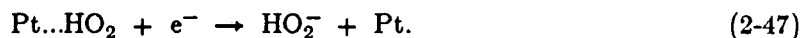
This work was carried out with care to obtain a reproducibly prerduced Pt surface, and currents were measured during slow (10 mV/sec) anodic potential sweeps from 0 V vs. RHE. They calculated rate constants for two parallel paths in the low-current-density (high-potential) region only and reported a Tafel slope for the global process of "a little less than RT/F." They claimed that this was due to the combined effects of the dominant 4-electron path, with a slope of RT/F and the 2-electron path with a slope of 2RT/3F. This slope for the 2-electron path agrees with that reported by Bowen and Urbach (37) in their studies of the O₂/H₂O₂ couple for a moderately oxidized surface (even though typographical errors in the Appel and Appleby article would have one believe differently). Also in agreement with Bowen and Urbach, they measured currents for the 2-electron process which increased with pH. From their recorded diagnostics, they proposed that both paths proceed through the same first step



followed by the rds for the 4-electron path



and for the 2-electron path

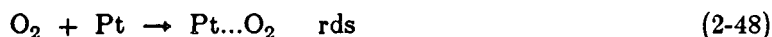


This mechanism results in a value of q_{H^+} equal to zero for the direct reduction path and $q_{\text{H}^+} = -\frac{1}{2}$ for the 2-electron path. For the global process, since the direct reduction is dominant on these surfaces, q_{H^+} is zero, in contradiction to the results of Sepa et al. (28).

The source of this contradiction is probably due to the neglect of the dual pathways by Sepa et al. Even if the pathways have the same rds, Damjanovic had already pointed out that the analysis of RDE data must be modified since the numbers of electrons transferred in the two pathways are different according to the discussion in Section 2-2. Another difference in the two works just discussed is the pretreatment of the surface. The steady-state surfaces will have higher oxide coverages and ages than the pre-reduced surfaces and, as we will see later, tend to

favor the 2-electron pathway for OR. If the surface in the work of Sepa et al. was moderately oxidized (instead of reduced) their reported transfer coefficient and pH reaction order agree with those of Appel and Appleby (for the 2-electron path)!

Bagotsky, Luk'yanycheva and Leites (32) reported that on a well-cycled and reduced platinum surface, OR in 0.1 M NaOH proceeds only 1% via the 2-electron-route in the potential range of 0.2-0.5 V vs. RHE depending on solution purity, and about 11% by this route at higher potentials (as opposed to the 23% reported by Damjanovic). Their reported rate constants, k_1 and k_2 , showed a similar dependence on potential with $k_1 > k_2$. They proposed yet another mechanism wherein the rds for the 4-electron pathway was the slow adsorption of oxygen at all current densities



For this rds, the potential dependence and therefore the reaction rate is controlled by the amount of free surface, θ_{Pt} , according to the relation

$$i_k = nFk_c^0 \theta_{\text{Pt}} \exp\left(-\sum_i \beta_i f_i \theta_i\right) \quad (2-49)$$

where $\theta_{\text{Pt}} = 1 - \sum_i \theta_i$ (for i possible surface species).

We can conclude from this review that the direct reduction pathway is dominant on surfaces of low oxide coverage in dilute alkaline electrolytes. From Appel's work the overall rate may have a weak kinetic dependence on pH in cases where the 2-electron pathway represents a significant portion of the current. The size and dependence of k_2 on potential seem to be a strong function of the platinum surface oxidation state. This topic has been investigated thoroughly by several Russian authors and is the subject of Section 2-5. Contrary to the authors discussed above, Bagotsky in conjunction with others (32,41,42), reports that measurements of OR kinetics with the RRDE technique are indeed sensitive to electrolyte impurities or time. It is not possible to ascertain whether the time-dependent behavior that they observe is due to impurities in the solution and not to platinum state or "age" since they both affect the surface.

However, impurity effects should not be as reproducible or as well-behaved as oxide effects.

2.3.3. Effect of Temperature

The dependence of OR kinetics on temperature should be a function of the dependence of a_1 and k_c on temperature according to Equation 2-1. Of the reactant activities, the solubility of oxygen is the most dependent on temperature, and the dependence of k_c is expected to follow the activation energy of the rds. The Tafel slope, b ,

$$b = \frac{-2.303RT}{\alpha FV} \quad (2-50)$$

is expected to be a linear function of T since the transfer coefficient (α), for even a complex reaction, is expected to be independent of potential and temperature. However, several authors have reported temperature-independent Tafel slopes for electrocatalytic reactions involving adsorbed species, such as OR on platinum in concentrated phosphoric acid (43,44), the discharge of bromine in acetonitrile (45) and more recently for OR on iridium in dilute aqueous electrolytes (46). Conway (47) studied this phenomenon in detail, and Yeager (48) suggested that Conway's explanation through entropy effects was the most plausible, but this area is far from being understood.

For OR on platinum in KOH, Park et al. (38) reported a classically temperature-dependent Tafel slope, for low current densities, as did Sepa et al. (49,50) for pH 1.9 and 11.6 M LiClO₄ solutions.

As will become obvious in the next section, the relative rates of the two pathways depend to a great extent on the amount of the oxide (and its age). Park also reported that the amount of oxide formed on a platinum electrode in alkaline electrolytes decreases with increasing temperature. It should not be surprising if α appears to be temperature dependent in some cases on platinum.

2.4. Dependence of Oxygen Reduction Kinetics on Oxide Coverage

Paucirova, Drazic and Damjanovic (51) studied the effect of oxide coverage on OR kinetics in acid electrolytes. They measured the current response to potential steps from a completely reduced surface (0.5 V) to the potential of interest. OR currents corresponding to zero coverage were obtained by extrapolating to zero time. They reported the relation

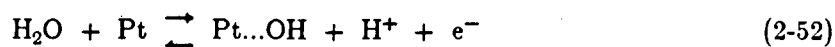
$$i_{\theta} = i_{\theta=0} \exp\left(\frac{-\beta f \theta}{RT}\right) \quad (2-51)$$

where $\beta f = 10$ J/mol. Their extrapolated $i_{\theta=0}$ values exhibited a potential dependence with a Tafel slope of about $2RT/F$ (120 mV/decade) for potentials up to 1 V. These results are consistent with the assumption that adsorption controls the potential dependence of OR. This type of mechanism should not be expected to hold in alkaline electrolytes, however, where adsorption begins at much lower potentials. By the potential where OR is kinetically limited, a much larger amount of oxide is on the surface and one needs to consider aging effects and the actual stoichiometry of the surface.

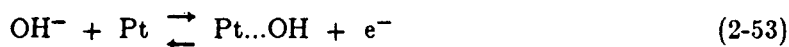
Several Russian authors have studied the effect of platinum oxidation state on oxygen reduction in alkaline electrolytes. They controlled the holding time at a series of oxidizing potentials as a means of varying the oxide "coverage" in the absence of dissolved oxygen. OR kinetics were then studied by measuring steady-state galvanostatic polarization curves with a RRDE, after an identical pretreatment. Tarasevich et al. (39) used electrodes that were well-cycled, well-reduced and then oxidized for 10 minutes at potentials up to 1.7 V. They observed the same dependence of current on coverage as in Equation 2-51. At the lower oxidation potentials, they correlated a change in OR Tafel slope from about 60 to 30-35 mV/decade with the decline in the observed value of βf to essentially zero at the highest oxidation potentials. They proposed that the low slopes are due to the complete suppression of the 4-electron path with the O_2/H_2O_2 couple at quasi-equilibrium on the highly oxidized surface. This slope is slightly lower than that reported by Bowen and Urbach (40 mV/decade), but their surface was also more highly oxidized (37).

Luk'yanycheva et al. (42) went further in their investigations of the oxide effect. They observed a decrease in βf , from 9 to 5, with holding time at a constant oxidation potential. They reported that the reaction rates of both pathways decrease as coverage increases at a constant oxide age, but that the rate of the 2-electron path increases with the age of the oxide at constant coverage! Therefore, as coverage and age increase, there is a trade-off between the decrease in rate due to coverage (especially the 4-electron path) and an increase in the rate of the 2-electron path (which is also becoming dominant as coverage increases). The net result is a slight increase in the global rate in some cases. Their analysis was based on partial currents i_1 and i_2 . They did not distinguish between changes in k_2 or $k_3 + k_4$.

Later, this same group reported the dependence of k_1 , k_2 and $k_3 + k_4$, calculated from RRDE measurements, on the oxidation potential used to pretreat the electrode (41). They found k_1 to decrease and k_2 to increase with increasing E_{ox} (oxide coverage and/or age), at a constant OR potential. They also found that the total rate at which the intermediate peroxide reacts further, either through reduction (k_3) or decomposition (k_4), to be fairly independent of E_{ox} . The Tafel slope for the total current decreased smoothly from 120 to 60 mV/decade as E_{ox} increased. They proposed the rate determining step mentioned above in Equation 2-48. The change in Tafel slope is attributed to a change in the potential dependence of the equilibrium coverage of dominant surface oxide species: PtOH at low potentials and high current densities, and PtO at high potentials and low current densities. At lower coverages PtOH is assumed to form according to



or more appropriately in alkaline electrolytes



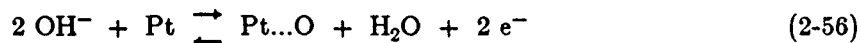
At equilibrium they write

$$\exp(-\beta f \theta_{\text{OH}}) = K_{\text{ads}} \left(\frac{\theta_{\text{OH}}}{1-\theta_{\text{OH}}} \right)^\beta (a_{\text{H}^+})^\beta \exp\left(\frac{-\beta FV}{RT}\right) \quad (2-54)$$

Rearranging and combining with 2-49 above yields an expression for current

$$i_k = nFk_c^o p_{O_2} \theta_{OH}^\beta (1-\theta_{OH})^\beta (a_{H^+})^\beta \exp\left(\frac{-\beta FV}{RT}\right) \quad (2-55)$$

The same type of development can be carried out for higher coverages where PtO is assumed to form according to



With this equilibrium and Equation 2-49, the expression for i_k is

$$i_k = nFk_c^o p_{O_2} \theta_O^\beta (1-\theta_O)^{1-\beta} a_{H^+}^{2\beta} \exp\left(\frac{-2\beta FV}{RT}\right) \quad (2-57)$$

This mechanism predicts diagnostic criteria which are consistent with the more-recent results of Sepa et al. for OR on iridium (46). The fact that the global Tafel slope decreased only to 60 mV/decade compared to the 30-40 mV/decade cited above may be a result of the lower oxidation times allowed by Luk'yanycheva et al. If this is the case we can argue that oxide age is responsible for the attainment of a quasi-equilibrium state for the peroxide (low Tafel slopes).

A mechanism suggested relatively early by Tarasevich (39) incorporated the dependence observed for the rate of the 4-electron pathway on coverage (Equation 2-51) with a limit of quasi-equilibrium for the peroxide reaction at high coverages. This combination of limiting cases can qualitatively predict Tafel slopes anywhere from 30 to 120 mV/decade.

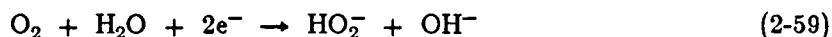
It seems clear that the rate of the 4-electron pathway decreases with increasing oxide coverage and age. The effect of the platinum oxidation state on the rate of the 2-electron pathway is less obvious in RRDE experiments because of the competing effects on the rate of peroxide production and further reaction. The observed Tafel slope will be intermediate to those for the participating parallel reactions. With these conclusions in mind we will review what has been learned about the kinetics of OR in concentrated alkaline electrolytes.

2.5. Oxygen Reduction in Concentrated Alkaline Electrolytes

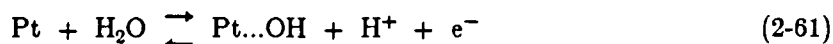
In their early work with concentrated electrolytes, Blurton and McMullin postulated that platinum is more active for OR in alkaline electrolytes than in acid electrolytes because the former supports higher peroxide production rates (52). Their preliminary "proof" was an observed change in Levich slope from $n = 2$ to just less than $n = 4$, with light platinization of the disk in RDE measurements. This was said to improve the rate of recycling of peroxide to oxygen through a catalytic process (step 4 in Figure 2-2). However, this behavior could also be observed if adsorbed impurities were blocking the surface (because of an increase in surface area to electrolyte volume ratio with platinization). The change in Levich slope for a reversible electrode process in conjunction with product recycling through a catalytic reaction was calculated by McIntyre (24)

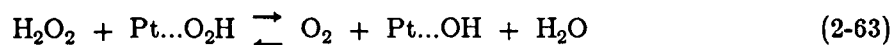
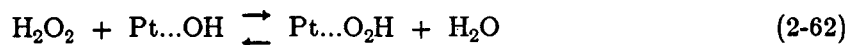
$$\lim_{k_4 \rightarrow \infty} (i_{L,r}) = \left(\frac{s}{s-1} \right) i_L \quad (2-58)$$

where k_4 is the s -order catalytic rate constant, i_L is the mass-transfer-limited current density ignoring recycling and $i_{L,r}$ is the observed i_L in the presence of the recycling. Blurton et al. assumed that step 4 was second-order ($s=2$), so as k_4 increased with platinization, $i_{L,r} \rightarrow 2i_L$ (which agrees with a shift of n from 2 to 4). For finite values of k_4 , the intercept of the Levich plot will pass through zero ($\lim_{\omega \rightarrow 0} (i_{L,r}) = 0$), but for higher rotation speeds, the plot of $i_{L,r}$ vs $\omega^{1/2}$ will exhibit downward curvature. Based on this analysis, Blurton and McMullin (53) proposed that neither the direct 4-electron path nor the further electrochemical reduction of H_2O_2 occur on platinum in 30% KOH at 70°. OR proceeds according to



with total recycling of the peroxide catalyzed by surface oxide according to





They attempted to measure peroxide production rates but those results were inconclusive.

More recently, Park et al. studied OR in KOH at concentrations of 0.1 to 6 M (38). They carried out RRDE measurements with an "oxidized" platinum surface, generated by holding at 1.2 V vs RHE for 2 to 3 minutes before measuring the polarization curves with slow cathodic potential sweeps. They reported rate constants for the three-step Damjanovic model for $C_{\text{KOH}} \leq 1\text{M}$ and concluded that their RRDE results at higher KOH concentrations were not satisfactory when examined with this model. They gave no reasons for this and did not attempt to use other models. From their RDE data, they did find that despite lower oxygen solubility, the rate of OR increases as KOH concentration increases.

It appears that a change OR mechanism may occur as concentration of KOH increases above 1 M. This is not too surprising for KOH considering that the thermodynamic properties of this electrolyte change dramatically at high concentrations. Chapter 4 presents our study this mechanism as a function of electrolyte concentration or hydroxide anion activity, and platinum oxidation state.

Chapter 3

Oxygen Reduction on Platinum in TFMSA and TFEDSA

3.0. Introduction

Trifluoromethane sulfonic acid (TFMSA) has been considered for low-temperature (< 110 °C) fuel cell applications due to the favorable oxygen reduction rate observed in this electrolyte compared with phosphoric acid (54). The use of the less-volatile, higher homolog of TFMSA, tetrafluoroethane -1,2-disulfonic acid (TFEDSA), was suggested by Baker et al. (55) to overcome the problems of high acid vapor pressure and low contact angle with PTFE observed with concentrated TFMSA. Preliminary investigations with TFEDSA (56) showed insignificant acid vapor pressure and acceptable water vapor pressure at 60-70 wt% acid, as well as high (non-wetting) contact angles with PTFE. However, it has been suggested that the reaction order with respect to oxygen concentration is $\frac{1}{2}$, based on the failure of the first-order model for mass transfer to a rotating disk electrode (RDE) (26). This reaction order has been shown to be unity in perchloric, sulfuric and phosphoric acid electrolytes (57-59). In this chapter, we report our measurements of the rate of OR in TFEDSA and TFMSA on smooth Pt with the RDE technique. Kinetic currents in the two electrolytes are compared at pH=1. Dependence of the reduction current on oxygen concentration was determined independently by varying the partial pressure of oxygen in contact with the electrolyte.

3.1. Experimental Procedure

Experiments were performed in a Pyrex cell with a surrounding water jacket. Circulation of thermostatically controlled water was used to maintain the cell temperature at 25 ± 0.5 °C. The working electrode (0.46cm² Pt), obtained from Pine Instruments Inc., was polished with a succession of alumina papers, followed by 6 μ m and then 1 μ m diamond paste. Rotation was

achieved with a Pine Instruments Analytical Rotator. A dynamic hydrogen reference electrode (DHE) (60) was held in a separate compartment which was connected to the main cell through a Luggin capillary. The DHE held a constant potential of 3 mV negative to an RHE at the same pH, as was checked with a standard calomel reference electrode. A 1-cm² Pt-foil counter electrode was used directly in the cell, placed well outside the diffusion boundary layer as can be seen in Figure 3-1. Premixed cylinders of oxygen and nitrogen (4.31 - 58.66% \pm 0.01% oxygen), pure oxygen and pure nitrogen were further purified by passing through 3 molecular-sieve beds as suggested by Hsueh et al.(21). All gases were humidified by bubbling through doubly distilled water at room temperature before entering the cell.

All glassware and electrodes (except the DHE) were cleaned by soaking in a mixture of concentrated sulfuric and 70% nitric acids for two days. This was followed by rinsing and soaking in freshly distilled water at least four times.

TFMSA, from 3M Corporation, was purified by a succession of steps devised by Ross et al. (61). This technique consisted of two successive distillations followed by the addition of about 10% hydrogen peroxide to oxidize any remaining organic impurities. The peroxide was decomposed and removed in a final distillation. The final distillate was collected over a boiling point range between that of the acid and its monohydrate (162 °C to 205 °C). The product was then cooled slowly to crystallize out the monohydrate and the remaining inorganics which favor the solid phase (62). Potassium tetrafluoroethane-disulfonate was received from KOR, and it was converted to the acid via ion-exchange with pre-purified resin in another laboratory (63). Complete conversion to the acid was checked by titration. Water was removed by vacuum distillation, leaving the acid dihydrate. The hygroscopic nature of this solid prevented exact knowledge of the water content. Solutions of both these electrolytes were prepared by dilution with ultra-pure water (Harleco) to a pH of unity. Solutions were pre-electrolyzed in the cell with large-area platinum gauze electrodes for at least 72 hours at a current of 1mA.

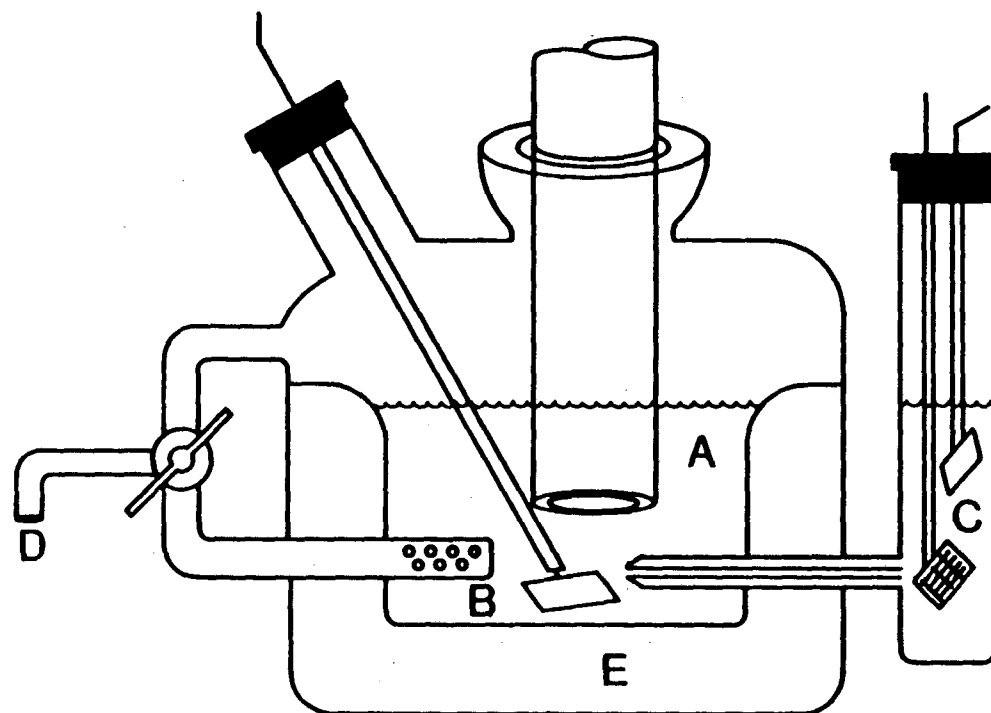


Figure 3-1: Electrochemical cell.
A, Rotating disk electrode;
B, Counter electrode;
C, Dynamic hydrogen reference electrode;
D, Gas inlet;
E, Water jacket.

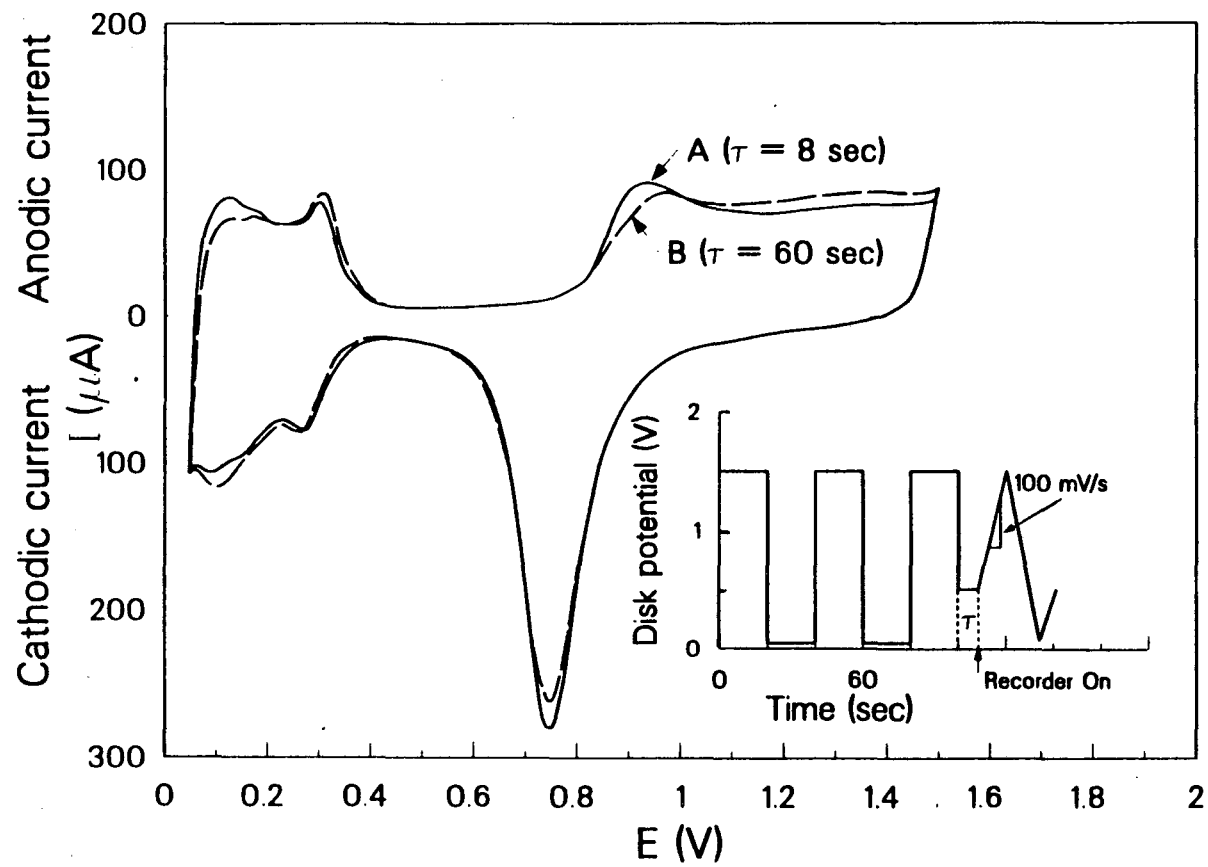
- XBL 8711-4752 -

The potential of the working electrode was controlled with a PAR model 173 potentiostat and a PAR model 175 universal programmer. Current-potential data for the experiments reported in this chapter were recorded with an HP7046B X-Y recorder.

3.2. Results

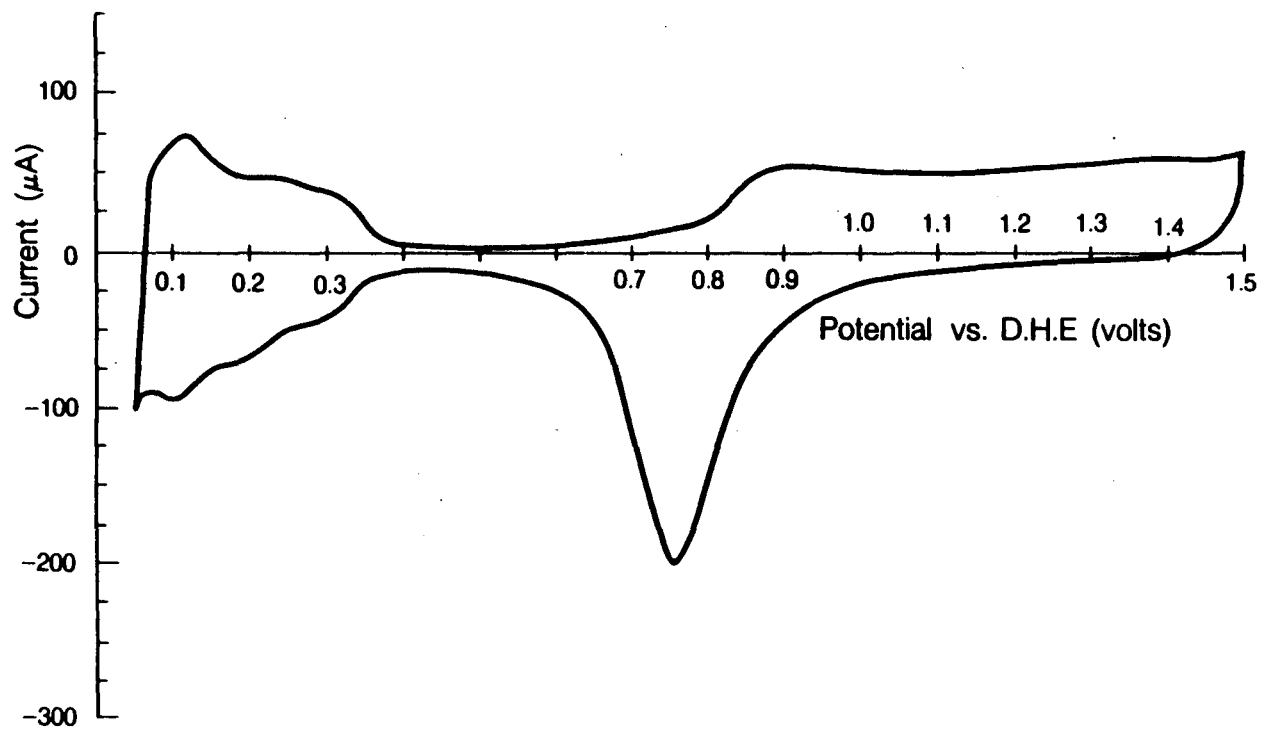
First-sweep cyclic voltammograms were recorded in both electrolytes. Two such traces in and TFEDSA and TFMSA at pH=1 are shown in Figure 3-2 and Figure 3-3, respectively, with the potential profiles used to generate these curves shown in the inset of Figure 3-2. Curve A was recorded on the stationary disk following pretreatment; curve B was recorded following the same pretreatment with the addition of a 1-minute hold at 0.4V vs DHE while rotating the working electrode at 1600 rpm before recording the voltammogram on the stationary electrode. The absence of any additional peaks or significant shifting of the existing peaks indicates satisfactory electrolyte purity. The charge associated with the hydrogen adsorption region of the curves was used to quantify the active electrode area and all mass-transfer-corrected or "kinetic" currents reported in this thesis are adjusted to an effective roughness factor of 1.0.

Current-potential sweeps at several rotation speeds were recorded in TFMSA and TFEDSA with several partial pressures of O₂. Those for TFEDSA in contact with 1 atm. oxygen are shown in Figure 3-4. The reduction currents were found to depend somewhat on sweep rate and sweep direction because of the changing oxidation state of the electrode as discussed in Chapter 2. Therefore, when comparing TFEDSA and TFMSA, only anodic sweeps at 10 mV/sec were used. Similar curves were recorded in the absence of O₂ to quantify the anodic currents associated directly with platinum oxidation which lead to non-zero baselines in the low O₂ pressure experiments. Relatively high (15 to 30 Ω) uncompensated solution resistances in these dilute electrolytes were estimated from conductance measurements between the working and counter electrodes and checked by the current-interrupt method. Data were adjusted after the experiment by reading the IR-free potential along lines with slopes of 1/R_Ω, as is indicated in Figure 3-4.



XCG 8410-13374

Figure 3-2: First-sweep cyclic voltammogram in TFEDSA, pH =1, 25°C, Argon atmosphere.
 A, recorded after pretreatment;
 B, recorded after pretreatment and holding 60 sec at 0.4 V while rotating at 1600 rpm.



XBL 844-9321

Figure 3-3: First-sweep cyclic voltammogram in TFMSA recorded after pretreatment, pH = 1, 25 °C, Argon atmosphere.

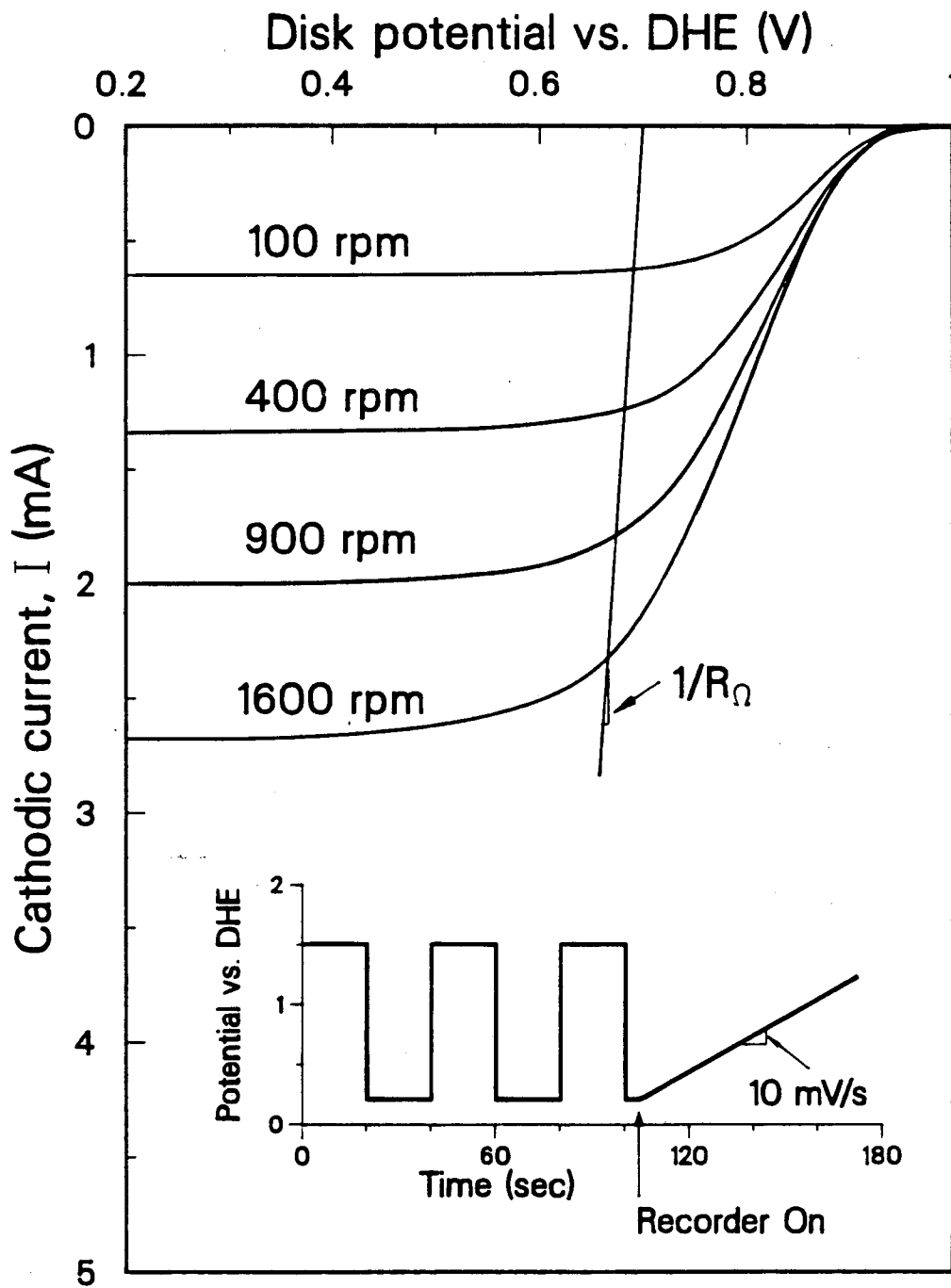


Figure 3-4: Current-potential sweeps for oxygen reduction at a Pt RDE in TFEDSA, pH = 1, 25 °C.

XCG 8410-13373

The observed limiting currents are plotted against $\omega^{1/2}$, according to the Levich equation (Equation 2-9), and are shown in Figure 3-5. If oxygen solubility follows Henry's law

$$C_{O_2} = H_{O_2} p_{O_2} \quad (3-1)$$

in these electrolytes, the slope of these plots should be proportional to the partial pressure of O_2 above the solution. Figure 3-6 shows the linear dependence of $\log B$ on $\log p_{O_2}$ for TFMSA and TFEDSA at $pH = 1$ and $25^\circ C$. Both lines have slopes close to one.

In sufficiently pure acid electrolytes, the reduction of oxygen can be assumed to proceed through a single 4-electron pathway on platinum. The measured disk current, i_d is defined as in Equation 2-2

$$i_d = nFk'_c (C_{O_2}^*)^{q_{O_2}} \exp\left(\frac{-\beta FE}{RT}\right) \quad (3-2)$$

where k'_c includes any dependence on pH . For a single reaction at a rotating disk, Equation 2-10 can be rearranged to obtain

$$C_{O_2}^* = \left(\frac{i_L - i_d}{i_L}\right) C_{O_2}^\infty \quad (3-3)$$

Combining Equations 3-2 and 3-3 using Equation 3-1, yields the following expression for the current at a disk electrode under conditions of mass-transfer control (for an irreversible reaction)

$$i_d = nFk'_c(H_{O_2})^{q_{O_2}} p_{O_2}^{q_{O_2}} \left(\frac{i_L - i_d}{i_L}\right)^{q_{O_2}} \exp\left(\frac{-\beta FE}{RT}\right) \quad (3-4)$$

For potentials near 0.9 V, the currents are insensitive to rotation speed above about 400 rpm, as shown in Figure 3-4. Under these conditions $i_d \ll i_L$, so that $\left(\frac{i_L - i_d}{i_L}\right)$ approaches unity, and $i_d = i_k$. According to Equation 3-4, the reaction order, q_{O_2} , can then be determined from the slope of a plot of $\log i_d$ vs $\log p_{O_2}$ at constant E. Figure 3-7 shows kinetically limited current as a function of P_{O_2} for TFMSA and TFEDSA. Part A, for $E = 900mV$, indicates that the reaction order is 1.0 ± 0.05 .

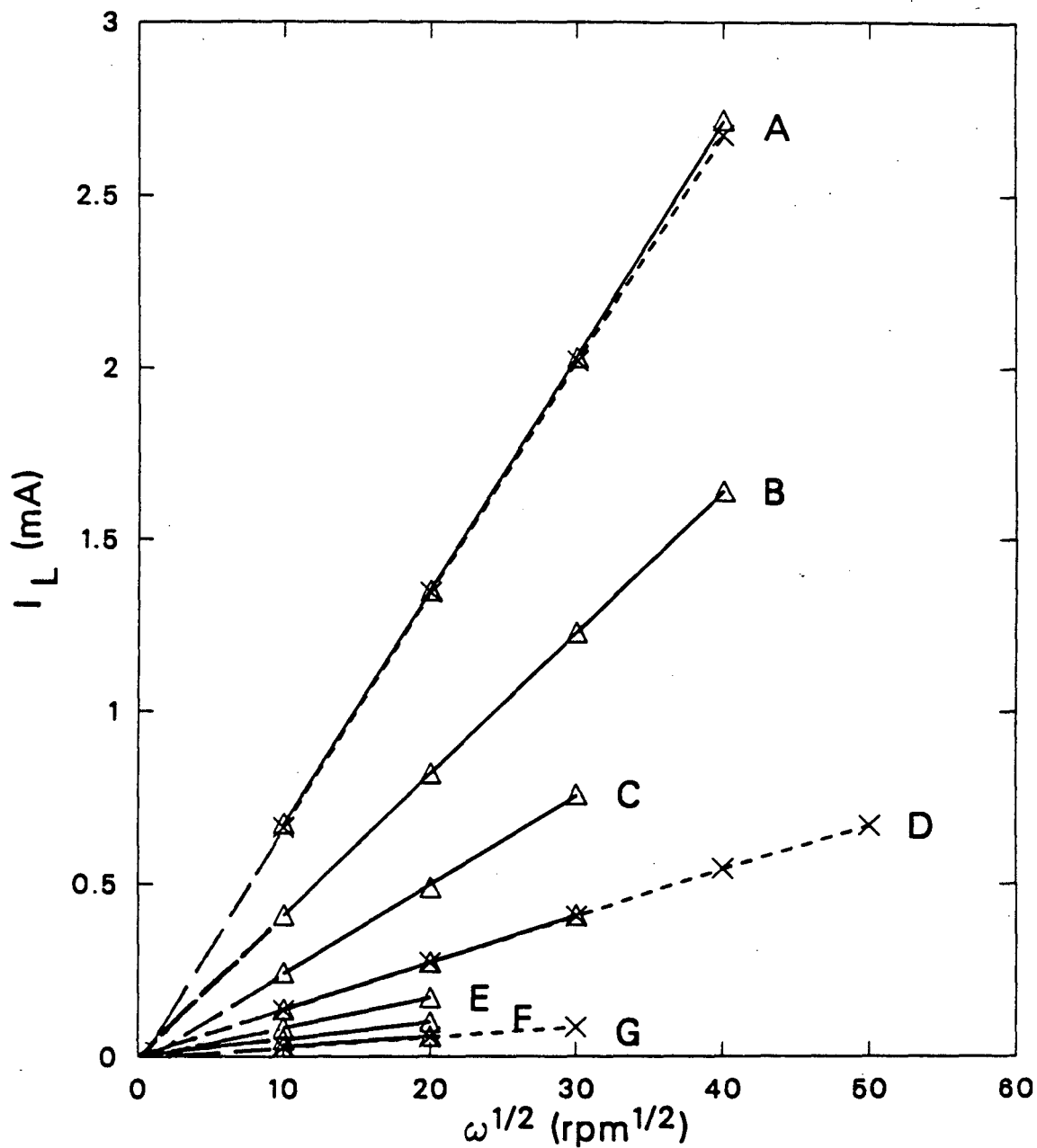


Figure 3-5: Levich Plots for TFEDSA and TFMSA at various oxygen partial pressures.
 ——— Δ , TFMSA, pH = 1;
 ——— \times , TFEDSA, pH = 1.
 A, 1.0 atm; B, 0.5866; C, 0.3503; D, 0.2028,
 E, 0.1258; F, 0.0753; G, 0.043.

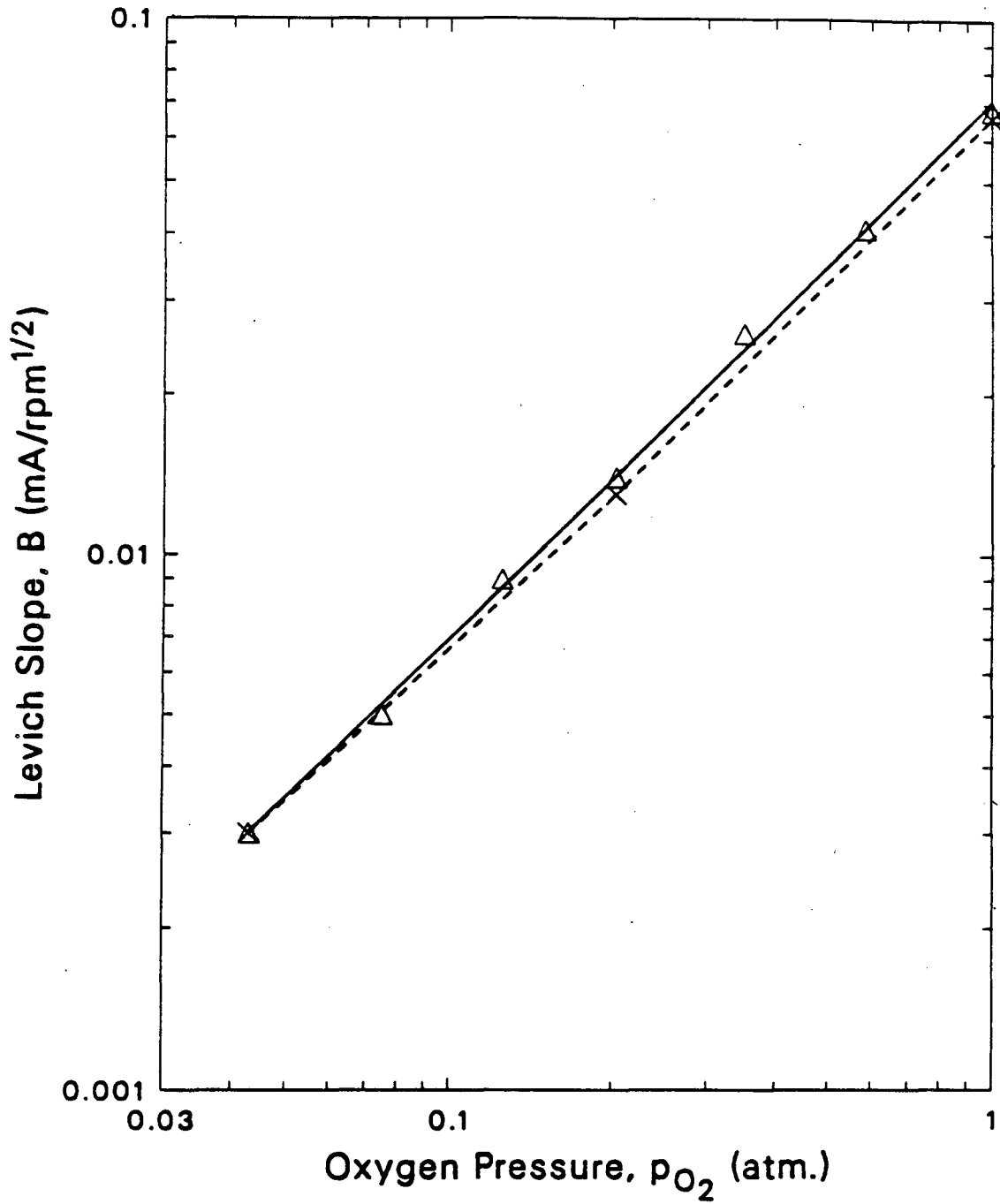


Figure 3-6: Levich Slopes from Figure 3-5.
———Δ, TFMSA;
-----×, TFEDSA;

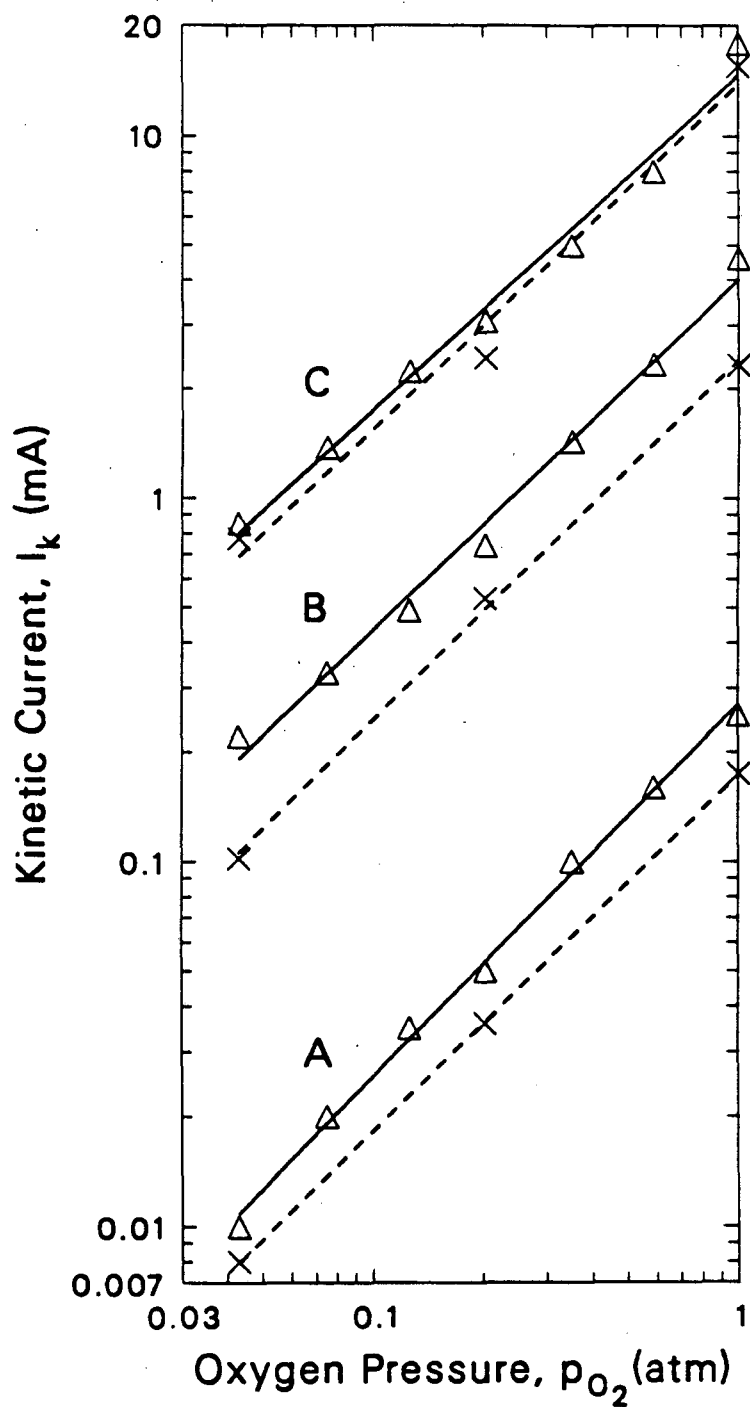


Figure 3-7: Kinetic current dependence on oxygen pressure in TFEDSA and TFMSA.
 —△, TFMSA;
 —×, TFEDSA;
 A, 0.90 V vs DHE; B, 0.80 V vs DHE; C, 0.70 V vs DHE.

When q_{O_2} is unity (at 0.90 V) Equation 3-4 can be simplified to Equation 2-12, where i_k is defined by Equation 3-2 with $C_{O_2}^*$ replaced by $C_{O_2}^\infty$. The kinetic current, i_k , may be obtained from the intercept of a plot of i_d^{-1} vs $\omega^{-1/2}$ at constant potential and oxygen pressure, since $i_L^0 = B^0\omega^{1/2}$. The values of i_k may then be used with Equations 3-1 and 3-2 to test the value of q_{O_2} by plotting $\log I_k$ vs $\log p_{O_2}$ where $I_k = i_k A$. This is shown in Figure 3-7 for 0.8 V (lines B) and 0.7 V (lines C), and the reaction order is seen to be unity within experimental error.

A direct comparison of the kinetic current densities for TFEDSA and TFMSA at pH = 1, one atmosphere of O_2 and 25 °C is shown in Figure 3-8. These current densities are based on the active area of platinum as mentioned above (roughness factor = 1). The similarity of the Levich slopes for the two electrolytes (0.46 and 0.44 mA-sec^{1/2}/cm² for TFMSA and TFEDSA, respectively) indicate that the oxygen solubility and diffusivity in the two acids are very similar. Over the potential range 0.67 to 1.0 V vs DHE, the kinetic currents are very similar. The change of slope is observed at 0.8 V, as discussed in Chapter 2. Exchange current densities calculated by extrapolation of the results obtained at higher potentials are 4×10^{-8} and 6×10^{-8} mA/cm² for TFMSA and TFEDSA, respectively. These can be compared with the exchange current density of 9×10^{-8} mA/cm² reported for 1.1 N TFMSA, 25 °C, by Appleby and Baker (64). The difference is probably due to the lower O_2 solubility in the more concentrated electrolyte.

3.3. Conclusions

From the experiments reported above, and the analysis of the data, it is concluded that the reaction order of the electrochemical reduction of oxygen on platinum in TFEDSA and TFMSA with respect to oxygen concentration is unity, over the full potential range studied (1 V to 0.65 V vs DHE). The kinetics of oxygen reduction on platinum in TFEDSA are very similar to those for TFMSA, the currents being very closely comparable at pH = 1 for identical overvoltages.

These results offer some promise for the use of fluorinated organic acids in high-performance fuel cells, while avoiding the high vapor pressure of TFMSA and its undesired wet-

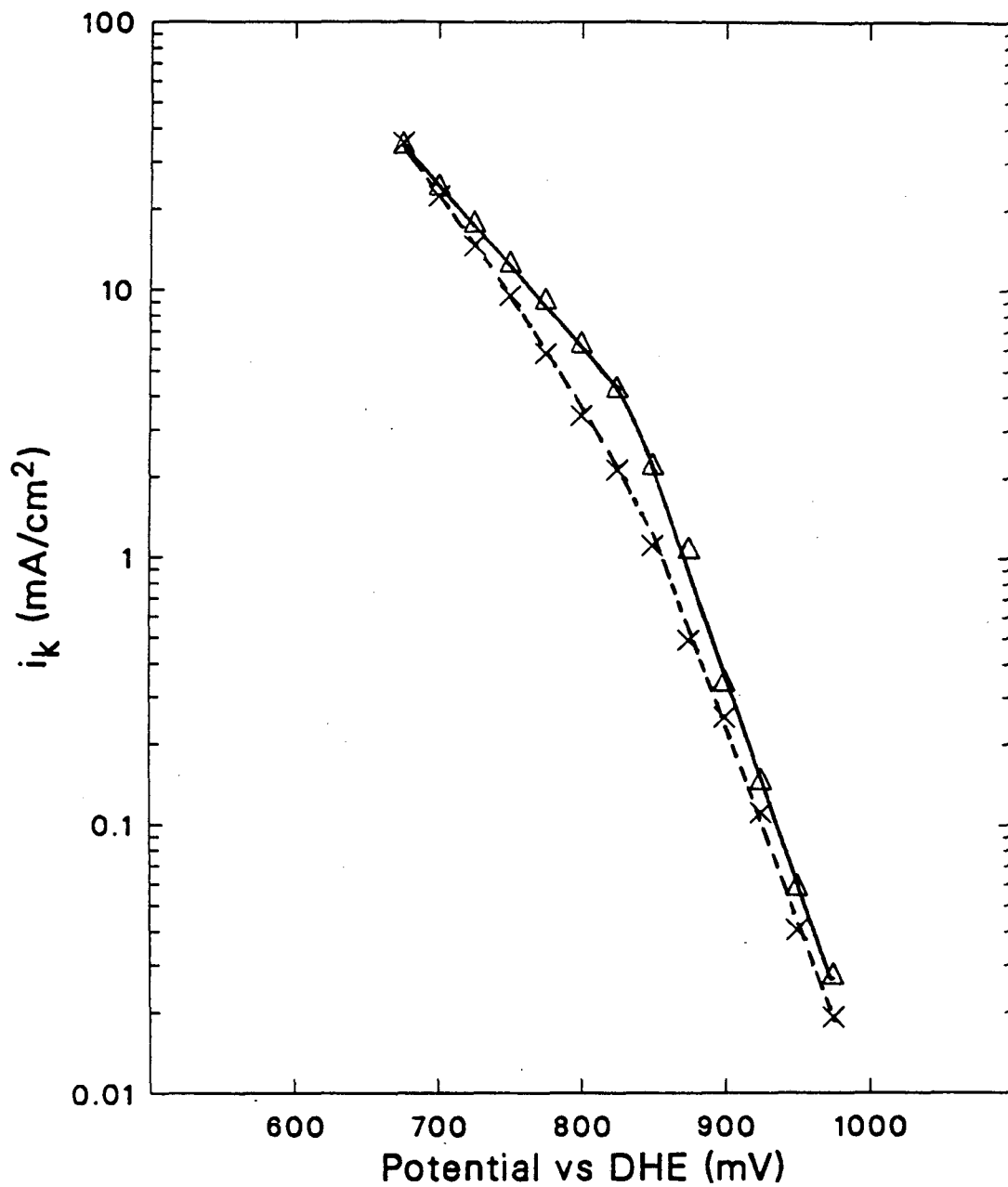


Figure 3-8: Kinetic current densities for oxygen reduction in "super-acid" electrolytes at 1 atm. oxygen, pH = 1.0 and 25 °C.

— Δ , TFMSA;
- - - x, TFEDSA;

ting of PTFE. Furthermore, pressurization is expected to improve significantly the performance of cathodes in fuel cells using TFEDSA and TFMSA.

Chapter 4

Kinetic Studies of Oxygen Reduction on Pt in Alkaline Electrolytes

4.0. Introduction

Alkaline electrolytes have long been known to support higher OR currents on platinum than those observed in acid electrolytes (65). The reasons for this are not well understood. In alkaline media, the potential of zero charge for platinum is closer to the region of OR activity than in acidic media, which should lead to more interference by specific anion adsorption. Higher peroxide production rates have been cited as the key to the higher OR currents (53) even though peroxide production results in the transfer of only 2 electrons per mole of O_2 which should result in lower currents, other things being equal.

The purpose of this work was to investigate and compare the kinetics of oxygen reduction in KOH and K_2CO_3 electrolytes over a wide range of concentration as one step toward determining the feasibility of using a carbonate-containing electrolyte (as a replacement for hydroxide) in low- to medium-temperature fuel cells operating with a CO_2 -containing hydrogen source.

We have performed RRDE experiments and RDE experiments in potassium and cesium hydroxides and carbonates at several concentrations at 23 °C, and some measurements were made at elevated temperatures. These experiments have been carried out with at least two different pretreatment potential profiles (with anodic and cathodic measuring sweeps) to aid in the identification of specific electrolyte effects as distinct from effects resulting from changes in the oxidation state of the platinum surface.

Section 4.1 covers the investigation of platinum/electrolyte interactions as a function of electrolyte properties and electrode pretreatments. Most of these studies involved cyclic voltammetry measurements at the beginning of each OR experiment. In addition, some unique potential

profiles were used to measure the amount of surface oxide present under various conditions. This information is then used as an indication of the amount of oxide expected during an oxygen reduction experiment.

Section 4.2 reports RRDE studies of OR in dilute electrolytes. The effect of carbonate ion concentration and pH on rate constants calculated for the three-step model of Damjanovic (22) are discussed.

Section 4.3 presents studies of OR kinetics for electrolytes with concentrations of 0.1 to 4M K_2CO_3 and 0.1 to 6.9M KOH. The effect of temperature from 23 to 95 °C was studied in some electrolytes.

Section 4.4 concludes the chapter with a summary of the results pertinent to the evaluation of the fuel cell cathode behavior to be presented in Chapter 5.

4.1. Platinum/Electrolyte Interactions

As introduced in Chapter 2, the oxidation state of a platinum surface varies considerably with potential history and electrolyte composition. The interactions between a metal and an ionic liquid are often studied with triangular-sweep or cyclic voltammetry. "Steady-state" or repeating cyclic voltammograms were recorded on a smooth platinum electrode at 100 mV/sec in several electrolytes under a nitrogen atmosphere. Figure 4-1 shows voltammograms for a series of electrolytes with an ionic strength of 0.7 M. The complete nominal ionic compositions for these experiments are listed in Table 4-2. Figures 4-2 and 4-3 show voltammograms for a range of concentrations of KOH and K_2CO_3 , respectively, with one curve for 0.1M Cs_2CO_3 included in Figure 4-3. The sharpness of every feature of the voltammograms increases with hydroxide ion activity. The dependence of specific features on electrolyte composition will be discussed by region. Table 4-1 lists potentials of the major peaks for these experiments as well as the charges due to hydrogen desorption Q_h (integrated as shown in Figure 2-1). HA1 and HA2 refer to the low- and high-potential anodic peaks associated with hydrogen desorption. OA1 and OA2 refer to the first and second platinum oxidation peaks. All potentials are referred to an RHE in the

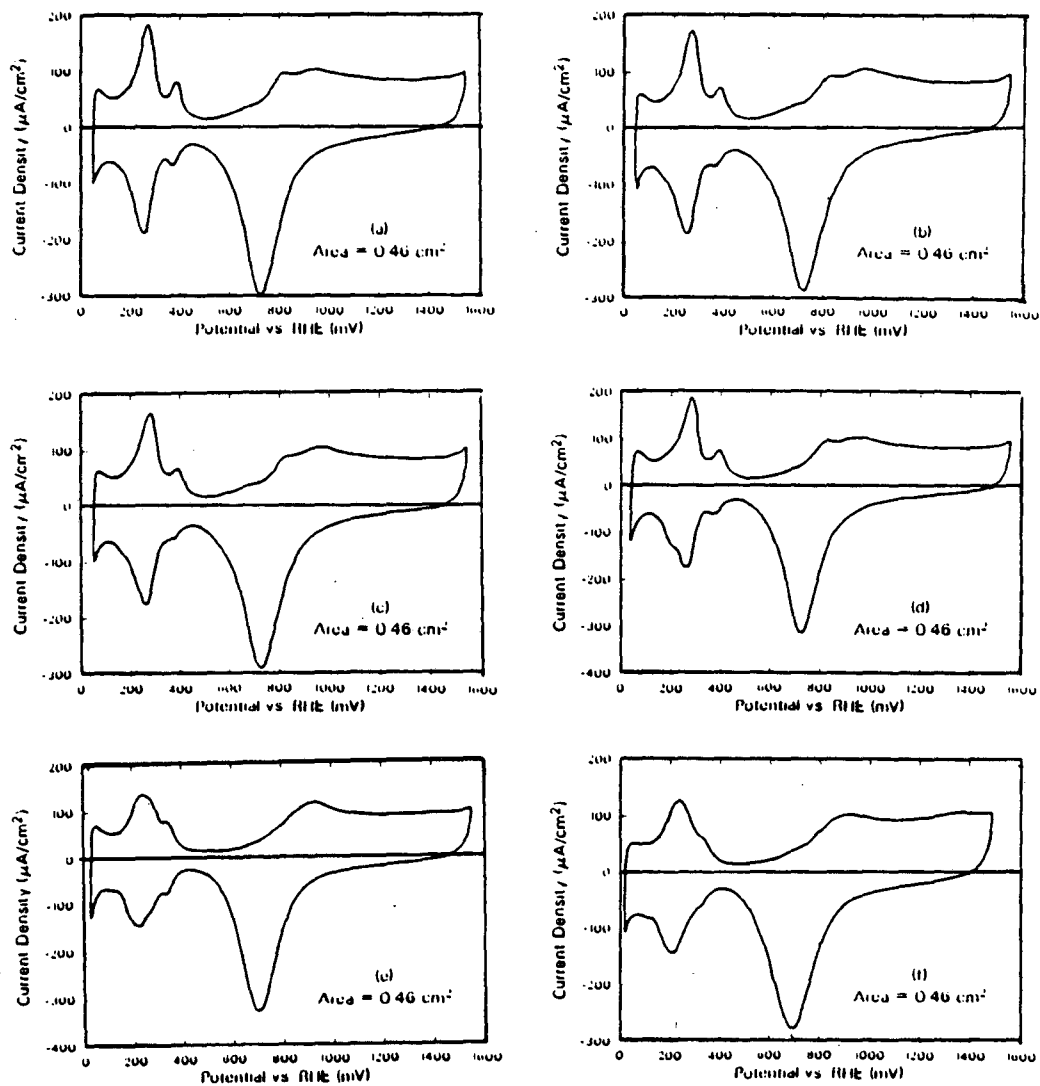
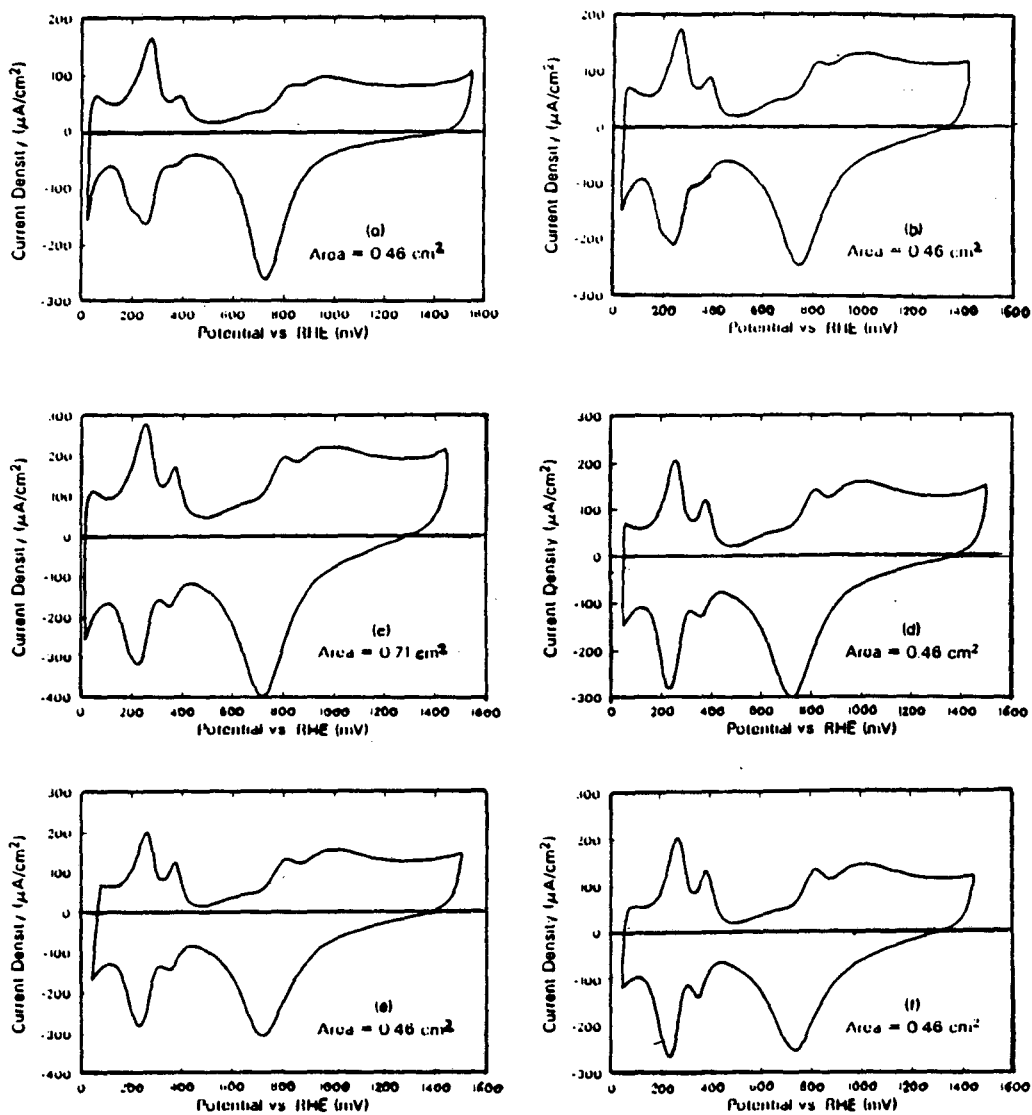


Figure 4-1: Cyclic voltammograms in dilute alkaline electrolytes with ionic strength of 0.7M (see Table 4-2 for complete nominal compositions). Curves recorded on smooth platinum with a sweep rate of 100mV/sec, 23 °C.

- (a), 0.2M CO_3^{2-} , pH = 13 (Ionic 1A);
- (b), 0.15M CO_3^{2-} , pH = 13 (Ionic 1B);
- (c), 0.1M CO_3^{2-} , pH = 13 (Ionic 1C);
- (d), 0M CO_3^{2-} , pH = 13 (Ionic 2A);
- (e), 0.2M CO_3^{2-} , pH = 11.4 (Ionic 2B);
- (f), 0M CO_3^{2-} , pH = 11.4 (Ionic 3).



- XBL 8711-4747 -

Figure 4-2: Cyclic voltammograms in KOH electrolytes. Curves recorded on smooth platinum with a sweep rate of $100 \text{ mV}/\text{sec}$, 23°C .
 (a), 0.5M ; (b), 1.0M ; (c), 2.0M ; (d), 3.3M ; (e), 5.4M ; (f), 6.9M .

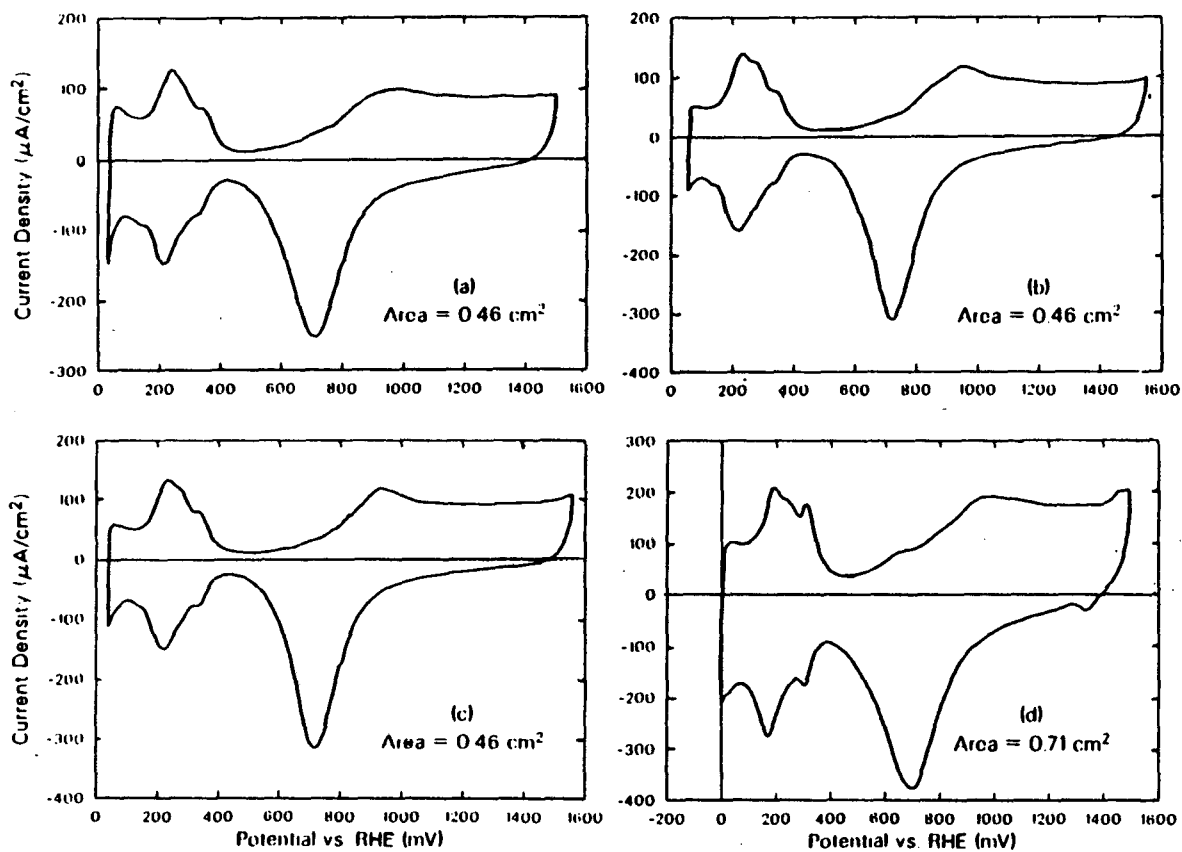


Figure 4-3: Cyclic voltammograms in alkali carbonate electrolytes. Curves recorded on smooth platinum with a sweep rate of 100mV/sec, 23 °C.
 (a), 0.1M Cs_2CO_3 , pH = 11.4; (b), 0.5M K_2CO_3 , pH = 11.6; (c), 1.0M K_2CO_3 , pH = 11.7; (d), 4.0M K_2CO_3 , pH = 12.7.

Table 4-1: Voltammetric Peak Potentials in Alkaline Electrolytes

Experiment Name	Q_{H_2} (μC)	Peak Potential (mV vs. RHE)			
		HA1	HA2	OA1	OA2
Ionic 1A	100	275	390	825	950
Ionic 1B	95	280	390	830	970
Ionic 1C	95	280	390	835 [†]	965
Ionic 2A	104	280	390	825	955
Ionic 2B	92	245(275) [‡]	345	830 [†]	930
Ionic 3	80	230	330	-	900
0.1M KOH	132	300	410	840	960
0.5M KOH	94	280	395	830	970
1.0M KOH	118	270	390	820	975
2.0M KOH	245 [*]	260	375	810	975
3.3M KOH	107	260	380	815	1000
5.4M KOH	130	270	375	815	1000
6.9M KOH	125	265	375	820	995
0.1M K ₂ CO ₃	91	245(275) [‡]	345	840 [†]	925 [†]
0.5M K ₂ CO ₃	95	233(275) [‡]	345	850 [†]	950 [†]
1.0M K ₂ CO ₃	92	205(267) [‡]	325	850 [†]	940 [†]
2.0M K ₂ CO ₃	143	210(270) [‡]	325	845 [†]	950 [†]
4.0M K ₂ CO ₃	239 [*]	195(250) [‡]	310	830 [†]	975 [†]

[†]Peak not very well defined

[‡]Shoulder on peak HA1

^{*}Performed with large-area electrode

electrolyte reported.

4.1.1. Hydrogen Region

Huang, O'Grady and Yeager carried out a detailed investigation of the effects of different ions in solution on the size and location of the peaks due to hydrogen adsorption and desorption in a cyclic voltammogram (66). Most of their work was concerned with acid electrolytes where the potential of zero charge lies close to this region and anion adsorption greatly affects the shape. For alkaline electrolytes, they proposed that the shifts they observed for cation (Ca⁺⁺ and Ba⁺⁺) additions to a 0.1M NaOH electrolyte were caused by changes in the structure of the double-layer, as opposed to specific anion adsorption. This seems reasonable since the size and relative position of peaks HA1 and HA2 were not affected. The absolute potentials of the

peaks were shifted cathodically toward a less strongly adsorbed state. They did not study the effect of pH on this behavior.

The low-pH electrolytes in Figure 4-1 exhibit two features not present at higher pH's, i.e. a small cathodic peak just before the onset of hydrogen evolution and an anodic shoulder on HA1. In the more-concentrated carbonate electrolytes the shoulder persists even though the pH is greater than or equal to 13. This shoulder was also shown in the work of Angerstein-Kozłowska (67) for 0.1M Na_2CO_3 .

The potentials for the two hydrogen oxidation peaks (E_{HA1} and E_{HA2}) shift slightly with increasing concentration. E_{HA1} shifts from 245 to 195 mV in K_2CO_3 electrolytes and from 300 to 265 mV in KOH. However, the separation between these peaks is essentially constant for all of the electrolytes tested. It is interesting that the location of the hydrogen region changes significantly with pH, beyond that due to the thermodynamic dependence.

Another shoulder was often observed on the negative side of the main cathodic hydrogen peak in KOH-containing electrolyte. This feature often coincided with a larger-than-normal platinum oxidation prewave and rotation-dependent OR polarization curves in the kinetically controlled region. All three features are probably due to traces of organic materials which are forming a "reduced- CO_2 " which has been proposed in studies of methanol oxidation and CO_2 in acid electrolytes. This species is then oxidized off the surface at around 675 mV (68,69). This phenomenon has also been suggested as occurring in carbonate electrolytes (68).

4.1.2. Platinum Oxidation Region

As the hydroxide concentration increases, so does the clarity of every peak and the separation between the two platinum oxidation peaks OA1 and OA2. The relative sizes of the peaks or amount of oxide formed at a given potential is found by integrating voltammograms shown in Figures 4-2 and 4-3 from the double-layer region (or minimum between the hydride and oxide regions) according to

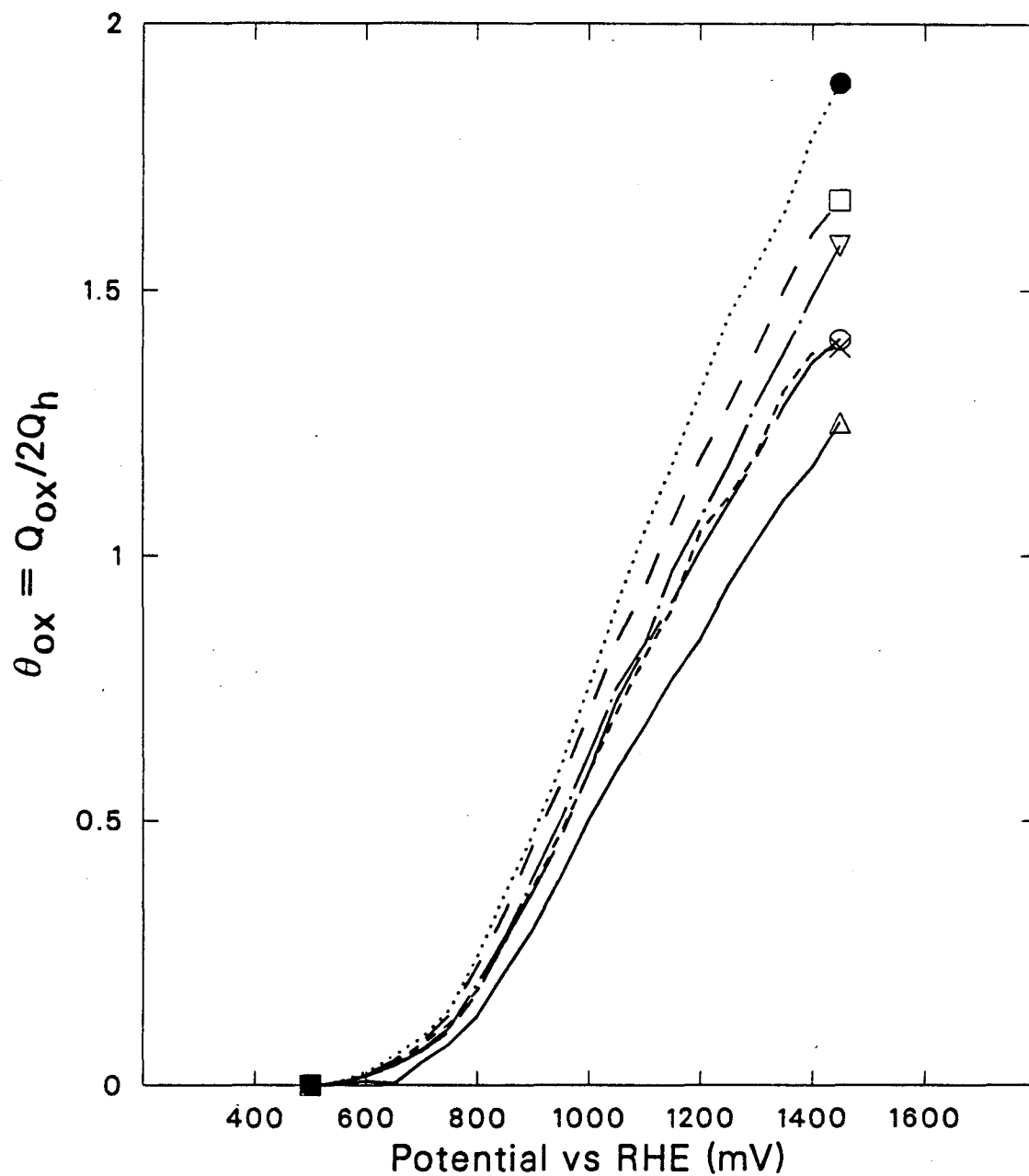
$$Q_{ox} = \frac{1}{v} \int_{E_{min}}^{E_{ox}} (i - i_{min}) dE \quad (4-1)$$

where i_{min} is the current minimum (an estimate of the double-layer charging current). Oxide coverage θ_{ox} is then calculated as in Equation 2-4. These results are shown in Figures 4-4 and 4-5 for KOH and K_2CO_3 , respectively. The slopes of these curves range from 1.85 to 2.5 V^{-1} in KOH and are constant at about 2.2 in K_2CO_3 . The slope of a steady-state plot of this form is an indication of the stoichiometry of the oxide, as discussed in Chapter 2. Quantitative calculations of stoichiometry are not suggested here because of the uncertainty in the absolute value of Q_h . Q_h is more commonly calculated by integrating the cathodic portion of the hydrogen region. This is not possible in alkaline electrolytes, however, due to interference of oxide reduction in this region, as discussed above. The relative values for Q_h and θ_{ox} should be adequate for inferring whether the mechanism of oxidation is changing as a function of concentration in KOH where it is not in K_2CO_3 . The data from Figure 4-4 for KOH are cross-plotted in Figure 4-6, showing the maximum in coverage at about 3.2M. This concentration may prove significant later when analyzing OR kinetic behavior.

Similar voltammograms (not shown) were recorded in 2M KOH over the temperature range of 23 to 82 °C) and integrated as above. Figure 4-7 shows the coverage as a function of potential at several temperatures. The amount of oxide formed on the surface at a given potential increases with temperature, contrary to the behavior reported by Park et al. (38).

The separation between the two OA peaks tended to increase with increasing KOH concentration and decrease with increasing temperature. Both of these phenomena are consistent with an increase in the hydroxide ion activity. This is probably due to changes in the thickness of the double-layer as suggested by Huang, O'Grady and Yeager (66) according to the following qualitative relationship between double layer parameters and electrolyte ionic strength.

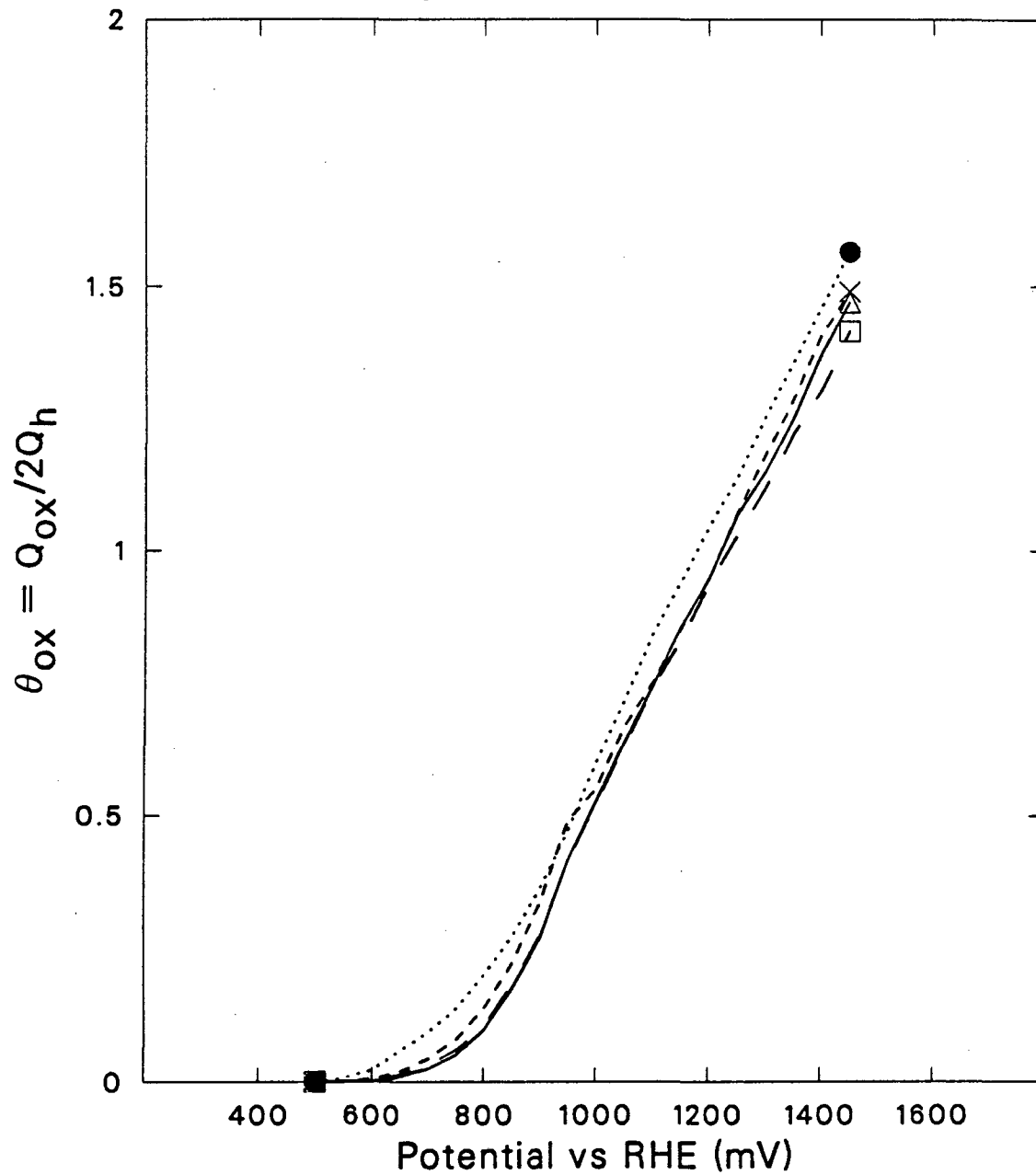
$$\delta = \left(\frac{\epsilon k_b T}{8\pi n^0 z^2 e_0^2} \right)^{1/2} \quad (4-2)$$



- XBL 8710-4339 -

Figure 4-4: Oxide Coverage in KOH electrolytes: Data from integrations of voltammograms recorded on Pt at 100mV/sec and 23 °C.

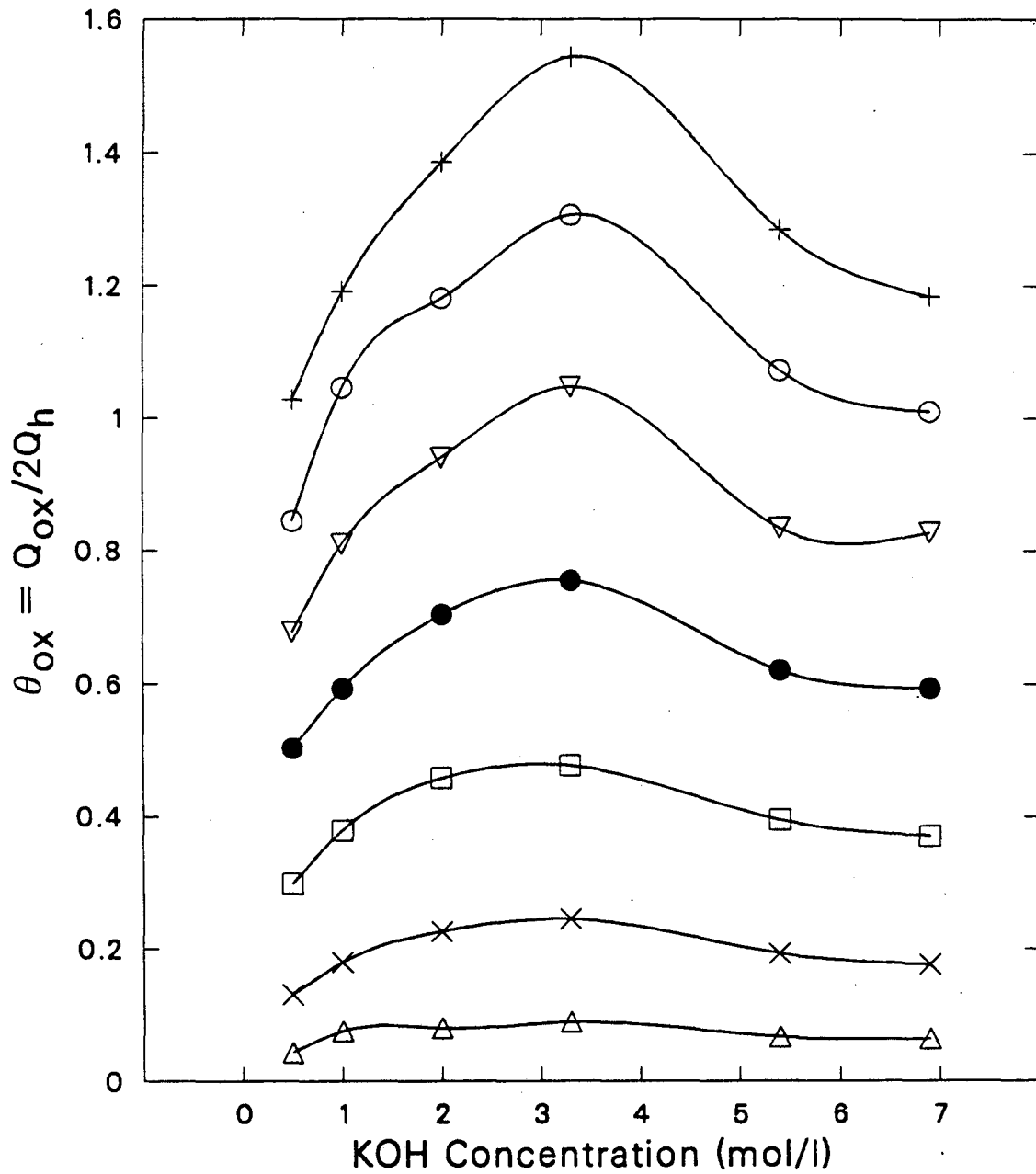
—Δ, 0.5M; —×, 1.0M; —□, 2.0M;
 ····•, 3.3M; —·—·—·—▽, 5.4M; —○, 6.9M.



- XBL 8710-4340 -

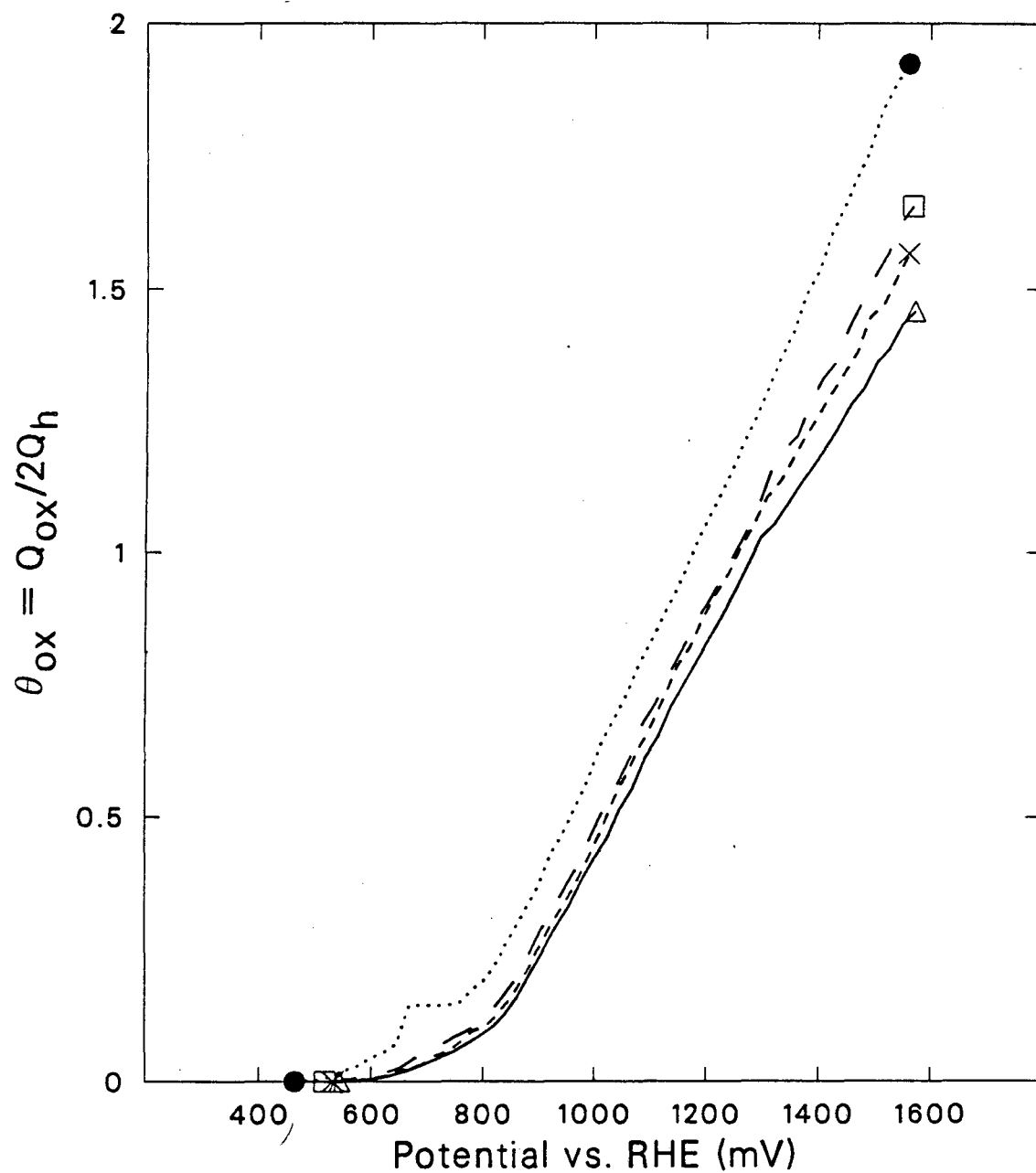
Figure 4-5: Oxide coverage in K_2CO_3 electrolytes: Data from integrations of voltammograms recorded on Pt at 100mV/sec and 23 °C.

—Δ, 0.1M; —×, 0.5M; —◻, 1.0M; ·····●, 4.0M.



- XBL 8710-4341 -

Figure 4-6: Oxide coverage dependence on KOH concentration.
 Δ , 700mV; \times , 800mV; \square , 900mV; \bullet , 1000mV; ∇ , 1100mV; \circ , 1200mV; $+$, 1300mV.



- XBL 8710-4342 -

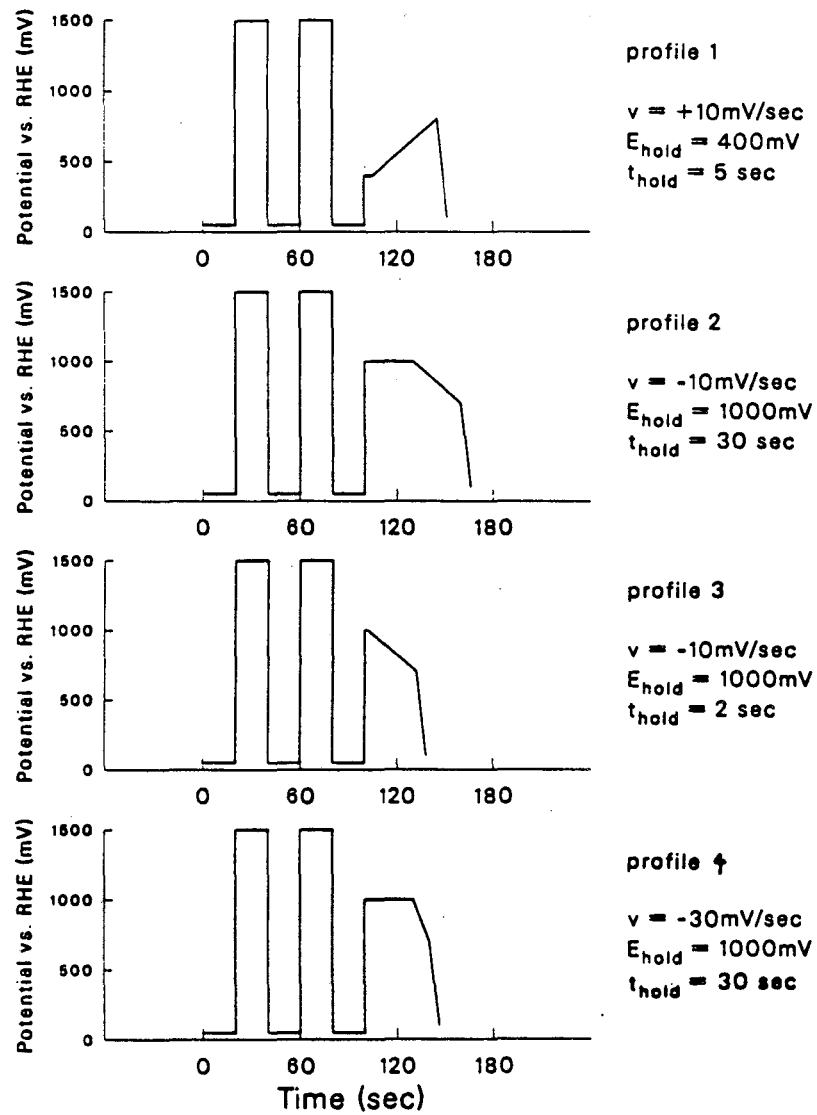
Figure 4-7: Temperature dependence of oxide coverage in KOH electrolyte. Data from integrations of voltammograms recorded 2.0M KOH on Pt at 100mV/sec.
 —△, 23 °C; —×, 44 °C; —□, 64 °C; ····•, 82 °C.

where n° is related to ion concentration, e_0 is the charge of an electron, and z is the valence of the ion (70). The relationship between the electrolyte/platinum interaction and observed OR activity will be discussed further in the next few sections.

4.1.3. Surface Coverage of Oxide during OR Sweep Experiments

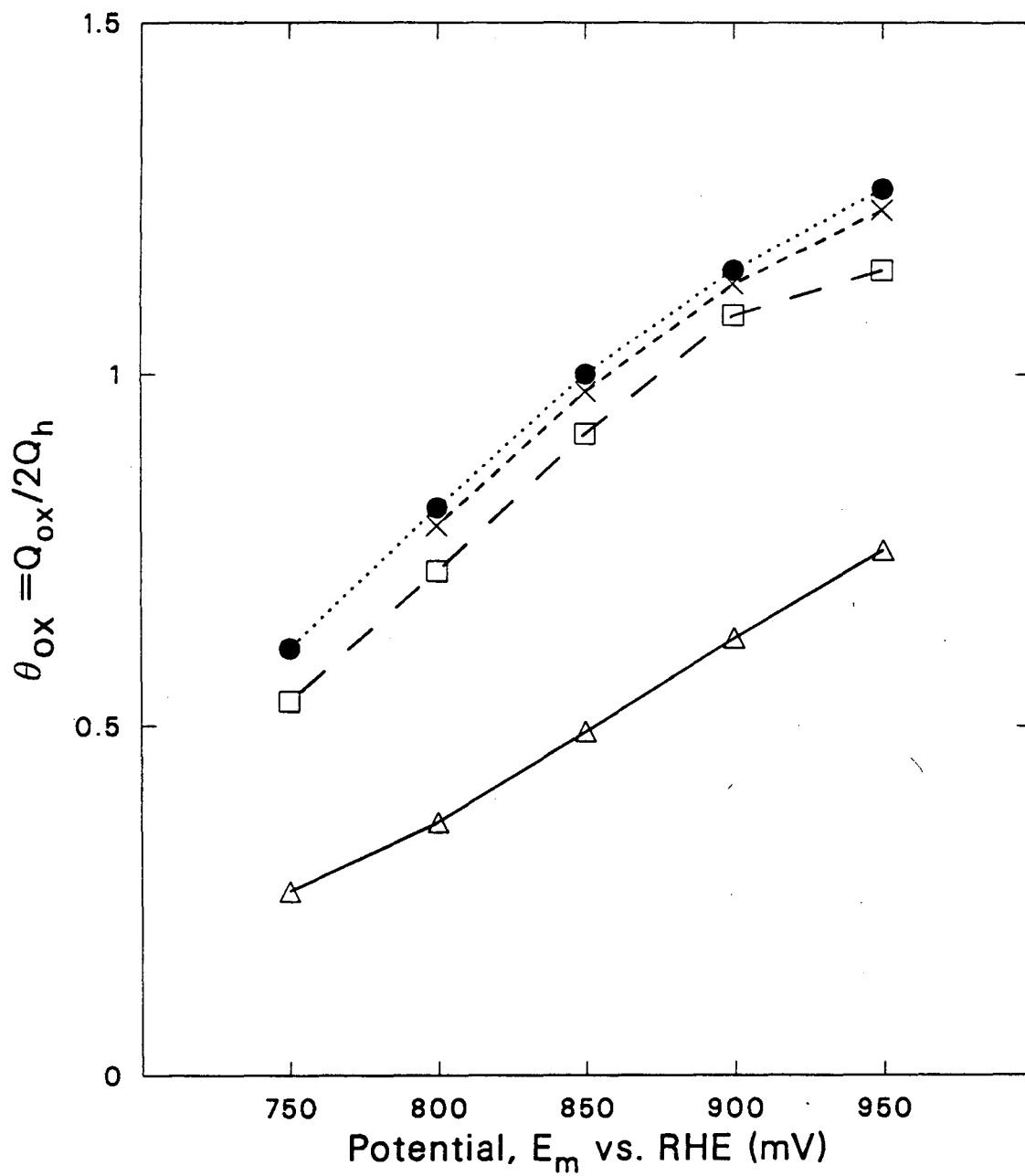
As discussed in Chapter 2, the kinetics of OR are known to be very dependent on the oxidation state of the platinum. Ideally, kinetic studies with such a potential-dependent surface would be carried out at steady state. The reasons for using potential sweep experiments in the study of OR have already been discussed. Accepting this necessity, the amount of oxide on the surface was measured during four different potential sweep experiments in 1N KOH in the absence of O_2 . The potential profiles used for this experiment are shown in Figure 4-8. They consist of an electrode pretreatment, the experimental linear potential sweep to a given potential (E_m), and finally a fast "measuring" sweep at 100 mV/sec to a potential in the hydrogen region. The coverage dependence on E_m , obtained by integrating the currents due to the measuring sweep and using Equation 2-4, are shown in Figure 4-9. The slope of the anodic sweep data in Figure 4-9 (profile 1) is $2.6 V^{-1}$, which agrees with that reported by Bagotsky (15) for steady-state coverage in this electrolyte (obtained by stepping from a bare "well-annealed" platinum surface to each potential). This value is higher than the $2.1 V^{-1}$ shown in Figure 4-4 obtained from the 100 mV/sec cyclic voltammogram in this electrolyte. This is consistent with others who have observed that charges measured by integrating reduction currents are higher than those obtained by integrating oxidation currents (71). This is probably a manifestation of the aging of the oxide.

The cathodic sweep experiments (profiles 2 to 4) show slopes of about $3.62 V^{-1}$ and significantly higher coverages over the whole potential range than the anodic result. Bagotsky did not measure steady-state coverages obtained by stepping from high potentials to low potentials. He did study the kinetics of reduction and oxidation by measuring the dependence of peak potentials on sweep rate. He found both oxidation peaks (OA1 and OA2) to be reversible (or



- XBL 8710-4343 -

Figure 4-8: Potential profiles for measurement of oxide surface charge existent during on oxygen reduction experiment.



- XBL 8710-4344 -

Figure 4-9: Oxide coverage during oxygen reduction experiment. See Figure 4-8 for potential profiles.
 — Δ , profile 1; — \times , profile 2;
 - - - \square , profile 3; ···· \bullet , profile 4.

independent of sweep rate) at sweep speeds up to about 2 V/sec. However, the potential of the reduction peak, OC1, was found to depend on sweep rate down to 10 mV/sec. The higher slope for the cathodic experiment (curve 2) is therefore due to either a change in the stoichiometry of the oxide on the surface (as observed by Bagotsky), or to the fact that the reduction kinetics are slow when compared with the sweep rates used.

The fact that the **intercepts and not the slopes** of curves 3 and 4 in Figure 4-9 increase with oxidation time and sweep rate must be due to aging by absorption, since a change in stoichiometry should change the slope.

4.1.4. Summary

There are several conclusions which can be drawn from the data presented so far in this chapter. In dilute electrolytes, there appears to be little change in the general features of the platinum oxidation region of the cyclic voltammogram due to the presence of CO_3^{2-} anion. As concentration of CO_3^{2-} increases, the clarity of the hydrogen-region peaks increases with little effect on the oxidation region. In KOH, in addition to the increase in peak clarity, the potential dependence of the oxide coverage is a function of concentration. The amount of oxide formed appears to pass through a maximum at a concentration of 3.2M KOH, indicating some mechanistic change in the oxidation of platinum that does not occur in K_2CO_3 . At a concentration of 2M KOH the amount of oxide formed at a given potential increases with temperature.

The oxidation state of a platinum surface in KOH during an OR experiment is a strong function of the potential profile used. The coverages measured for the profiles used will be useful when trying to interpret the role of the oxide in the mechanism of electrochemical oxygen reduction.

4.2. RRDE Studies in Dilute Alkaline Electrolytes

Rotating ring-disk studies of the OR reaction were carried out in three series of dilute electrolytes. Series 1 consists of 0.1 M CsOH to which two additions of Cs_2CO_3 were made. Series 2

and 3 include electrolytes of various carbonate concentrations and with a constant ionic strength of 0.7 M at two levels of pH. Table 4-2 lists the nominal ionic compositions of the electrolytes along with the measured Levich slopes, predicted oxygen solubilities, and Tafel slopes observed at low current densities.

The three potential profiles used in these OR experiments are shown in Figure 4-10 and are similar to those used to study oxide coverage, discussed above. Profile A consists of a pulse pretreatment, a short holding period at a potential where OR is controlled by mass-transfer followed by a 10 mV/sec anodic sweep to zero current. Profiles C1 and C2 consist of the same pulse program followed by a 30-second potential hold at 1100 or 1300 mV vs. RHE to allow the formation of a relatively steady oxide coverage before sweeping cathodically at 10 mV/sec to the limiting current for OR. Profile A produces a surface with only "young" oxide. Profiles C1 and C2 will produce a much more highly oxidized surface than profile A with possibly a different stoichiometry. There could also be a difference in the oxide structure between profiles C1 and C2.

Table 4-2: Summary of Dilute Electrolyte Results

Series	Experiment Name	Nominal Ionic Conc. (mol/l)				$\frac{C_{O_2}}{C_{O_2}^{water}} \dagger$	Levich Slope ($\frac{mA \cdot sec^{1/2}}{cm^2}$)	Tafel Slope (mV/dec)	
		K ⁺ /Cs ⁺	CO ₃ ⁻	OH ⁻	F ⁻			prof.A	prof.C1
1	CsOH A0	0.1	0	0.1	0	0.969	0.439	67.4	38.5
1	CsOH A1	0.24	0.07	0.1	0	0.923	0.416	76.7	39.4
1	CsOH A2	0.33	0.11	0.1	0	0.897	0.399	73.4	-
2	Ionic 1A [†]	0.5	0.2	0.1	0	0.809	0.364	53.6	78.1
2	Ionic 1B [‡]	0.55	0.15	0.1	0.15	0.790	0.35	59.2	-
2,3	Ionic 1C [‡]	0.60	0.10	0.1	0.3	0.772	0.351	70.3	74.2
2,3	Ionic 2A [†]	0.70	0	0.1	0.6	0.736	0.406	59.8	66.2
3	Ionic 2B [‡]	0.60	0.1	trace	0.4	0.768	0.399	65.3	74.5
3	Ionic 3 [‡]	0.70	0	trace	0.7	0.734	0.351	55.5	69.2
	0.1 M KOH	0.1	0	0.1	0	0.961	0.445	64	-
	0.1 M K ₂ CO ₃	0.2	0.1	trace	0	0.918	0.416	76	-
	0.1 M Cs ₂ CO ₃	0.2	0.1	trace	0	0.932	0.418	65	54

$\dagger C_{O_2}^{water} = 1.26 \times 10^{-3}$ mol/l

\ddagger K⁺ anion

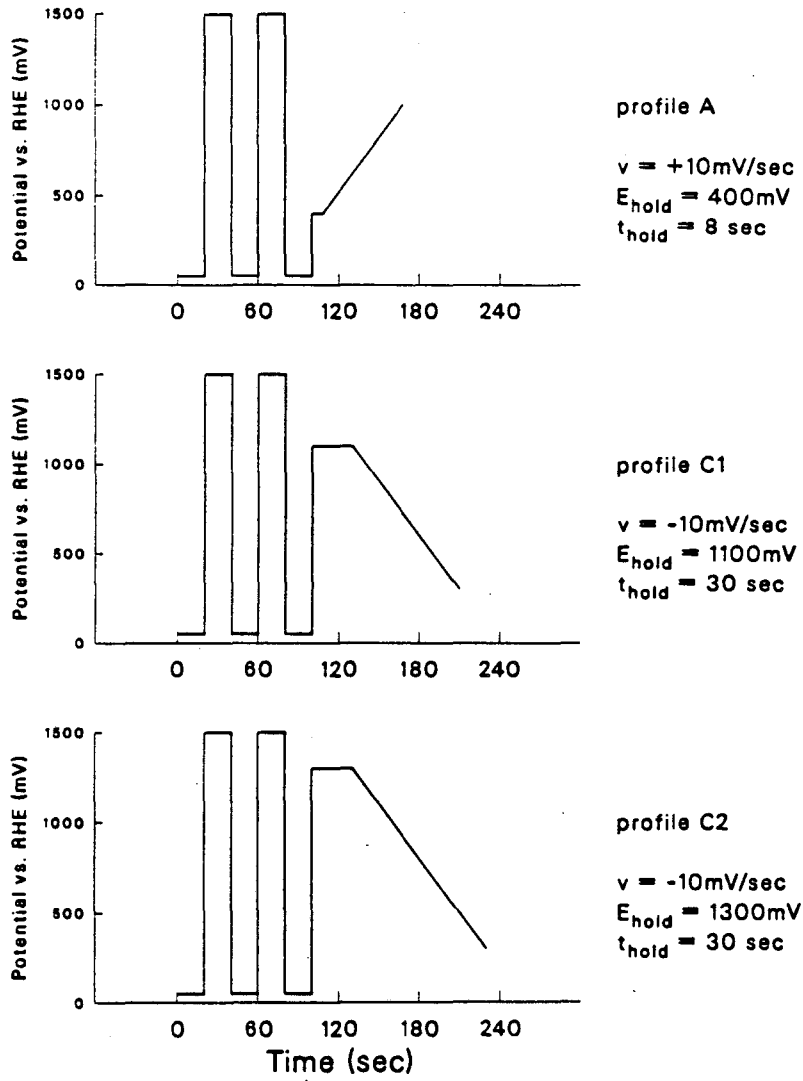


Figure 4-10: Potential profiles for oxygen reduction experiments.

As we saw in Chapter 2 (Figure 2-1), the oxide that was formed at potentials greater than 1.2 V required a lower potential to be fully reduced than that formed at less than 1.2 V.

4.2.1. Experimental Equipment and Procedures

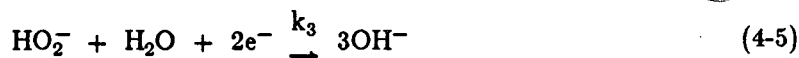
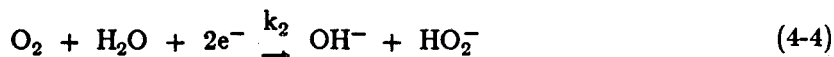
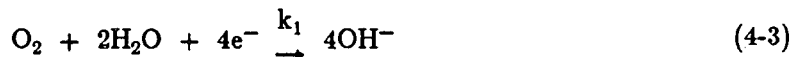
Experiments were performed using the glass cell described in Chapter 3. Electrolytes were prepared primarily from ultrapure salts (Alpha ultrapure KOH, ultrapure Cs_2CO_3 and 99.9% CsOH; Aesar 99.995% $\text{K}_2\text{CO}_3 \cdot 1.5\text{H}_2\text{O}$ and 99.994% KF; and GFS ultrapure KOH), however Baker reagent-grade KF was used in Ionic 1B and 1C. Solutions were pre-electrolyzed in the cell, although this procedure showed little effect on recorded voltammograms and OR currents. The high-collection-efficiency Pt-Pt ring-disk electrode obtained from Pine Instruments Inc. had areas of 0.458 and 0.428 cm^2 for the disk and ring respectively. A collection efficiency (N_c) of 0.42 was determined from the tables supplied by Albery and Bruckenstein (72) and verified with the $\text{Fe}^{+3}/\text{Fe}^{+2}$ redox couple. The counter and reference electrodes as well as all polishing and cleaning procedures were discussed in Chapter 3. The ring was maintained at a constant potential of 1.1 to 1.2 V vs. RHE during the experiments in order to minimize the platinum oxidation background currents.

4.2.2. Electronics

Ring and disk electrode potentials were controlled with a Pine RDE4 bipotentiostat. Potentials proportional to the two current signals were recorded simultaneously on the two channels of a Nicolet 2090 digital oscilloscope and an HP7046B dual pen XY-recorder. The potential profiles required for electrode pretreatment and linear sweep experiments were generated by a real-time program implemented on an IBM PC. This program also controlled the transfer of data via digital I/O lines from the oscilloscope for storage on disk. Disk rotation speeds of 100 to 3600 rpm were controlled with a Pine Analytical Rotator.

4.2.3. Analysis of RRDE data

The procedure used for data analysis will be illustrated for experiment Ionic 2A, which had a composition of 0.1 M KOH + 0.6 M KF. Figure 4-11 shows the results of RRDE experiments generated with the three potential profiles shown in Figure 4-10 at a rotation speed of 1600 rpm. Current-potential curves were recorded at several rotation speeds in binary data files for analysis by computer. The program performed the analysis and prepared the appropriate data for plotting. Correction for the uncompensated solution resistance was performed as discussed previously (Section 3.2). Potential-dependent rate constants for the electrochemical reactions which make up the three-step model, proposed by Damjanovic



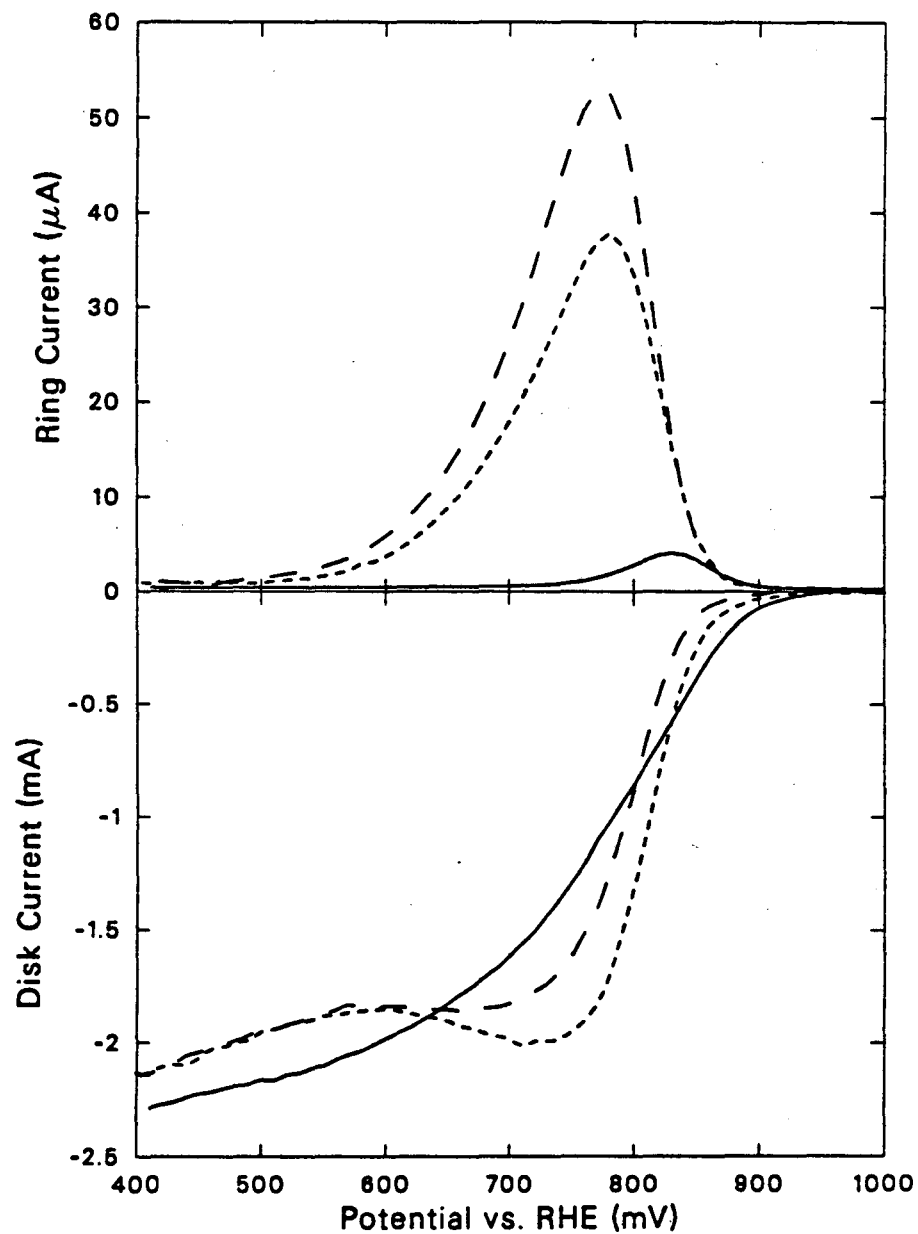
are determined from linear plots of the data according to the expressions developed in Chapter 2. Sample plots of $1/i_d^*$ vs $1/\omega^{1/2}$ (plot #1) and $i_d N_c / i_r$ versus $1/\omega^{1/2}$ (plot #2), according to equations 2-17 and 2-18, are shown in Figure 4-12 for the data generated with profile C1. These plots were visually inspected for linearity before the regression analysis was performed by the program. The mass-transfer-corrected or "kinetic current" obtained from the intercept of plot #1 has the form

$$i_k^* = nFC_{\text{O}_2}^\infty(k_1 + k_2) \quad (4-6)$$

Rate constants for this model were calculated from the slopes and intercepts of these two plots according to

$$k_1 = \frac{\xi_{\text{O}_2} S_1 (J_2 - 1)}{(J_2 + 1) J_1} \quad k_2 = \frac{2\xi_{\text{O}_2} S_1}{(J_2 + 1) J_1} \quad \text{and} \quad k_3 = \frac{\xi_{\text{H}_2\text{O}_2} S_2}{(J_2 + 1)} \quad (4-7)$$

where J_1 , S_1 , J_2 , and S_2 are the intercepts and slopes of plots 1 and 2, respectively. ξ_{O_2} was calculated with Equation 2-9; Levich slopes from limiting-current data; and oxygen solubilities in



- XBL 8710-4346 -

Figure 4-11: RRDE data in Ionic 2A for three different potential profiles.
 See Figure 4-10 for profiles and Table 4-2 for electrolyte composition.
 ———, profile A;
 ·····, profile C1;
 - - - - , profile C2;

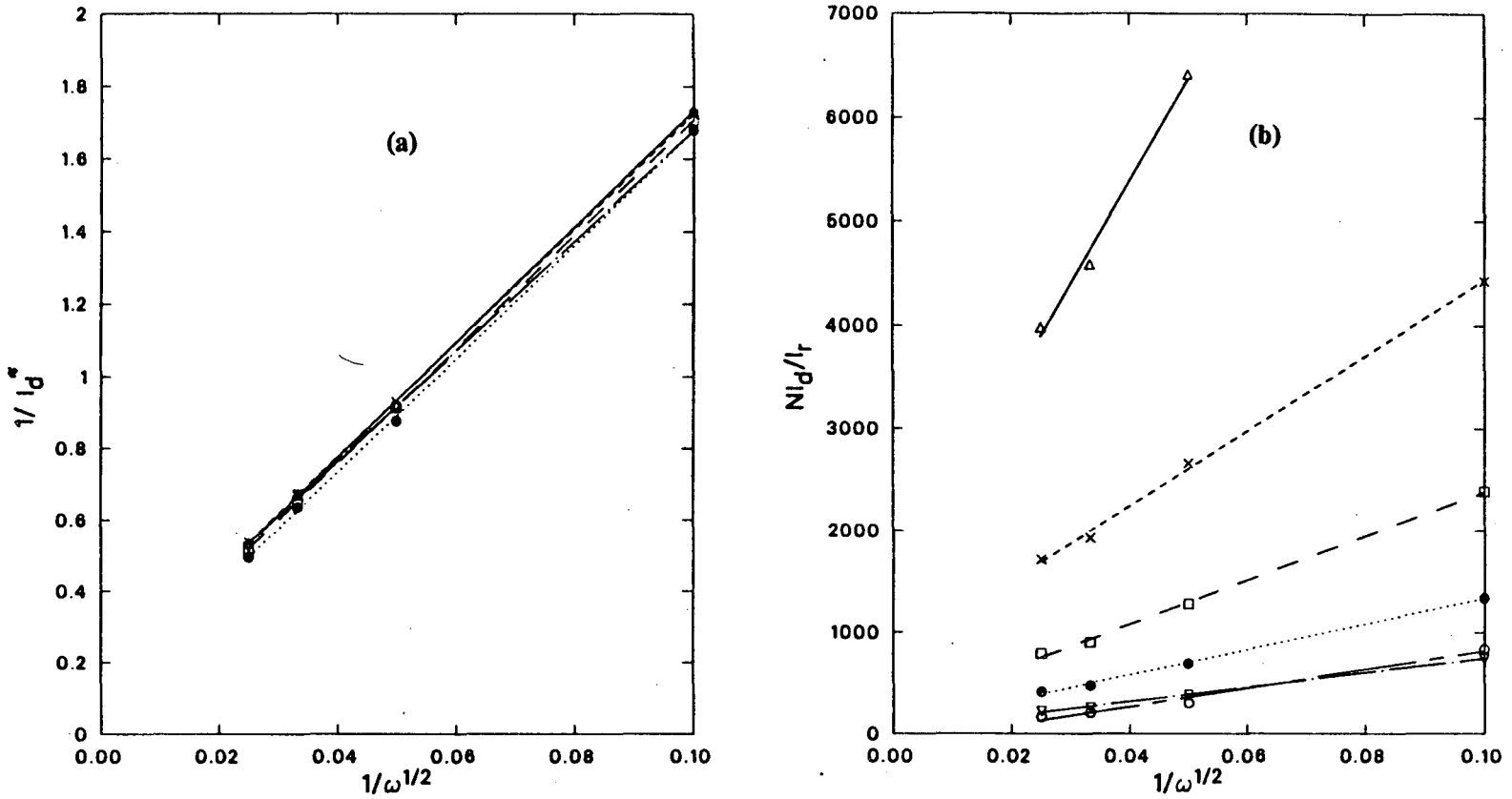


Figure 4-12: Data analysis plots at several potentials for experiment Ionic 2A.
 (a) Plot #1, according to Equation 2-18; (b) Plot #2, according to Equation 2-19;
 ———— Δ , 600mV; - - - - - \times , 650mV; - · - · - \square , 700mV;
 ······ \bullet , 750mV; - · - · - ∇ , 800mV. - - - - - \circ , 850mV.

- XBL 8710-4347 -

the mixed electrolytes with the following correlation from Schumpe, Adler and Deckwer (73)

$$\log_{10} C_{O_2} = \log_{10} C_{O_2}^{H_2O} - \sum_{i = \text{\#ions}} H_i I_{ci} \quad (4-8)$$

where $I_{ci} = \frac{1}{2} C_i z_i^2$ and the values for the Henry coefficients for salting out, H_i , are shown in Table 4-3. As shown previously, ξ_i depends only on D_i and ν . Because of the lack of data for peroxide diffusivities in mixed salts, we assumed that $\xi_{H_2O_2} = \xi_{O_2}$.

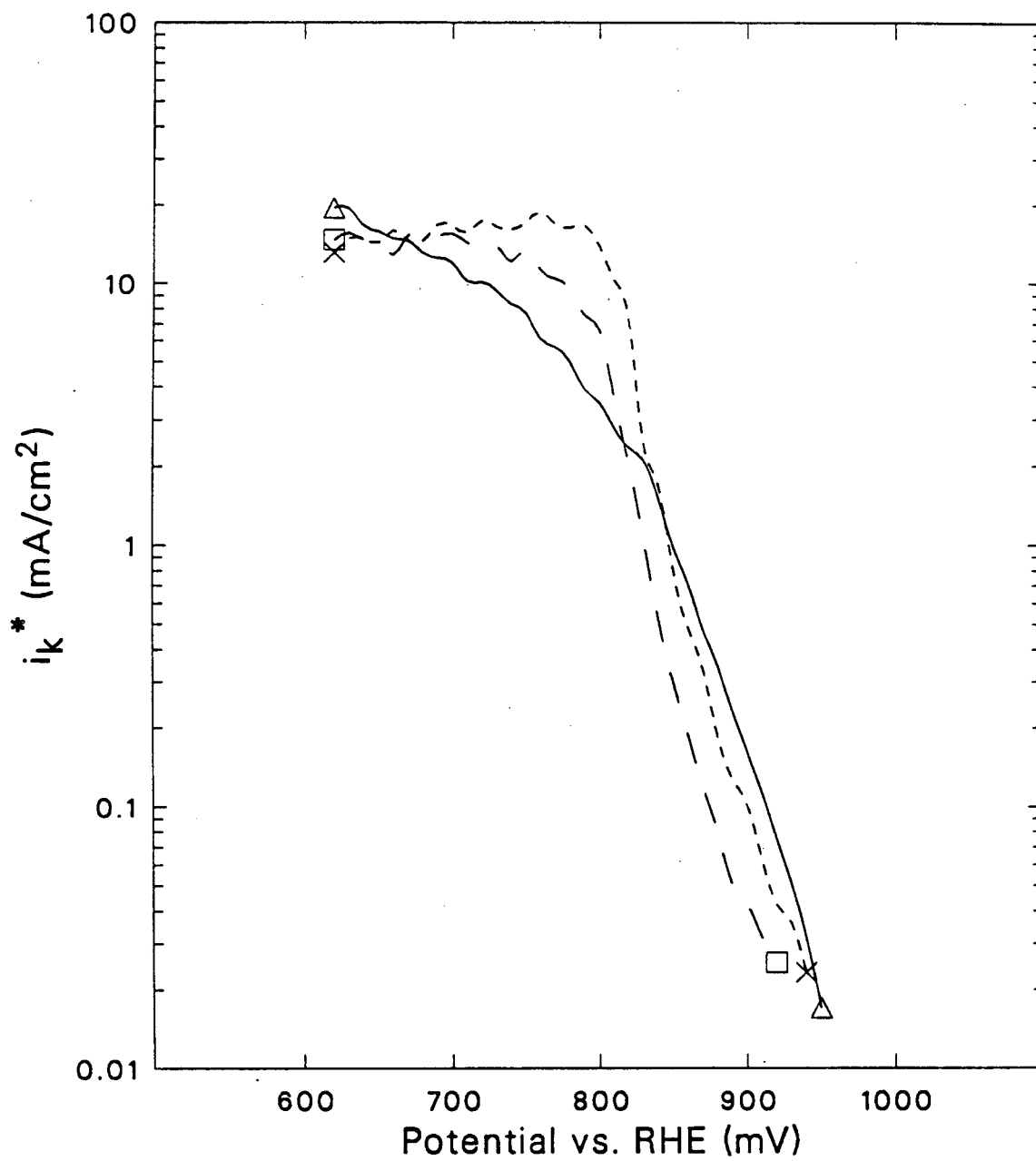
4.2.4. General Results for Dilute Alkaline Electrolytes

Figure 4-13 shows the dependence of the log i_k -potential plot on the pretreatment profile for Ionic 2A (generally observed in the dilute electrolytes). The anodic sweep results show 2 Tafel regions (as is generally observed in acid electrolytes) with a slope of around 60 mV/decade (or $\alpha = 1$) for the low-current-density region and a slope of anywhere from 2 to 3 times this in the high-current density region. The cathodic results show an essentially potential-independent region at high current density indicating that a chemical reaction step is rate-controlling. There is a very steep potential dependence and a medium-slope region at very low current density. This last region is probably due to the added effects of platinum reduction which is occurring simultaneously and but is of the order of magnitude of the OR currents only at these potentials.

At high potentials, the lowest-oxide-coverage surface shows the highest activity. At low potentials, the lowest-oxide-coverage surface shows the least activity but the intermediate-oxide-coverage surface shows the highest activity. The rate constants calculated from these data are shown as functions of potential in Figure 4-14.

Table 4-3: Henry's Law Coefficients for Salting Out of Oxygen in Mixed Electrolytes (l/mol) (73)

Cations		Anions		
K ⁺	Cs ⁺	OH ⁻	CO ₃ ⁻	F ⁻
-0.596	-0.666	0.941	0.485	0.982



- XBL 8710-4348 -

Figure 4-13: Kinetic current density for various electrode pretreatments in 0.1M KOH + 0.6M KF (Ionic 2A).
—△, profile A;
---×, profile C1;
---□, profile C2.

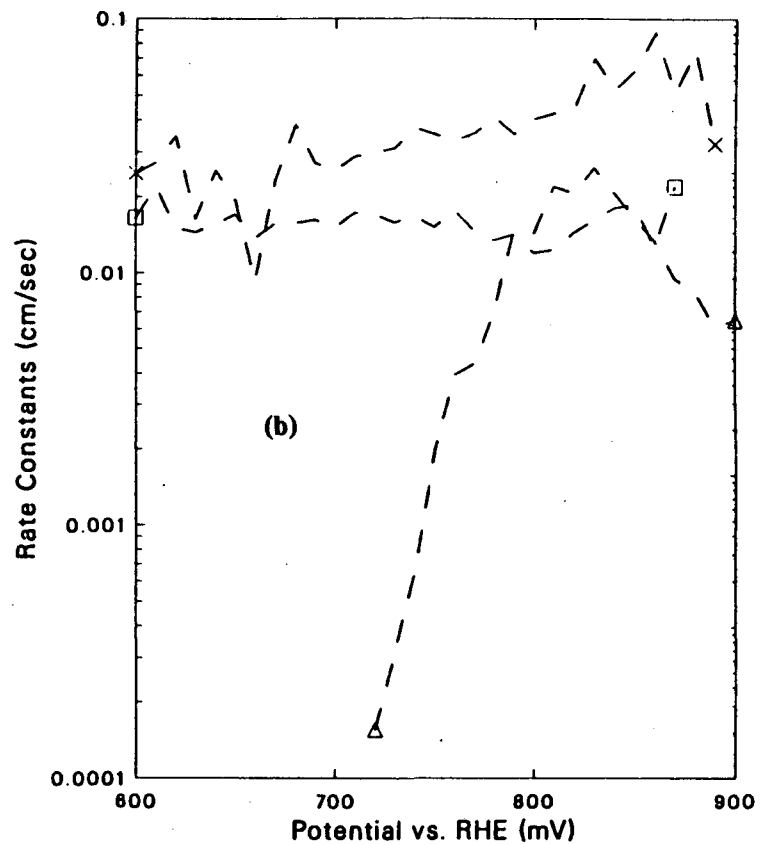
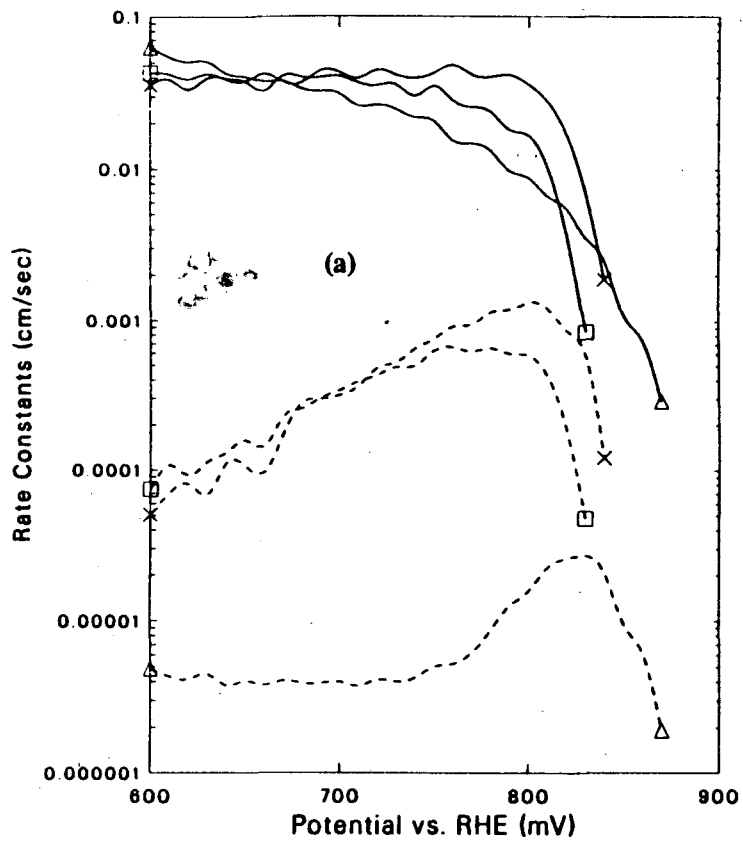


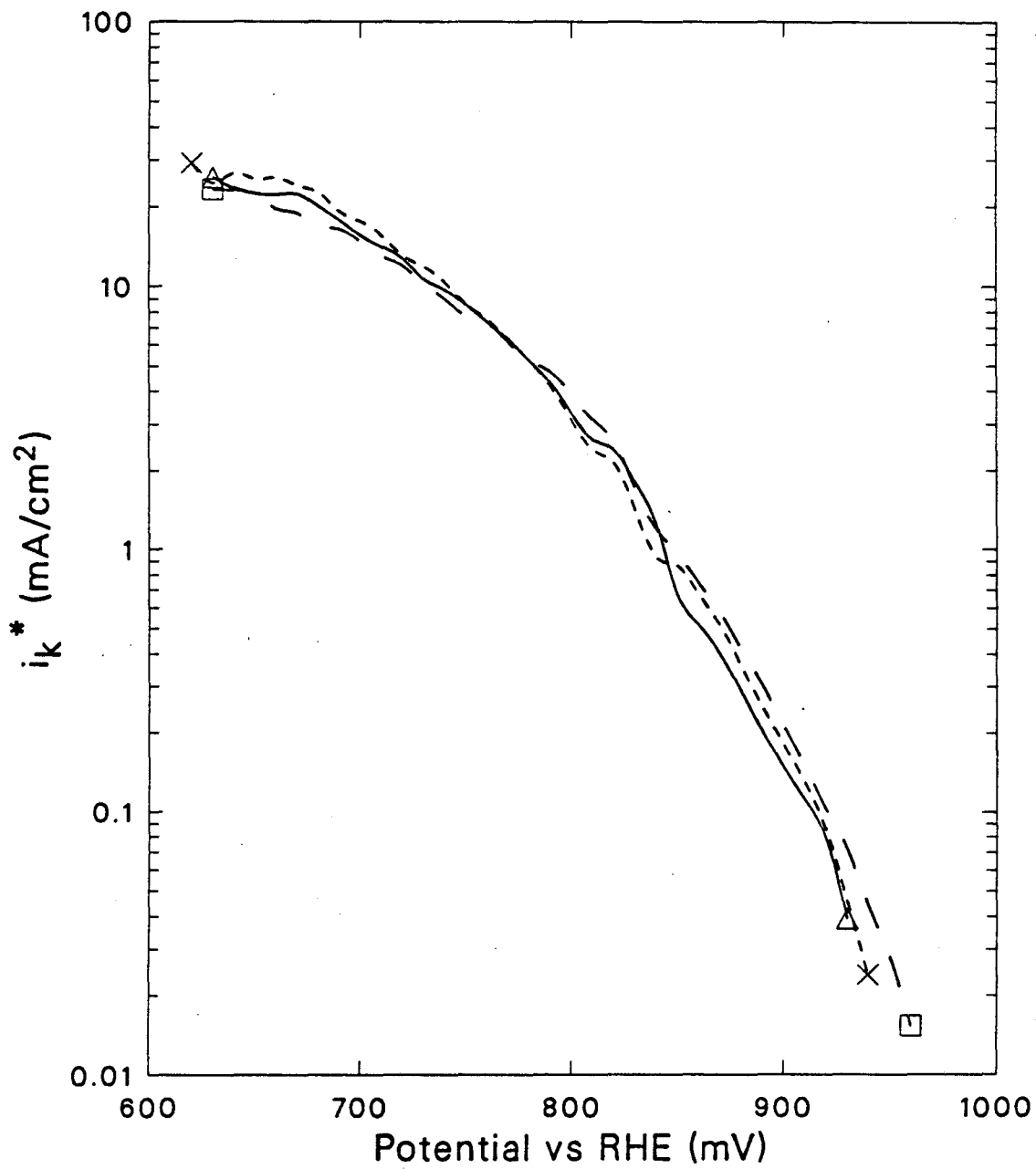
Figure 4-14: 3-Step Model Rate Constants for 0.1M KOH + 0.6M KF (Ionic 2A). (a) — k_1 ; - - - k_2 ; (b) - - - k_3 .
 Δ , profile A;
 \times , profile C1;
 \square , profile C2.

The value of k_1 parallels the previous Tafel plots closely as the 4-electron process is dominant in these dilute, relatively pure electrolytes. The value for k_2 , for the anodic sweep, is independent of potential up to about 750 mV and an order of magnitude smaller than that for the cathodic sweep profiles. The fact that k_2 is independent of potential even though there is some coverage of oxide may be an indication that k_2 is accelerated only by a minimum coverage or by coverage with a certain form of oxide that is older than the initial PtOH. In the cathodic sweep experiments, $\log k_2$ increases linearly with potential in the direction of higher oxide coverages. A maximum occurs at the point where the Tafel behavior for this reaction takes over (at about 800 mV) and then k_2 decreases with approximately the same slope as k_1 . This behavior is consistent with the cathodic sweep experiments of Park et al. (38) for in 0.1 M KOH. However, Damjanovic et al. (35) reported a similar potential dependence for k_1 and k_2 over a wider potential range. Their results were for a steady-state measurement on a "prereduced" surface which is not well defined. The higher kinetic current densities for profile C1 over C2 may reflect the relative abilities of these surfaces to reduce the peroxide formed, as indicated by the fact that k_3 is greatest for profile C1.

It is concluded that the presence of oxide adversely affects the OR activity of the Pt surface at high potentials. At lower potentials, where k_1 shows negligible dependence on potential, an intermediate coverage with oxide is more active than either the bare surface or the aged oxide surface. In the case of the "bare" or well-reduced surface, one might suggest an interference by adsorbing impurities; however no rotation dependence was observed in the kinetically-controlled region of the RDE curves.

4.2.5. Series 1: Carbonate Addition to Hydroxide

Kinetic current densities recorded with the anodic sweep (profile A) for Series 1 electrolytes containing CsOH and Cs_2CO_3 are shown in Figure 4-15. At a given potential, i_k^* increases slightly with carbonate concentration at potentials greater than 850 mV vs RHE. This trend may be due to ionic strength differences, and was considered only as an indication of the absence of a



-- XBL 8710-4349 --

Figure 4-15: Kinetic current density for Series 1 electrolytes, anodic sweep 10mV/sec.
— Δ , 0.1M CsOH (A0);
- - - x, 0.1M CsOH + 0.07M Cs₂CO₃ (A1);
- · - \square , 0.1M CsOH + 0.11M Cs₂CO₃ (A2).

detrimental effect due to the presence of carbonate anion.

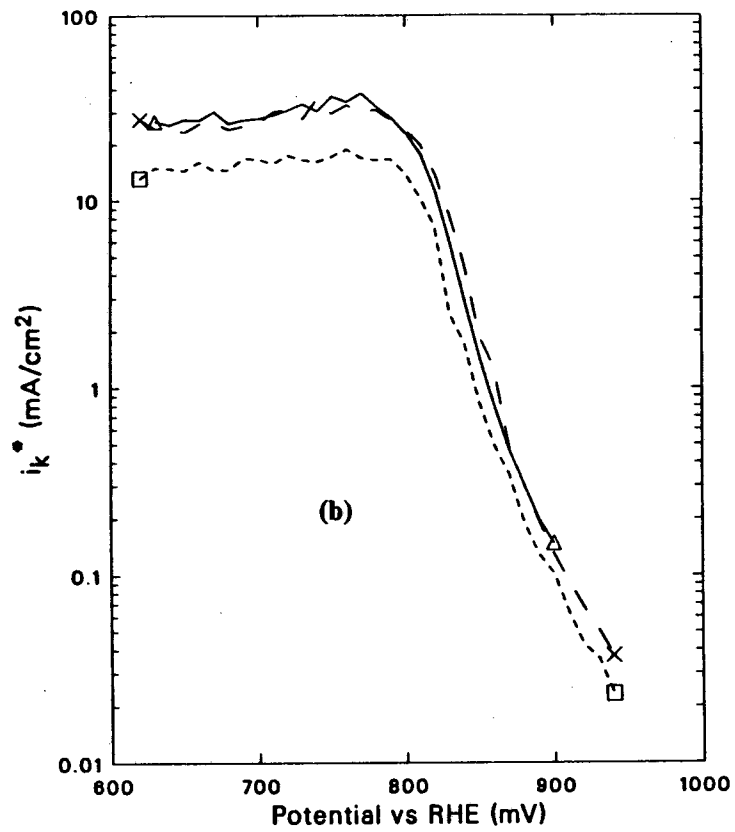
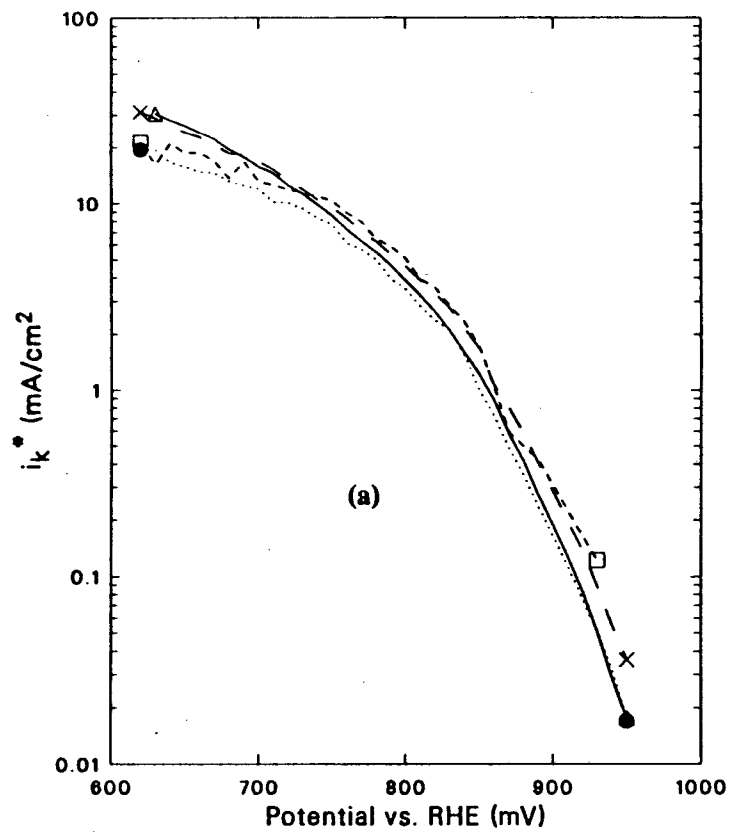
4.2.6. Series 2: Effect of CO_3^- at Constant Ionic Strength and pH

Series 2 was composed of electrolytes with varying carbonate anion concentrations all having the same ionic strength (maintained by the addition of the non-adsorbing and presumably non-interfering fluoride anion). Kinetic current densities measured with profiles A and C1 are shown in Figure 4-16. Rate constants for series 2 and series 3 electrolytes at 700 and 820 mV vs. RHE for three potential profiles are listed in Table 4-4 along with pertinent ionic compositions. The effect of the presence of carbonate on the rate of the 4-electron pathway, or k_1 , is not large. However, for the cathodic sweeps an increase in $C_{\text{CO}_3^-}$ depresses the rate of the peroxide path as indicated by the values of k_2 and k_3 .

4.2.7. Series 3: Effects of Carbonate Concentration and pH

Series 3 kinetic current densities are shown in Figure 4-17a and b, for profiles A and C1, respectively. Again referring to Table 4-4, the effect of carbonate on the values of k_1 and k_2 on the anodic sweep surface (profile A) is not large. However, with a decrease in pH, k_1 increases and k_2 decreases in agreement with the results of Appel and Appleby (36) discussed in Chapter 2. On the cathodic surface, both an increase in $C_{\text{CO}_3^-}$ and decrease in pH lead to promotion of the 4-electron over the 2-electron pathway.

In all of the pH 13 electrolytes, the cathodic surface generated with profile C1 showed greater values for k_1 and k_2 than those for the less-oxidized surface generated with profile A. This is the case for potentials less than 820 mV vs RHE, which was the limit at which these separate rate constants could be calculated. At higher potentials, the kinetic currents are indicative of the sum $k_1 + k_2$. These kinetic currents show the expected trend of decreasing as oxidation state increases. At the lower potentials, the increase in oxidation state from C1 to C2 further increased k_2 but tended to reduce k_1 in agreement with the work presented in Section 2.4. The calculation of k_3 was relatively difficult for the anodic surface because of the extremely low



- XBL 8710-4350 -

Figure 4-16: Kinetic Current Density for Series 2 Electrolytes, pH 13.

(a) Anodic Profile, A; (b) Cathodic Profile, C1

- △, 0.2M CO₃²⁻ (Ionic 1A);
- ×, 0.15M CO₃²⁻ (Ionic 1B);
- , 0.10M CO₃²⁻ (Ionic 1C);
- , 0M CO₃²⁻ (Ionic 2A).

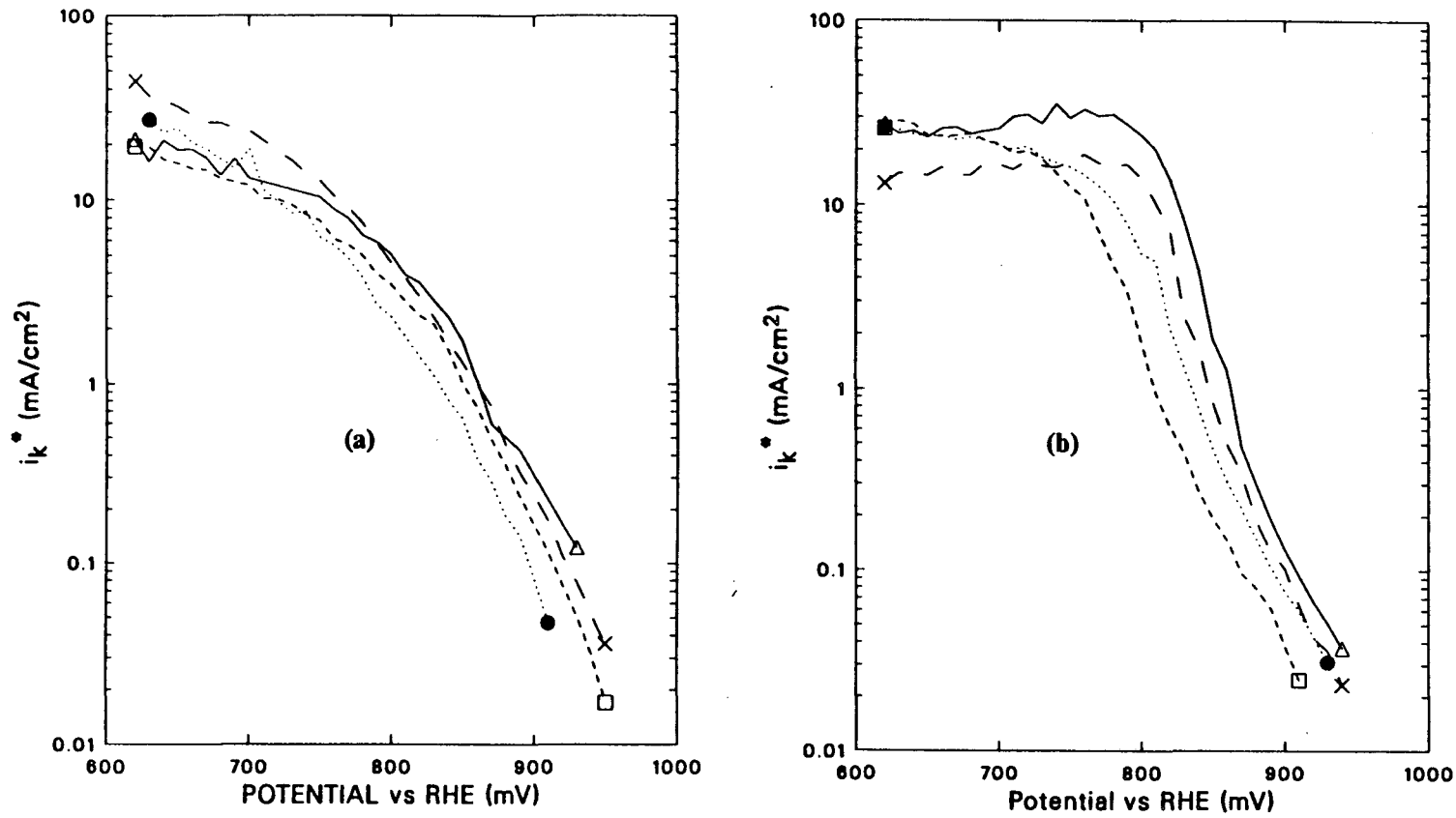


Figure 4-17: Kinetic Current Density for Series 3 Electrolytes.
 (a) Anodic Profile, A; (b) Cathodic Profile, C1
 —△, 0.1M CO₃²⁻, pH 13 (Ionic 1C);
 —×, 0M CO₃²⁻, pH 13 (Ionic 2A);
 - -□, 0M CO₃²⁻, pH 11.4 (Ionic 3);
 ·····●, 0.1M CO₃²⁻, pH 11.4 (Ionic 2B).

- XBL 8710-4351 -

Table 4-4: Three-step Model Rate Constants in Dilute Electrolytes
Part A: Rate Constants at 700 mV vs. RHE

Series	Exp. Name	pH	$C_{CO_3^-}$ (mol/l)	$k_1 \times 10^2$ (cm/sec)			$k_2 \times 10^6$ (cm/sec)			$k_3 \times 10^3$ (cm/sec)		
				profile			profile			profile		
				A	C1	C2	A	C1	C2	A	C1	C2
2	1A	13	0.2	4.2	7.5	5.2	2.8	95	82	‡	5.6	3.8
2	1B	13	0.15	4.3	†	†	9.1	†	†	7.1	†	†
2,3	1C	13	0.1	3.0	5.2	7.1	12.4	125	156	‡	8.4	7.1
2,3	2A	13	0	3.2	6.7	4.1	4.1	320	345	40	26	15
3	2B	11.4	0.1	6.2	4.4	5.7	0.6	39	49	‡	190	12
3	3	11.4	0	8.4	5.6	4.9	*	24	31	*	4.2	4.4

Part B: Rate Constants at 820 mV vs. RHE

Series	Exp. Name	pH	$C_{CO_3^-}$ (mol/l)	$k_1 \times 10^2$ (cm/sec)			$k_2 \times 10^6$ (cm/sec)			$k_3 \times 10^3$ (cm/sec)		
				profile			profile			profile		
				A	C1	C2	A	C1	C2	A	C1	C2
2	1A	13	0.2	5.6	29	9.6	5.6	260	162	1.8	10	7.3
2	1B	13	0.15	7.6	†	†	12	†	†	6.4	†	†
2,3	1C	13	0.1	1.6	34	15	6.9	356	27	41	11	8.4
2,3	2A	13	0	5.6	17	3.8	26	864	191	21	45	15
3	2B	11.4	0.1	8.6	4.9	5.5	2.4	‡	79	‡	‡	4.6
3	3	11.4	0	1.1	1.9	‡	*	2.5	‡	*	7.4	13

† Experiment not done

* uncalculable, no peroxide detected

‡ uncalculable, noisy data

level of peroxide produced, but it appears to be an inverse function of oxide coverage.

4.2.8. Summary of Anion Effects

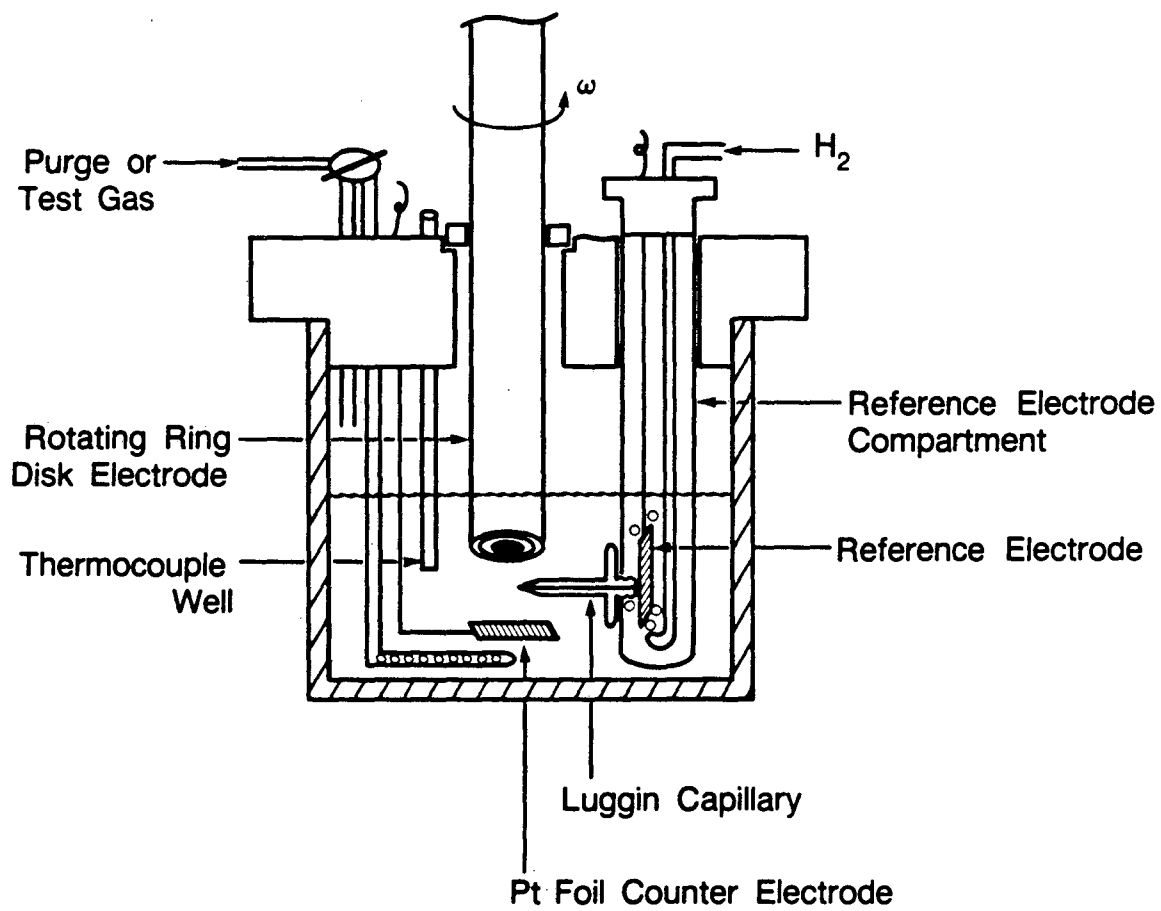
The presence of carbonate anion in an alkaline electrolyte tends to depress the rate of the 2-electron path for OR (k_2) and increase the rate of the 4-electron pathway (k_1), but not in proportion to the concentration. The OH^- ion exhibits the same effect as CO_3^{2-} on k_1 , while increasing the rate of the 2-electron path. These observations are made on a relatively small number of experiments and should be taken primarily as a starting point in the analysis of the behavior of concentrated electrolytes, to be discussed in the next section.

4.3. Oxygen Reduction in Concentrated Alkaline Electrolytes

Many investigators have studied oxygen reduction in KOH at concentrations of 1 M or less. Only one recent investigation has been carried out at higher concentrations, as reviewed in Chapter 2. No kinetic analyses in aqueous carbonate electrolytes have been reported, although carbonates have been used in at least one work as a pH-buffering medium. In this section we report the results of oxygen reduction kinetic studies with the RDE and RRDE for 0.5 to 6.9 M KOH and 0.1 to 4.0 M K_2CO_3 .

4.3.1. Experimental Equipment and Procedures

An all-PTFE cell was constructed for the study of concentrated alkaline electrolytes at elevated temperatures. A diagram of this cell is shown in Figure 4-18. Elevated temperatures were achieved with heating tape on the walls of the cell. N_2 (99.999%) and O_2 (99.96%) were bubbled through all-PTFE, heated bubblers filled with the working electrolyte for gas presaturation, to prevent dehydration of the electrolyte. Every part in contact with the electrolyte was constructed of PTFE with the exception of the nylon wick used in the Luggin capillary. This wick was found to be essential at the higher concentrations to maintain contact with the reference electrode and to prevent flow between the two chambers. A bubbling hydrogen reference electrode was used instead of the DHE due to a severe lack of stability in low-pH carbonate



XBL 8610-3867 A

Figure 4-18: All-PTFE rotating ring-disk electrode test cell.

electrolytes observed with the latter. Under all conditions the reference electrode was maintained at the same temperature and water vapor pressure as the working electrode. The active part of the RHE was either a high-area platinized platinum gauze or a piece of a supported platinum-on-carbon fuel cell electrode partially immersed in the electrolyte. A small flow of H_2 was bubbled continually through the electrolyte in the reference electrode compartment and out through a gas trap.

Electrolytes were prepared from the ultrapure salts listed in Section 4.2.1, but no preelectrolysis was carried out. The KOH concentrations were checked by dilution of 1 ml samples, acidification and back titration. Total carbonate in the K_2CO_3 electrolytes was determined by dilution of 1 ml samples, precipitation (by addition of $BaCl_2$), drying and weighing of $BaCO_3$.

RRDE experiments were carried out at room temperature in the manner discussed previously. However, the all-PTFE electrode is unsuitable for high-temperature kinetic measurements since the PTFE tends to flow if held for a long time at elevated temperature. Upon cooling, leaks form between the metal electrode and the PTFE, which doesn't return to its original shape. A new rotating disk electrode was designed and built with a nickel shaft and outer removable ring. The platinum disk was enclosed in a small piece of Kel-F and had an area of 0.71 cm^2 . The ring, which was removed when polishing the disk, enables the Kel-F spacer to maintain its shape. No leakage was detected after several experiments to 95°C .

The RDE current-potential sweeps were controlled and measured with a PAR 273 potentiostat. This instrument in turn was controlled by an IBM PC through a GPIB bus. Data were analyzed with the programs discussed previously.

4.3.2. Subtraction of Background Currents

The extremely low solubility of oxygen in high-concentration electrolytes reduces the measurable cathodic OR currents to the order of magnitude of the anodic platinum oxidation currents, even at low sweep rates. Therefore, the anodic background currents were measured in the absence of oxygen (with the electrode subjected to each of the profiles intended for OR study)

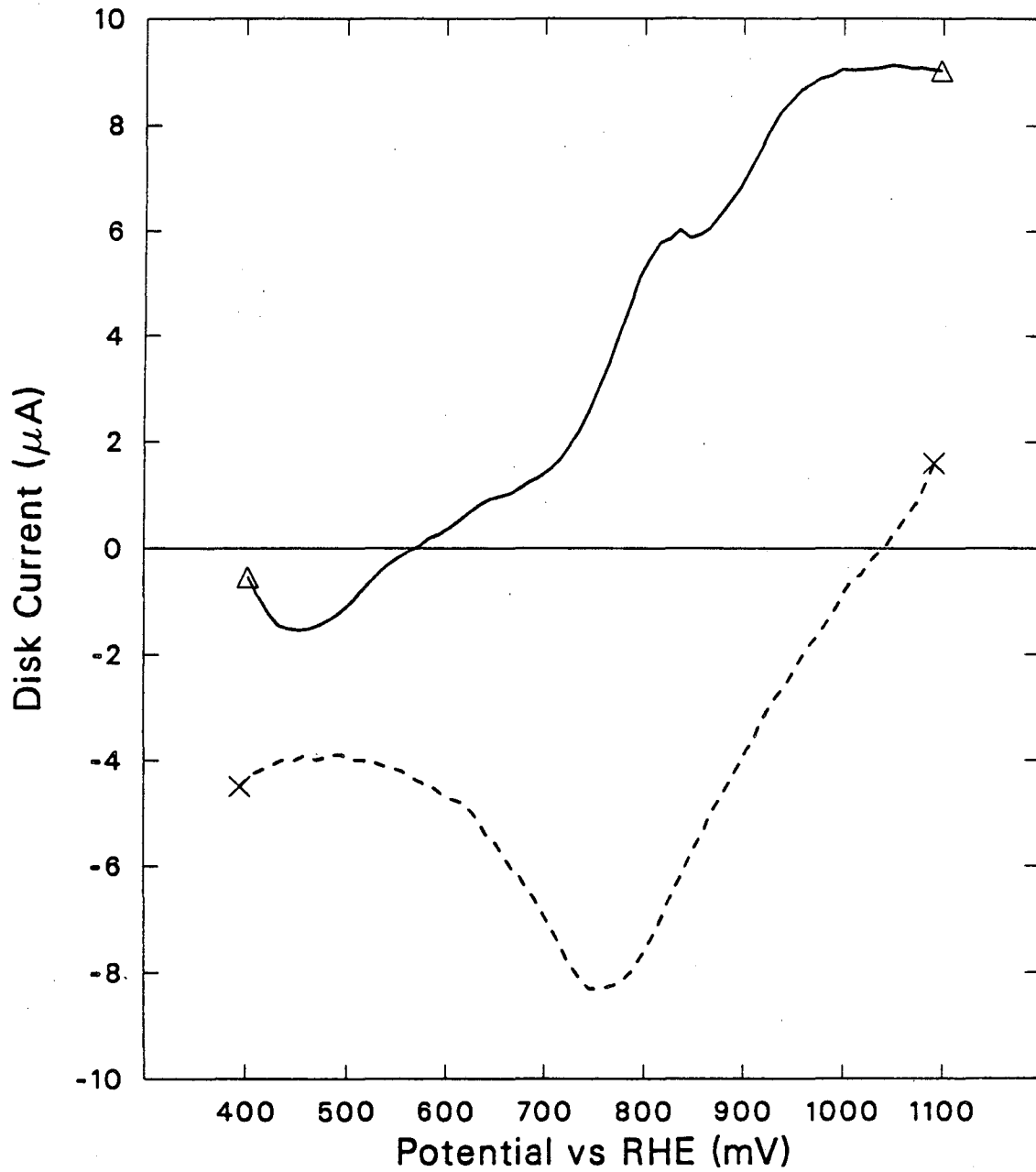
and then subtracted from the currents measured with oxygen-saturated solution. Background curves recorded at 900 rpm with an anodic sweep profile (A) and a cathodic sweep profile (C) in 5.4 M KOH under N₂ atmosphere are shown in Figure 4-19. Figure 4-20 shows RRDE data recorded with the same two profiles along with the corrected disk currents. In most cases, background currents were recorded before the electrolyte was saturated with oxygen. In this case, rotation of the electrode showed little effect, and curves at an intermediate rotation speed (900 to 1600 rpm) were used. In some cases it was necessary to record the background curves after some of the OR experiments (when several temperatures were investigated). In these cases, background data were recorded on the stationary electrode because of the difficulty of removing traces of oxygen remaining in the solution.

4.3.3. Analysis of RRDE and RDE Data with Multiple Reactions

With an RDE, only the "global" reaction rate can be measured. The equations used in Chapter 3 for the analysis of data were valid for a single reaction only. In the presence of a significant fraction of the current passing through a parallel pathway, the correction for mass transfer by extrapolation takes on a different meaning. With the 3-rate-constant model of Damjanovic, we can recompute the form of this correction. If the current due to step three is small compared to the sum $i_1 + i_2$, the following replacement for Equation 2-17 can be obtained by combining Equations 2-13 and 2-15

$$\frac{1}{i_d} = \frac{2(k_1 + k_2)}{2k_1 + k_2} \frac{1}{B\omega^{1/2}} + \frac{1}{2FC_{O_2}^\infty(2k_1 + k_2)} \quad (4-9)$$

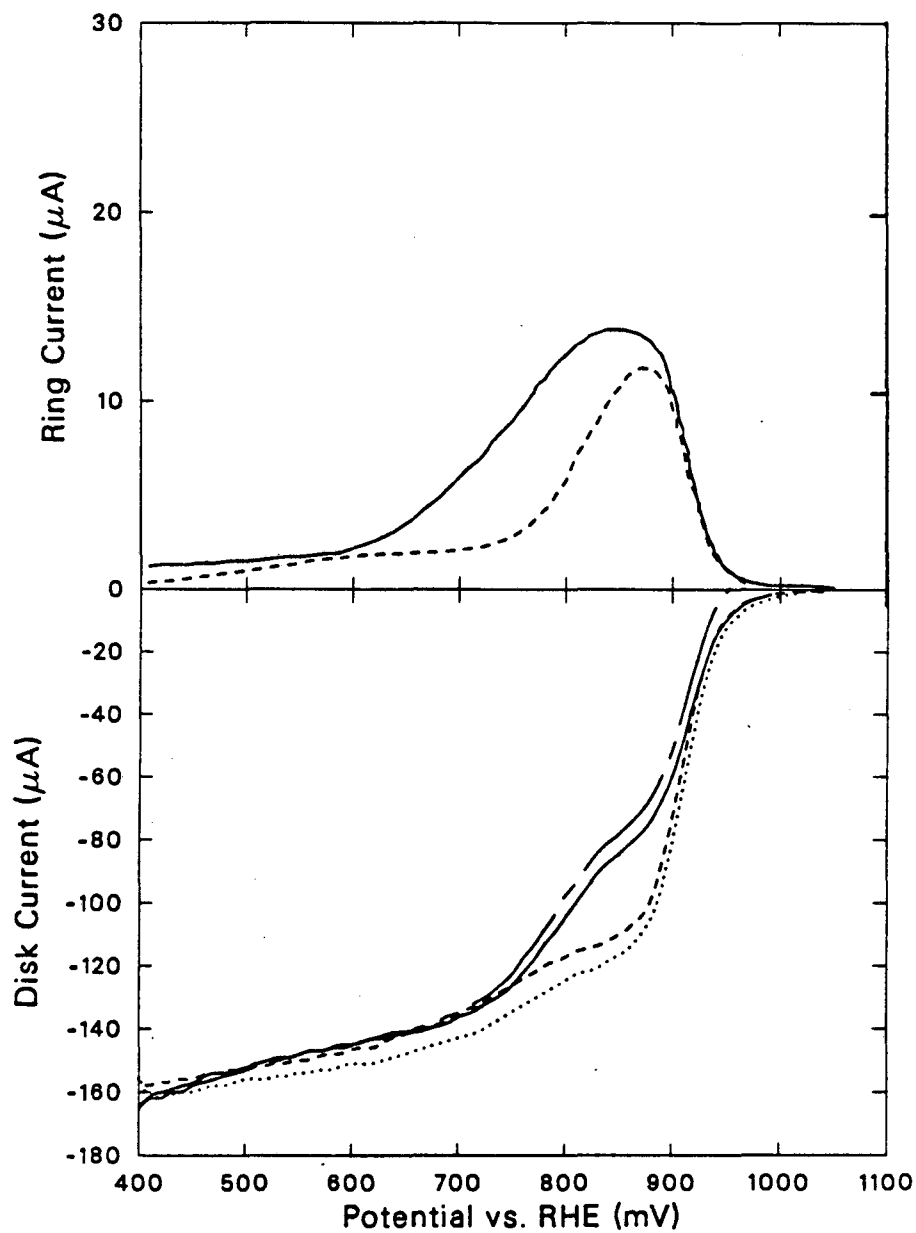
When $k_2 = 0$ this reduces to the classical relation in Equation 2-12, for a single reaction. When $k_2 \neq 0$, plots of $1/i_d$ vs $1/\omega^{1/2}$ should still be linear, but the slope may be a function of potential. This analysis points out the problem of using Equation 2-12 to calculate kinetic currents with the value of the Levich slope B from limiting current data. This analysis also suggests that non-linear plots of $1/i_d$ versus $1/\omega^{1/2}$ may be due to multiple reaction paths rather than to impurities.



- XBL 8710-4352 -

Figure 4-19: "Background" platinum oxidation currents in 5.4M KOH with two profiles at 25 °C.

— Δ , profile A (+10mV/sec);
- - - \times , profile C (-10mV/sec).



- XBL 8710-4353 -

Figure 4-20: RRDE data in 5.4M KOH, before and after the subtraction of "background" currents, for two potential profiles.

See Figure 4-10 for profiles.

- , Background subtracted data, profile A;
- , Background subtracted data, profile C1;
- · - · - ·, raw disk current data, profile A;
- , raw disk current data, profile C1.

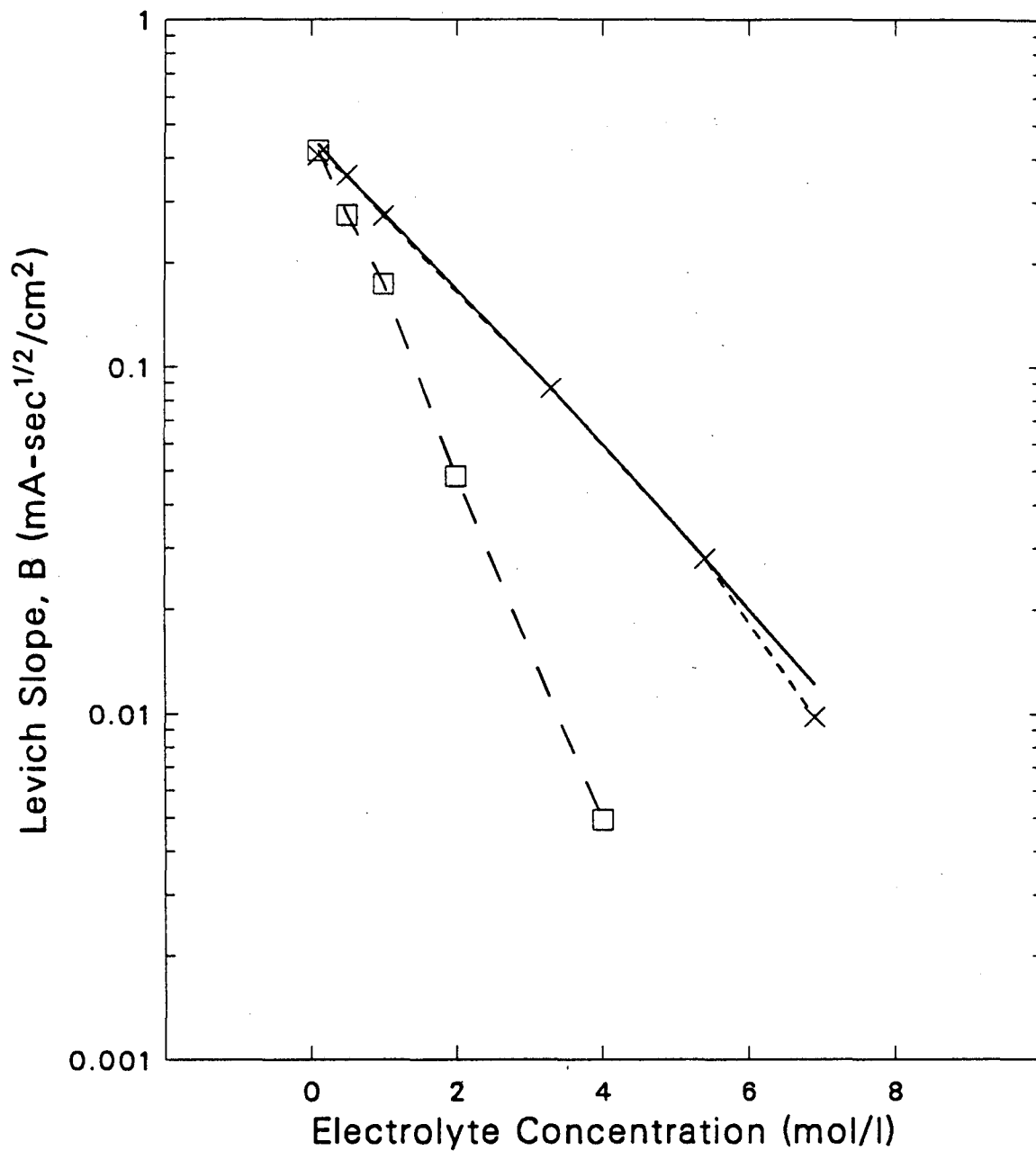
The analysis of the RRDE results in the high-concentration KOH electrolyte, according to the three-step model, and Equations 2-17 and 2-18, was unsatisfactory (yielding negative rate constants over part of the potential range studied) in many cases, even though the diagnostic plots were relatively linear. This could be due to the compound errors involved with the subtraction of background currents and the digital averaging of small signals. However, it seems more likely that this is an indication that the three-step reaction scheme is too simple. More-complex schemes could be proposed as discussed in Chapter 2; however the relatively small amount of data (four rotation speeds for each experiment in most cases) does not warrant numerical fitting to calculate rate constants. The kinetic interpretation given here will be based on three factors: (i) i_k^* computed from the RRDE data is an indicator of the total rate of oxygen conversion through the parallel pathways if all peroxide were reacted to water. (ii) The potential dependence of i_k^* will be intermediate to that of the two pathways. (iii) The maximum percentage of oxygen reacting through the 2-electron pathway can be estimated from

$$\% \text{H}_2\text{O}_2 = \frac{I_{2e^-}}{I_{4e^-}} * 100 = \frac{I_r}{I_r + NI_d} * 100 \quad (4-10)$$

at the potential where the ring current is a maximum. Plots of the ratio of J_2/S_2 (intercept/slope of the plot of $I_d N_c / I_r$ versus $\omega^{1/2}$) against potential will be used as an indication of the rate of the further reaction of peroxide, as suggested by Appleby and Savy (23) for several lumped-parameter mechanisms.

4.3.4. General Results for Concentrated Electrolytes

Figure 4-21 shows the measured Levich slopes for both KOH and K_2CO_3 electrolytes as a function of concentration. A log scale is used for the ordinate since $C_{\text{O}_2}^\infty$ depends on $\log C_{\text{salt}}$ (see Equation 4-8) and D_{O_2} is a much weaker linear function of electrolyte concentration. The solid curve, calculated from literature data for KOH for $n = 4$, compares quite well with the observed values. These data were obtained from the slopes of plots of $1/i_d^*$ according to Equation 2-17. Table 4-5 lists the values of these Levich slopes and physical properties for the electrolytes



- XBL 8710-4354 -

Figure 4-21: Concentration dependence of Levich slope in alkaline electrolytes, 25 °C.
 ———, KOH, predicted from literature data in Table 4-5;
 ———x, KOH data;
 ———□, K₂CO₃ data.

discussed in this section.

Figure 4-22 shows a comparison of the kinetic current densities calculated from the background-corrected data in Figure 4-21 using the procedures discussed in Section 4.2 and Equations 2-17 and 4-9 to determine i_k^* and i_k , respectively. The anodic sweep data generally show two to three regions of Tafel behavior whereas the more oxidized surface generated by the

Table 4-5: Experimental and Predicted Levich Slopes
Part A: KOH Electrolytes

Conc. (mol/l)	Levich slope (mA-sec ^{1/2} /cm ²)		Electrolyte Properties					
	EXP.	PRED.	$\frac{C_{O_2}}{C_{O_2}^{water}}$ ^g	$D_{O_2}^7 \times 10^5$ (cm ² /sec)	ρ^f (g/cm ³)	μ^f (cp)	a_w	a_{OH^-} (mol/kg)
0.1	0.420	0.440	0.971	1.87	1.00	1.01	0.997 ^a	0.07 ^a
0.5	0.358	0.354	0.818	1.74	1.025	1.06	0.983 ^a	0.36 ^a
1.0	0.273	0.278	0.669	1.65	1.045	1.12	0.961 ^c	0.74 ^c
3.3	0.087	0.0863	0.265	1.20	1.12	1.47	0.822 ^c	6.8 ^c
5.4	0.028	0.028	0.114	0.818	1.24	1.94	0.671 ^c	22 ^c
6.9	0.0103	0.0122	0.063	0.607	1.29	2.4	0.578 ^c	41 ^c

Part B: K₂CO₃ Electrolytes

Conc. (mol/l)	Levich slope (mA-sec ^{1/2} /cm ²) EXP.	Electrolyte Properties			
		$\frac{C_{O_2}}{C_{O_2}^{water}}$ ^b	ρ^c (g/cm ³)	a_w^d	$a_{OH^-}^d$ (mol/kg)
0.1	0.422	0.918	1.0	0.995	0.0022
0.5	0.292	0.560	1.0	0.979	0.0036
1.0	0.173	0.423	1.120	0.956	0.0049
2.0	0.049	0.179	1.203	0.899	0.0083
4.0	0.0046	0.032	1.385	0.709	0.033

^aStokes and Robinson (74)

^bSalting-out Correlation (73)

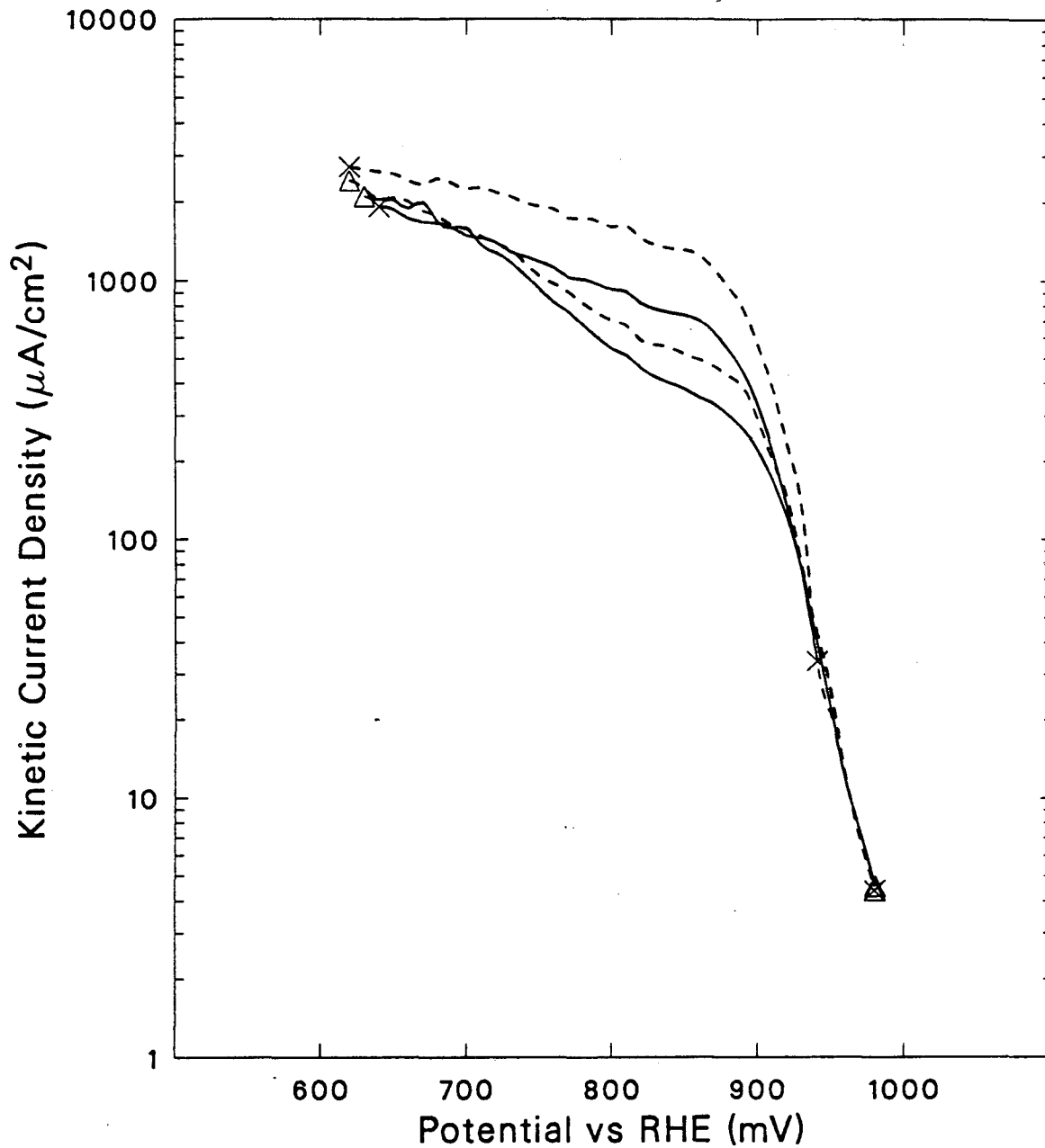
^cMacdonald et al. (75)

^dRoy et al. (76)

^emeasured by volumetric technique

^fFalk and Salkind (78)

^gGubbins and Walker (79)



- XBL 8710-4355 -

Figure 4-22: Comparison of calculation techniques for oxygen reduction kinetic current density in 5.4M KOH, 23 °C.

— i_k ;
 — i_k ;

Δ, anodic profile; ×, cathodic profile.

cathodic sweep usually exhibits a very steep rise to a potential-insensitive current below about 800 mV. The higher-slope region at very low current densities, noted for the cathodic sweep experiments in Section 4.2, disappears at concentrations greater than 0.5 M in both KOH and K_2CO_3 .

4.3.5. OR Dependence on KOH Concentration at 23 ° C

Table 4-6 lists Tafel slopes, potential ranges over which they are valid, values of i_k^* at 700 and 900 mV versus RHE and the maximum percentage of peroxide generated for the KOH electrolytes tested. Exchange current densities are not reported because of the uncertainty involved in the long extrapolation to E^0 . Figure 4-23 shows the potential dependence of kinetic current density at several KOH concentrations measured with anodic and cathodic potential profiles. These data were not corrected for differences in O_2 solubility, only electrode area. In order to isolate the effect of hydroxide concentration, a "normalized" current density, i_k^{*0} was calculated according to

Table 4-6: Kinetic Parameters in KOH Electrolytes
Part A: Anodic Profile Experiments

Conc. (mol/l)	i_k^* (mA/cm ²)		Tafel Slope (mV/dec)	Potential Range (mV)	%H ₂ O ₂ @ max
	@700 mV	@900 mV			
0.1	15.8	0.123	64	800-925	1.4
0.5	11.7	0.197	67	880-950	0.76
1.0	10.7	0.203	76	860-920	0.95
3.3	3.3	0.304	40	900-970	22
5.4	1.52	0.398	41	910-960	31
6.9	1.23	0.431	34	930-990	32

Part B: Cathodic Profile Experiments

Conc. (mol/l)	i_k^* (mA/cm ²)		Tafel Slope (mV/dec)	Potential Range (mV)	%H ₂ O ₂ @ max
	@700 mV	@900 mV			
0.5	14.0	0.098	47	880-910	1.3
3.3	3.7	0.35	29	910-950	15
5.4	1.86	0.51	34	910-980	28
6.9	1.76	1.02	28	920-970	32

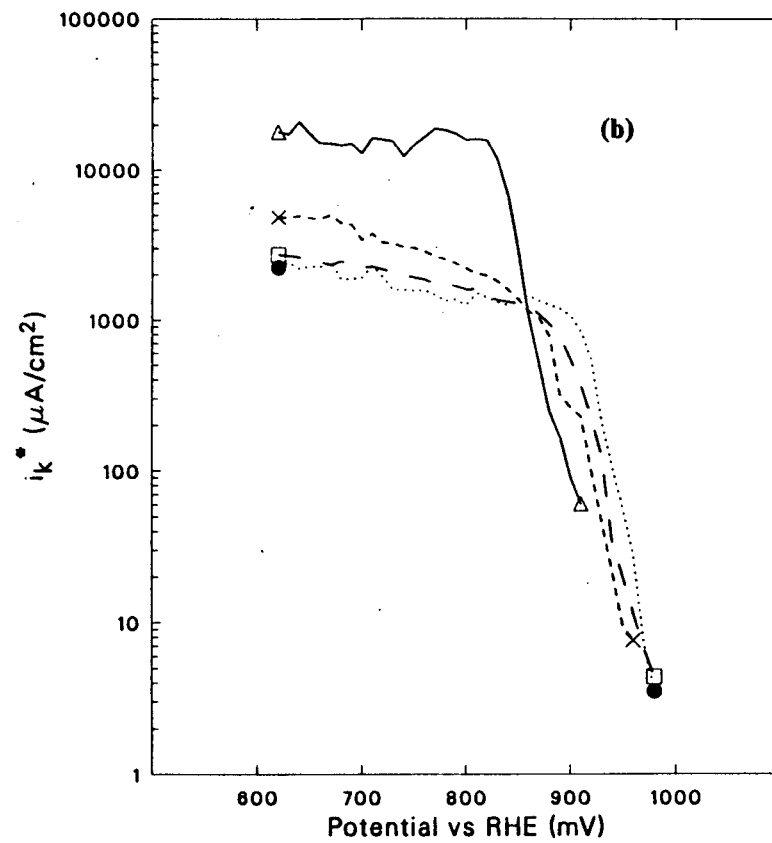
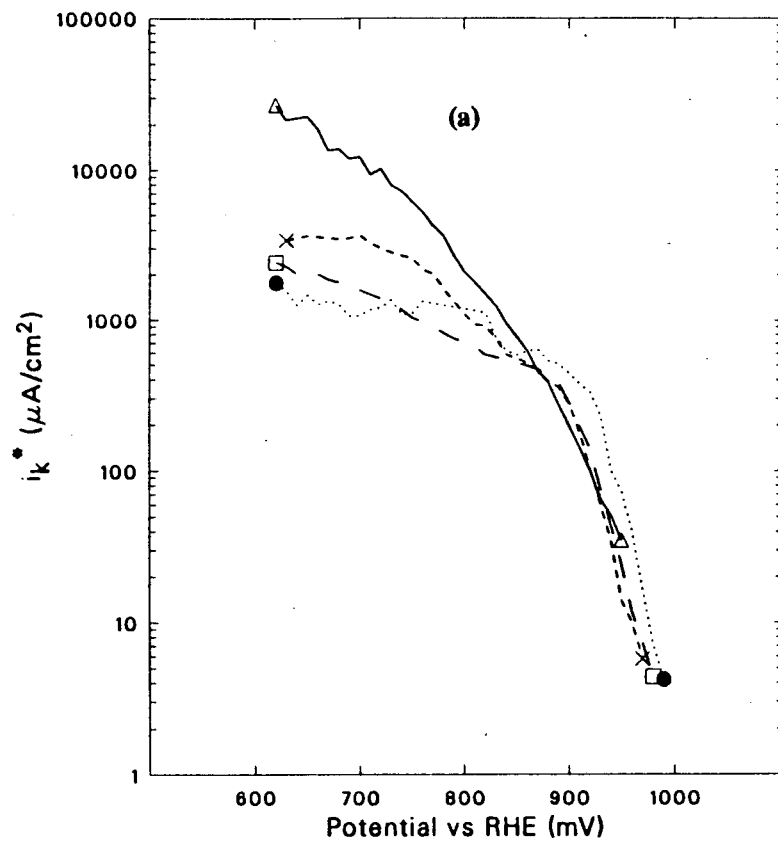


Figure 4-23: Concentration Dependence of Kinetic Current Density in KOH Electrolytes.

(a) Anodic Profile, A; (b) Cathodic Profile, C1

—Δ, 0.5M; —X, 3.3M; —□, 5.4M; ·····●, 6.9M.

- XBL 8710-4356 -

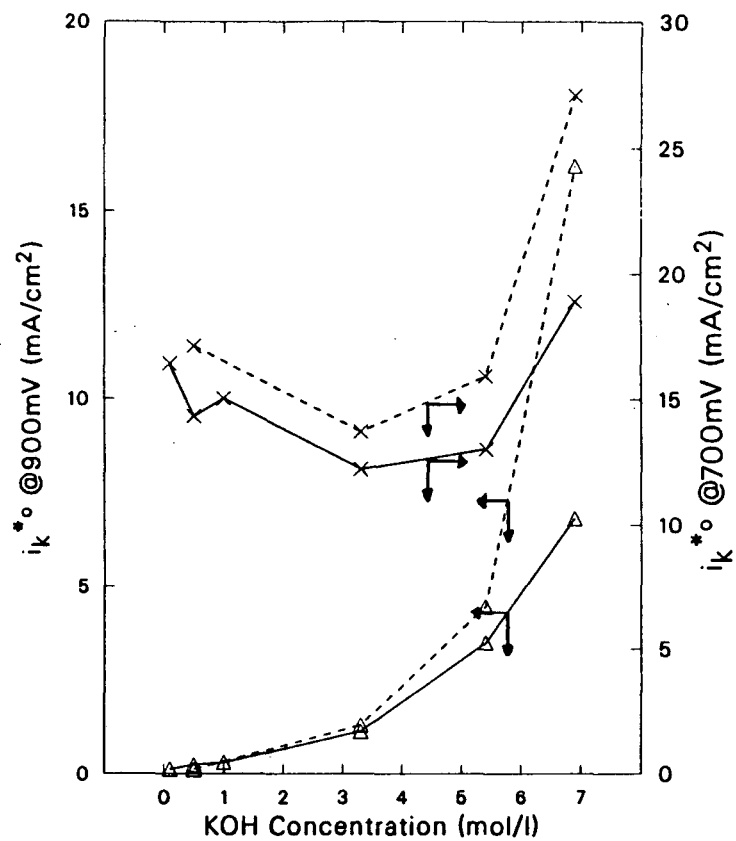
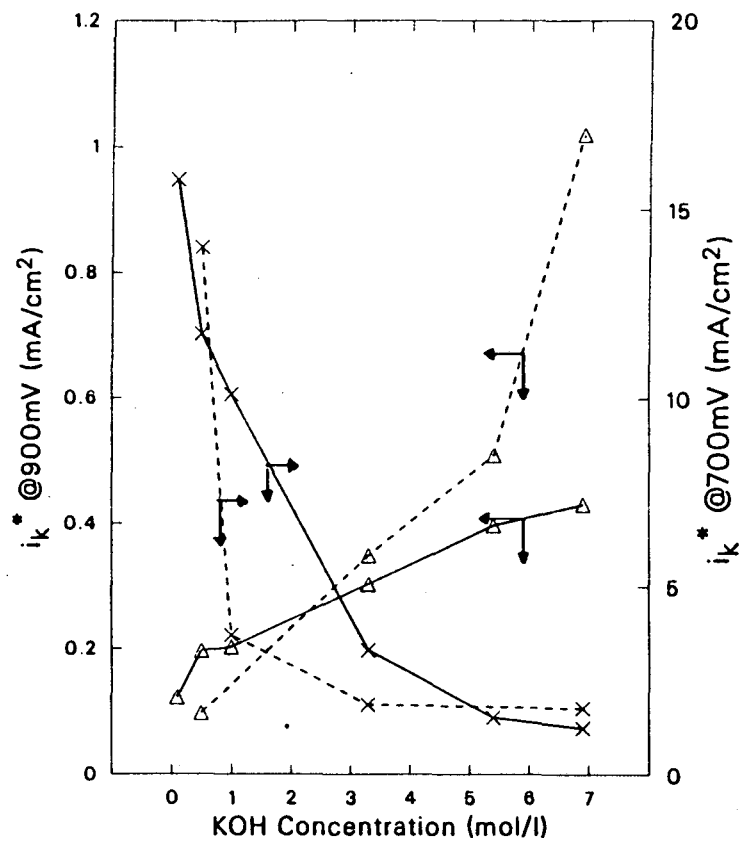
$$i_k^* = \frac{(C_{O_2}^{\infty})_{\text{water}}}{(C_{O_2}^{\infty})_{\text{electrolyte}}} i_k^* \quad (4-11)$$

Regular and normalized kinetic current densities at 700 and 900 mV vs. RHE are shown in Figure 4-24a and b. The value of i_k^* can be seen to increase with concentration at 900 mV vs. RHE and decrease with concentration at 700 mV. After correction for the difference in oxygen concentration, i_k^* at 700 mV exhibits a minimum in activity around 3.3 M. The data from Figure 4-24b are replotted in Figure 4-25 as a function of hydroxide ion activity. At 900 mV, the normalized OR activity is almost a linear function of hydroxide activity for both surfaces up to 5.4 M KOH. The dependence of the maximum percentage of peroxide on KOH concentration is shown in in Figure 4-26.

Figures 4-25 and 4-26 both show a change in concentration dependence at approximately 3.3 M KOH coincident with the change in the potential-dependence of the oxide coverage noted in Section 4.1. The Tafel slope for these experiments can also be seen to drop from around 60 mV/decade at low current densities and low concentrations to around 30 to 40 mV/decade in the higher-concentration electrolytes. A Tafel slope of 30 mV/decade is indicative of O_2/HO_2^- couple at pseudo-equilibrium. Such a mechanism is very much different from the model of Damjanovic. Therefore, it is not surprising that the simple 3-reaction lumped-parameter model fails at the high concentrations.

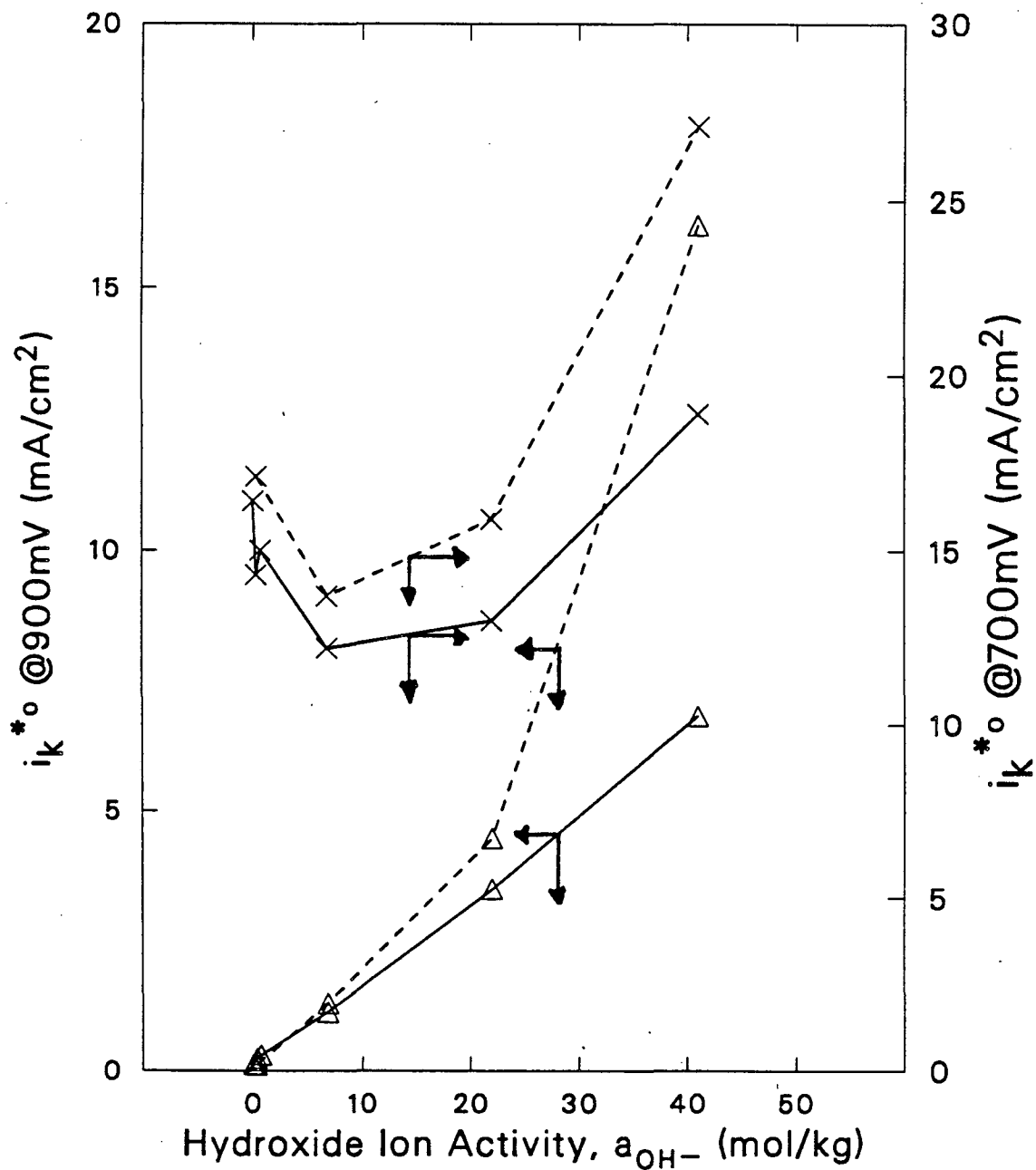
J plots for some of the high-concentration experiments are compared in Figure 4-27. In dilute electrolytes, the rate of further reduction of peroxide, k_3 , was seen to decrease as the electrode surface became more oxidized. From Figure 4-27a it appears that the rate for further reaction of peroxide is highest at the intermediate concentration of 3.3 M. These data are noisy because of the error involved with extrapolation to $1/\omega^{1/2} \rightarrow 0$, compounded with the subtraction of background currents, etc.

It appears now that a more-aged oxide structure results in lower rates of peroxide consumption. This was evident in the decrease of k_3 in going from profile C1 to C2 in the dilute-



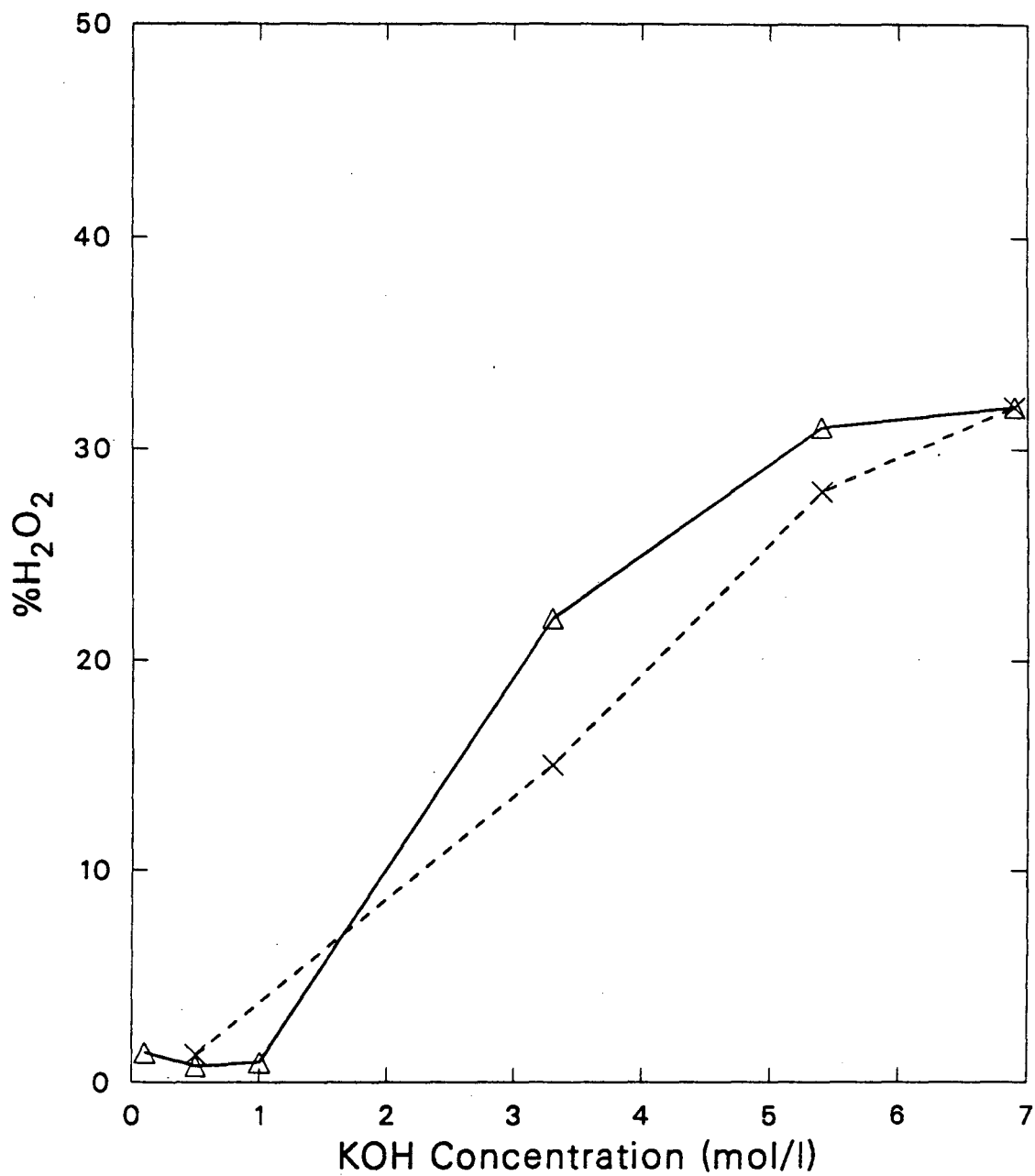
- XBL 8710-4357 -

Figure 4-24: Concentration-dependence of i_k^* and i_k^o , in KOH electrolytes, 25 °C.
 ———, Anodic profile; - - - - - , Cathodic profile;
 X, 700mV; Δ, 900 mV.



- XBL 8710-4358

Figure 4-25: Hydroxide activity dependence of normalized current density, i_k^* , in KOH electrolytes, 25 °C.
 ———, Anodic profile; - - - - - , Cathodic profile;
 X, 700mV, Δ, 900 mV.



- XBL 8710-4359 -

Figure 4-26: Percentage of kinetic current proceeding through the 2-electron pathway on platinum in 5.4M KOH, 23 °C.
———Δ, anodic profile; ———X, cathodic profile.

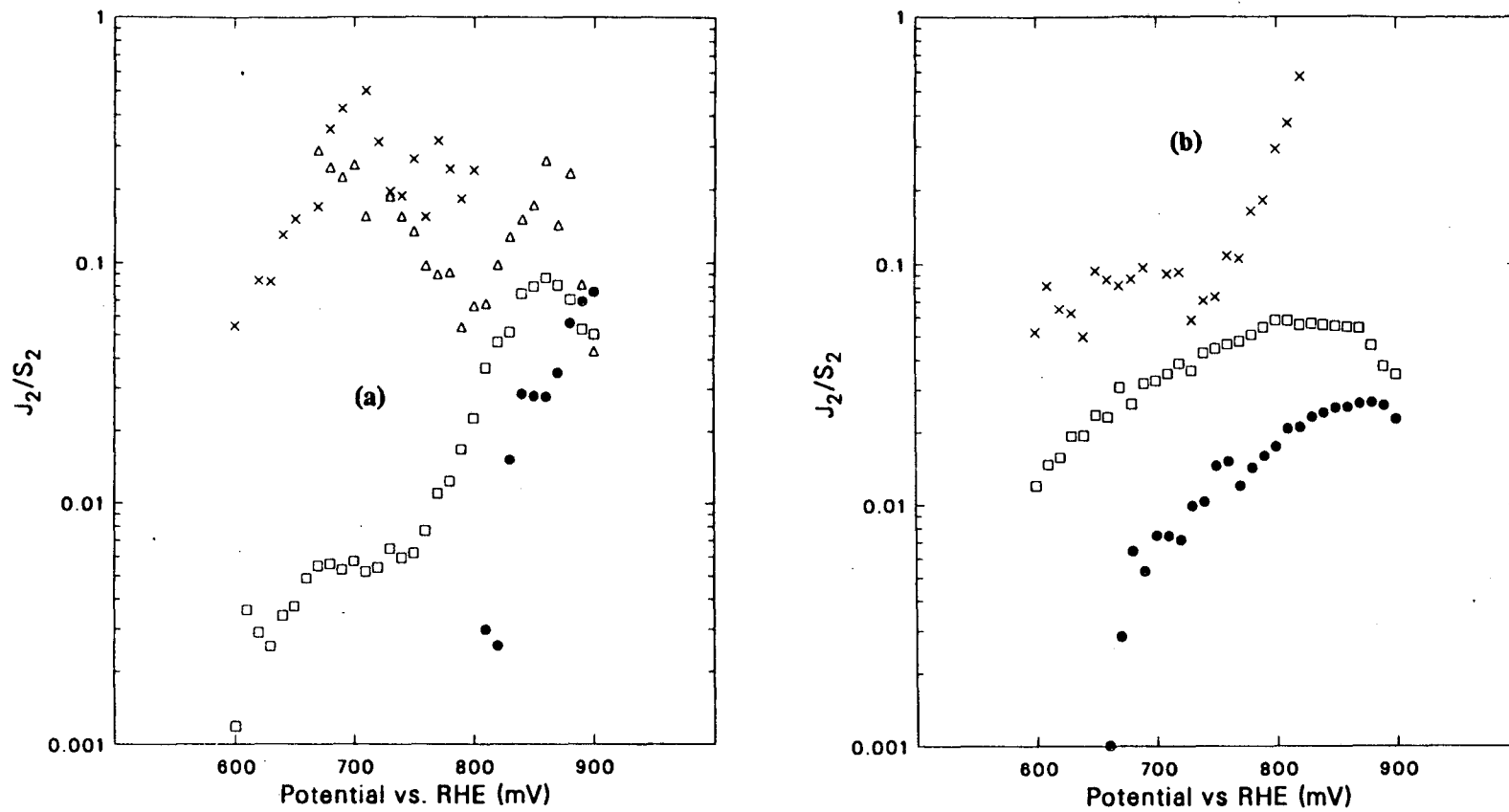


Figure 4-27: J-Plots in KOH Electrolytes. $J_2/S_2 = k_3 + k_4$ according to some lumped-parameter models (23).

(a) Anodic Profile; (b) Cathodic Profile;

—△, 0.5M; - - - - - ×, 3.3M; — — — □, 5.4M; · · · · · ●, 6.9M;

- XBL 8711-4744 -

electrolyte studies. It can also be inferred from the lowering of the sum $k_3 + k_4$ shown in these J-plots coinciding with the change in platinum oxidation mechanism as noted in Section 4.1.

4.3.6. OR Rate Dependence on K_2CO_3 Concentration at 23 ° C

Figure 4-28 shows the Tafel behavior for OR in K_2CO_3 at several concentrations and from two potential profiles. Tafel slopes and kinetic current densities are listed in Table 4-7 for K_2CO_3 . Kinetic current densities, at 700 and 900 mV, corrected for the dramatic changes in oxygen concentration (according to Equation 4-11), are shown in Figure 4-29. The activity at both potentials generally increases with concentration in contrast to the results at the low potentials in KOH, which showed a minimum at a concentration of about 3 M. The maximum percentage peroxide current was less than 1% for cathodic sweep experiments performed at 1 and 2 M and essentially zero for all of the anodic sweep experiments ($I_r < 0.1\mu A$).

4.3.7. KOH versus K_2CO_3 at 23 ° C

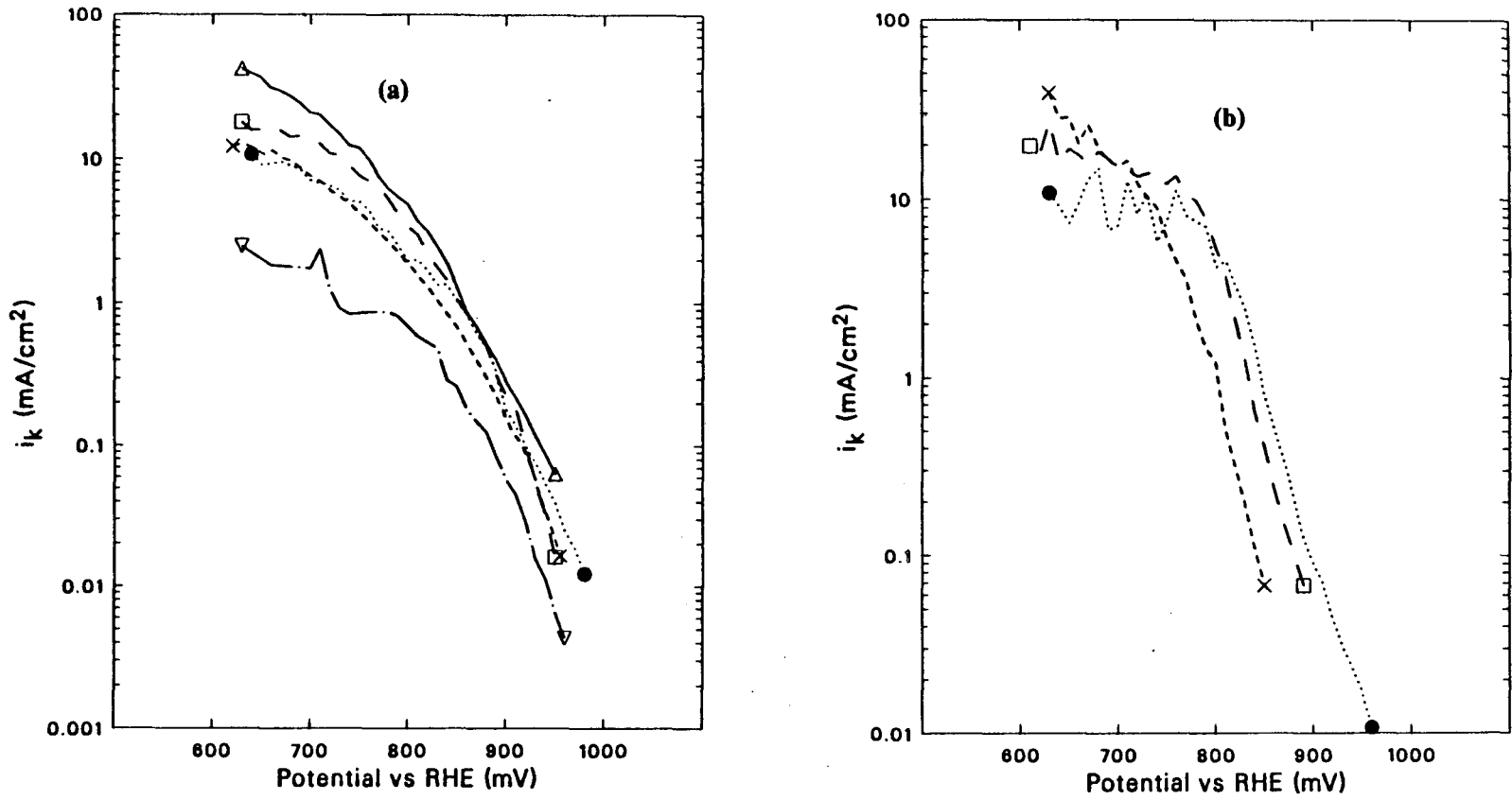
Whereas i_k^* has mechanistic significance, the truer measure of the observable mass-transfer-corrected current density, i_k , will be used to compare the rates of oxygen reduction in

Table 4-7: Kinetic Parameters in K_2CO_3 Electrolytes
Part A: Anodic Profile Experiments

Conc. (mol/l)	i_k^* (mA/cm ²)		Tafel Slope (mV/dec)	Potential Range (mV)
	@700 mV	@900 mV		
0.1	22	0.293	76	830-950
0.5	18	0.349	69	860-980
1.0	19	0.286	58	880-950
2.0	7.1	0.217	66	860-980
4.0	1.8	0.064	51	900-960

Part B: Cathodic Profile Experiments

Conc. (mol/l)	i_k^* (mA/cm ²)		Tafel Slope (mV/dec)	Potential Range (mV)
	@700 mV	@900 mV		
0.5	14	0.0058	47	770-850
1.0	19	0.086	58	860-920
2.0	9.9	0.109	56	810-960



- XBL 8710-4360 -

Figure 4-28: Concentration dependence of kinetic current density in K_2CO_3 electrolytes. (a) Anodic Profile; (b) Cathodic Profile; — Δ , 0.1M; - - - \times , 0.5M; - - - \square , 1.0M; ····· \bullet , 2.0M; - · - · ∇ , 4.0M.

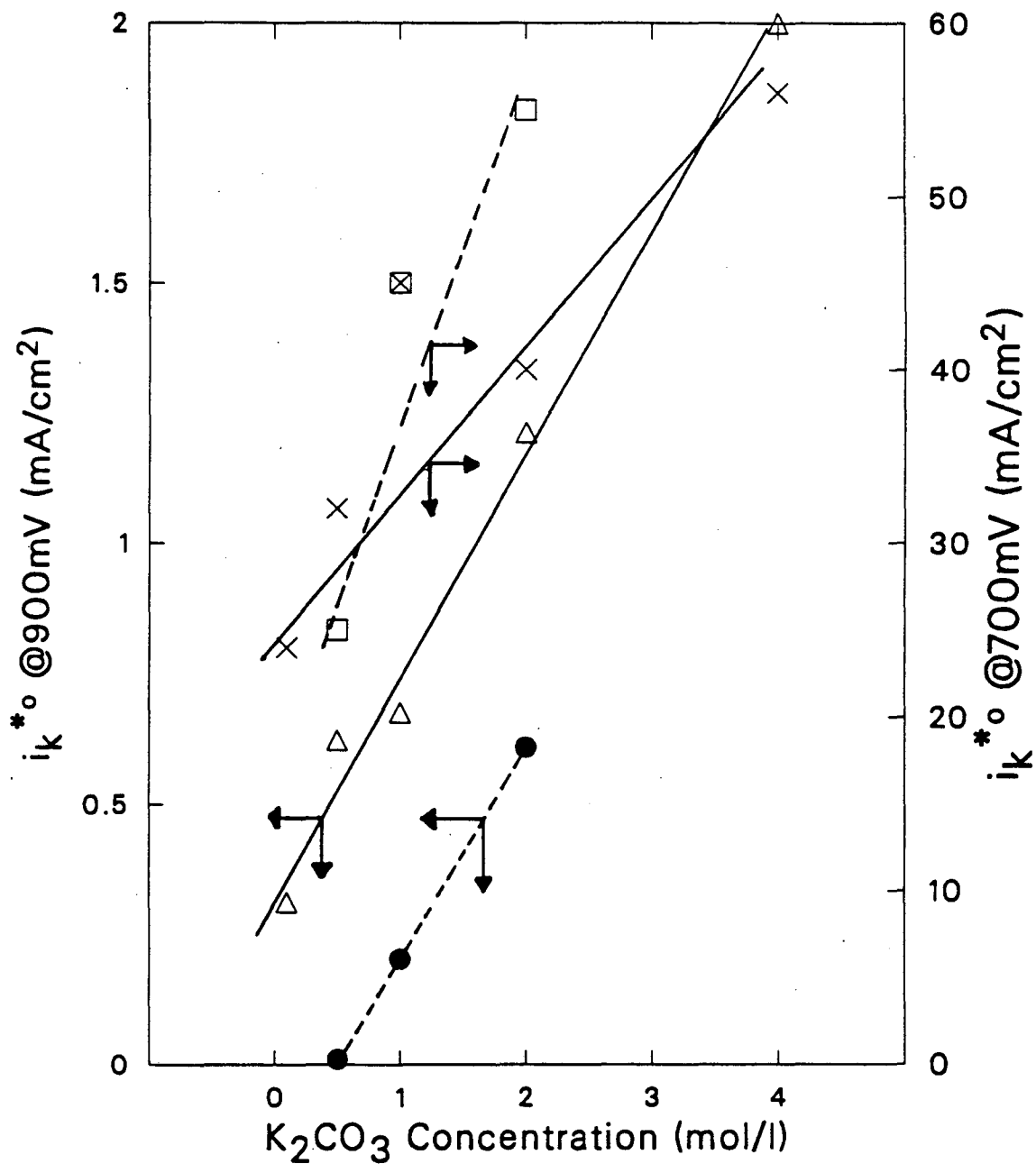


Figure 4-29: Concentration dependence of normalized current density, i_k^* , in K_2CO_3 electrolytes, 23 °C.

—, Anodic profile: x, 700mV; Δ, 900 mV;
 —, Cathodic profile: □, 700mV; ●, 900 mV.

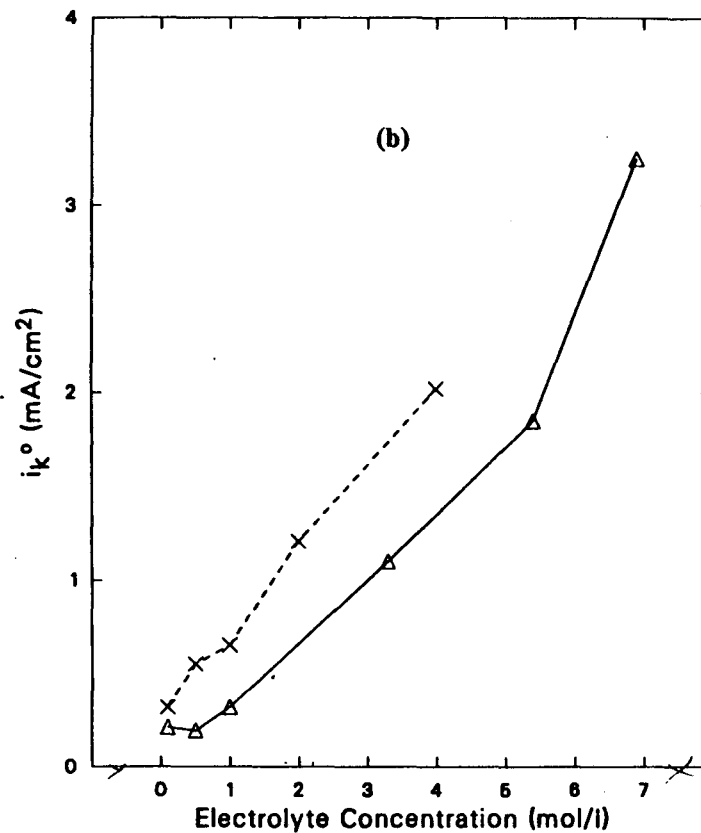
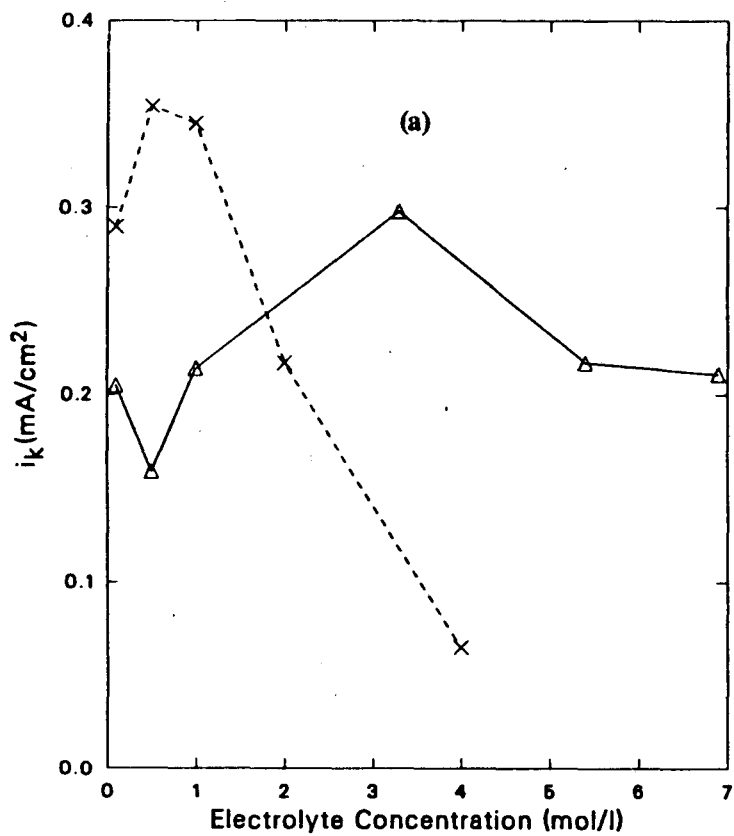
KOH and K_2CO_3 . Figure 4-30 shows i_k and i_k^0 as functions of electrolyte concentration for the two salts. At low concentrations, K_2CO_3 shows higher OR currents as we reported earlier (109). At an electrolyte concentration above 3 N, the low solubility of oxygen limits the activity in K_2CO_3 . When normalized to the oxygen concentration in pure water, the activity for OR in K_2CO_3 is greater than in KOH. The dramatic rise in OR rate in KOH noted in Figure 4-24 is countered by the reduction in the rate of further reaction of the peroxide. K_2CO_3 has an additional advantage over KOH, because peroxide has been suggested to be detrimental to carbon-supported electrodes.

4.3.8. Temperature Dependence of Oxygen Reduction in Concentrated Alkaline Electrolytes

Oxygen reduction experiments were performed at three or four temperatures in 1.0 M KOH, 1.0 M K_2CO_3 , and 6.9 M KOH. In all cases the hydrogen reference electrode was held at the same temperature and water vapor pressure as the working electrode. Levich slopes are shown as a function of temperature in Figure 4-31. In all three electrolytes a maximum is observed due to the competing effects of oxygen solubility and diffusivity. In pure water, C_{O_2} decreases with T and D_{O_2} increases with T. Data for C_{O_2} and D_{O_2} at various temperatures are not available for either KOH or K_2CO_3 solutions.

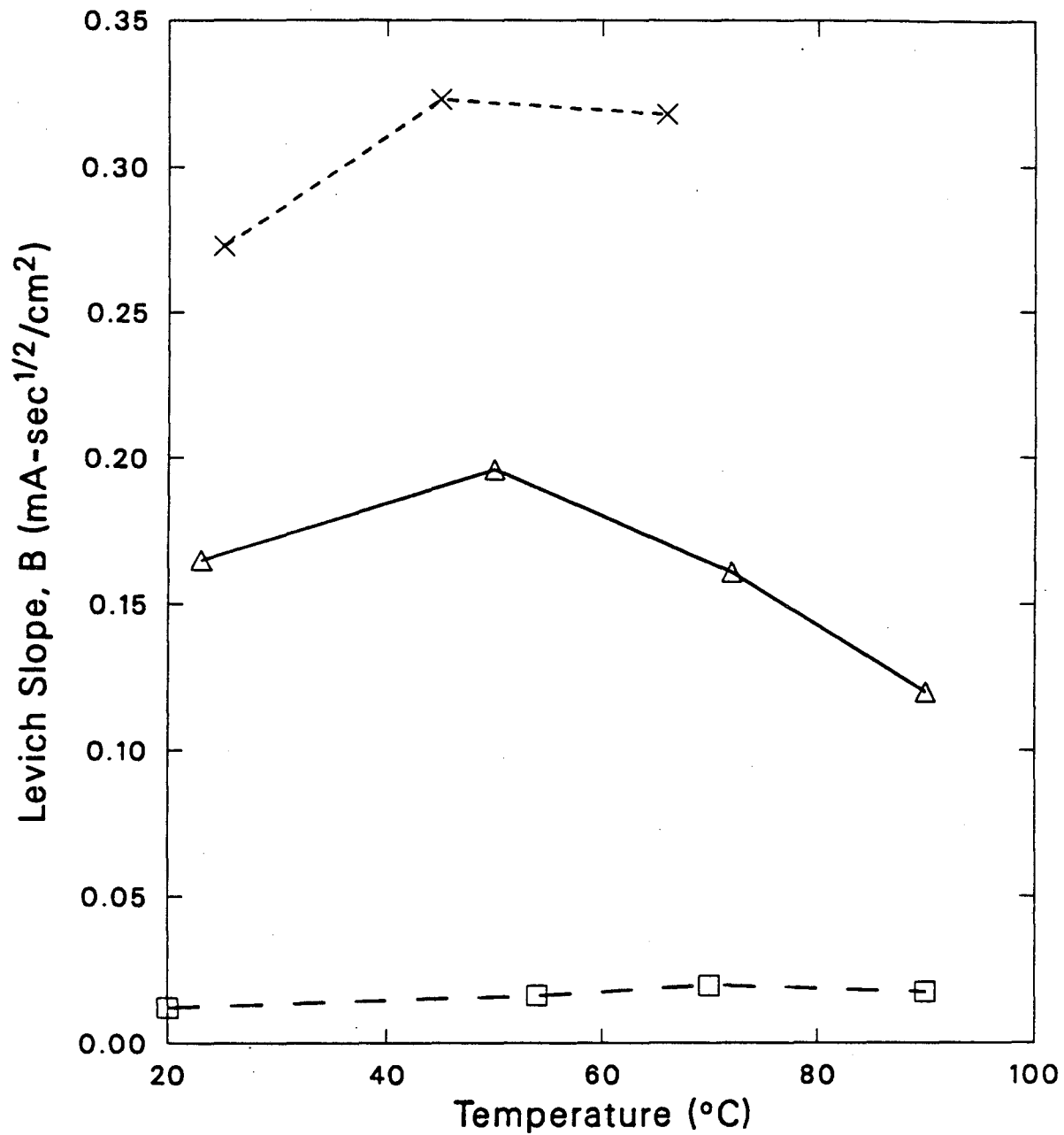
The kinetic behavior expected for the oxygen cathode in a fuel cell is directly demonstrated by kinetic current density plots without corrections for water vapor pressures. Figure 4-32 shows i_k^* for 1 M K_2CO_3 and 6.9 M KOH at several temperatures. In both electrolytes the high-current-density region shows little dependence on temperature, and the Tafel region shows a minimum activity at an intermediate temperature around 50 °C. Both electrolytes show a negative effect of temperature in the Tafel region.

In order to obtain any mechanistic information, data must be corrected to a constant reference electrode potential and oxygen pressure. According to the Nernst equation for the hydrogen electrode in alkaline media



- XBL 8710-4361 -

Figure 4-30: Comparison of mass-transfer-corrected current density in KOH and K₂CO₃ electrolytes, at 900mV vs. RHE, 23 °C.
 (a) i_k corrected for electrode roughness.
 (b) Normalized current density, i_k^0 , corrected for roughness and $C_{O_2}^\infty$ differences.
 — Δ, KOH; - - - ×, K₂CO₃.



XBL 8710-4362

Figure 4-31: Temperature dependence of the Levich slope for oxygen reduction in alkaline electrolytes.
——— Δ , 1.0M K₂CO₃;
----- \times , 1.0M KOH;
- - - \square , 6.9M KOH.

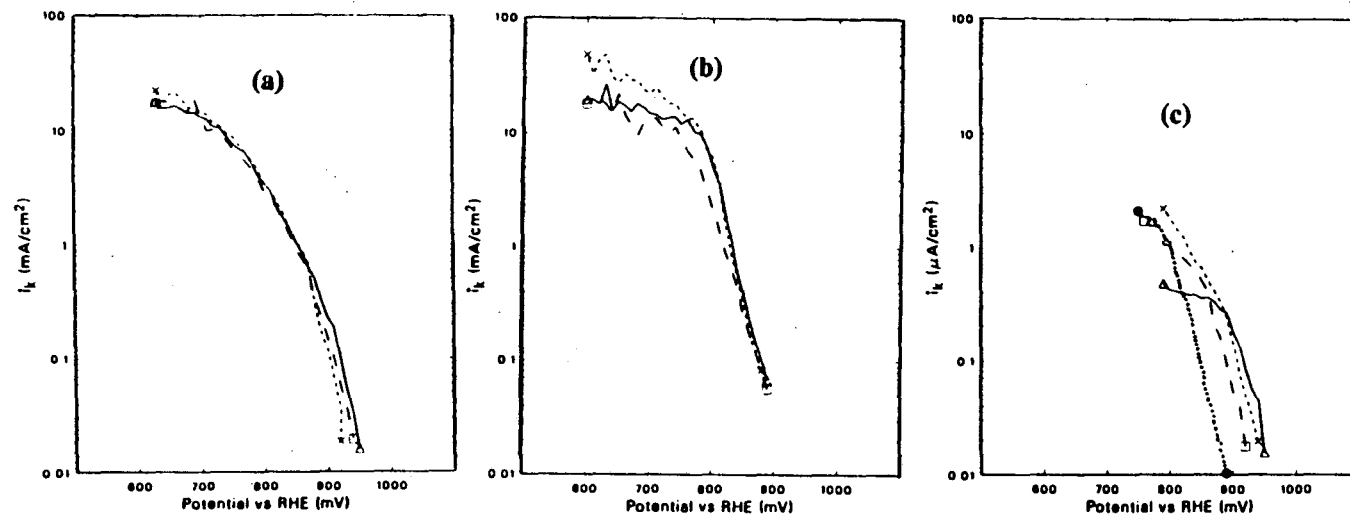


Figure 4-32: Dependence of kinetic current density on temperature in alkaline electrolytes.
 (a) 1.0M K_2CO_3 , Anodic Profile; (b) 1.0M K_2CO_3 , Cathodic Profile; (c) 30% KOH, Cathodic Profile.
 ———— Δ , 23 °C; - - - - - \times , 50 °C; — — — \square , 70 °C; ····· \bullet , 90 °C.

- XBL 8711-4742 -

$$E_{\text{RHE}}(T) - E_{\text{RHE}}(T_{\text{ref}}) = -\frac{RT}{2F} \left[2 \ln \frac{a_w(T)}{a_w(T_{\text{ref}})} - \ln p_{\text{H}_2} + 2 \ln \frac{\gamma_{\text{KOH}}(T_{\text{ref}})}{\gamma_{\text{KOH}}(T)} \right] \quad (4-12)$$

where γ_{KOH} is the mean ionic activity coefficient for KOH and a_w is the water activity. Activity coefficients and water activities are available from at least two sources for KOH at temperatures up to 120 °C (74,75). However, values from these sources differ significantly at the higher temperatures and concentrations. Corrections were made to the KOH data with the activity values listed in Table 4-8. Only room-temperature data are available for K_2CO_3 . Water activities vary only slightly with temperature in most electrolytes, so corrections were made with the room-temperature value of a_w and the appropriate vapor pressures of pure water. Table 4-8 lists Tafel slopes and current densities at 900 mV vs RHE at 25 °C. The dependence of Tafel slope on temperature is not large. The most significant conclusion from these data is that even though OR may be an activated process, as indicated in the literature, the decrease in oxygen solubility, and possibly changes in the oxidation state of the platinum, combine to render a small negative temperature effect in both KOH and K_2CO_3 . There may be other factors such as heat and water rejection requirements that necessitate the use of elevated temperature, but there seems to be no kinetic reason for it in the temperature range 25-90 °C.

4.4. Conclusions

Cyclic voltammetry is a useful tool for the characterization of the platinum surface for the study of oxygen reduction in electrolytes of various concentrations. In alkaline electrolytes, roughness factors calculated by integration of the hydrogen region of the voltammogram are probably low due to interference by the platinum oxidation/reduction reaction. The amount of oxide and rate of formation at a given potential are functions of hydroxide ion activity and should be studied more fully. The amount of oxide on the surface during an OR experiment is a strong function of the potential-time profile and the surface cannot be regarded as reduced, except possibly in very fast anodic sweep or potential step experiments. Anodic and cathodic sweeps may also result in surfaces with different oxide structures and/or stoichiometries.

Table 4-8: Summary of Variable-Temperature Experiments

Thermodynamic Properties						Anodic Profile			Cathodic Profiles		
T (°C)	a_w	γ_{KOH}	$P_{\text{H}_2\text{O}}$ (atm.)	ΔE_{RHE} (mV)	Lev.Slope (mA-sec ^{1/2} /cm ²)	$i_k(.9\text{VvsRHE}^T)$ (mA/cm ²)	Tafel Slope (mV/dec)	E-Range (mV)	$i_k(.9\text{VvsRHE}^T)$ (mA/cm ²)	Tafel Slope (mV/dec)	E-Range (mV)
1.0M KOH											
25	0.961	0.562	0.030	0.4	0.273	0.112	76	860-920	†	†	†
45	0.963	0.434	0.086	8.2	0.323	0.096	49	830-920			
66	0.965	0.324	0.250	20	0.318	0.239	74	870-940			
6.9M KOH											
25	0.578	5.4	0.018	0.2	0.0121	0.044	30	940-990	0.019	41	910-980
54	0.607	3.5	0.089	15	0.0162	-	-	-	0.038	49	890-970
70	0.614	3.0	0.189	22	0.0197	0.023	43	850-910	0.0191	45	860-950
90	0.623	2.7	0.404	33	0.0175	0.027	83	890-950	0.0039	41	830-920
1.0M K₂CO₃											
25	0.956	0.715	0.03	0.4	0.165	0.440	38	910-950	0.057	48	800-920
49	-	-	0.11	2	0.196	0.278	47	880-920	0.036	43	800-910
73	-	-	0.33	6	0.161	0.321	49	880-940	0.082	55	780-920
90	-	-	0.66	17	0.120	-	-	-	-	-	-

†Experiment not done

In all of the alkaline electrolytes studied here, the amount of peroxide formed with cathodic sweep profiles was greater than that formed with anodic sweeps. In general the rate of the 2-electron pathway is accelerated by the presence of oxide on the surface and the rate of the 4-electron reaction is slowed. In dilute electrolytes, increases in carbonate concentration and decreases in pH suppress the rate of the 2-electron pathway, in agreement with the results of Appel and Appleby (36).

In concentrated electrolytes, measured disk currents must be corrected for background currents due to platinum oxidation or platinum oxide reduction before kinetic results can be calculated. Corrections for mass transfer in the presence of parallel reactions may be carried out by extrapolation of plots of $1/i_d$ versus $1/\omega^{1/2}$ to infinite rotation speed for certain cases of mechanistic parameters.

The following phenomena were found to occur at a KOH concentration near 3.3 M: i) a change in the platinum oxidation mechanism as indicated by the amount of oxide formed at a given potential passing through a maximum. ii) a minimum in the normalized high-overpotential kinetic current density iii) a decrease in the rate of further conversion of peroxide during OR, and iv) an increase in the amount of current passing through the 2-electron OR pathway. The last two phenomena may couple to increase the local concentration of peroxide with the result that the 2-electron pathway approaches a quasi-equilibrium state, as indicated by a decrease in the Tafel slope to about 30 mV/dec in some cases for an oxidized surface.

Finally, kinetic current densities normalized using the concentration of oxygen in pure water are somewhat higher in K_2CO_3 than in KOH when compared at the same electrolyte concentration and potential (vs. RHE). Peroxide production is significantly lower in the carbonates and should result in a longer electrode life. However, the actual currents attainable in a carbonate electrolyte probably will be lower than in KOH at the same concentration because the oxygen solubility in this electrolyte is lower by a factor of almost one third.

Chapter 5

Fuel Cell Cathode Studies in Alkaline Electrolytes

5.0. Introduction

In Chapter 4 we reported kinetic studies of the oxygen reduction (OR) reaction on smooth platinum electrodes in alkaline fuel cell electrolytes. The large areas of electrocatalyst necessary for a practical fuel cell are obtained by dispersing very small crystallites of platinum on a support material of suitable conductivity, stability and pore structure such as graphitized carbon. In this chapter, we present studies of the reduction of oxygen in K_2CO_3 as compared with KOH in this more-complex electrode structure.

The reduction of oxygen on platinum in a supported porous electrode structure such as that shown in Figure 1-1 involves several limiting factors besides kinetics. The rate of mass-transfer of the reactants and products to and from catalyst sites is much less well understood than in the case of the rotating disk electrode discussed previously. Finite values of electrical conductivity in the solid phase and ionic conductivity in the liquid phase may also affect the measured performance. We have studied the performance of this type of electrode as a function of electrolyte composition, temperature, and oxygen partial pressure.

Section 5.1 presents a review of the literature related to this topic, including performance studies, catalyst-support interactions and particle size effects on electrocatalysis. The chemistry of the aqueous carbonate system will also be reviewed in this section.

In Section 5.2 the electrodes, electrolytes and the design of the half-cell used in these studies are described. Experimental techniques and their implications for the results are also discussed.

Section 5.3 presents the cyclic voltammetry results through which we obtain an indication of the degree to which the electrolyte wets the electrode, and the local electrolyte composition. Composition changes, in the case of carbonate electrolytes, are found to be extreme and are responsible for most of the added polarization observed with this electrolyte when compared to KOH. The examinations of the electrodes with optical and scanning electron microscopy (SEM) are also presented in this section.

Section 5.4 reports our oxygen cathode performance measurements in KOH electrolytes under various conditions. Comparisons are made with the kinetically-limited currents reported in Chapter 4.

Section 5.5 presents the performance studies in several concentrations of K_2CO_3 . Also included in this section are studies carried out with the addition of CO_2 to the oxygen stream as one way to control the buildup of hydroxide anion in the pores of the electrode.

Section 5.6 presents a summary of the results obtained, and suggestions for modeling and further work.

5.1. Previous Work

Several works have been devoted to determining the optimum structure for a porous PTFE-bonded gas-diffusion electrode (GDE), and manufacturing techniques required to attain that structure (80-84,87,88). The performance of the type of electrode shown in Figure 1-1 has been studied extensively in acid electrolytes. The related areas of crystallite size effects and catalyst-support interactions have been studied primarily in acid electrolytes. These areas will be reviewed separately. The various mathematical treatments of GDE performance will be reviewed in Chapter 6.

5.1.1. Performance and Structure

Kordesch et al. (80) provide a good outline of the various aspects involved in producing a porous GDE and some performance data to go along with various techniques. The choices include type of carbon support, catalyzation method, heat treatments, the number of layers, binder content, catalyst loading, and thickness of the active layer, all of which can be varied independently. Most performance studies are involved with these last few parameters and their effects on electrode polarization and lifetime.

Some recent studies correlating microscopic phenomena with electrode life and polarization have been carried out. Vielstich and Holze (82) used impedance techniques to measure charge-transfer resistances and "double-layer" capacities C_{dl} of their electrodes. They were able to correlate decreases in C_{dl} with increases in electrode fabrication pressure, increases in binder content and increases in electrode age. However, their measured values were extremely low, indicating that they were only detecting about 0.2% of the electrode area as measured with BET. Olender et al. (85) and later Singer and Srinivasen (86) used cyclic voltammetry to measure the area of platinum in contact with the electrolyte by integrating the hydrogen-region currents for the charge due to hydrogen adsorption in acid electrolytes. Neither group reported voltammograms with any significant peak definition.

Watanabe, Motoo and various co-workers have made comprehensive studies of the relationship between performance and the structure of their new electrodes (87,88). They measured two ranges of pore sizes in PTFE-bonded Pt on carbon electrodes made with their new process and were able to correlate performance, utilization, and pore-size distribution with PTFE content. They utilized cyclic voltammetry on electrodes made with and without PTFE to measure utilization based on the platinum on the exposed surfaces of the carbon instead of platinum weight, although they did not show any voltammograms.

Kunz and Gruver (89) studied GDEs made of 5 to 15% Pt on XC-72 carbon black from Cabot corporation. They reported 220 m²/g BET surface area for this support and deposited Pt

from a chloroplatinic acid solution. They measured crystallite sizes of 1.6 to 3 nm with transmission electron microscopy (TEM), which corresponds to 109 to 175 m²/g for spherical particles. This agrees quite well with other authors' results for this type of catalyst (90). They measured a lower area (60 to 70m²/g) with cyclic voltammetry after fabrication into a PTFE-bonded electrode because of incomplete wetting, coverage and electrical isolation of a fraction of the Pt particles. Kunz and Gruver found good agreement between kinetic currents measured on smooth Pt for OR in 96% H₃PO₄ and currents measured with a porous electrode.

5.1.2. Platinum Particle Size Effects

The major factor limiting cathode performance in any low-temperature fuel cell cathode is the kinetics of the reaction. For this reason, any changes in the structure and environment of the electrocatalyst are expected to play a role in the performance.

Lundquist and Stonehart studied particle size effects on platinum oxidation and reduction in 1 M H₂SO₄ (91). At low potentials (< 1.2 V) they found no difference in oxidation rates for supported Pt, Pt black and Pt sheet. However, at relatively high oxidation potentials (1.4 V) and short times (low coverages) they found lower oxidation rates on the smaller Pt particles. They did not attribute this to steric effects due to the smaller amount of room for oxygen atoms inside the particles because their conclusions were based on low-coverage data. These authors also studied the reduction of the oxide formed on small Pt particles. They noted, as did Ross (13) and Peuckert et al. (92), that as Pt particle size is decreased, the cyclic voltammetry peak corresponding to oxide reduction in acid electrolytes shifts to a lower potential (for a more irreversible process). This is attributed to the higher surface energies on the smaller particles (due to higher curvature) through higher heats of adsorption (13) or through higher fractions of the oxide drawn inside the particles (91).

The dependence of OR rates on particle size has been studied by several authors (13,92-97). Blurton et al. (96) and Bregoli (97) found a decrease in activity for OR in acid electrolytes when

the Pt particle diameter was less than 3nm. This conclusion was supported recently by Peuckert et al. (92). In all of these works, particle size was inferred from surface area measurements, which can only reflect average particle size, and OR activity was compared at low overpotential to avoid complications due to mass-transfer effects. Luss (98) found activity measurements to be distorted when the distribution of particle sizes is wide. Another complication to these conclusions is that very small particles tend to "sinter" when cycled electrochemically as noted by Stonehart and Lundquist (91), and have different crystallographic surface structures as discussed by Ross (13).

Pt particle sizes for the catalysts used in this work are assumed to be time-invariant and in the range of 2 to 3 nm as measured by Kunz and Gruver with TEM (89).

5.1.3. Catalyst Support Activity and Interactions

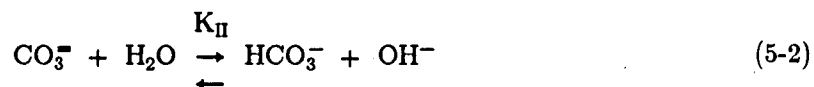
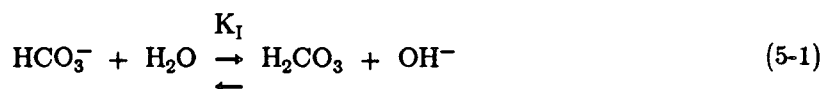
In the case of any supported catalyst, there is the possibility of the support material showing activity for the reaction being catalyzed (or electrocatalyzed) as well as interactions between the small particles of catalyst and the large-area support. All of the authors cited above, who used Pt supported on carbon along with Pt black and Pt sheet in their studies of size effects, found results related solely to particle size, indicating an absence of influence from the support material. As mentioned above, however, particle-size-effect studies are carried out at low overpotentials where carbon activity for OR is low. Appleby and Marie (99) studied the kinetics of OR on several types of carbon materials. They looked at the effects of BET area, pH, oxygen pressure and temperature. OR on carbon is known to proceed to peroxide which must then be transported away from the reaction site. They measured concentration-dependent Tafel slopes for this process that decreased from 80 to 100 mV/decade to 40 mV/decade as KOH concentration increased from 1 to 6N. The transition pH for this change in Tafel slope was found to increase with decreasing carbon surface area. This was explained by a change in the rate-determining step as a function of water activity and solid surface area to electrolyte volume ratio. Different

carbons were compared on a weight basis due to the uncertain connection between BET surface area and the surface area actually wetted by the electrolyte in a PTFE-bonded structure. The medium-area furnace blacks (80 to 250 m²/g BET area as received) all showed Tafel slopes of 45 to 62 mV/decade in 6N KOH at room temperature. The closest in area to the Vulcan XC-72 used in this study showed an activity of about 1mA/mg at 900 mV vs RHE under these conditions. This activity will be compared with our results for platinum-catalyzed electrodes in Section 5.4.1.

5.1.4. The CO₂/HCO₃⁻/CO₃⁼ System

Sodium and potassium carbonates are used frequently in the laboratory as buffer reagents.

The two equilibria written from the point of view of alkaline electrolytes are



where these reactions are instantaneously fast and the thermodynamic equilibrium constants, at 25 °C, are

$$K_I = \frac{a_{\text{H}_2\text{CO}_3} a_{\text{OH}^-}}{a_{\text{HCO}_3^-} a_w} = 4.7 \times 10^{11} \text{ M} \quad (5-3)$$

$$K_{II} = \frac{a_{\text{HCO}_3^-} a_{\text{OH}^-}}{a_{\text{CO}_3^{=}} a_w} = 4.69 \times 10^3 \text{ M} \quad (5-4)$$

and a_w is the water activity. The observed or "apparent" equilibrium constants expressed in terms of concentrations will depend on the activity coefficients of the individual ions and the activity of water. The thermodynamics of aqueous carbonate solutions must be treated with mixed electrolyte theories because of reactions 5-1 and 5-2 (100). Data predicted for potassium carbonate over a wide range of concentrations have recently been published for solutions at room

temperature (76). The pH and water activity of aqueous K_2CO_3 and KOH solutions are compared as a function of nominal salt molality in Figure 5-1. The second dissociation constant K_{II} and other thermodynamic parameters and data are discussed in Appendix A.

5.2. Experimental Apparatus and Procedures

5.2.1. Cell Design

The cell used to study the performance of oxygen fuel-cell cathodes was inspired by that of Watanabe et al. (77). All of the parts in contact with the electrolyte were constructed of PTFE. A diagram of the cell is shown in Figure 5-2 and a photograph, including some of the accompanying hardware is shown in Figure 5-3. The working electrode (WE) was held with a platinum mesh current collector and two FEP gaskets between the two bottom plates of the cell, which have circular openings of 1cm^2 . Test gases may be passed behind the WE through the gas chamber or used to purge the electrolyte above the WE. The counter electrode was a large-area Pt gauze with a hole in the center to allow passage of the Luggin tip from the reference chamber. The reference electrode chamber is threaded into the top plate for precise positioning with respect to the WE. The bubbling hydrogen reference electrode was described in Section 4.3.1, and as in the previous cell, the Luggin capillary contained a nylon wick to prevent flow between the two chambers. The electrolyte in the reference chamber was checked and replaced frequently with fresh solution, especially during the higher-temperature experiments, in order to insure a composition identical to that of the bulk electrolyte.

The cell was heated through the thin cell wall with heating tape and from the bottom with an aluminum plate fitted with cartridge heaters. The temperatures of the heating tape, plate and bubbler heating block were controlled with on-off controllers (made in-house) at temperatures no higher than 200°C . Temperature was monitored in the H_2 bubbler, in the bulk electrolyte and at a position in the lower PTFE block near to the WE with thermocouple probes.

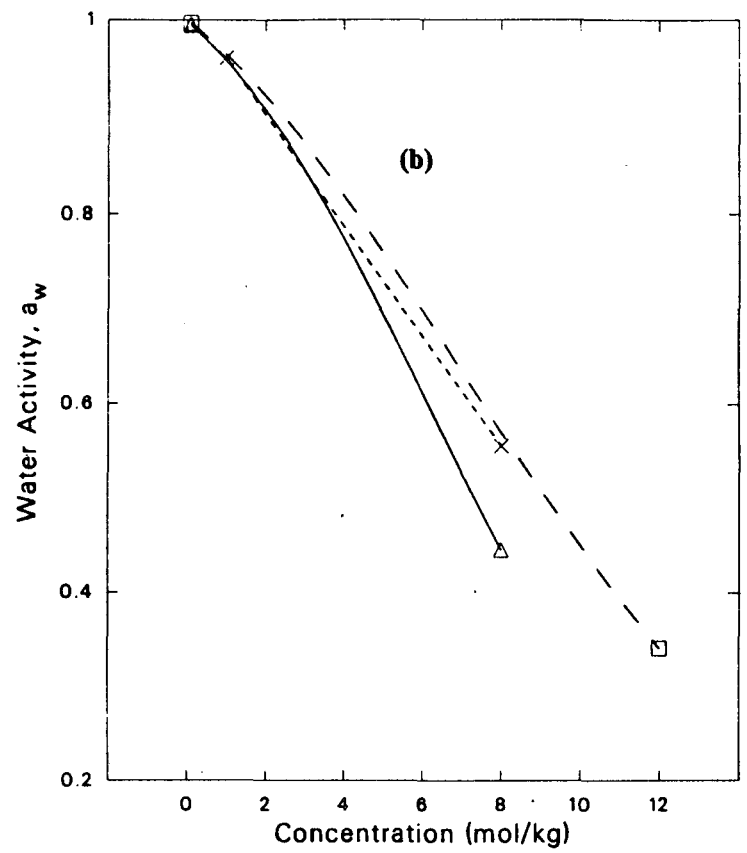
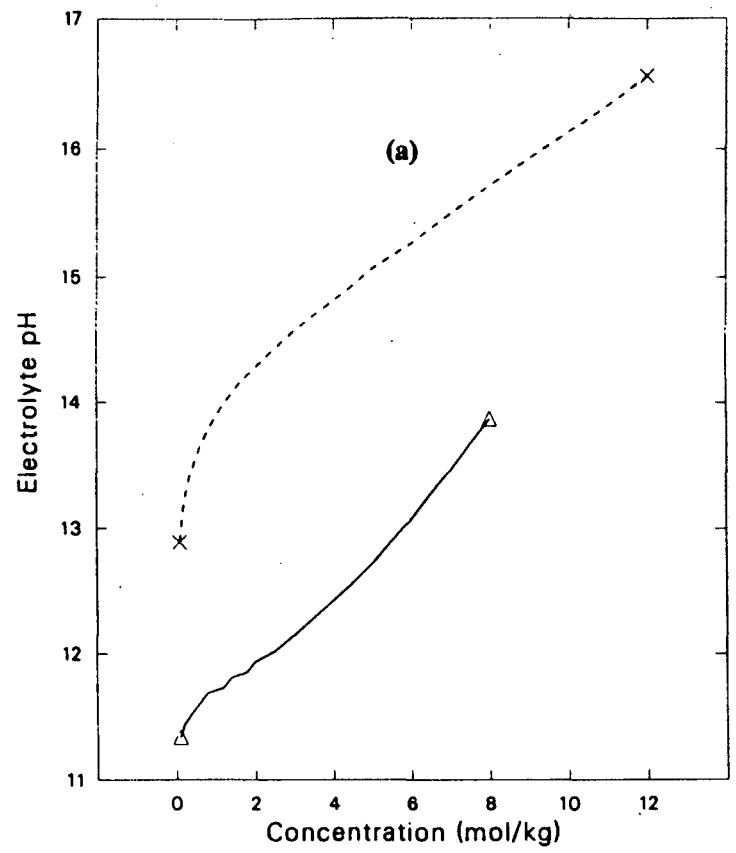
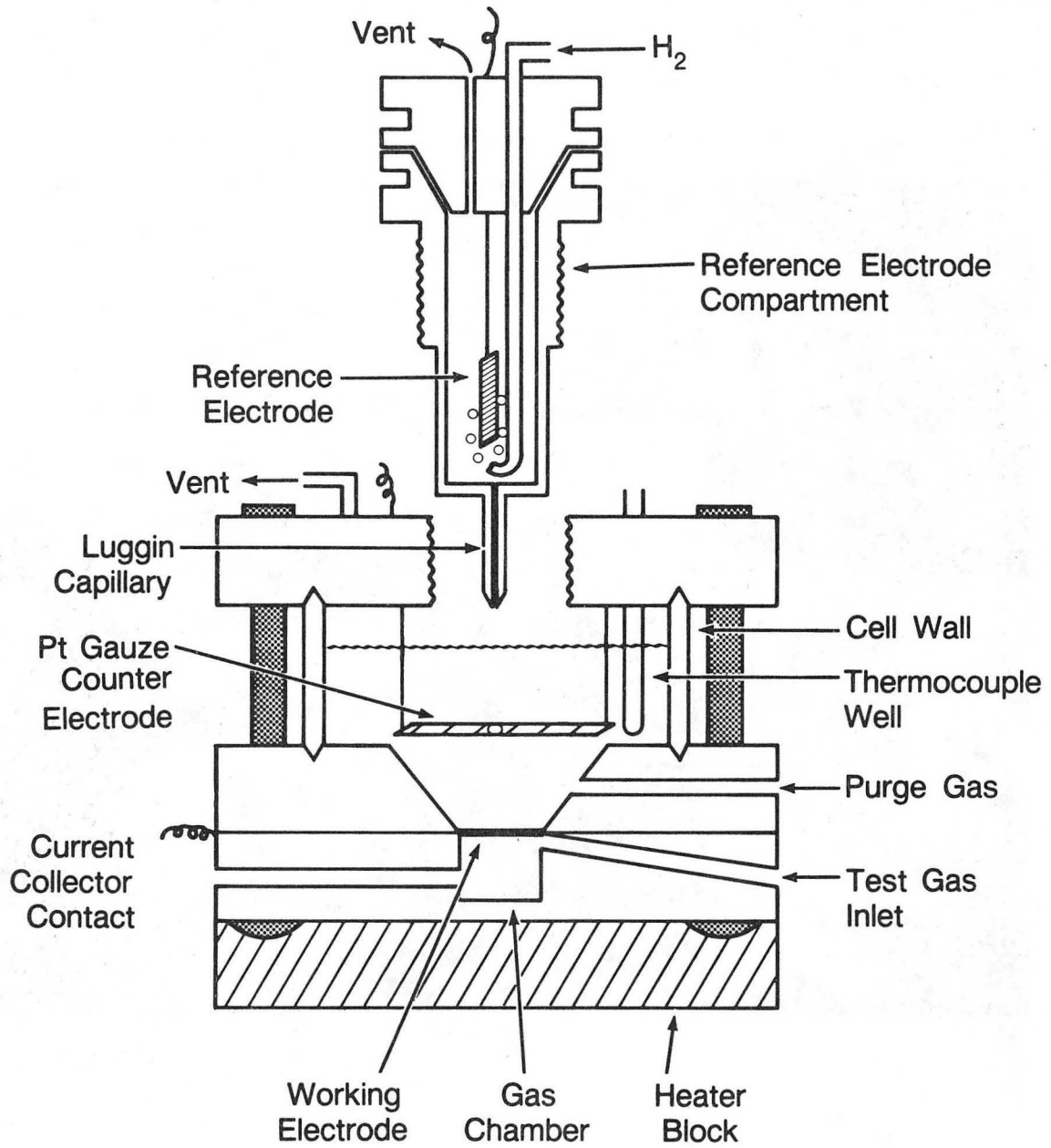


Figure 5-1: pH and water activity of KOH and K₂CO₃ solutions at 25 °C.
 —△—, K₂CO₃, Roy et al. (76);
 - - - ×, KOH, Stokes and Robinson (74);
 — — — □, KOH, MacDonal (75).

- XBL 8711-4741 -



XBL 8610-3866 A

Figure 5-2: Diagram of fuel cell electrode test apparatus.



CBB 860-8013

Figure 5-3: Fuel cell polarization study test setup.

About 1.5 hours were required for heat-up to 100 °C, but the temperature was easy to maintain because of the low thermal conductivity of the PTFE parts. The most difficult problem with high-temperature experiments was maintenance of the electrolyte composition. Samples of 1 ml were taken from the reference and electrolyte chambers periodically and their concentrations were checked as discussed in Section 4.3.1.

5.2.2. Electrolytes and Gases

Electrolytes were prepared from reagent-grade KOH and K_2CO_3 (Mallinkrodt) and deionized water, which passed through 2 columns each of "Universal" and "Research" ion exchange resins from Cole-Parmer Instrument Co. O_2 (99.96%) and N_2 (99.999%) were used as received from Pacific Oxygen Co. Certified standard gas mixtures containing N_2 with 4.13%, 20.28% and 58.66% O_2 , and O_2 with 173 ppm, 0.17% and 1.57% CO_2 were obtained from Matheson Gas Products. All gases were bubbled through electrolyte at the same conditions as the working electrolyte to prevent dehydration and control water transport. The bubbler solutions for the CO_2 -containing test gases were adjusted to the same CO_2 equilibrium pressure by the addition of $KHCO_3$ (according to the data of Roy et al. (76)), and then water activities were matched as well as possible. The electrochemical measurements made with this cell were independent of the gas flow rates to either the reference or working electrode chambers. These flow rates were therefore maintained as low as possible (< 0.5 cc/min) and monitored by passing exit streams through a water trap.

5.2.3. Electrodes

Most of the electrodes tested in this work were cut from one 7.5 cm by 7.5 cm piece of Prototech PC-206 fuel cell electrode (designated as P20, P23 etc). This electrode contains a thin "active" layer supported on a thicker gas-supply layer. The catalyst in the active layer is 10wt% Pt on Vulcan XC-72 furnace black which is prepared by Prototech using a colloidal method described in the patent literature (101). Before teflonation, this catalyst contained about

120m²/g platinum when measured by CO adsorption (90). A weight of 5 ±0.5 mg of the catalyst was mixed ultrasonically with 30 wt% PTFE to form the active layer. This layer is filtered or pressed onto a hydrophobic piece of carbon Stackpole PC206 paper (25% by weight PTFE) about 0.4mm thick, which serves as the gas-supply layer.

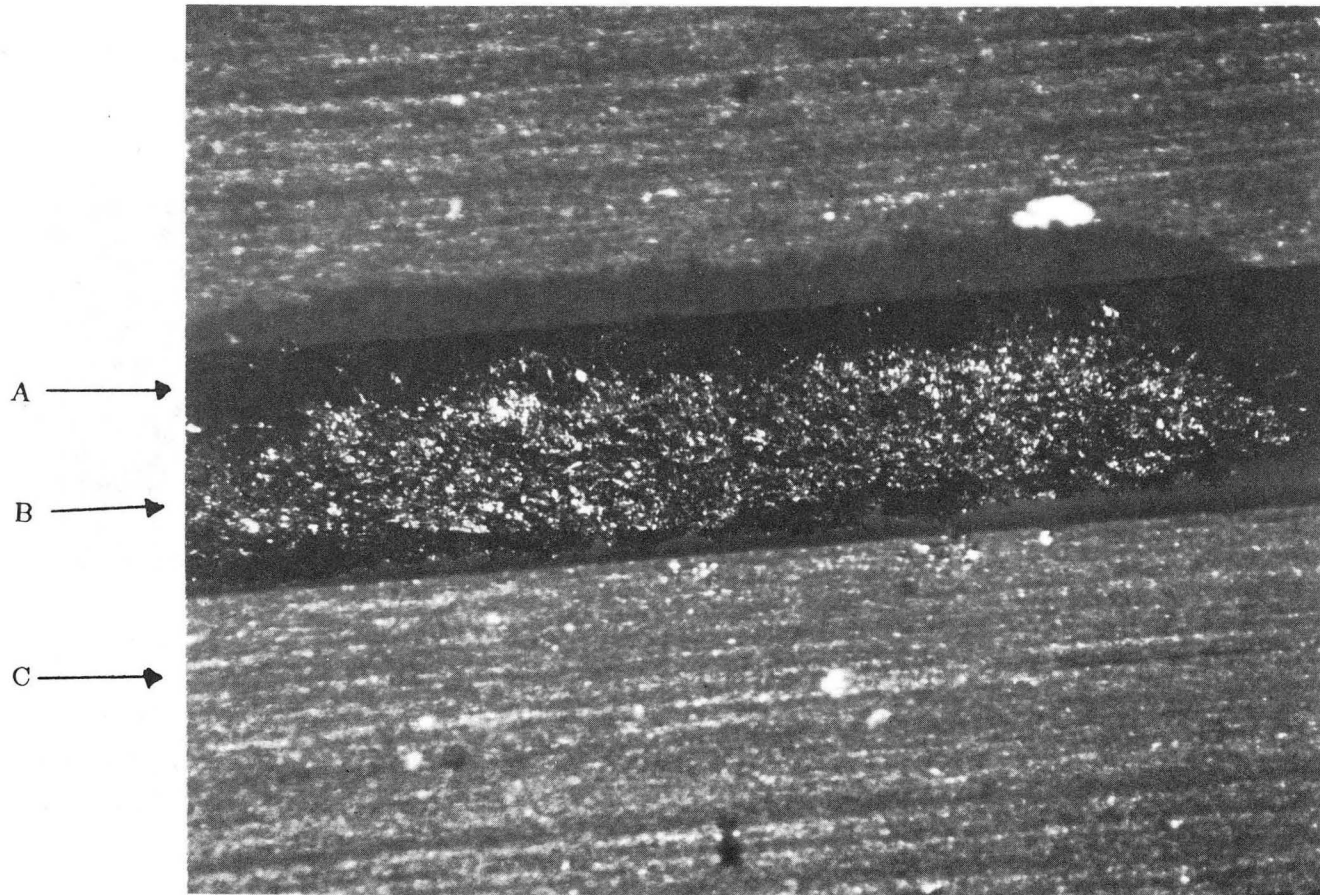
Electrodes L24, L27 and L28 were prepared by Mr. Lee Johnson of Lawrence Berkeley Laboratory following techniques similar to those of Prototech. Electrodes EM-A and -B were obtained from Electromedia Inc. The active layer of EM-A was made following the suggestions of Watanabe et al. (102) and "united with a hydrophobic gas-supply layer." EM-B was a single-layer electrode of Electromedia's design.

Catalyst layer thicknesses were measured from optical micrographs, as shown in Figure 5-4 for a new Prototech electrode. These values along with composition and all available parameters are shown in Table 5-1. A scanning electron micrograph (SEM) of the surface (uncoated) of a new Prototech electrode is shown in Figure 5-5 at two magnifications. The small carbon agglomerates are approximately 0.1 to 0.2 μm, in agreement with the measurements of Stonehart and Klinedinst (103).

Electrodes were cut with a #7 cork borer (diameter 1.335 cm) and rinsed with water before soaking in the working electrolyte, catalyst-side down for at least one day prior to the experiment.

Table 5-1: Gas Diffusion Electrode Characteristics

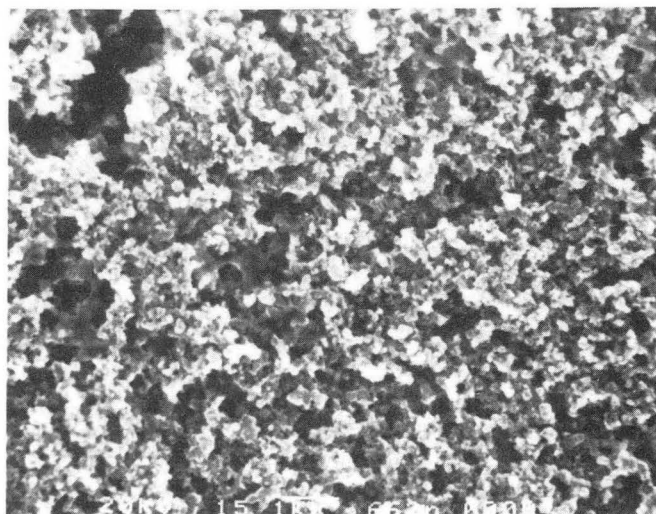
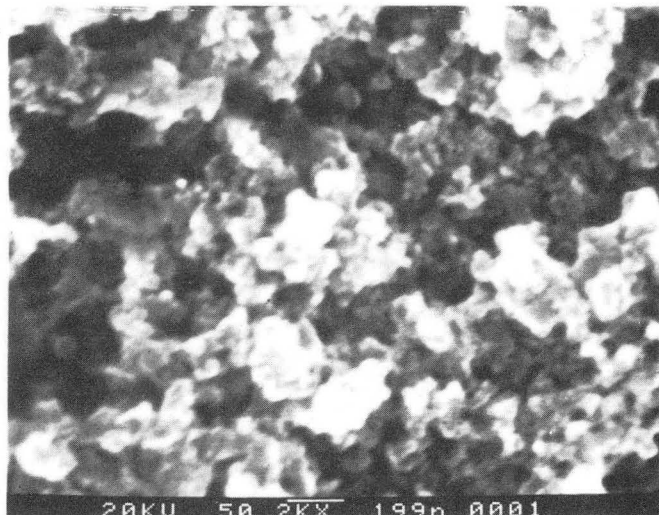
Manufacturer	Designation	Composition of Active Layer			
		Pt (mg/cm ²)	Carbon (mg/cm ²)	Teflon (wt%)	Thickness (mm)
Prototech Co.	P 20-23,26,29	0.5	4.5	30%	0.10-0.12
LBL	L 24	0.5	4.5	34%	0.07
LBL	L 27	0.25	2.5	34%	0.05
LBL	L 28	0.25	7.5	34%	0.09
Electromedia Inc.	EM-A	?	?	?	0.10
Electromedia Inc.	EM-B	?	?	?	0.30





XBB 870-8827

Figure 5-4:

Optical micrograph of Prototech electrode: —|— 0.01"
A, Active layer; B, Stackpole graphite paper; C, Glass slide holder.



XBB 870-8828

Figure 5-5: SEM of active layer of new Prototech electrode at 20kV.
(a) 15,000 ×:  662nm
(b) 50,000 ×:  100nm

5.2.4. Electronics

Galvanostatic polarization curves and voltammetric triangular potential sweeps were generated, controlled, measured and then stored with a PAR Model 273 Potentiostat/Galvanostat. This instrument was in turn controlled by an interactive Basic program running on an IBM PC through an National Instruments GPIB parallel interface. The analog-to-digital converter in the PAR273 yielded measurements that were about 0.65% high. This value was checked at the beginning of each experiment, and the data were corrected accordingly.

The potentiostat contained an automatic current-interrupt circuit for the measurement of the uncompensated solution resistance, R_{Ω} , between the WE and the RE. In potentiostatic mode, the current was interrupted for a total of 190 μsec . The potential was measured at 10 and 20 μsec following the interruption, and a value for the potential drop due to IR_{Ω} was calculated by extrapolation to zero time.

5.2.5. Experiment Design

Cyclic voltammetry measurements were made with triangular potential sweeps at 50 mV/sec, while N_2 flowed through the gas chamber and the Luggin tip was positioned so that the non-conducting wick just touched the WE surface. This position resulted in the sharpest voltammetric peaks with minimal over-compensation in potentiostatic control. The areas under the peaks were relatively insensitive to the position of the Luggin tip.

The charge due to hydrogen desorption was measured by first cycling at least twice through the window of electrolyte stability (between H_2 and O_2 evolution potentials) followed by three cycles between the onset of H_2 evolution and an anodic potential in the double-layer region (usually about 500 mV vs. RHE) to ensure complete reduction of the platinum oxide formed during the full sweeps. The third cycle through this potential region was recorded digitally, and the anodic portion was integrated numerically as indicated in Figure 2-1.

Stable rest potentials with 100% O₂ flowing through the gas chamber were recorded after 30 to 45 minutes. Steady-state polarization curves were recorded galvanostatically by stepping the current incrementally from 0.02 mA to a maximum current of either 100 mA or 1 A (cathodic direction) or by starting at the high current and stepping down (anodic direction). The potential was measured at 30-second intervals until three successive measurements fell within 1 mV. Current, potential and the time required to reach steady-state potential were recorded by the computer for subsequent analysis. The polarization curves were measured with the reference tip about 1.2 mm (one quarter turn) away from the WE surface to avoid shielding.

The value of R_{Ω} was measured at several potentials immediately following a set of polarization measurements as described above. The value of R_{Ω} ranged from 0.1 to 0.5 Ω for all electrolytes with an estimated accuracy of $\pm 10\%$.

Due to the large composition changes and the resulting hysteresis observed with the carbonate electrolytes, another type of polarization measurement was made in some cases. Several successive sets of cathodic- and then anodic-direction measurements were made with a 7-minute interval at open circuit between "cycles." A maximum time of 5 minutes was allowed for steady-state to be achieved, at each current, before the potential was recorded and the next current imposed. These polarization measurements will be referred to as cycling curves.

5.3. Cyclic Voltammetry in Supported-Pt Gas-Diffusion Electrodes

Most of the cyclic voltammograms reported in the literature for porous GDEs show minimal peak definition, even at low sweep rates, because of the high uncompensated solution resistances typically encountered in a fuel cell electrode test apparatus. High R_{Ω} coupled with high capacitance of the support material renders such measurements difficult. The extremely low R_{Ω} in our test cell allowed us to record well-defined voltammograms at sweep rates of 50 mV/sec, from which estimates for the wetted catalyst area and total wetted areas could be calculated. The position of the peaks also allowed us to compare the behavior of the small Pt particles with that of smooth Pt and to monitor the pH of the electrolyte in the pores of the electrode.

Figure 5-6 shows cyclic voltammograms for a smooth Pt electrode (at 100 mV/sec) and a porous Pt/C electrode (at 50 mV/sec) in 6.9 M KOH. The different scales indicate the vastly different platinum areas involved. Except for the generally lower sharpness in the peaks from the supported electrode, the hydrogen-region peaks are quite similar for the two electrodes. The lower peak resolution is probably due to the higher resistivity of the solid phase of the porous electrode (about 1 Ω -cm for the active layer (104) compared with 0.011 m Ω -cm for platinum metal (105)).

The regions for oxidation and reduction of the platinum show significantly different peak structure. The first anodic platinum oxidation peak is fairly similar for the two electrodes, which is to be expected for an adsorption process, as in the hydrogen region. The second anodic oxidation peak is almost non-existent for the supported electrode although there is a non-zero current plateau indicating that further oxidation is occurring. These oxidation currents were integrated from the double-layer region to various oxidation potentials and compared with the corresponding experiment on a smooth electrode (see Figure 4-4). This comparison, shown in Figure 5-7, can be interpreted as a lower oxidation rate occurring on the smaller supported Pt particles at potentials higher than 900 mV, in agreement with the results of Stonehart et al. (91) for acid electrolytes. The reduction of this oxide shows greater irreversibility, also in agreement with the previously-discussed results for acid electrolytes.

Figure 5-8 shows cyclic voltammograms for smooth and supported Pt electrodes in 2 M K_2CO_3 . Peak definition for the supported electrode is low due to the lower degree of wetting and somewhat lower electrolyte conductivity. The Pt oxidation region is essentially featureless for both electrodes. The porous electrode voltammogram is shifted about 45 mV cathodically due to residual hydroxide in the pores of the electrode; this phenomenon will be discussed a little later. The poor peak definition precludes the detailed comparisons made for KOH, but it can be noted that the oxide reduction peak appears to occur at a potential much closer to that for the smooth electrode, suggesting a pH-dependency of the particle-size effect on Pt oxide reduction.

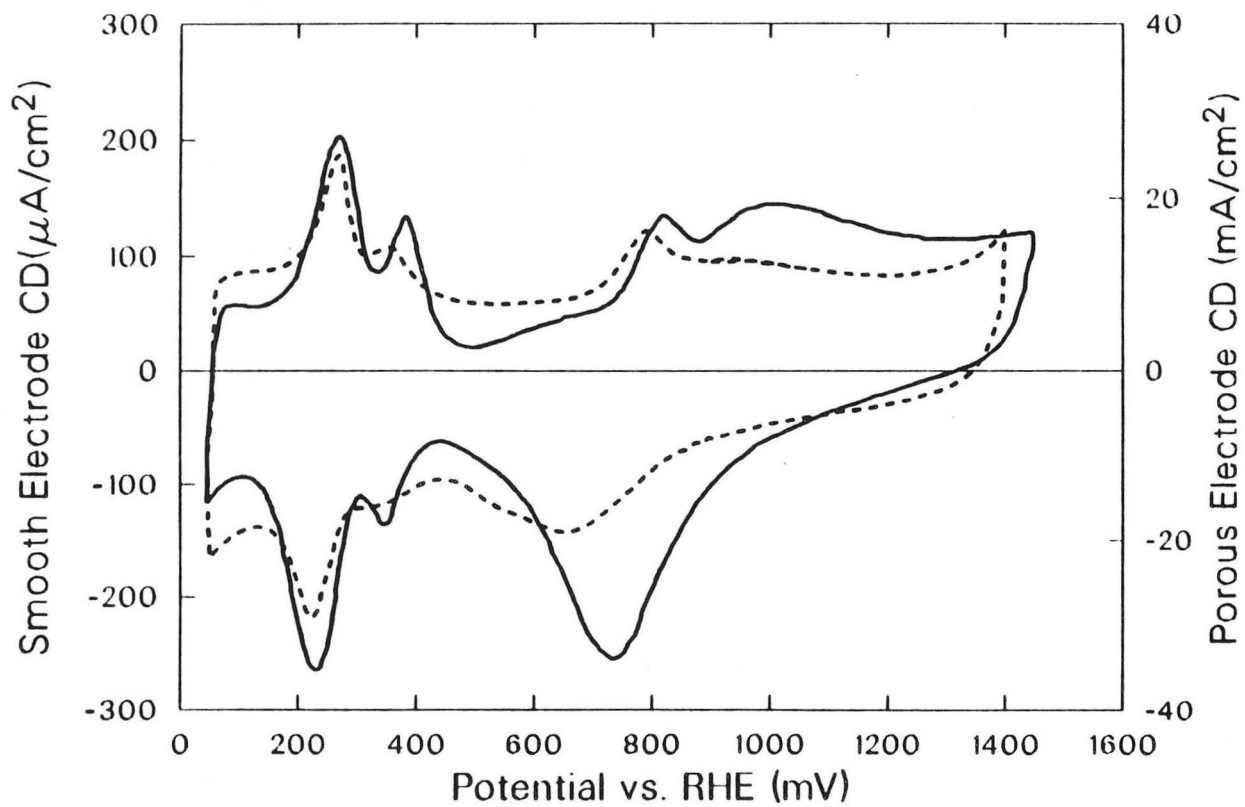


Figure 5-6: Cyclic voltammograms in 6.9M KOH at 23 °C.
— 100mV/sec, smooth Pt;
- - - 50mV/sec, Prototech Pt-on-C GDE.

- XBL 8711-4740 -

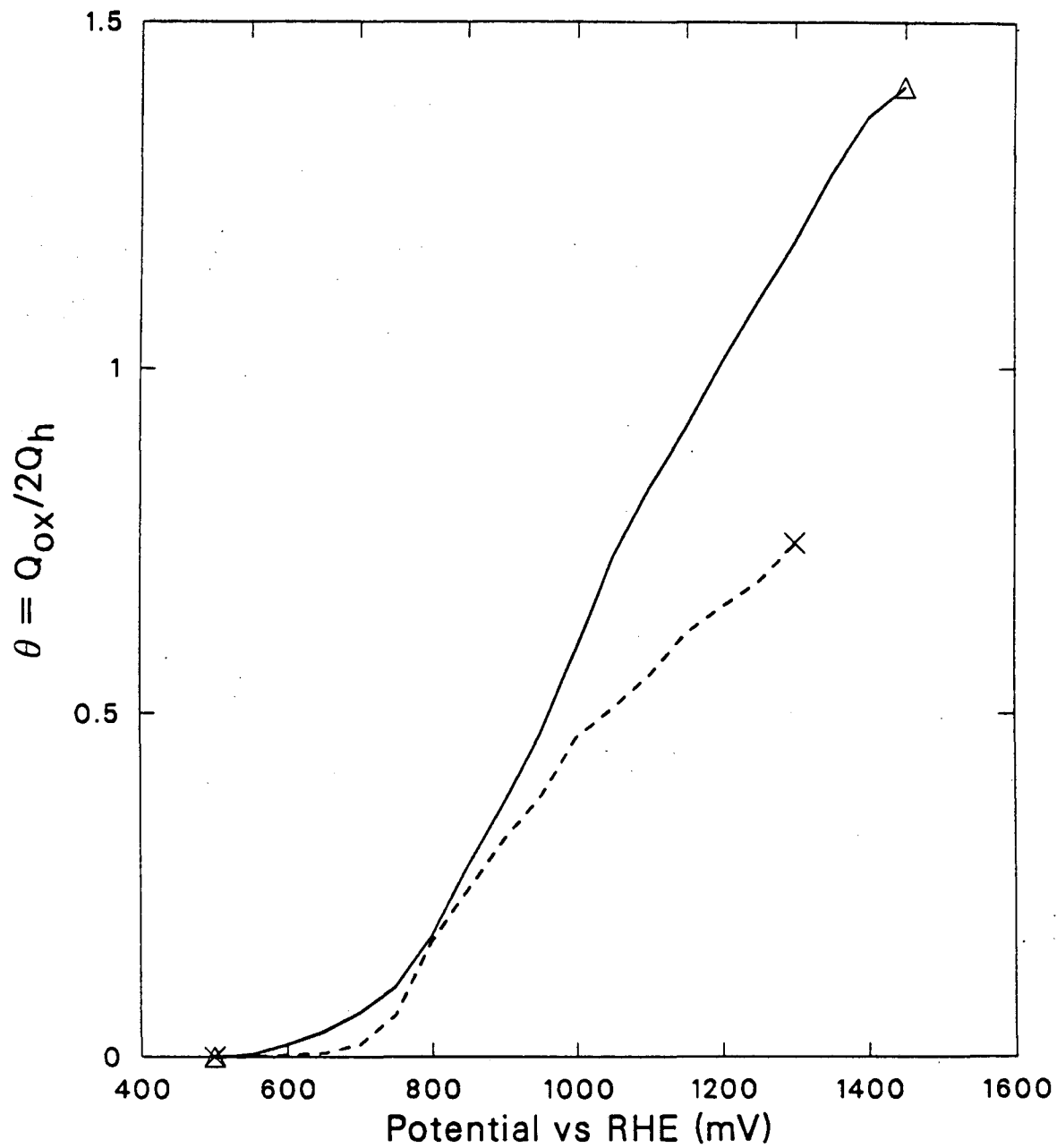


Figure 5-7: Platinum oxide coverage in 6.9M KOH, 23 °C.
— Δ , smooth Pt; — \times , Pt-on-C GDE.

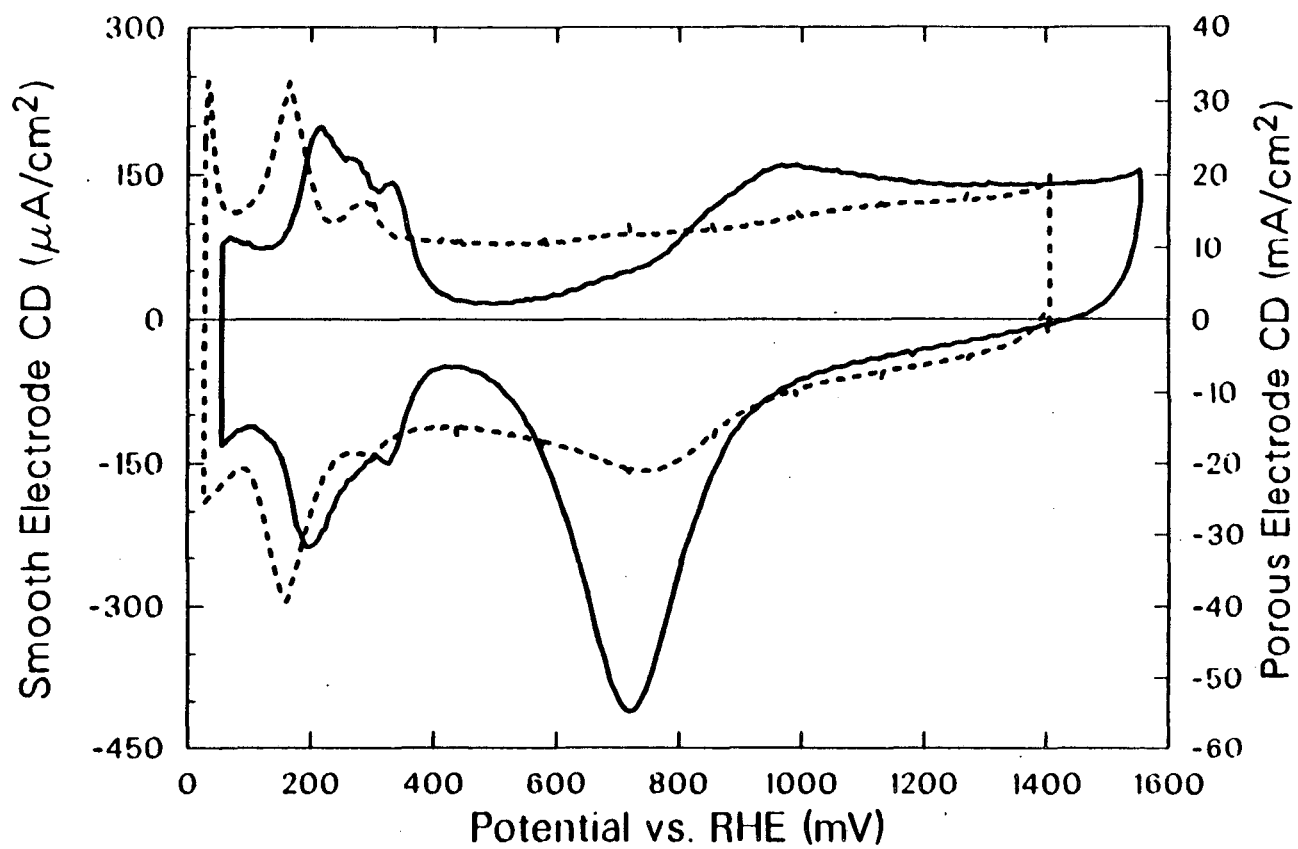


Figure 5-8: Cyclic voltammograms in 2.0M K₂CO₃, at 23 °C.
—— 100mV/sec, smooth Pt;
----- 50mV/sec, Prototech Pt-on-C GDE.

5.3.1. Electrode Activation and Wetting

The voltammograms recorded with new electrodes reflect a very small wetted area and corresponding lack of peak definition. Both the charge due to hydrogen desorption and the double-layer charging current grow with the passage of OR current as indicated in Figure 5-9 for several electrodes and electrolyte conditions. Most of the scatter in these plots is due to small amounts of oxygen remaining in the electrode, which affects I_{dl} , but not Q_H . The difference in porosities indicated in Table 5-1 (L24 has the same catalyst loading as P23 but is formed in a thinner layer) results in a lower maximum degree of wetting but the same slope in Figure 5-9A. The electrodes with only 5 wt% Pt in the active layer (L27 and L28) show approximately half the slope in this figure. The slight downward curvature is probably due to the gas-supply layer becoming flooded by the electrolyte. This effect became more pronounced as temperature was increased or electrolyte concentration was decreased. The slope of this plot, or the ratio of Q_h to I_{dl} , is related to the fraction of total area covered by Pt according to

$$\frac{Q_h}{I_{dl}} = \frac{\theta_{Pt} Q_h^o}{v \bar{C}_{dl}} \quad (5-5)$$

where \bar{C}_{dl} is an average double-layer capacitance for the platinum and carbon surface (dominated by the carbon), v is the potential sweep rate and Q_h^o is the charge associated with a monolayer of hydrogen adsorbed on platinum (usually taken as 0.22 mC/cm²Pt). The average slope for the Prototech electrodes was about 5 seconds. Using the specific areas reported by Ross (90) for this catalyst (120 m²/g for Pt and 260 m²/g for Vulcan XC-72), we can estimate a value of 0.34 to 0.37 for θ_{Pt} and a corresponding value of 300 $\mu\text{F}/\text{cm}^2$ for \bar{C}_{dl} . This value has the same order of magnitude as the values for C_{dl} reported for glassy carbon: 500 $\mu\text{F}/\text{cm}^2$ (106) and 330 $\mu\text{F}/\text{cm}^2$ (107), lending support to our interpretation of I_{dl} .

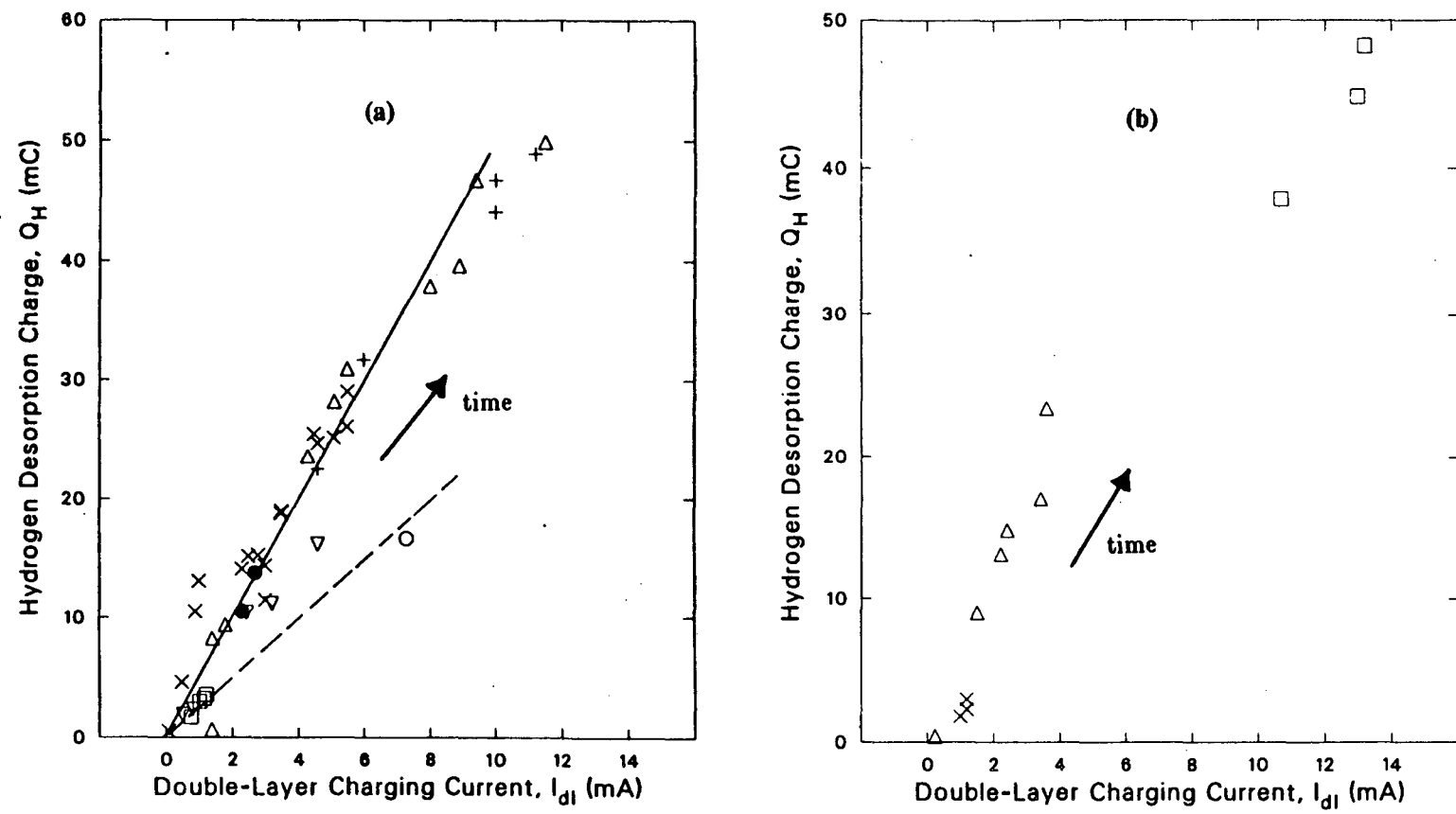


Figure 5-9: Wetting progression in different fuel-cell electrodes.
 (a) 6.9M KOH, Δ , P23; \times , P24; \square , EM-A; \bullet , EM-B; ∇ , P27; \circ , P28; $+$, P29 (2.0M KOH).
 (b) K_2CO_3 , Δ , P23, 5.5M; \times , EM-A, 5.5M; \square , P29, 2.0M.

XBL 8711-4737

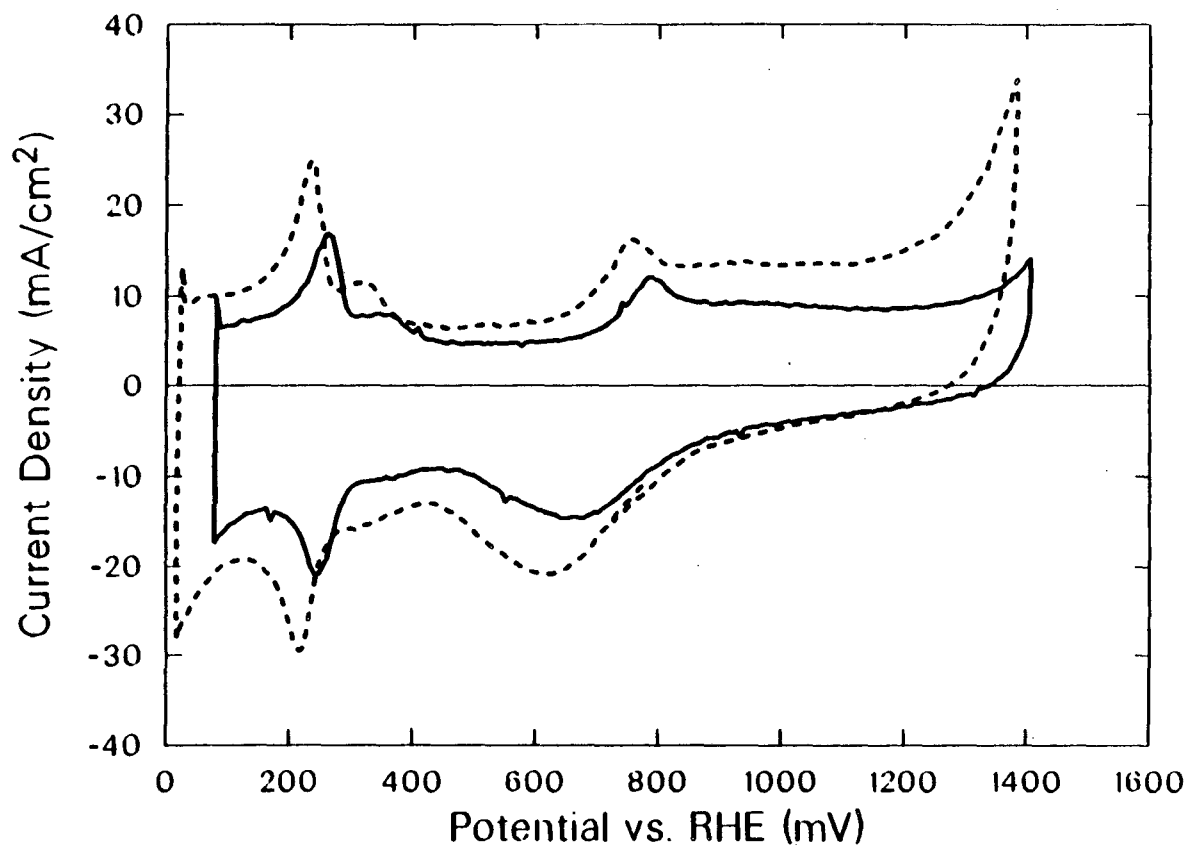
5.3.2. Local Electrolyte Composition in Electrode Pores

Voltammograms recorded on well-wetted electrodes such as those of Figures 5-6 and 5-8 are extremely reproducible so long as no OR current is passed. In a KOH electrolyte, following an OR polarization measurement which concluded with a current density greater than $100\text{mA}/\text{cm}^2$, the voltammograms before and after the polarization measurement show certain reproducible differences.

Voltammograms recorded before and after a polarization measurement in 6.9 M KOH are shown in Figure 5-10. The whole curve grows with an increase in the degree of wetting and is shifted about 10 mV cathodically. This shift disappears after about 15 minutes and is more extreme the higher the last OR current density used. This is probably due to local depletion of water and production of OH^- in the pores (due to OR), both of which act to raise the local pH relative to the constant-pH reference electrode.

The other difference is a premature onset of oxygen evolution. This phenomenon disappears with cycling into this region but not readily with time. It is probably due to peroxide build-up in the pores of the electrode during OR in concentrated KOH. This peroxide is reoxidized with cycling above 1.2 V. This phenomenon is difficult to separate from the shift of the whole voltammogram already mentioned.

The potential shift in the voltammogram due to oxygen reduction is much more dramatic in carbonate electrolytes, sometimes reaching 150 mV. Figure 5-11 shows this shift with voltammograms recorded before and after OR in 2 and 5.5 M K_2CO_3 . The only logical cause for this is a build-up of hydroxide anion in the pores of the electrode while the reference electrode pH remains constant. The maximum pH changes for these electrolytes, assuming that the inventory of K^+ remains constant, are 2.8 and 3.2 pH-units for 2 and 5.5 M K_2CO_3 , respectively (from the thermodynamic data in Appendix A). This corresponds to somewhat larger potential shifts than were recorded. It should be noted that the pH gradient generated by OR adjusts itself continually following the removal of oxygen from the gas chamber with an N_2 purge. The alkalination



- XBL 8711-4736 -

Figure 5-10: Cyclic voltammograms before and after O₂ polarization in 6.9M KOH at 23 °C, 50mV/sec.
——, before;
-----, after.

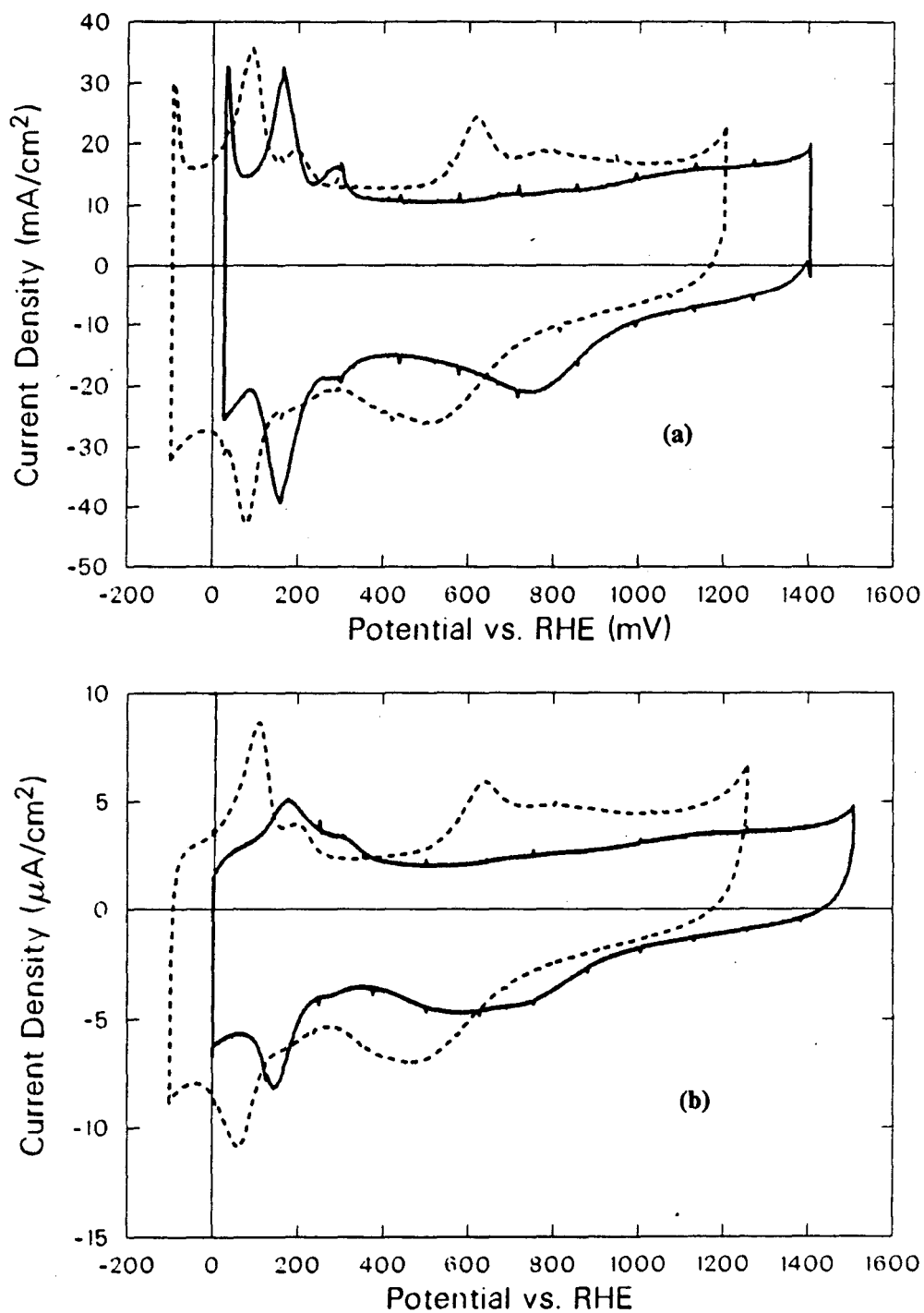


Figure 5-11: Cyclic Voltammograms before and after oxygen polarization measurement in carbonate electrolytes, 50mV/sec, 23 °C.
 (a) 2.0M K₂CO₃; (b) 5.5M K₂CO₃.
 —, before; - - -, after.

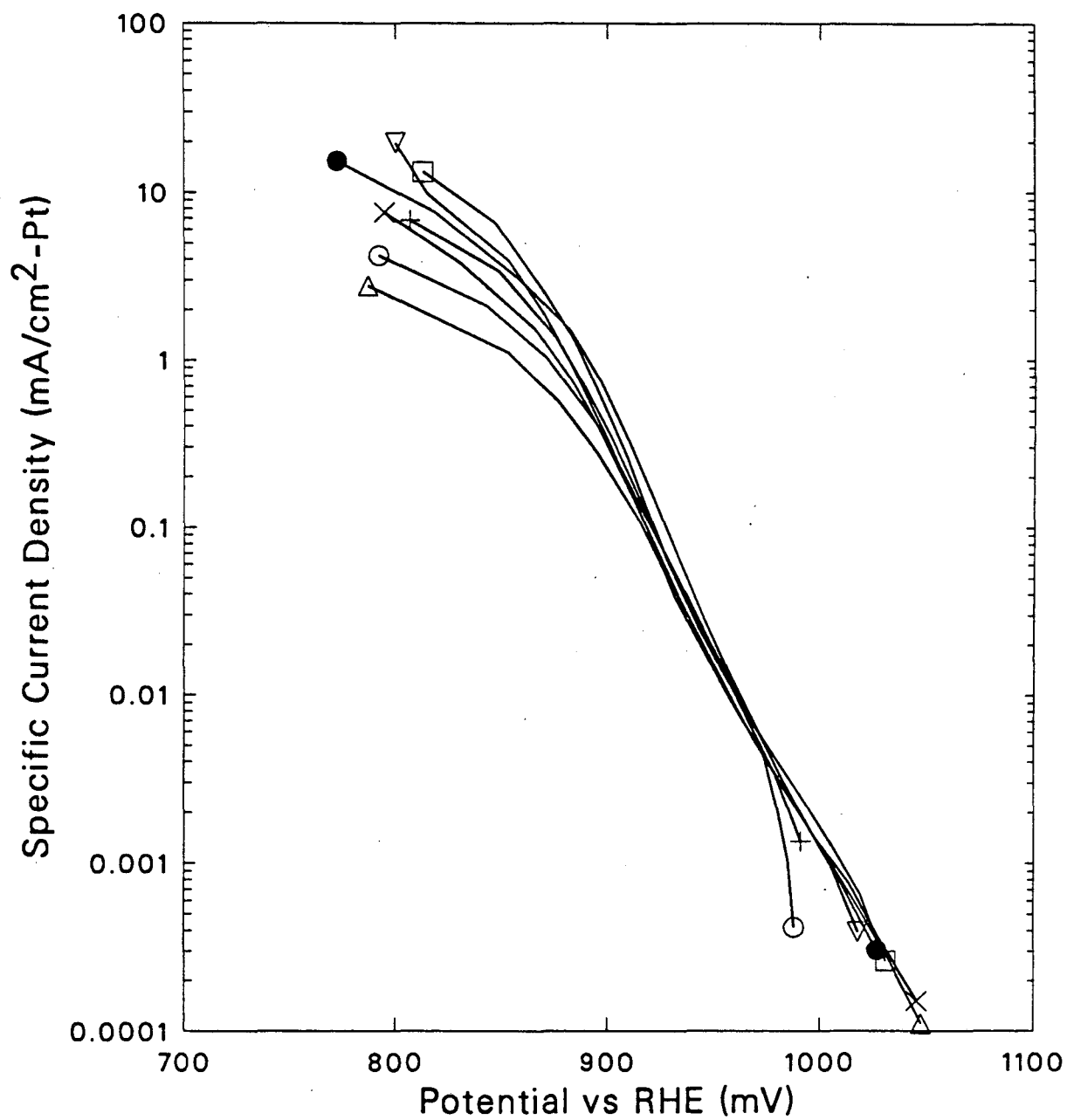
of the electrode is also indicated by the fact that voltammetric peaks become more characteristic of KOH electrolytes (see Figure 5-6).

5.4. Cathode Performance in KOH Electrolytes

Performance curves for OR with 100% O₂ at room temperature in several concentrations of KOH were measured with several different electrodes. Performance curves with lower oxygen partial pressures or elevated temperatures were measured at some concentrations. Voltammetry measurements were made before and after each polarization measurement in order to monitor the wetted areas and allow comparison of polarization measurements on the basis of equal amounts of wetted platinum.

Cathode polarization curves recorded in the cathodic direction on several different electrodes in 6.9 M KOH with 100% O₂ at room temperature are shown in Figure 5-12 (see Table 5-1 for electrode structural details). Measured currents on the 1 cm² working electrodes have been divided by the area of wetted Pt, calculated from Q_H measured immediately before the polarization measurement. This quantity will be referred to as a specific current density. The low specific current densities (within 12 mV over 3 decades of current) exhibit a Tafel slope of 44 mV/decade and an $i_0 = 7.5 \times 10^{-9}$ mA/cm² Pt. The deviations at the highest potentials (low overpotentials) in Figure 5-12 are due to local composition changes (from previous measurements) that have not had time to relax. At high overpotential, the specific current densities in the mass-transfer limited region (with an average Tafel slope of about 100 mV/decade) are inversely related to the wetted Pt area; which means that current density in this region is proportional to A_{Pt}^m , where $m < 1$. The flooded agglomerate model predicts a half-order dependence on Pt loading when both diffusion and kinetics are controlling (89). Partial electrode wetting is mathematically different from variable Pt loading and is examined in more detail in Chapter 6. The high-current-density data are also more sensitive to small errors in R_Ω.

Figure 5-13 shows the performance of two electrodes with different degrees of wetting at three oxygen partial pressures. In the kinetically-controlled region, the current densities exhibit



- XBL 8711-4734 -

Figure 5-12: Oxygen reduction polarization measurements in 6.9M KOH corrected to current per unit area of wetted Pt, 23 °C.
Wetted Pt areas used for correction (cm²): Δ , 180; \times , 132; \square , 76; \bullet , 66; ∇ , 51; \circ , 48; +, 15.

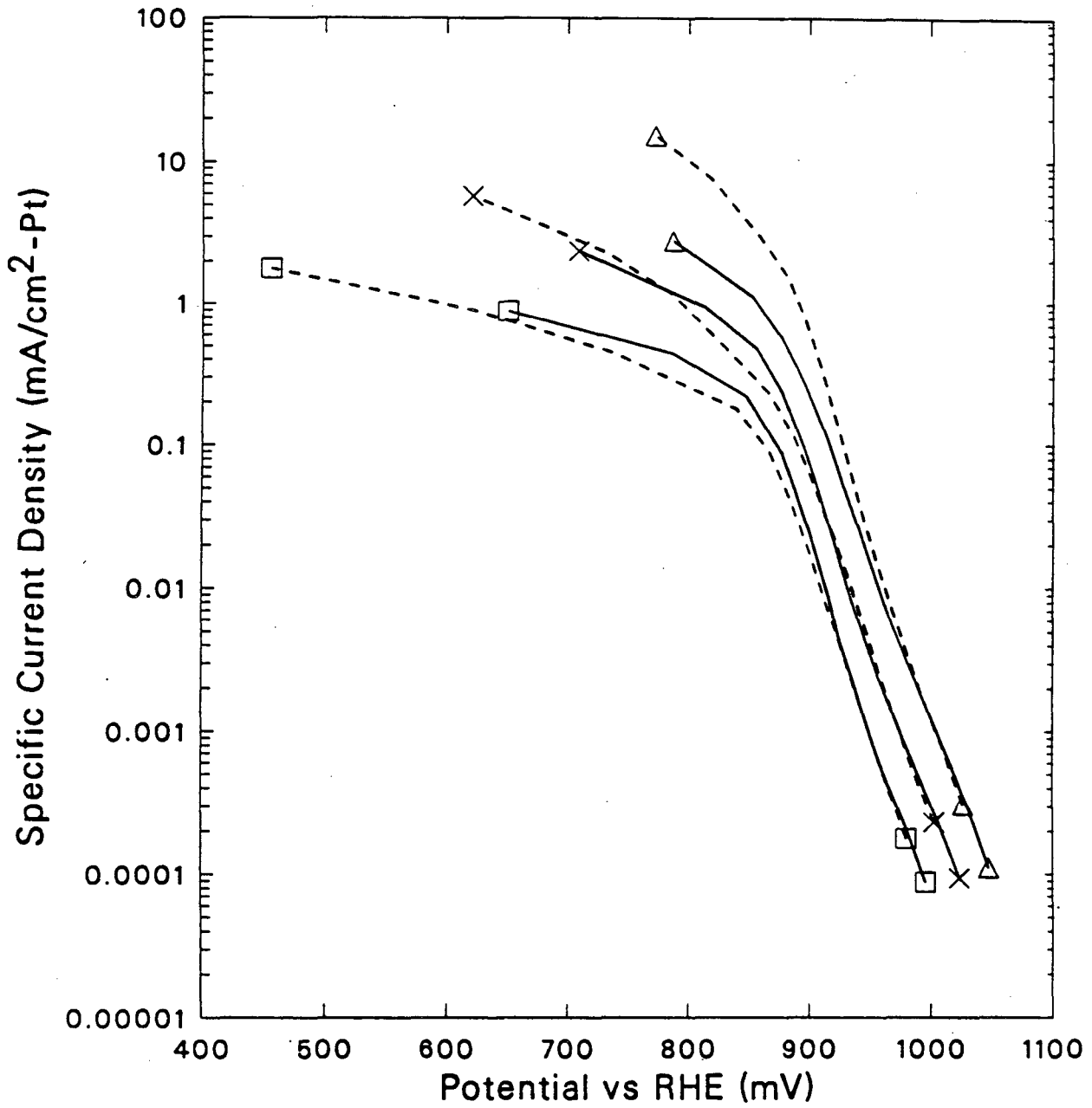


Figure 5-13: O₂ partial pressure dependence of polarization in 6.9M KOH, corrected to current per unit area of wetted Pt, 23 °C.
 ———, FC23; - - - - -, FC24.
 Δ, 1 atm O₂; ×, 0.203 atm; □, 0.0413 atm.

a linear dependence on p_{O_2} . The dependence of current density on oxygen partial pressure in the mass-transfer-controlled region is more complex due to the variation of wetted area already discussed and the possibility of a gas-phase resistance.

5.4.1. Smooth versus Supported Platinum

Cathode performance at 23 °C is compared with kinetically-limited current densities, presented in Chapter 4, which have been multiplied by the area of wetted Pt in the porous electrode, in Figures 5-14A and B for 3.3 and 6.9 M KOH, respectively. At low overpotentials, current densities at a given potential lie within a factor of 2 to 3 of one another. At high overpotentials, the activity of the supported Pt is higher than what would be measured with a smooth electrode of the same area. Kinetic currents in concentrated KOH are limited by a non-electrochemical process (as evidenced by the extremely high Tafel slopes) at high overpotentials. In Chapter 4, we proposed that this was due to the decrease in peroxide production on the less-oxidized Pt at these potentials. The possibility that the carbon in the electrode, which starts to reduce oxygen to peroxide at an appreciable rate in this potential range, is responsible for the higher currents was investigated.

The activity of unplatined electrodes was not measured directly, but an estimate of the activity of the carbon can be made from the data of Appleby and Marie (99). They report OR performance data for Monarch 1100 furnace black (BET area of 227 m²/g as compared with 220 to 260 m²/g for Vulcan XC-72) in 6N KOH at 23 °C. The carbon currents shown in Figure 5-14b were estimated by assuming that the weight fraction of wetted Carbon in the Prototech structure is equal to the area fraction of wetted Pt, as measured with cyclic voltammetry. This area fraction was calculated assuming a theoretical area of 120 m²/g for the Pt in the Prototech electrode. It appears from this plot that the activity of the carbon could easily be responsible for the high current densities observed at low potentials in 6.9 M KOH, since the actual benefit derived from the carbon support is probably double that shown in Figure 5-14b if the HO₂⁻ produced on the carbon is further reduced by neighboring platinum crystallites.

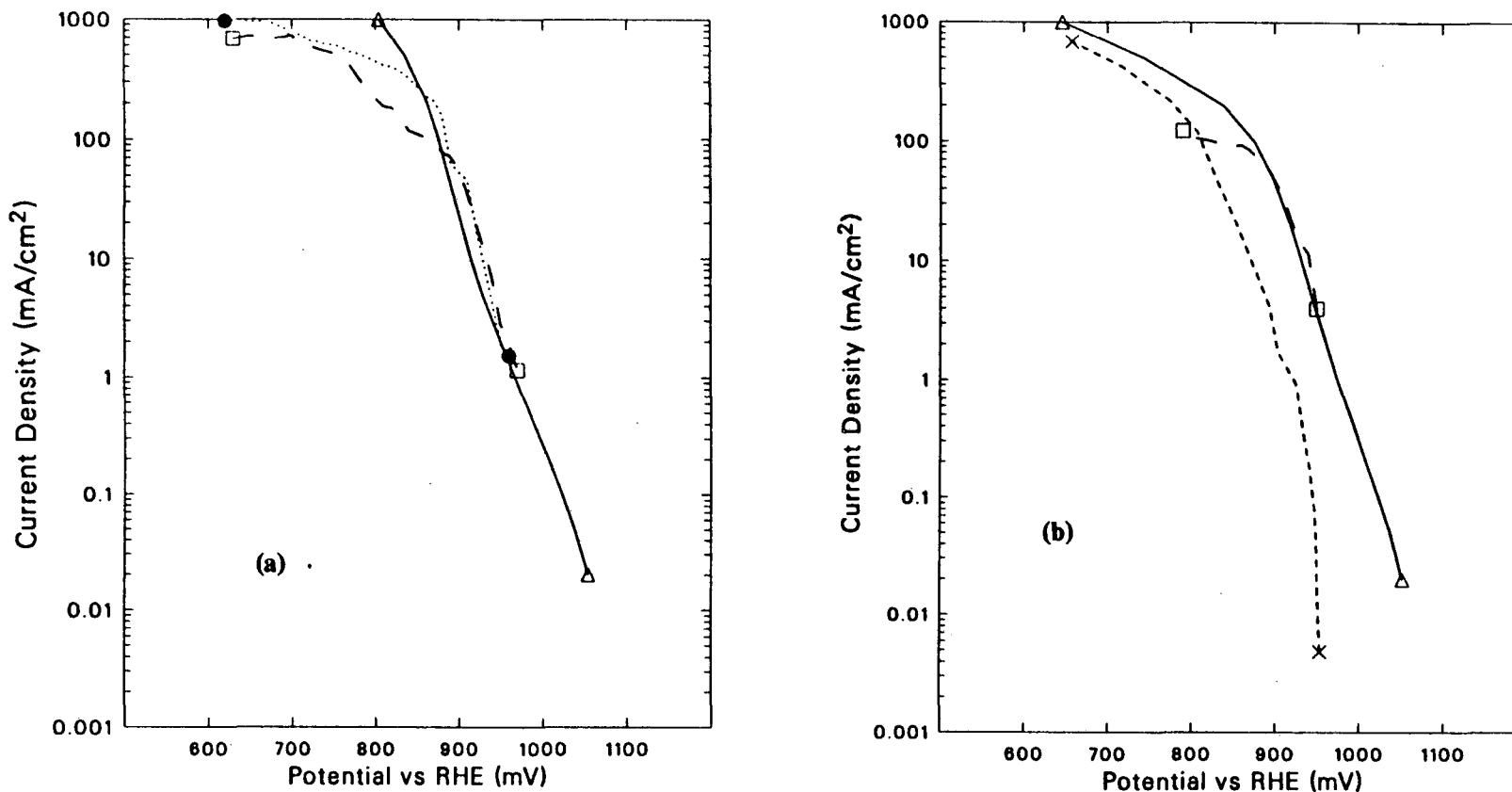


Figure 5-14: Comparison between oxygen reduction on smooth Pt and Pt-on-C GDE, 23 °C. (a) 3.3M KOH; (b) 6.9M KOH.

- Δ, Porous Pt-on-C GDE;
- - - □, Kinetic data recorded with anodic sweep corrected to the roughness of the corresponding porous GDE;
- ⋯ ⋯ •, Kinetic data recorded with cathodic sweep corrected to the roughness of the corresponding porous GDE;
- - - - X, Carbon activity estimated for 4.5mgC from Appleby and Marie (99).

5.4.2. Electrolyte Concentration Effects

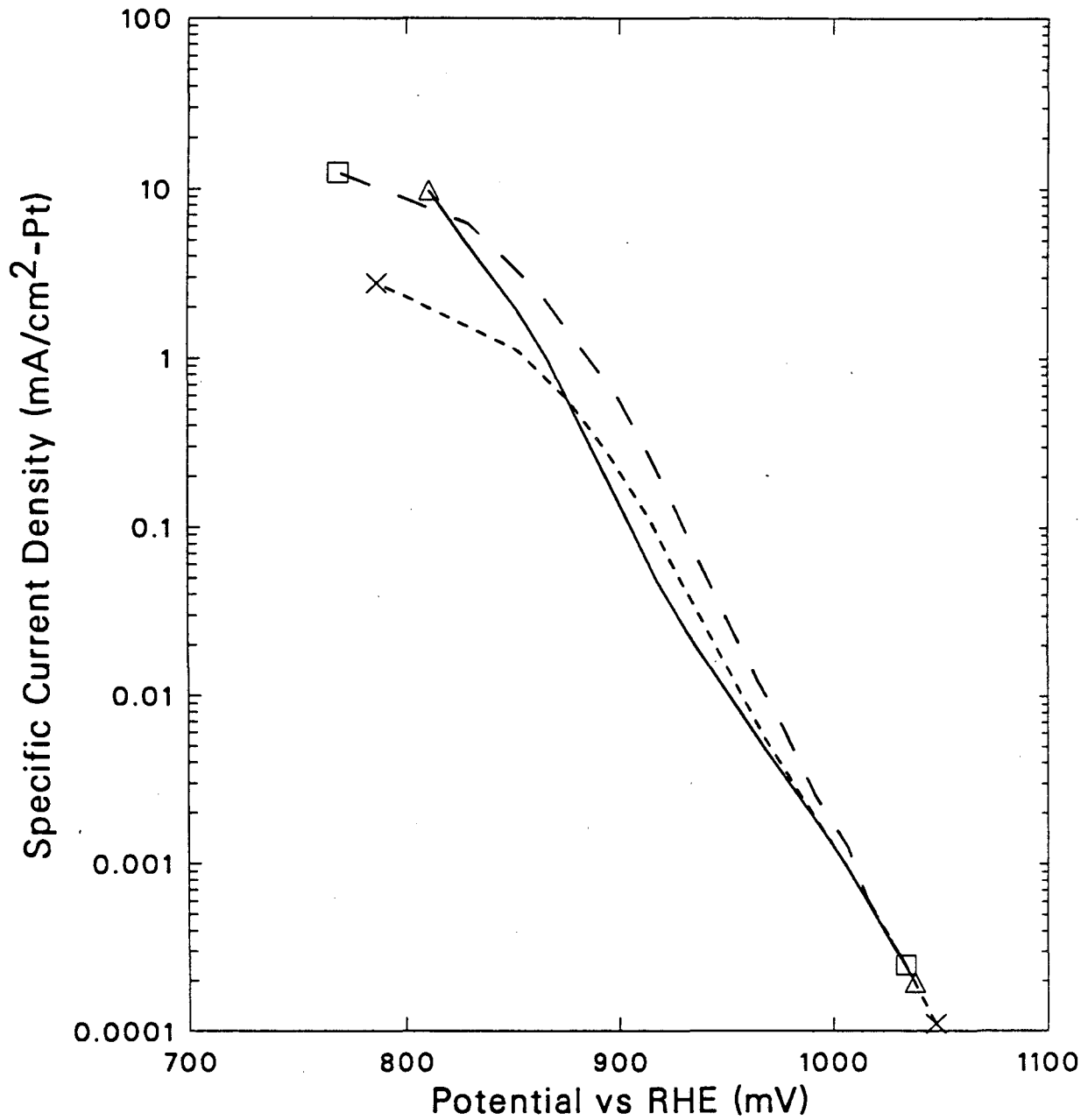
Polarization curves with 100% O₂ for 3.3, 6.9 and 11 M KOH are shown in Figure 5-15 on a specific area of Pt basis. These curves exhibit Tafel slopes of 47, 44 and 39 mV/decade, respectively. The large change in kinetic currents with oxygen solubility differences noted in Chapter 4 do not show up here. The reaction rate is indeed sensitive to oxygen concentration, as was indicated in Figure 5-14, but there appears to be a compensating factor. The fact that the Tafel slope changes with concentration may be an indication of either local pH changes (which are a function of current) or a manifestation of the influence of the carbon support. Appleby and Marie interpreted the decrease in Tafel slope with increasing KOH concentration, for OR on carbon, as a change in the rate-determining step caused by the decrease in water activity.

It is interesting to note that the onset of mass-transfer control appears in 6.9 M and 11 M at current densities in the range of 1 to 10 mA/cm²Pt but not in the low-concentration KOH, probably because of the much-higher O₂ solubility.

5.5. Cathode Performance in K₂CO₃ Electrolytes

Concentrated carbonate electrolytes wet the type of porous GDE used in this study to a much lower degree than do the KOH electrolytes. Even after soaking in the working electrolyte for several days, the resistance of the working electrode is often too high for the control circuit of the potentiostat. Sufficient wetting is achieved only by the reduction of oxygen. This process essentially transforms the electrolyte in the pores into a hydroxide electrolyte which then wets the electrode. After sitting for 24 hours or more, the composition in the pores equilibrates with the bulk, and the electrode remains wetted.

Large fluctuations in wetted area along with the composition changes discussed in Section 5.2 render difficult the measurement of polarization curves that are truly characteristic of a carbonate electrolyte. The two types of measurements discussed in Section 5.1 were performed: first-polarization curves were recorded immediately after a voltammetric characterization of the wetted area and the electrolyte composition in the pores. Then cycling measurements were



- XBL 8711-4731 -

Figure 5-15: Specific current densities for oxygen reduction on a Prototech electrode in KOH electrolytes, 23°C.
——— Δ , 3.3M KOH; ——— \times , 6.9M KOH; — — — \square , 11M KOH.

performed in an attempt to characterize the reversibility (or lack thereof) of the system.

Figure 5-16 shows specific current densities for first polarizations recorded in 2 and 5.5 M K_2CO_3 at 23 °C with 100% O_2 , along with the kinetic result for 2.0 M K_2CO_3 from Chapter 4 corrected as in Figure 5-14. At low overpotentials, the measured currents are not proportional to the area of Pt wetted by the electrolyte, but rather show a square-root dependence on wetted area. This observation, along with the fact that the Tafel slope for the porous electrode in 2 M K_2CO_3 is almost twice that measured with the smooth electrode, indicates that a mass-transfer process along with the kinetic process are controlling the reaction rate.

Figure 5-17 shows first polarization measurements made in 4 M K_2CO_3 at three oxygen partial pressures. These measurements were made (in one day) by measuring potentials at each of the three gas compositions before increasing the current. A half-order dependence of current density on p_{O_2} at a constant potential is shown in Figure 5-18. A limiting rate of O_2 diffusion into the pores of the agglomerates will not result in a half-order dependence on oxygen pressure (99). It has been suggested by Ross (90) that ionic migration of H^+ ion is responsible for anomalous dependencies on oxygen pressure in phosphoric acid fuel cell cathodes at high currents. The ionic mass-transfer resistance due to build-up of OH^- ion in a carbonate system will be shown in Chapter 6 to result in similar behavior.

Figure 5-19 shows first polarization curves for 5.5 M K_2CO_3 at 23 and 100 °C along with data reported by Cairns et al. (3) for a Cs_2CO_3 electrolyte at 107 °C on an electrode with a very high loading of Pt black. The high-temperature data indicate that the kinetically-controlled region may be extended to slightly higher current densities with an increase in temperature. The performance in Cs_2CO_3 shows the same ionic-mass-transfer-limited Tafel slope with higher currents due to a much-larger platinum loading. Cairns et al. did not observe the large concentration changes we have noted here. This is due to the fact that both anode and cathode concentrations shifted while the reference electrode was maintained at an average composition through electrolyte circulation.

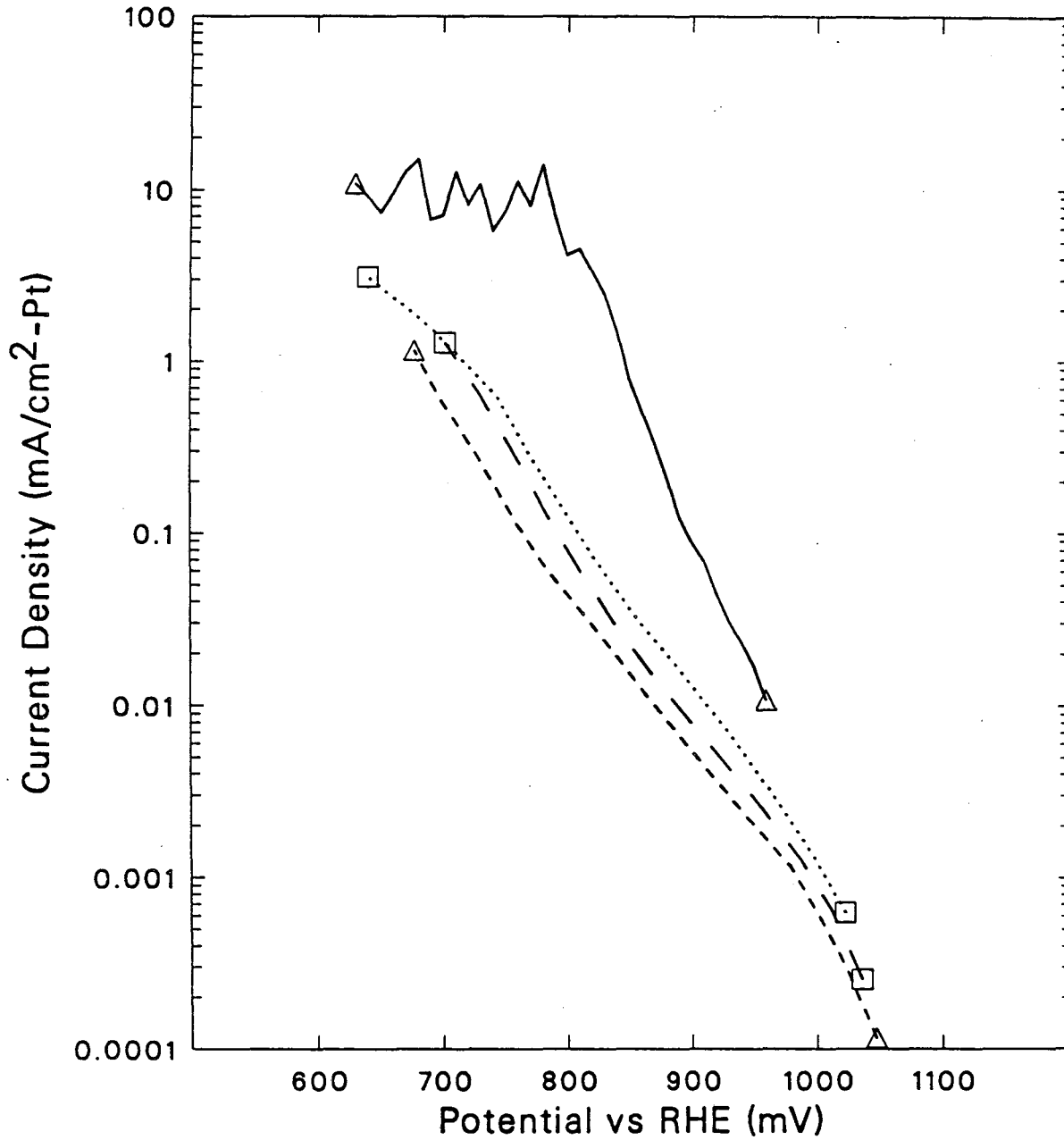


Figure 5-16: Specific current densities for oxygen reduction on smooth Pt and Prototech porous GDE in K₂CO₃ electrolytes, 23 °C.

- △, smooth Pt electrode in 2.0M K₂CO₃;
- △, porous electrode (A_w = 172 cm²) in 2.0M K₂CO₃;
- , porous electrode (A_w = 78 cm²) in 5.5M K₂CO₃;
-□, porous electrode (A_w = 32 cm²) in 5.5M K₂CO₃.

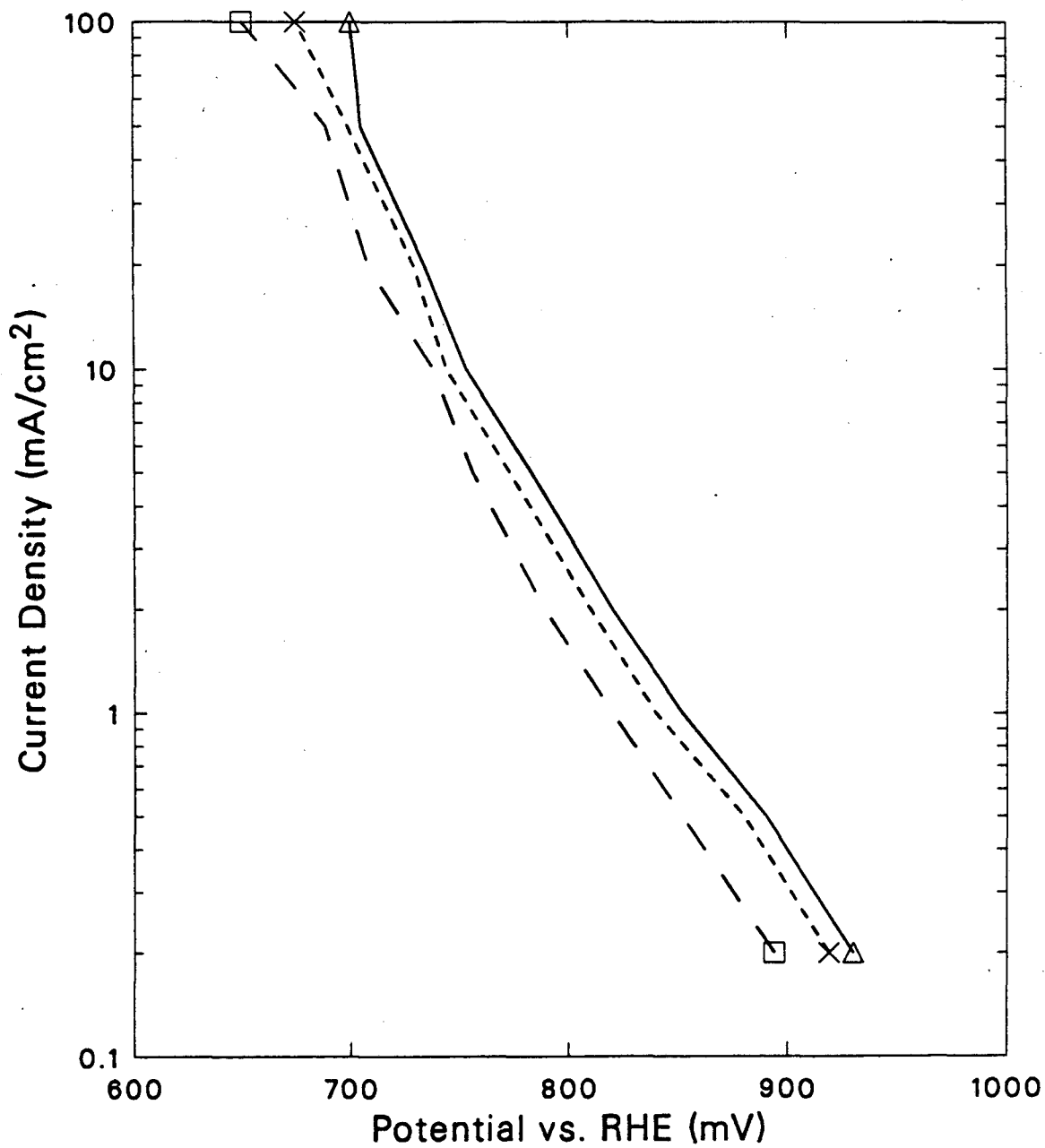


Figure 5-17: Polarization behavior in 4.0M K₂CO₃ at various O₂ partial pressures, 23 °C.

—Δ, 1 atm O₂;
- - - ×, 0.59 atm O₂;
- - - □, 0.21 atm O₂.

- XBL 8711-4729 -

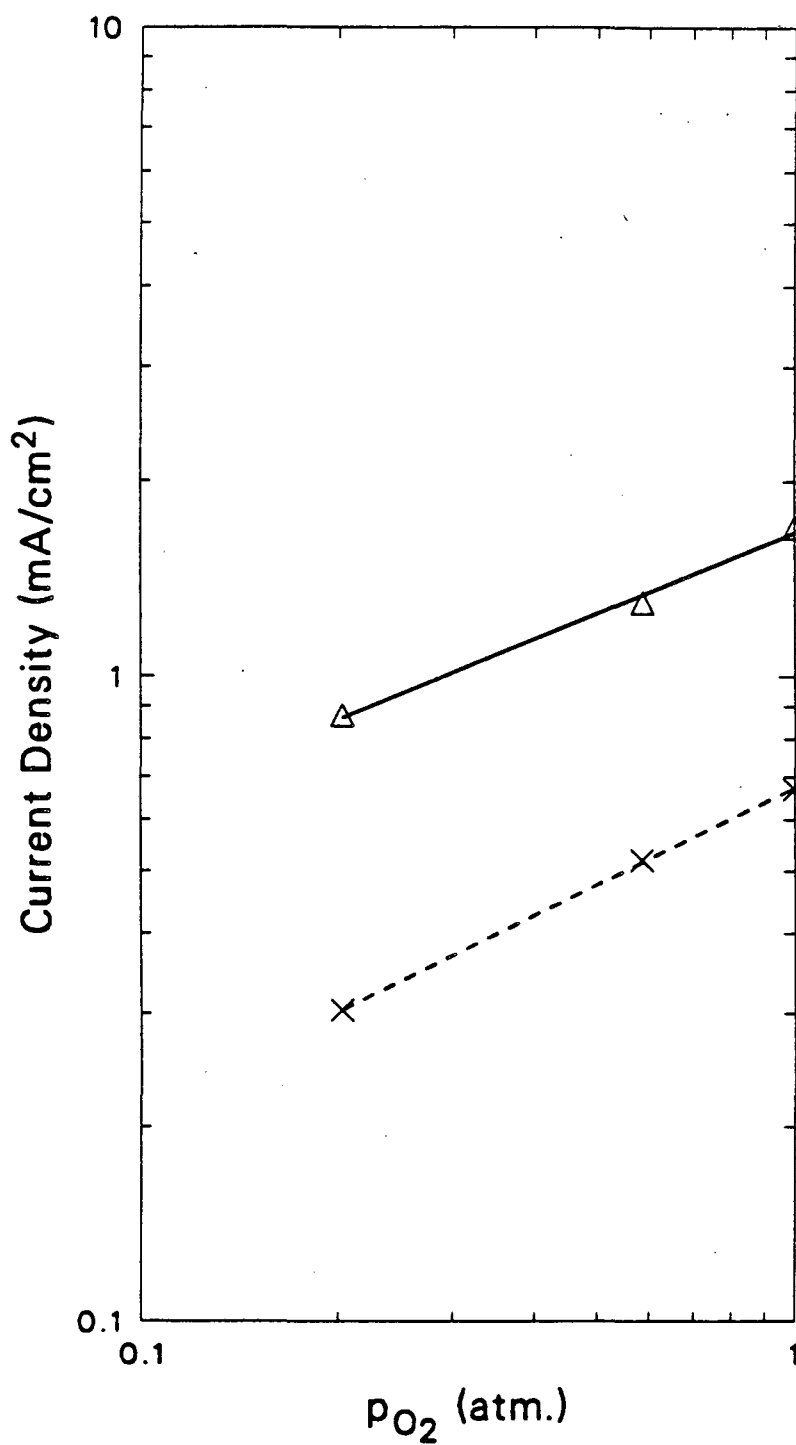
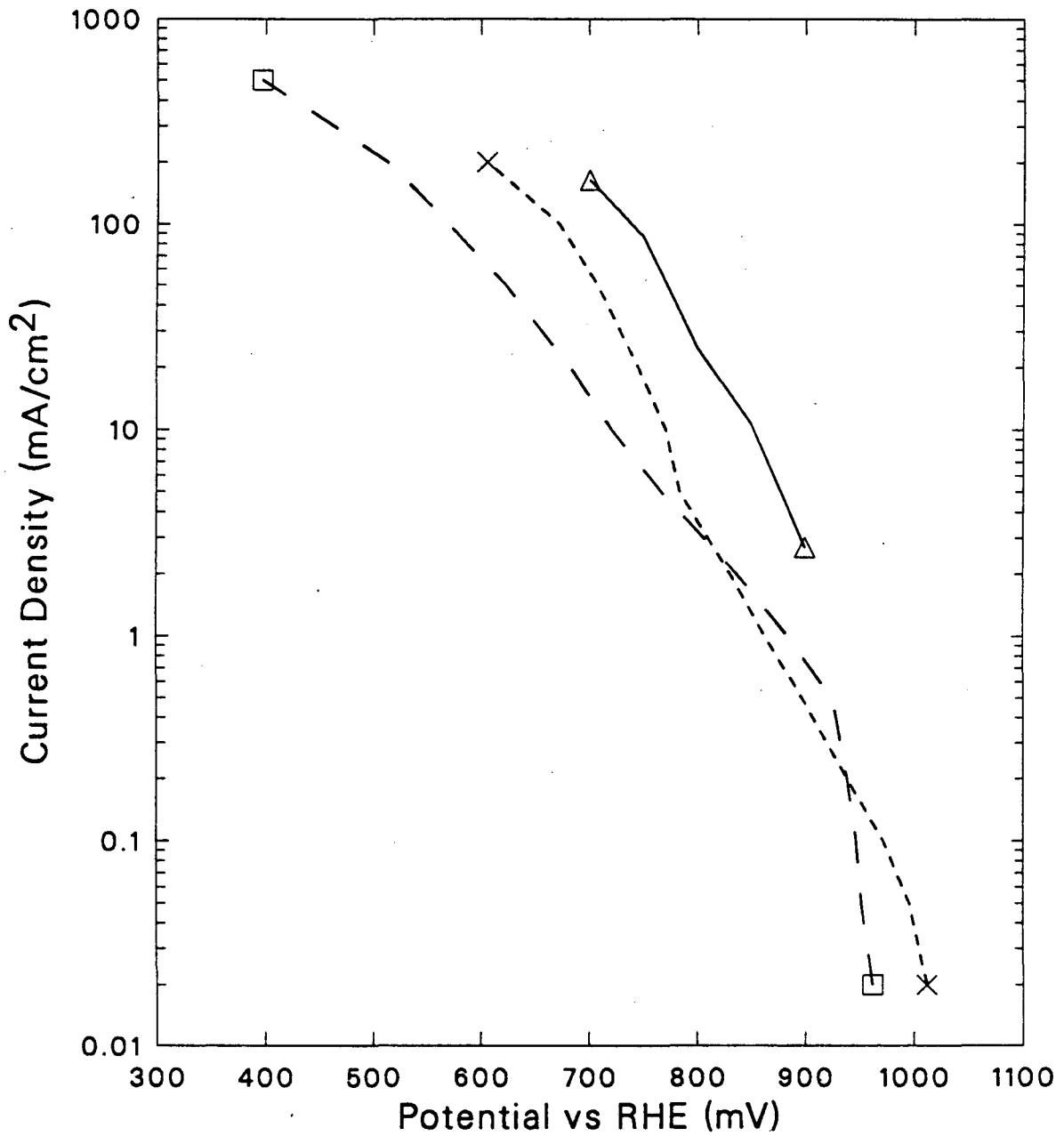


Figure 5-18: Dependence of current density on p_{O_2} at constant potential in 4.0 K_2CO_3 , 23°C.

— Δ , 825 mV vs. RHE;

- - - \times , 875 mV vs. RHE.

- XBL 8711-4728 -



- XBL 8711-4727 -

Figure 5-19: O_2 polarization behavior in carbonate electrolytes at various conditions.
 — Δ , Cs_2CO_3 at 107 °C (3);
 — \times , 5.5M K_2CO_3 , 23 °C;
 — \square , 5.5M K_2CO_3 , 100 °C;

First and cycling polarization measurements for 100% O₂ are shown in Figure 5-20A for 2.0 M K₂CO₃ as compared with 3.3 M KOH on a Prototech electrode and in Figure 5-20B for 5.5 M K₂CO₃ as compared with 6.9 M KOH on electrode EM-A (prepared according to the procedures of Motoo et al. (102)). The hydroxide anion appears to remain in the pores at a sufficiently high concentration that transport of hydroxide ion out of the pores no longer affects the Tafel slope. However, the whole curve is shifted cathodically since the new composition has a pH which is different from that of the reference electrode. Both of the electrodes in Figure 5-20 have been optimized for the transport of O₂ to the reaction site (short pathway) at the expense of a large diffusion path in the liquid phase. The fact that this hysteresis was not seen in the work of Cairns et al. (3) is a result of the fact that the electrode structure used in the mid-1960's contained an active region which was much more two-dimensional and thus contained more equal diffusion pathway for liquid and gaseous reactants and products. The double-Tafel slope in the early work could be due to either O₂ or OH⁻ diffusion limitation.

CO₂ Addition

One approach to reducing the buildup of OH⁻ during OR in K₂CO₃ is the addition of CO₂ to the oxygen stream. CO₂ reacts very rapidly with hydroxide ion at these pH's (108) to form bicarbonate and water. In a real system, it is not inconceivable that CO₂ from the anode gas could be used for this purpose. First and cycling polarization measurements made with pure O₂ in 5.5 M K₂CO₃ are compared with cycling measurements with different partial pressures of CO₂ in Figure 5-21. The first polarization curve from part a is repeated in parts b-d. 173 ppm CO₂ appears to have little effect on the polarization behavior. With 0.17% CO₂ there is a shift in potential at the low currents due to a lowering of the pH (an aqueous solution will maintain a pH around 9.6 in contact with 1 atm of CO₂). As current (and OH⁻ production rate) increases, the pH shifts back to a high value. With 1.57% CO₂, this shift occurs at higher currents, and the Tafel slope up to that point is about 75 mV/decade. The kinetic Tafel slope in this electrolyte was not measured. Further interpretation of these results is difficult because of the fact that

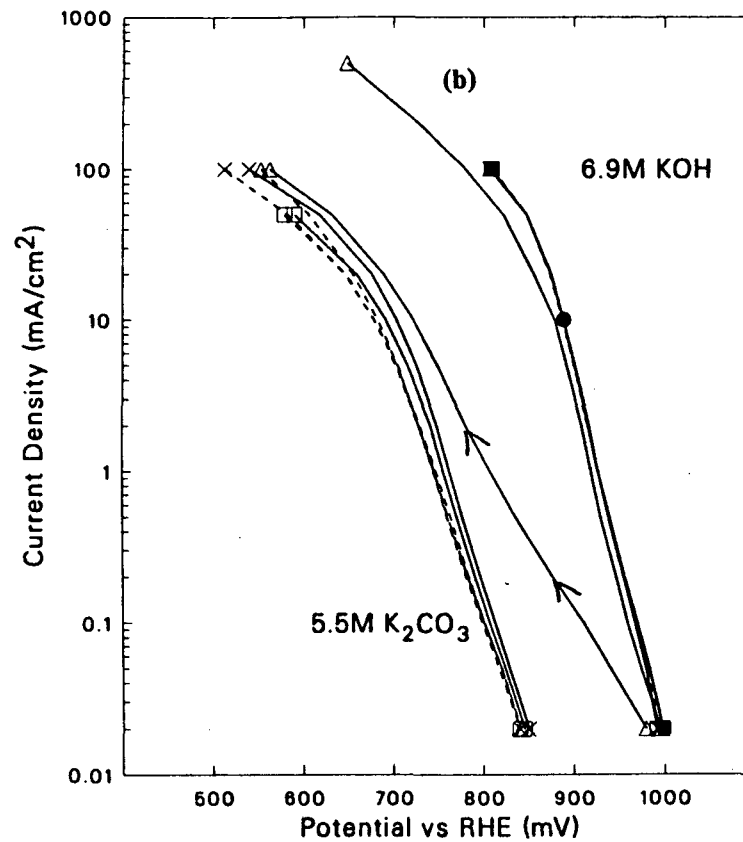
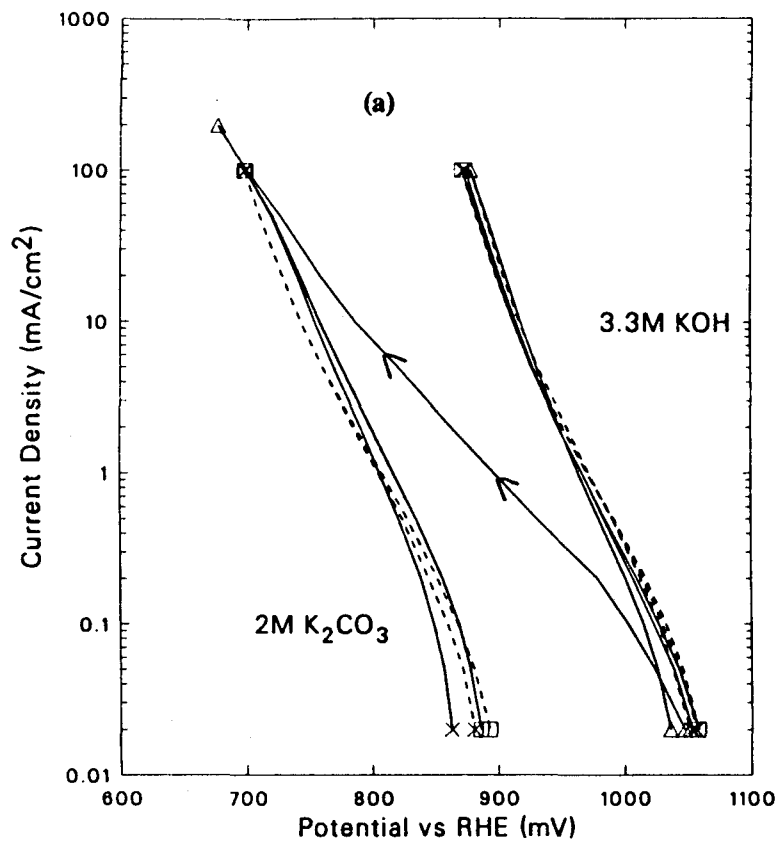
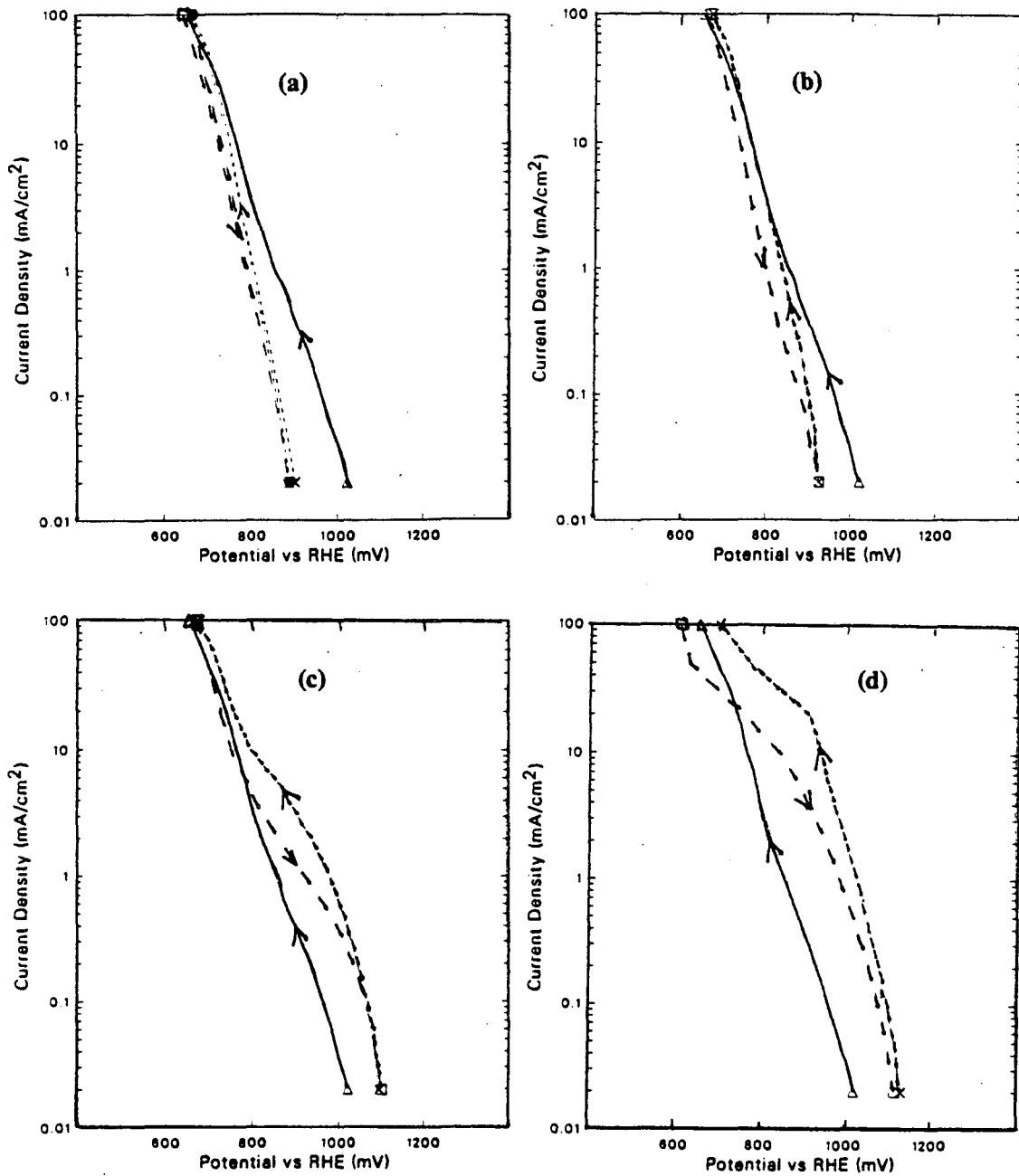


Figure 5-20: "Cycling" polarization measurements in alkaline electrolytes 23 °C.
 (a) P29 with 3.3M KOH and 2.0M K₂CO₃; (b) EM-A with 6.9M KOH and 5.5M K₂CO₃.
 ——— cathodic direction; - - - - - anodic direction;
 Δ, first cycle; X, second cycle; □, third cycle.

- XBL 8711-4726 -



- XBL 8711-4725

Figure 5-21: The effect of CO₂ addition on O₂ cycling polarization measurements in 5.5M K₂CO₃, 23 °C.
 a-d: ———Δ, first polarization with 100% O₂.
 (a) cycling with 100% O₂;
 (b) cycling with 173ppm CO₂;
 (c) cycling with .17% CO₂;
 (d) cycling with 1.57% CO₂.

with continued exposure to CO_2 , the bulk electrolyte composition begins to change.

5.6. Summary and Recommendations

Cyclic voltammetry of platinum-on-carbon electrodes performed in a cell with a sufficiently low uncompensated resistance yields valuable information regarding the degree of electrode wetting and local electrolyte composition. With this technique, lower Pt oxidation rates were measured on supported Pt than on smooth Pt in alkaline electrolyte, in agreement with previous results for acid electrolytes. The reversibility of the reduction of this oxide may depend on electrolyte pH as well as Pt particle size. An estimate for the double-layer capacity for the carbon-Pt surface of the electrode of $300 \mu\text{F}/\text{cm}^2$ compares well with that measured on a smooth graphite surface. Evidence for product build-up (OH^- and HO_2^-) and/or reactant depletion (H_2O) in the pores of an oxygen cathode in 6.9 M KOH was obtained.

Polarization curves recorded at varying degrees of electrode wetting yielded information about the limiting processes, similar to that obtained by varying Pt loading. The oxygen cathode in KOH is controlled strictly by kinetics at low current densities. As current density increases (and potential decreases), the chemical limitations observed in the kinetic measurements may be overcome by the added activity of the carbon support. The electrocatalytic effect of the carbon support may compensate for lower oxygen solubilities as KOH concentration increases.

Performance in the carbonate-containing electrolyte is limited by ionic mass-transfer of product OH^- . The large barrier to ion transport in the pores also manifests itself as an extreme hysteresis effect which requires times as long as 24 hours to fully equilibrate with the bulk electrolyte. This hysteresis is probably due to the lower wettability in the carbonate relative to the hydroxide. This represents a surface-tension resistance to rapid equilibration of the pH gradient that forms in a carbonate-containing cathode. The hysteresis was not observed in the work of Cairns et al., probably because of the vastly different electrode structures involved in that work.

A numerical model of the oxygen cathode in carbonate electrolyte will be presented in Chapter 6. Such modeling efforts might lend suggestions on electrode structures which would

result in more reversible for use in carbonate electrolytes. More work at higher temperature should also yield new information.

Chapter 6

Modeling of the Aqueous Carbonate Fuel Cell Cathode

6.0. Introduction

In Chapter 5 we presented a comparison between O_2 cathode polarization behavior with concentrated K_2CO_3 and KOH electrolytes. The kinetic results of Chapter 4 allowed us to identify the observed Tafel slopes of the performance curves as kinetically-limited or mass-transfer-limited. Hydroxyl ion transport was identified as a possible limiting process with the carbonate electrolyte. In this chapter we present a steady-state model of the gas-diffusion electrode based on the flooded-agglomerate model, including the effects of the carbonate chemistry.

In Section 6.1 previous models for the gas diffusion electrode are reviewed. Early work was based on the assumption that the active layer region for the contact between the three phases was essentially two-dimensional. Modern electrodes, constructed of supported Pt, are presumed to have a more three-dimensional active layer as depicted in Figure 1-1.

Section 6.2 presents our version of a steady-state flooded agglomerate model for a cathode operating with 100% O_2 in pure KOH electrolyte. Ohmic losses in the solid phase, and migration and diffusion in the liquid phase are considered, along with the reaction and diffusion of O_2 . The results are compared with the performance data reported in Chapter 5 for high potentials in order to provide estimates for some of the electrode structural parameters.

Section 6.3 presents a similar model developed for the carbonate cathode, including the transport of and the equilibrium reaction between the three anions present in the electrolyte. Model results, calculated with no adjustable parameters, are compared with performance data reported in Chapter 5.

Section 6.4 presents our conclusions regarding the O_2 cathode in concentrated carbonate electrolyte based on the experimental and theoretical work reported in this thesis. Directions for

future experimental and modeling work are discussed.

6.1. Previous Work

Early modeling of fuel cell electrodes dealt with various microscopic approximations of the complex structure (110,111) or continuum approximations (112) which were too abstract to allow more than correlation parameters to be determined. Most of the controversy regarded the actual structure of the active region. Bennion and Tobias (113) modeled the active region of a porous O_2 cathode as a thin stable electrolyte film extending from a flooded region of porous electrode. They measured current distributions along a film-covered Pt electrode and modeled the migration and diffusion of KOH along the film using concentrated-electrolyte theory. They predicted the KOH concentration to rise above the saturation limit if it was assumed that the reactant water was supplied only through the electrolyte. It was concluded that a significant fraction of the reactant water was supplied by condensation from the gas phase. Bockris and Cahan modeled the active region as existing entirely within the meniscus formed at the three-phase boundary. They were also able to fit their model to their experiments in a model cell (111).

Modern PTFE-bonded porous GDEs are envisioned to have an active region which is much closer to a three-dimensional structure as depicted in Figure 1-1. This type of structure was first envisaged by Giner and Hunter in 1969 (114). They modeled a PTFE-bonded Pt black electrode as a series of flooded cylindrical agglomerates which have small diameters compared with the thickness of the electrode, fed by parallel hydrophobic gas pores. They assumed that water transport equilibrated through the gas phase and ignored ohmic losses in the solid phase. These assumptions resulted in an analytic solution of the O_2 problem (in terms of modified Bessel functions) separate from the ohmic conduction problem in the liquid phase. They explained the "double-Tafel slope" observed as a switch from activation control to mass-transfer control inside the agglomerates.

The most comprehensive model based on the idea of the flooded agglomerate was developed by Iczkowski and Cutlip, for the O_2 cathode in phosphoric acid electrolyte (115). They included the possibility of a thin film covering the agglomerates, which is necessary in order to explain the observation of limiting currents (not caused by gas transport when operating with 100% O_2). They used Ohm's law for conductivity losses in the solid and liquid phases, and assumed gas-phase losses in the active and backing layers to occur via Knudsen and/or molecular diffusion. They also assumed that water (a product in an acid electrolyte) equilibrates through the gas phase. They estimated voltage losses for each of the processes in an electrode operating on air. The most significant losses (after kinetics) were found to be ohmic drop in the electrolyte, and gas transport in the active layer.

Ross (90) suggested that the neglect of migration effects may not be valid with a phosphoric acid-containing cathode. In this electrolyte, hydrogen ion may not be in large enough excess to act as a supporting electrolyte, since it is being consumed by the reaction and the phosphoric acid is not fully dissociated. He modeled the electrode as a series of flooded spherical agglomerates and used a form of Fick's law to describe transport of H^+ in the liquid phase, neglecting ohmic and gas-phase losses. Limiting-case studies were used to show that the increased polarization and corresponding anomalous current ratios (non-first-order dependence on O_2 pressure), often observed in phosphoric acid fuel cells at high current densities, can be explained by a local depletion of H^+ . This "resistance polarization" can lead to a "double Tafel slope" without O_2 transport limitations.

In concentrated acid electrolytes, resistance polarization manifests itself only at relatively high current densities. In the carbonate cathode, we have reported similar symptoms (anomalous current ratios and non-kinetic Tafel slopes) even at low current densities. In this case, however, we are dealing with the buildup of a product upon which there is a strong thermodynamic potential dependence. After discussing a model for the O_2 cathode in KOH, a flooded-agglomerate model based upon a K_2CO_3 electrolyte will be developed.

6.2. Oxygen Cathode with Concentrated KOH Electrolyte

6.2.1. Model Development

A steady-state model will be developed in this section to predict the potential under controlled-current operation. The assumed electrode structure and geometry for the model are shown in Figure 6-1. The assumptions are as follows:

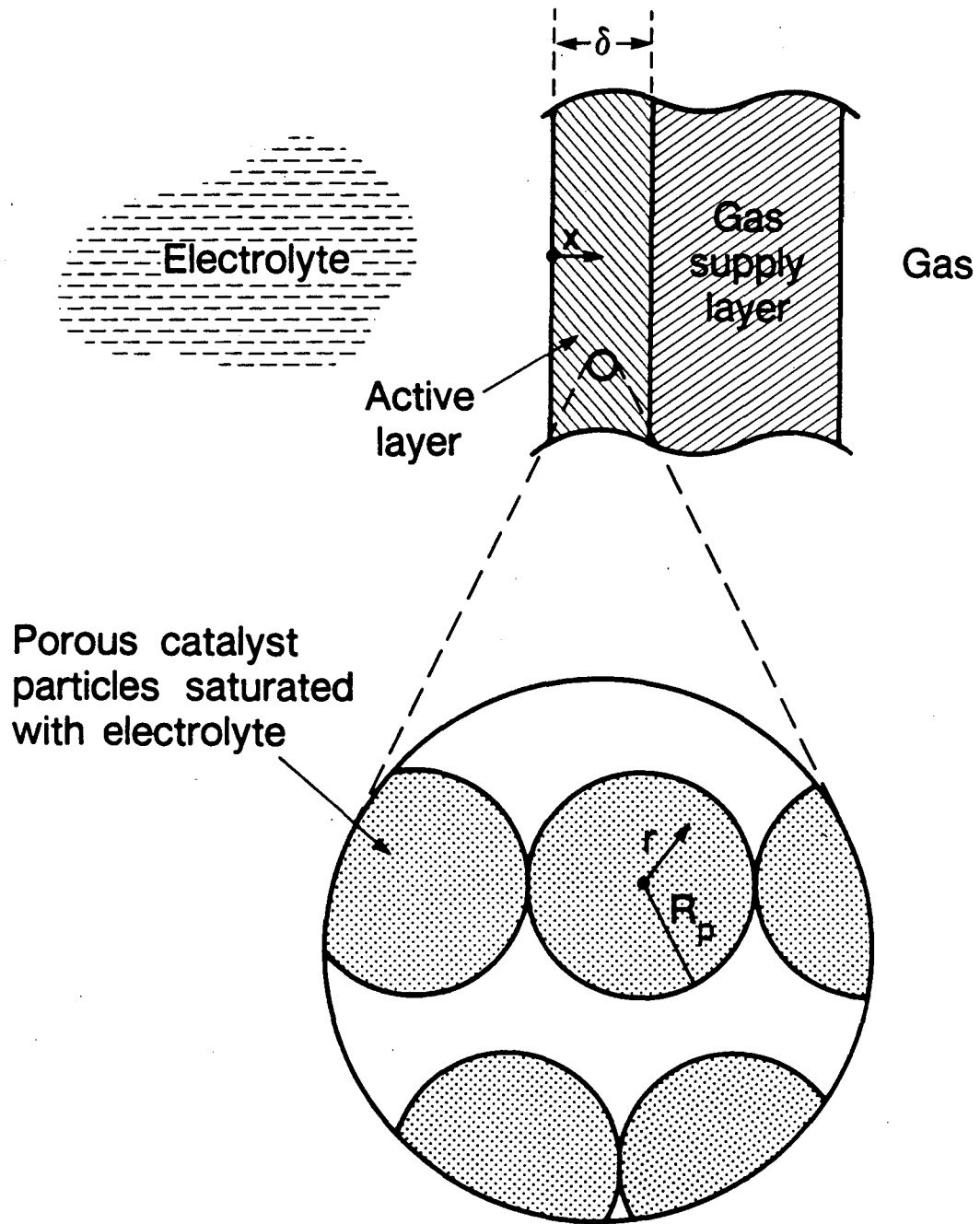
- 1 Oxygen reduction occurs only via the direct 4-electron pathway and only on the platinum in the electrode.
- 2 Ionic mass transfer is adequately described by the expressions for dilute electrolytes.
- 3 The electrocatalyst is fully wetted by the electrolyte. The behavior of a partially wetted electrocatalyst is examined for the case of pure kinetic/ O_2 diffusion control.
- 4 The radius of the spherical agglomerates is small compared to the active layer thickness so that the electrolyte ionic composition, and the potential in the liquid and solid phases are uniform over each agglomerate.
- 5 With 100% O_2 , all gas-phase resistances to transport are negligible.
- 6 Reactant water is supplied by rapid condensation from the gas phase.

R-Direction O_2 Diffusion Problem

Assumption 4 above permits solution of the r-direction equations for diffusion and reaction of O_2 in the agglomerates, independent of the ionic migration/diffusion problem in the x-direction. Assuming spherical particles, the simultaneous reaction and diffusion of O_2 is described by

$$\frac{D_{O_2}\epsilon_a}{\tau_a} \left[\frac{1}{r^2} \frac{d}{dr} \left(r^2 \frac{dC_{O_2}}{dr} \right) \right] = \frac{i_{local}a_0}{nF\delta(1-\epsilon_e)} \quad (6-1)$$

where ϵ_a and τ_a are the agglomerate microporosity and tortuosity factors, $(1 - \epsilon_e)$ is the volume fraction of agglomerates in the electrode, δ is the thickness of the active layer, and a_0 is the Pt



XBL 8711-8177

Figure 6-1: Flooded agglomerate model of the fuel cell GDE.

area per unit area of the electrode. i_{local} is the local current per square cm of Pt for the irreversible consumption of O_2 which is described by a form similar to Equation 2-2 written for an alkaline electrolyte

$$i_{\text{local}} = nFk_c^{\circ}(a_{\text{O}_2})^{\alpha} \exp\left(-\frac{\alpha FE}{RT}\right) \quad (6-2)$$

where E is the potential of the solid with respect to a reversible hydrogen electrode just outside the boundary layer, or $E = \Phi_S - E_{\text{RHE}}^{\text{local}}$. For a first-order reaction with respect to O_2 concentration $s_{\text{O}_2} = 1$ and $E_{\text{RHE}}^{\text{local}}$ can be expressed as

$$E_{\text{RHE}}^{\text{local}} = E_{\text{RHE}}^{\circ} + \Phi_L(x) - \Phi_L^{\circ} + \frac{RT}{F} \ln \frac{a_{\text{OH}^-}}{a_{\text{OH}^-}^{\circ}} \quad (6-3)$$

We will define $\Phi_L^{\circ} = E_{\text{RHE}}^{\circ}$ so that when activities are replaced by concentrations the expression for i_{local} takes the following form

$$i_{\text{local}} = nFk_c^{\circ} C_{\text{O}_2} \left(\frac{C_{\text{OH}^-}}{C_{\text{OH}^-}^{\circ}}\right)^{-\alpha} \exp\left(-\frac{\alpha F(\Phi_S - \Phi_L)}{RT}\right) \quad (6-4)$$

The potentials of the solid and liquid phases (Φ_L and Φ_S) and the ionic composition of the electrolyte (C_{OH^-}) are assumed to be uniform throughout the agglomerate, in accordance with assumption 4 above ($R_p \ll \delta$). The general solution to Equation 6-1 is

$$C_{\text{O}_2} = \frac{K_1}{r} \cosh(\phi r) + \frac{K_2}{r} \sinh(\phi r) \quad (6-5)$$

where

$$\phi^2 = \zeta^2 \left(\frac{C_{\text{OH}^-}}{C_{\text{OH}^-}^{\circ}}\right)^{-\alpha} \exp\left(-\frac{\alpha F(\Phi_S - \Phi_L)}{RT}\right) \quad (6-6)$$

and

$$\zeta^2 = \frac{a_0 k_c^{\circ} \tau_a}{D_{\text{O}_2} \delta \epsilon_a (1 - \epsilon_e)} \quad (6-7)$$

For complete wetting of the agglomerate particles, the boundary conditions

$$\text{BC 1:} \quad @r = R_p \quad C_{O_2} = C_{O_2}^\infty \quad (6-8)$$

$$\text{BC 2A:} \quad @r = 0 \quad \nabla C_{O_2} = 0 \quad (6-9)$$

lead to the solution

$$\frac{C_{O_2}}{C_{O_2}^\infty} = \frac{R_p}{r} \frac{\sinh(\phi r)}{\sinh(\phi R_p)} \quad (6-10)$$

If progressive wetting (observed in the results in Chapter 5) is assumed to occur in the r-direction, the second boundary condition is

$$\text{BC 2B:} \quad @r = R_w \quad \nabla C_{O_2} = 0 \quad (6-11)$$

where R_w is the radius to which wetting has proceeded. This leads to the more complex solution

$$\frac{C_{O_2}}{C_{O_2}^\infty} = \frac{R_p}{r} \left[\frac{(\phi R_w - \tanh(\phi R_w))}{B \cosh(\phi R_p)} \cosh(\phi r) + \frac{(1 - \phi R_w \tanh(\phi R_w))}{B \cosh(\phi R_p)} \sinh(\phi r) \right] \quad (6-12)$$

where

$$B = \phi R_w - \tanh(\phi R_w) + \tanh(\phi R_p) - \phi R_w \tanh(\phi R_p) \tanh(\phi R_w) \quad (6-13)$$

This expression reduces to Equation 6-10 when $R_w = 0$.

The current per cm^3 of electrode is obtained from the flux of O_2 into an agglomerate times the agglomerate surface area and the number of agglomerates per cm^3 ,

$$N_p = \frac{3(1 - \epsilon_e)}{4\pi R_p^3} \quad (6-14)$$

The interfacial current per unit volume of electrode produced by the reduction of O_2 is

$$\bar{J} = -nF4\pi R_p^2 N_p \left(-\frac{D_{O_2} \tau_a}{\epsilon_a} \frac{dC_{O_2}}{dr} \right) \Big|_{r=R_p} \quad (6-15)$$

which reduces to

$$\bar{J} = k'[\phi R_p \coth(\phi R_p) - 1] \quad (6-16)$$

for complete wetting, and

$$\bar{J}_w = \frac{k'}{B} \left\{ [\phi R_w - \tanh(\phi R_w)][\phi R_p \tanh(\phi R_p) - 1] + \right. \\ \left. [1 - \phi R_w \tanh(\phi R_w)][\phi R_p - \tanh(\phi R_p)] \right\} \quad (6-17)$$

for a partially wetted electrode where

$$k' = \frac{3nFC_{O_2}^{\infty} D_{O_2} \epsilon_a (1 - \epsilon_e)}{R_p^2 \tau_a} \quad (6-18)$$

Figure 6-2 shows the functional relationship between \bar{J}_w/k' and ϕR_p for different values of R_w/R_p . If the potential and composition over the entire electrode are assumed to be constant, i.e. kinetic control, the current to the fully-wetted electrode takes the familiar form for small values of ϕR_p , where $[\phi R_p \coth(\phi R_p) - 1] \rightarrow (1/3)(\phi R_p)^2$

$$I = \delta \bar{J} = a_0 n F k_c^{\circ} C_{O_2}^{\infty} \exp\left(-\frac{\alpha F E_m}{RT}\right) \quad (6-19)$$

where E_m is the measured potential between the current collector at $x = \delta$ and an RHE in the liquid at $x = 0$. For large values of ϕR_p , $(\phi R_p \coth(\phi R_p) - 1) \rightarrow (\phi R_p - 1)$, yielding the expression for mixed diffusion and kinetic control

$$I = \delta \bar{J} \propto n F C_{O_2}^{\infty} \frac{3}{R_p} \left[\frac{a_0 k_c^{\circ} \delta \epsilon_a D_{O_2} (1 - \epsilon_e)}{\tau_a} \right]^{1/2} \exp\left(-\frac{\alpha F E_m}{2RT}\right) \quad (6-20)$$

This expression reduces to that reported by Kunz and Gruver (89) if the micro- and macroporosities are considered equal. The transition between these two regions can be estimated, (from a log-log plot of the data in Figure 6-2) to occur at $(R_p \phi)_t \sim 2$, for the fully wetted agglomerate.

The partially wetted electrode will show similar behavior at small values of ϕR_p where \bar{J}_w/k' is proportional to the fraction of wetted area, A_w

$$A_w = 1 - \left(\frac{R_w}{R_p}\right)^3 \quad (6-21)$$

as can be determined from Figure 6-2. The value of ϕR_p at which mass transfer begins to play a

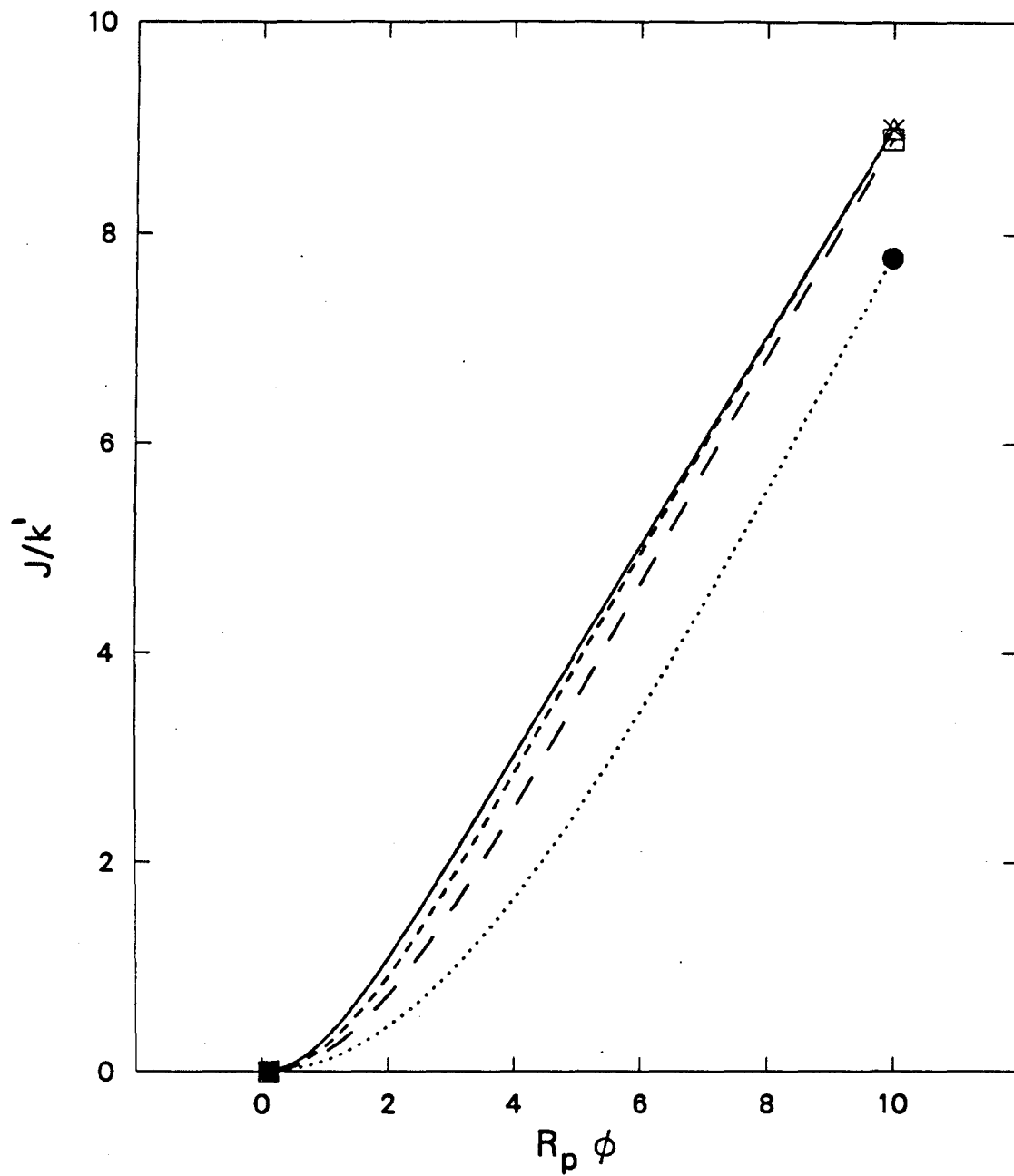


Figure 6-2: Effect of partial agglomerate wetting on the O_2 diffusion/reaction function.

- Δ , $R_w = 0$
- - - \times , $R_w = 5R_p/8$
- · - \square , $R_w = 3R_p/4$
- \bullet , $R_w = 7R_p/8$

role, $(\phi R_p)_t$, is proportional to $A_w^{-1/2}$. For large values of ϕR_p , the functional form of \bar{J}_w/k' is more complex. These calculations are consistent with the results presented in Section 5-2 for Prototech electrodes with varying degrees of wetting by 6.9 M KOH electrolyte.

X-Direction Liquid-Phase Problem

Assumptions 2 and 6 above lead to the following expression for a dilute binary electrolyte

(5),

$$\frac{D_{\pm} \epsilon_a}{r_a} \nabla^2 C_{K^+} + \frac{u_+ \bar{J}}{(u_+ + u_-)F} = 0 \quad (6-22)$$

and

$$\nabla \Phi_L = -\frac{D_+}{u_+ F} \nabla \ln C_{K^+} \quad (6-23)$$

where \bar{J} arises due to the production of OH^- by the reduction of O_2 and is described by Equation 6-16. For the KOH model we neglect the dependence of \bar{J} on C_{OH^-} through ϕ in Equation 6-6.

We define Ψ as the potential difference between the liquid and solid phases so that

$$\nabla^2 \Psi = \nabla^2 \Phi_S - \nabla^2 \Phi_L \quad (6-24)$$

Eliminating $\nabla^2 \Phi_S$ by differentiating Ohms law in the solid phase and $\nabla^2 \Phi_L$ by differentiating Equation 6-23 yields

$$\nabla^2 \Psi = -\frac{\nabla i_S}{\sigma} + \frac{D_+}{u_+ F} \nabla^2 \ln C_{K^+} \quad (6-25)$$

The expression for conservation of current in the electrode, $\bar{J} = \nabla i_S$, results in two coupled non-linear ordinary differential equations (6-22 and 6-25), in the unknowns Ψ and C_{K^+} ($= C_{\text{OH}^-}$), to be solved with the boundary conditions

$$\text{BC1, @}x = 0: \quad \nabla \Psi = \frac{I}{\kappa'} - \frac{F(D_- - D_+)}{\kappa^0} \nabla C_{K^+}, \quad C_{K^+} = C_{K^+}^0 \quad (6-26)$$

and

$$\text{BC2, @x} = \delta: \quad \nabla \Psi = -\frac{I}{\sigma}, \quad \nabla C_{K^+} = 0 \quad (6-27)$$

where κ' is the effective conductivity of the electrolyte in the agglomerates according to

$$\kappa' = \frac{\epsilon_a \kappa^0}{\tau_a} \quad (6-28)$$

σ is the conductivity of the solid matrix and I is the current density applied to the electrode. The details of the numerical solution of these equations are given in Appendix B. The solution is in the form of an electrolyte concentration profile and a potential difference profile at each value of current. The measured potential is defined by

$$E_m = \Phi_S(\delta) - \Phi_L(0) \quad (6-29)$$

and is calculated by integrating the potential difference profile as follows:

$$E_m = \Psi(0) - \frac{1}{\sigma} \int_0^\delta \left(\int_0^x \bar{J}(x) dx \right) dx + \Phi_L(0) \quad (6-30)$$

6.2.2. Parameter Estimation

Table 6-1 lists the electrolyte and kinetic parameters used in the model for 6.9 M KOH electrolyte along with those used in the carbonate model to be presented later. The electrode structural parameters σ , τ_a and R_p were taken from various sources. σ for this type of electrode was reported by Cutlip et al. (116) from fits of their version of the flooded-agglomerate model to O_2 cathode data for phosphoric acid electrolyte. The tortuosity factor for carbon black has been suggested to fall in the range of 4 to 6 (90). A value of 5 was used in this work. Stonehart et al. measured an agglomerate radius of about 10^{-5} cm for PTFE-bonded carbon particles. This value seems reasonable from our examination of an SEM of the active layer in Figure 5-5. From geometric considerations we have the additional relation

$$\delta = \frac{W_C/\rho_C + W_{\text{PTFE}}/\rho_{\text{PTFE}}}{(1 - \epsilon_a)(1 - \epsilon_e)} \quad (6-31)$$

Table 6-1: Parameters for GDE Models
Part A: Electrolyte Dependent Parameters

Parameter	Electrolyte		
	KOH	K ₂ CO ₃	
Nominal Concentration (mmol/cc)	6.9	2.0	4.0
K _{II} ^{app} (cc/mol) ^a	-	7.71 × 10 ⁶	10.75 × 10 ⁶
C _{O₂} (μmol/cc) ^b	0.0768	0.226	0.04
D _{O₂} (cm ² /sec) ^c	0.25 × 10 ⁻⁵	0.585 × 10 ⁻⁵	0.36 × 10 ⁻⁵
n (equiv/mol)	4	4	4
i _o = k _c ^o /nFC _{O₂} [∞] (A/cm ²)	1.01 × 10 ⁻¹¹	case 1: 6.05 × 10 ⁻¹¹ case 2: 1.36 × 10 ⁻¹⁰	2.13 × 10 ⁻¹¹
b = 2303 RT/αF (mV/decade)	44	case 1: 57 case 2: 62.5	51
κ ^o (Ω-cm) ⁻¹	0.65 ^d	0.194 ^e	0.223 ^e
$\frac{(D_- - D_+)u_{+f}}{D_{\pm}(u_+ + u_-)}$	0.359	-	-
$\left(\frac{2D_{OH^-}}{D_{CO_3^-}}\right)^g$	-	10.82	11.65
$\left(\frac{2D_{HCO_3^-}}{D_{CO_3^-}}\right)^g$	-	2.65	2.85
$\left(\frac{2D_{K^+}}{D_{CO_3^-}}\right)^g$	-	4.25	4.25
a _o (cm ² Pt/cm ² electrode) ^h	255	172	100

Part B: Prototech Electrode Parametersⁱ

$\sigma = 0.971 (\Omega\text{-cm})^{-1}$	$\tau_s = 5$	$R_p = 10^{-5} \text{ cm}$
$\delta = 0.012 \text{ cm}$	$W_C = 4.5 \text{ mg/cm}^2$	$W_{\text{PTFE}} = 2.1 \text{ mg/cm}^2$

^a Calculated in Appendix A

^b Calculated with Equation 4-8

^c Calculated from measured Levich slope and C_{O₂}[∞]

^d ref.78

^e measured

^f calculated from infinite dilution values (5)

^g ref.118

^h measured with cyclic voltammetry; see Chapter 5

ⁱ see text

where W_C , ρ_C , W_{PTFE} and ρ_{PTFE} are the loading and density of carbon and PTFE, and δ is the measured thickness of the active layer. This leaves freedom to vary only one of the porosities.

6.2.3. Results and Implications for Carbonate Model

For the limiting case of pure kinetic/ O_2 -diffusion control in the agglomerates, the transition from a kinetic Tafel slope to a double Tafel slope yields an estimation for the group of structural parameters:

$$(R_p\zeta)_t = R_p \left(\frac{\tau_a}{\epsilon_a(1 - \epsilon_e)} \right)^{1/2} \quad (6-32)$$

where $(R_p\zeta)_t$ is calculated from the transition potential assuming a value of $R_p\phi = 2$. Performance data for two different electrodes (P23 and L24) in 30% KOH yielded a value for $(R_p\phi) = 2.9 \times 10^{-4}$. Assuming that $R_p = 10^{-5}$ cm and porosities of 0.5, a value of $\tau_a \sim 40$ is estimated. This high value results from the neglect of the effect of porosity and tortuosity on electrolyte conductivity.

Figure 6-3 shows model results, including electrolyte transport, for 3 values of ϵ_a (with $\tau_a = 5$) compared with performance data recorded on electrode P23 in 30% KOH with 100% O_2 . The fit appears to be relatively insensitive to the choice for ϵ_a since the condition expressed in Equation 6-31 balances ϵ_a and ϵ_e . For this reason and the fact that the SEM of the active layer suggests a relatively large value for ϵ_e we will take $\epsilon_a = 0.5$ (which gives $\epsilon_e = 0.49$ for this electrode) as the best fit in Figure 6-3. Figure 6-4 shows the current distribution and electrolyte concentra-

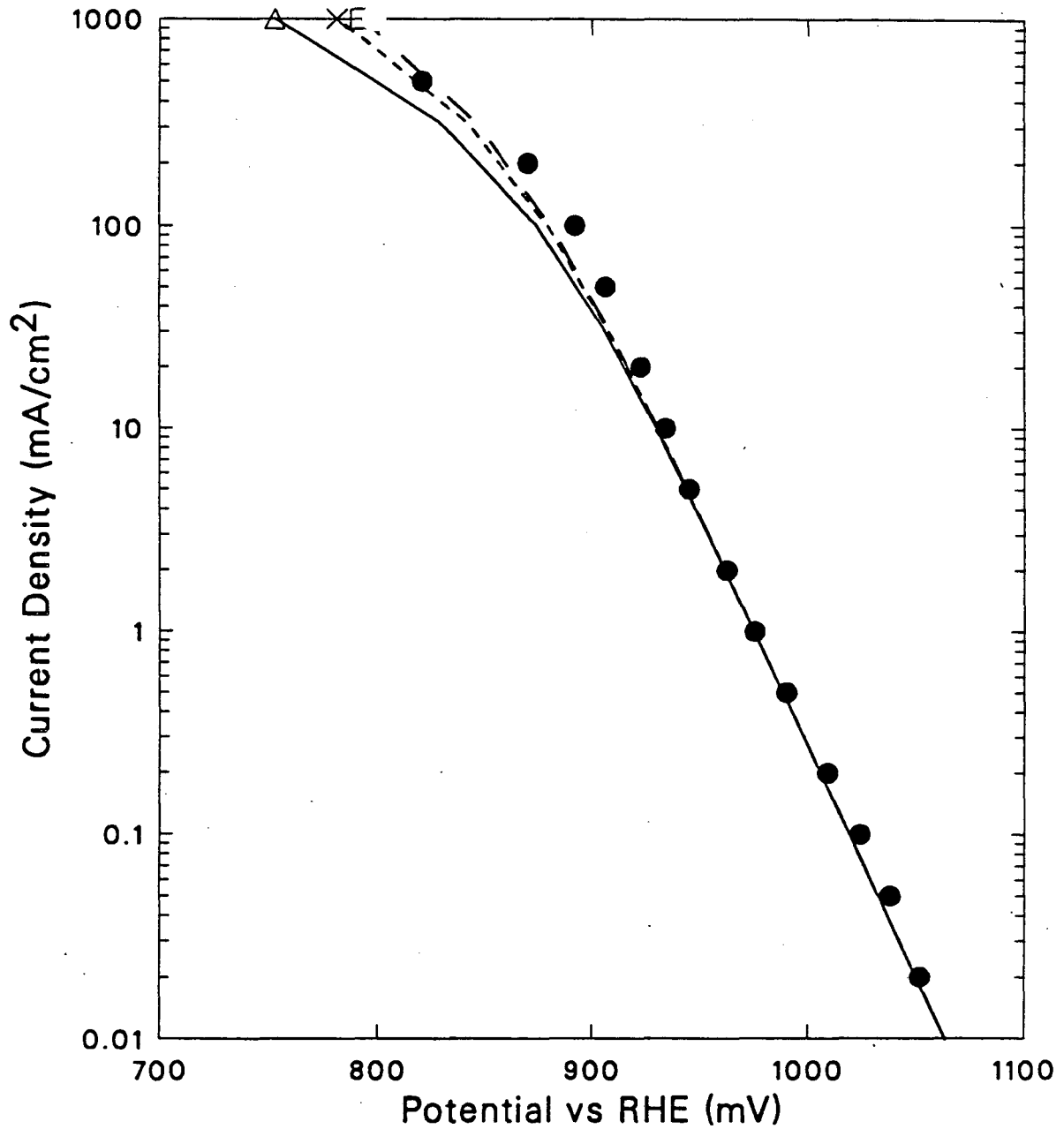


Figure 6-3: Prototech electrode P23 with 6.9M KOH and 100% O₂, 23 °C.

- , data,
- △, KOH Model with $\epsilon_s = 0.2$,
- ×, KOH Model with $\epsilon_s = 0.5$.
- , KOH Model with $\epsilon_s = 0.8$,

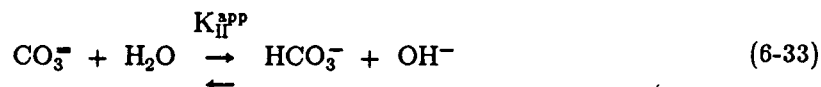
tion profiles for several currents for the case of $\epsilon_s = 0.5$. The model predicts an electrolyte concentration 3.5 times the bulk value at a current density of 1 A/cm². This corresponds to a value greater than the solubility of KOH. This could be due to the fact that we have used dilute electrolyte theory for a concentrated system or to the neglect of gas-phase water transport.

We can conclude that the approximations for the electrode structural parameters are reasonable, and that the model adequately predicts the behavior of the O₂ cathode in 6.9 M KOH. At lower electrolyte concentrations a transition to the double Tafel slope region was not observed within the range of currents accessible to measurement (≤ 1 A). This behavior can also be predicted by the model but is relatively uninteresting, due to the lack of fittable features. The more-complex carbonate problem will now be discussed.

6.3. Concentrated K₂CO₃ Cathode Model

6.3.1. Model Development

The r-direction problem of O₂ reaction and diffusion in the flooded agglomerates is identical to that discussed above for KOH. Ionic transport in this electrolyte is more complex due to the presence of three interacting anions according to the dynamic equilibrium



Steady-state material balances for the 3 anions, including production and consumption terms from OR and the above reaction, can be combined to eliminate the rate of the equilibrium reaction as suggested by Hseuh and Newman in their work on the effects of H₂SO₄ dissociation (117)

$$\nabla \cdot N_{\text{OH}^-} + \nabla \cdot N_{\text{CO}_3^{2-}} - \frac{\bar{J}}{F} = 0 \quad (6-34)$$

$$\nabla \cdot N_{\text{HCO}_3^-} + \nabla \cdot N_{\text{CO}_3^{2-}} = 0 \quad (6-35)$$

The fluxes N_i are expressed as

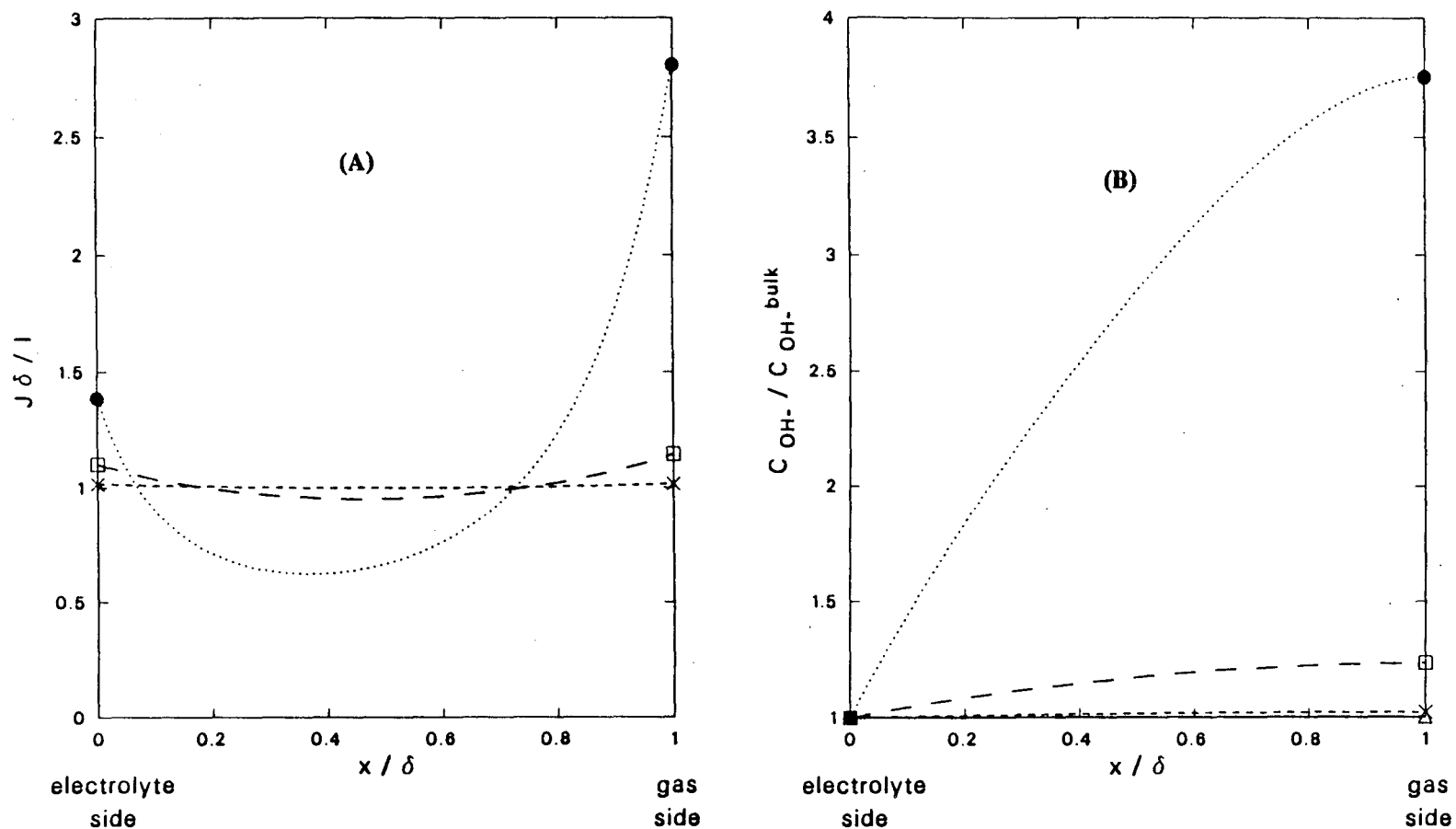


Figure 6-4: Predicted current density (A) and electrolyte concentration (B) profiles from KOH model for 6.9M KOH with $\epsilon_s = 0.5$.

- Δ , $I = 1 \text{ mA/cm}^2$,
- - - \times , $I = 10 \text{ mA/cm}^2$,
- · - \square , $I = 100 \text{ mA/cm}^2$,
- · · \bullet , $I = 1 \text{ A/cm}^2$.

$$N_i = -z_i u_i F C_i \nabla \Phi_L - D_i \nabla C_i \quad (6-36)$$

for dilute electrolyte conditions with no convection. The material balance on K^+ can be solved immediately for the potential gradient in the liquid phase as for the KOH problem (see Equation 6-23). Following that development further gives the same expression for the potential difference function,

$$\nabla^2 \Psi + \frac{\bar{J}}{\sigma} - \frac{D_{K^+}}{u_{K^+} F} \nabla \ln C_{K^+} = 0 \quad (6-37)$$

Finally, the expressions for equilibrium

$$C_{CO_3^-} = K_{II}^{app} C_{OH^-} C_{HCO_3^-} \quad (6-38)$$

and electroneutrality

$$2C_{CO_3^-} + K_{II}^{app} C_{OH^-} + C_{HCO_3^-} = C_{K^+} \quad (6-39)$$

round out the 5 non-linear coupled ordinary differential equations in the 5 unknowns: C_{K^+} , $C_{CO_3^-}$, $C_{HCO_3^-}$, C_{OH^-} , and Ψ .

The boundary condition at the gas-supply-layer interface is the same as in Equation 6-27 with the addition that $\nabla C_i = 0$ holds for all 4 ions. Two conditions at the electrolyte/electrode boundary were evaluated. Assuming that the bulk electrolyte is well mixed we have $C_i(0) = C_i^\infty$ and

$$\nabla \Psi = -\frac{I}{\kappa'} + \frac{F}{\kappa^o} \left[D_{CO_3^-} \nabla C_{CO_3^-} + D_{HCO_3^-} \nabla C_{HCO_3^-} + D_{OH^-} \nabla C_{OH^-} - D_{K^+} \nabla C_{K^+} \right] \quad (6-40)$$

For a finite rate of mass transfer into the bulk, Equation 6-40 will still hold but the interfacial transport of the ions is also subjected to the condition

$$D_i \nabla C_i = h_{mt} [C_i(0) - C_i^\infty] \quad (6-41)$$

where h_{mt} is the mass-transfer coefficient. The details of the numerical solution of these equa-

tions and boundary conditions in dimensionless form are given in Appendix B.

6.3.2. Parameter Estimation

Oxygen and electrolyte diffusion parameters for 2.0 and 4.0 M K_2CO_3 electrolyte were listed in Table 6-1. The O_2 solubilities were calculated from Equation 4-8 and the O_2 diffusivities were calculated using this solubility with the measured value of the Levich slope reported in Table 4-5. Exchange current densities and Tafel slopes were obtained from Chapter 4 kinetic data. Electrode structural parameters were obtained from the fit of KOH data discussed in Section 6.2.2. The apparent dissociation constants, K_{II}^{app} , were estimated from the activity data as discussed in Appendix A. Ionic diffusivity ratios were estimated following the suggestions of Winnick et al. (118) with viscosity data from their work with Cs_2CO_3 . The uncertainty in these transport parameters led us to invoke the Nernst-Einstein equation and use only one diffusivity ratio, $D_i/D_{CO_3^-}$ for $i = OH^-$, HCO_3^- , and K^+ . The electrolyte conductivity was measured at room temperature with a Wayne-Kerr self-balancing conductivity bridge and a dipping conductivity cell from Yellow Springs Instr. Co. This leaves no adjustable parameters.

6.3.3. Results and Discussion

The calculated performance curves are compared with the experimental data from Chapter 5 in Figures 6-5a and 6-5b for 2.0 and 4.0 M K_2CO_3 , respectively. Case 2 for the 2 M fit was calculated with a value of i_0 obtained from the low-current supported-electrode data. The model predicts a transition to the double-Tafel slope at much lower current densities than in the pure KOH, but not quite as low as those experimentally observed in the carbonates. The superior fit of the 2 M data, as compared to 4 M, could be due to the fact that the electrode was wetted more completely by this electrolyte.

Current distribution profiles are shown in Figure 6-6 for the two concentrations (case 2 for 2 M) at several values of applied current density. Except for the very front of the electrode,

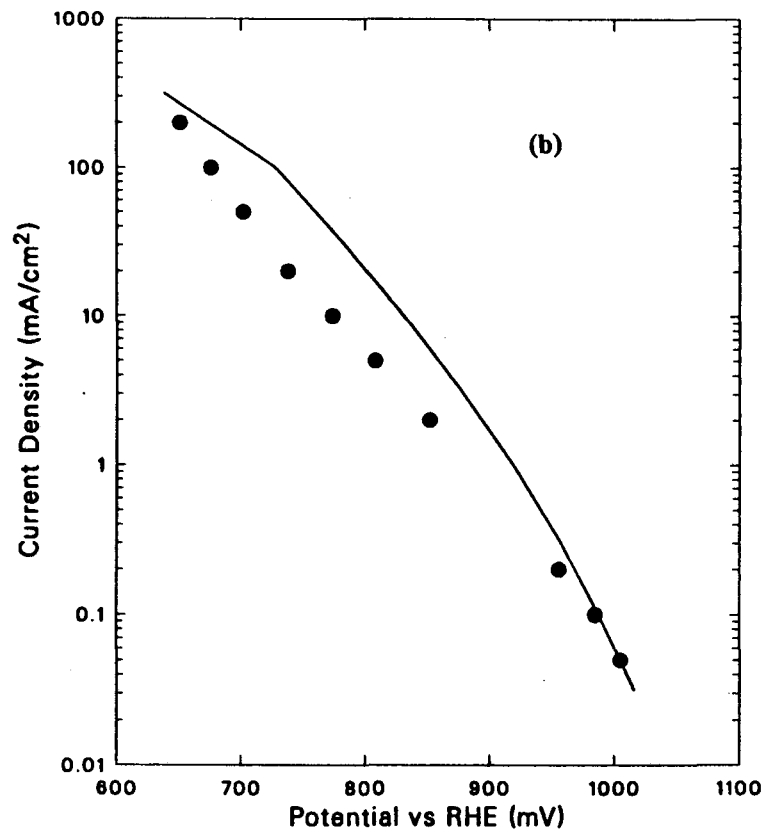
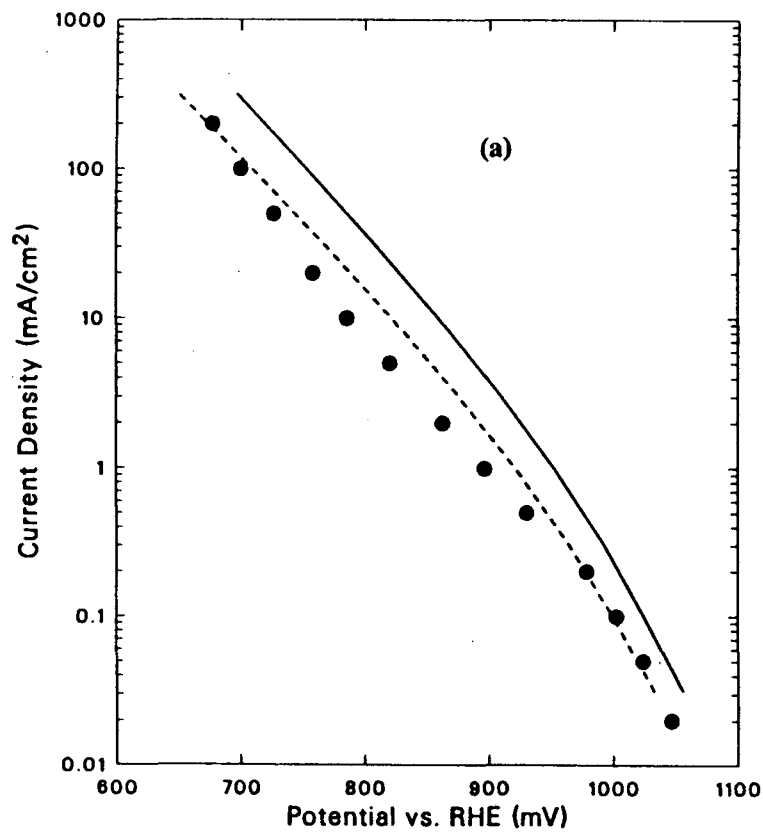


Figure 6-5: Comparison between steady-state model and observed performance behavior for a Prototech electrode K_2CO_3 with 100% O_2 .
 (a) 2M K_2CO_3 (P29), (b) 4M K_2CO_3 (P20).
 •, data;
 —, Model with i_0 from kinetic data in Chapter 4;
 - - - -, Model with i_0 from supported data.

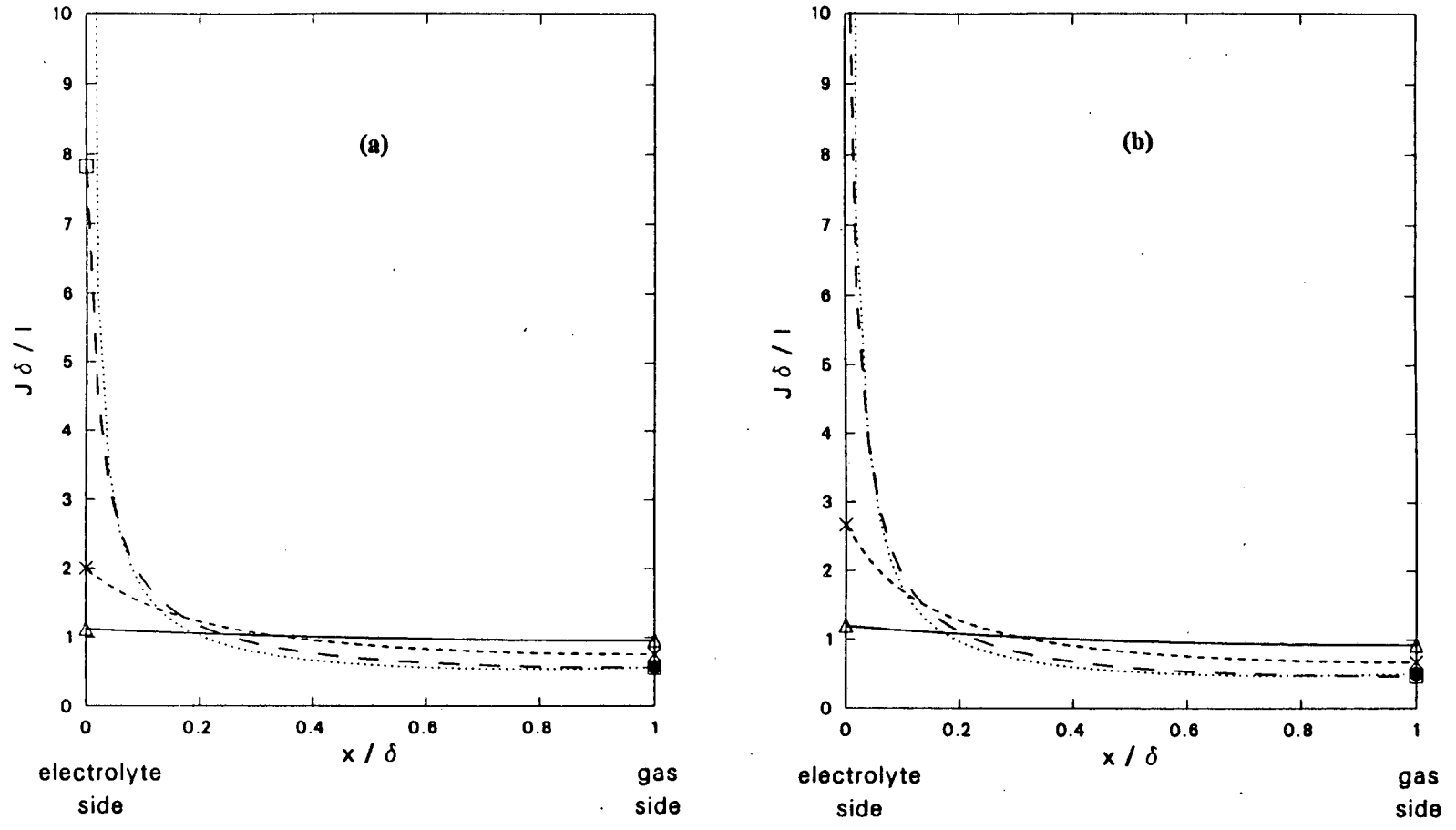


Figure 6-6: Predicted current density profiles from K_2CO_3 model.
(a) 2M K_2CO_3 , (b) 4M K_2CO_3 .
— Δ , $I = 0.1 \text{ mA/cm}^2$,
- - - \times , $I = 1 \text{ mA/cm}^2$,
- · - \square , $I = 10 \text{ mA/cm}^2$,
· · · · \bullet , $I = 100 \text{ A/cm}^2$.

- XBL 8711-4721 -

current is distributed fairly evenly throughout, in contrast to that predicted for the KOH electrode in Figure 6-4. These curves suggest that electrode structure could be optimized with a thinner active layer, effectively producing a shorter diffusion path in the liquid phase.

Calculated ionic concentration profiles are shown for the 2 M electrolyte in Figure 6-7. The hydroxide ion concentration at the gas-supply side reaches a value of $132\times$ the bulk value of 0.017 M at a current density of only 100 mA/cm². The average hydroxide ion concentration (over the electrode) at this current is $95\times$ or 1.6 M. If changes in the activity coefficients are neglected, this corresponds to a pH change of 2 units or 120 mV, which can be compared with the 160 mV shift between the low current potentials in the hysteresis experiment shown in Figure 5-16 for 2 M K₂CO₃.

The general behavior of the model is investigated for 2 M K₂CO₃, in Appendix B, by varying input values for the dimensionless parameters. The "base case" values were calculated with the parameters in Table 6-1 (case 2). Table B-4 shows the parameter ranges investigated. The electrolyte resistance shows the greatest influence on electrode performance, as expected for an ionic mass-transfer-limited process. Use of the finite mass-transfer boundary condition was also investigated in Appendix B. The low current data for 4 M K₂CO₃ could be fit with this parameter at the expense of predicting a premature limiting current due to OH⁻ transport. In the electrode, the observed limiting currents were probably abnormally high due to the increase in electrode wetting as the hydroxide concentration of the local electrolyte increased.

Finally, the effect of O₂ pressure was calculated to result in a half-order dependence at moderate current densities, as observed in Chapter 5 and as concluded by Ross (90) for the mathematically-similar problem in H₃PO₄.

6.4. Conclusions and Recommendations

We have constructed steady-state models for the 100% O₂ cathode in KOH and K₂CO₃ electrolytes, including expressions for ionic transport in dilute electrolytes and ohmic conduction in the solid phase. The KOH model was used to fit data in 30% KOH with reasonable values for

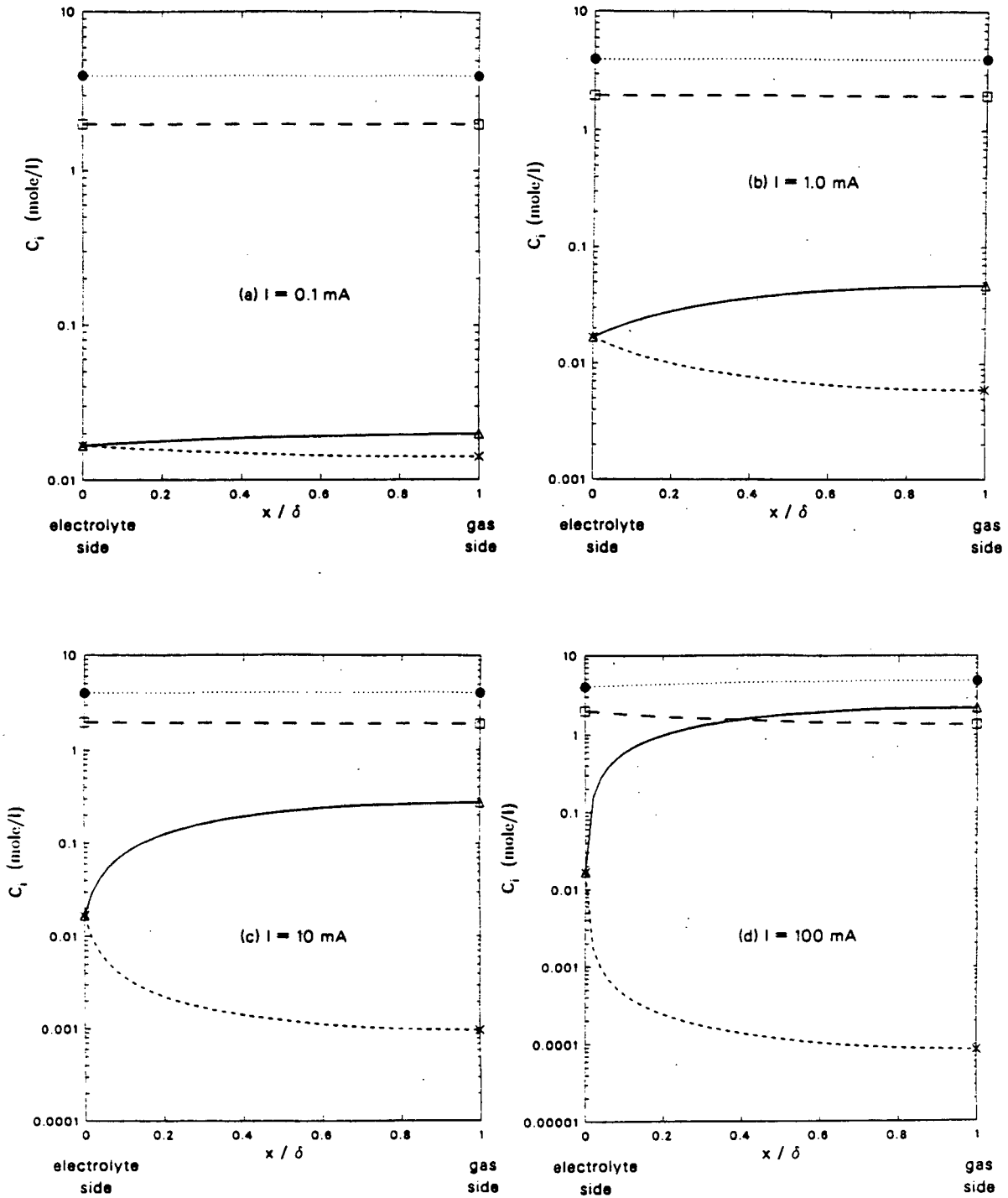


Figure 6-7: Ionic concentration profiles from model for 2M K_2CO_3 , 100% O_2 .

- Δ , C_{OH^-} ;
- \times , $C_{\text{HCO}_3^-}$;
- \square , $C_{\text{CO}_3^{2-}}$;
- \bullet , C_{K^+} .

the electrode structural parameters.

The carbonate electrolyte model successfully predicts the low-current transition to the double-Tafel slope region and the half-order dependence on O_2 partial pressure that are observed experimentally. Calculated performance curves agree remarkably well with the data for 2 and 4 M K_2CO_3 electrolytes, especially considering there are *no adjustable parameters* and the variation in the data due to variable degrees of wetting.

Calculated current and ionic concentration distributions indicate that a thinner active layer and/or a smaller liquid diffusion pathway would improve electrode performance. Performance would also be improved with a higher effective electrolyte conductivity which would result from a more open structure in the catalyst (agglomerate) particles. Changes in the size of the agglomerate particles should not have much effect on performance.

The hysteresis phenomenon discussed in Chapter 5 cannot be predicted by a steady state model of this type. It is most likely a result of the variation of the extent of electrode wetting with electrolyte composition.

Nomenclature

Roman

a	activity
a_o	Pt area per unit electrode area
A	area (cm^2)
A°	geometric constant, Equation 4-2
b	Tafel slope (mV/decade)
B	variable wetting function, ch6
C	concentration (mole/ cm^3 or mole/liter)
C_{dl}	double layer capacity (F/cm^2)
D	diffusion coefficient (cm^2/sec)
e_o	electron charge
E	potential vs. RHE (volts)
F	Faraday (96,487 C/equiv)
f	heterogeneity factor
ΔG_θ	Gibbs free energy for adsorption (Joule/mole)
h_{mt}	mass transfer coefficient (cm/sec)
H	Henry's law constant (mole/cc-atm)
I	current (A)
I_o	ionic strength (mole/liter)
i	current density (A/cm^2)
i_o	exchange current density (A/cm^2)
i_d	measured disk current density (mA/cm^2)
i_d^*	corrected disk current density, Eqn. 2-17 (mA/cm^2)
i_k	kinetic current density (mA/cm^2)

i_k°	normalized kinetic current density (mA/cm ²)
$i_k^{\circ*}$	normalized corrected kinetic current density (mA/cm ²)
i_L	mass-transfer limited current density (A/cm ²)
i_L	ch6, current density in liquid phase (A/cm ²)
J_1, J_2	intercepts of plots 1 and 2, ch4
\bar{J}	Interfacial current per unit vol. (A/cm ³)
K_{II}^{app}	apparent equilibrium constant
k_b	Boltzmann constant, 1.381×10^{-23} J/K
k_c	chemical rate constant (cm/sec)
k_d	rate constant for diffusion (cm/sec)
k_1, k_2 etc	potential-dependent rate constants (cm/sec)
k'	effective reaction parameter, ch.6 (A/cm ³)
L	function defined by Equation B-34
m_i	molality (mole/kg)
M_i	molecular weight (g/mole)
n	number of electrons
N	flux (mole/cm ² -sec)
N_c	collection efficiency
p	partial pressure (atm)
q_i	thermodynamic reaction order
Q	charge (mC)
Q_h°	charge due to a monolayer of hydrogen on Pt ($\mu\text{C}/\text{cm}^2\text{Pt}$)
r	radial coordinate
R	gas constant (J/mole-K)
R_p	particle radius (cm)
R_w	agglomerate radius to which wetting has occurred (cm)
R_{Ω}	uncompensated solution resistance (Ω)

S_1, S_2	slopes of plots 1 and 2, ch4
s_i	reaction order
t	time (sec)
T	temperature (K)
u	ionic mobility ($\text{cm}^2\text{-mole/J-sec}$)
v	potential sweep rate (volts/sec)
V	potential vs. SHE (volts)
W_C	Carbon loading (mg/cm^2)
W_{PTFE}	PTFE loading (mg/cm^2)
W_{Pt}	Pt loading (mg/cm^2)
x	distance coordinate
Z_1	Dimensionless liquid conductivity ratio, $i_{o,a_0}\delta F/\kappa RT$, ch6
Z_s	Dimensionless solid conductivity ratio, $i_{o,a_0}\delta F/\sigma RT$, ch6
z	multiple of electron charge

Greek

α	transfer coefficient
β_e	symmetry factor, for electron transfer process
β_a	symmetry factor, for electroadsorption process
γ	activity coefficient
δ	electrode thickness (cm)
ϵ_a	agglomerate porosity
ϵ_e	electrode porosity
ϵ_d	dielectric constant
κ	electrolyte conductivity ($\Omega^{-1}\text{cm}^{-1}$)
λ	$(D_- - D_+)u_+/(u_+D_- + u_-D_+)$, Appendix B
θ	coverage

μ	viscosity (g/cm-sec)
ν	kinematic viscosity (cm ² /sec)
ρ	density (g/cm ³)
ρ_C	density of carbon, 2.0 g/cc
ρ_{PTFE}	density of PTFE, 2.7 g/cc
σ	matrix conductivity ($\Omega^{-1}\text{cm}^{-1}$)
ϕ	Theile Modulus
Φ_L	potential in liquid (volts)
Φ_S	potential in solid (volts)
τ_a	agglomerate tortuosity factor
ω	rotation rate (rad/sec)
ξ_i	$0.62D_i^{2/3}\nu_i^{-1/6}$, Eqn. 2-9
ζ	Thiele coefficient, Equation 6-7
ζ^*	ζR_p , Dimensionless Thiele coefficient

Subscripts

ads	adsorption
c	cathodic
d	disk, diffusion
h	hydride
k	kinetic
m	measured
n	nominal
L	limiting or liquid phase
ox	oxide
p	peak
r	ring

ref	reference
w	water

Species

1	O_2
2	HO_2^-
3	OH^-
4	HCO_3^-
6	CO_3^{2-}
7	K^+

Superscripts

*	dimensionless variable
‡	activation
eq	equilibrium
∞	at bulk conditions
o	at $x = 0$, or standard state

Abbreviations

A	anodic profile, Figure 4-10
AFC	alkaline fuel cell
C1	first cathodic profile, Figure 4-10
C2	second cathodic profile, Figure 4-10
FEP	fluorinated ethylenepropylene
GDE	gas-diffusion electrode
HA1	first anodic hydrogenation peak
HA2	second anodic hydrogenation peak
ICEV	internal combustion engine vehicle

OA1	first anodic oxidation peak
OA2	second anodic oxidation peak
OR	oxygen reduction
PAFC	phosphoric acid fuel cell
PTFE	polytetrafluoroethylene
RDE	rotating disk electrode
RHE	reversible hydrogen electrode
RRDE	rotating ring-disk electrode
rds	rate determining step
SCE	saturated calomel electrode
SEM	scanning electron microscopy
SHE	standard hydrogen electrode
SPEFC	solid polymer electrolyte fuel cell
TFEDSA	tetrafluoroethane-1,2-disulfonic acid
TFMSA	trifluoromethane sulfonic acid
TEM	transmission electron microscopy
WE	working electrode

References

1. S. S. Penner, "Assessment of Research Needs for Advanced Fuel Cells," *Int'l. J. Energy* **11**, (1986).
2. B. D. McNichol and D. A. J. Rand, *Power Sources for Electric Vehicles*, Elsevier, Amsterdam, The Netherlands, 1984.
3. E. J. Cairns and D. C. Bartosik, "A Methanol Fuel Cell with an Invariant Alkaline Electrolyte," *J. Electrochem. Soc.* **111**, 1205 (1964).
4. M. R. Tarasevich, A. Sadkowski and E. Yeager, "Oxygen Electrochemistry," in *Comprehensive Treatise of Electrochemistry*, vol. 7, J. O'M Bockris, B. E. Conway, E. Yeager, S. U. M. Khan and R. E. White, eds., Plenum Publishing Corporation, New York, 1983.
5. J. Newman, *Electrochemical Systems*, Prentice-Hall, Englewood Cliffs, 1973, page 217.
6. B. V. Tilak, B. E. Conway and H. Angerstein-Kozłowska, "The Real Condition of Oxidized Pt Electrodes, Part III. Kinetic Theory of Formation and Reduction of Surface Oxides," *J. Electroanal. Chem.* **48**, 1 (1973).
7. S. B. Brummer, J. Ford and M. J. Turner, "The Adsorption and Oxidation of Hydrocarbons on Noble Metal Electrodes I. Propane Adsorption on Smooth Platinum Electrodes," *J. Phys. Chem.* **69**, 3424 (1965).
8. V. S. Bagotski and M. Tarasevich, "Oxygen Adsorption on Platinum Metals, Part I. Investigation of the Adsorption Mechanism by the Potentiodynamic Method," *J. Electroanal. Chem.* **101**, 1 (1979).
9. A. K. N. Reddy, M. A. Genshaw and J. O'M. Bockris, "Ellipsometric Study of Oxygen-Containing Films on Platinum Anodes," *J. Chem. Phys.* **48**, 671 (1968).

10. A. Damjanovic, L.-S. R. Yeh and J. Wolf, "Formation of Oxide Films at Platinum Anodes in Alkaline Solutions, Part I. Question of Kinetics and Mechanisms," *J. Electrochem. Soc.* **127**, 1945 (1980).
11. K. J. Vetter and J. W. Schultze, "The Kinetics of the Electrochemical Formation and Reduction of Monomolecular Oxide Layers on Platinum in 0.5M H₂CO₃, Part I. Potentiostatic Pulse Measurements," *J. Electroanal. Chem.* **34**, 131 (1972).
12. D. Gilroy and B. E. Conway, "Surface Oxidation and Reduction of Platinum Electrodes: Coverage, Kinetic and Hysteresis Studies," *Can. J. Chem.* **46**, 875 (1968).
13. P. N. Ross, "Structure Sensitivity in the Electrocatalytic Properties of Platinum," *J. Electrochem. Soc.* **126**, 78 (1979).
14. H. Angerstein-Kozłowska, B. E. Conway and W. B. A. Sharp, "The Real Condition of Electrochemically Oxidized Platinum Surfaces, Part I. Resolution of Component Processes," *J. Electroanal. Chem.* **43**, 9 (1973).
15. Y. B. Vassiliev, V. S. Bagotski and V. A. Gromyko, "Kinetics and Mechanism of the Formation and Reduction of Oxide Layers on Platinum, Part I. Oxidation and Reduction Platinum Electrodes," *J. Electroanal. Chem.* **178**, 247 (1984).
16. D. B. Sepa, M. J. Vojnovic, and A. Damjanovic, "Reaction Intermediates as a Controlling Factor in the Kinetics and Mechanism of Oxygen Reduction at Platinum Electrodes," *Electrochim. Acta* **26**, 781 (1981).
17. A. J. Bard and L. R. Faulkner, *Electrochemical Methods*, John Wiley and Sons, New York, 1980, p.409.
18. Yu. V. Pleskov and V. Yu. Filinovskii, *The Rotating Disk Electrode*, Consultants Bureau, New York, p.90 (1976).
19. L. Muller and L. Nekarosov, "Untersuchung des Elektrochemischen Reduktionsprozesses von Sauerstoff an Platin mit der Rotierenden Scheibenelektrode mit Ring," *Electrochim.*

- Acta* **9**, 1015 (1964).
20. V. S. Bagotskii, M. R. Tarasevich, and V. Yu. Filinovskii, "Allowance for the Adsorption Stage in the Calculation of Kinetic Parameters for the Reactions of Oxygen and Hydrogen Peroxide," *Elektrokhim.* **8**, 84 (1972).
 21. K.-L. Hsueh and D.-T. Chin, "Electrode Kinetics of Oxygen Reduction, A Theoretical and Experimental Analysis of the Rotating Ring-Disk Electrode Method," *J. Electroanal. Chem.* **153**, 79 (1983).
 22. A. Damjanovic, M. A. Genshaw, and J. O'M. Bockris, "Distinction Between Intermediates Produced in Main and Side Electrode Reactions," *J. Chem. Phys.* **45**, 4057 (1966).
 23. A. J. Appleby and M. Savy, "Kinetics of Oxygen Reduction Reactions Involving Catalytic Decomposition of Hydrogen Peroxide, Application to Porous and Rotating Ring-Disk Electrodes," *J. Electroanal. Chem.* **92**, 15 (1978).
 24. J. D. E. McIntyre, "The Kinetics of Electrode Processes with Coupled Heterogeneous Chemical Catalytic Reactions," *J. Phys. Chem.* **71**, 1196 (1967).
 25. P. K. Adanuvor and R. E. White, "Simulation of the Polarization Curves of Oxygen Reduction at a Rotating Disk Electrode," *J. Electrochem. Soc.* **134**, 1093 (1987).
 26. K.-L. Hsueh, H. H. Chang, D.-T. Chin and S. Srinivasan, "Electrode Kinetics of Oxygen Reduction on Platinum in Trifluoromethane Sulfonic Acid," *Electrochim. Acta* **30**, 1137 (1985).
 27. A. Damjanovic, M. A. Genshaw, and J. O'M. Bockris, "The Role of Hydrogen Peroxide in Oxygen Reduction at Platinum in H₂SO₄ Solution," *J. Electrochem. Soc.* **114**, 466 (1967).
 28. D. B. Sepa, M. J. Vojnovic, and A. Damjanovic, "Kinetics and Mechanism of O₂ Reduction at Pt in Alkaline Solutions," *Electrochim. Acta* **25**, 1491 (1980).
 29. E. Yeager, "Electrocatalysts for O₂ Reduction," *Electrochim. Acta* **29**, 1527 (1984).

30. P. Fischer and J. Heitbaum, "Mechanistic Aspects of Cathodic Oxygen Reduction," *J. Electroanal. Chem.* **112**, 231 (1980).
31. M. M. Ghoneim, S. Clouser and E. Yeager, "Oxygen Reduction Kinetics in Deuterated Phosphoric Acid," *J. Electrochem. Soc.* **132**, 1160 (1985).
32. V. I. Luk'yanycheva, A. V. Yuzhanina, B. I. Lentsner, L. L. Knots, N. A. Shumilova and V. S. Bagotskii, "The State of the Adsorbed Oxygen and its Effect on the Mechanism of Molecular Oxygen Reduction at a Platinum Electrode in an Alkaline Solution," *Elektrokhim.* **7**, 1287 (1971).
33. D. B. Sepa, M. J. Vojnovic, Lj. M. Vracar and A. Damjanovic, "Different Views Regarding the Kinetics and Mechanisms of Oxygen Reduction at Pt and Pd Electrodes," *Electrochim. Acta* **32**, 129 (1987).
34. J. O'M Bockris and A. K. N. Reddy, *Modern Electrochemistry*, Plenum Press, New York, 1970, Chapter 9.
35. A. Damjanovic, M. A. Genshaw, and J. O'M. Bockris, "The Mechanism of Oxygen Reduction at Platinum in Alkaline Solutions with Special Reference to H_2O_2 ," *J. Electrochem. Soc.* **114**, 1107 (1967).
36. M. Appel and A. J. Appleby, "Contribution a L'Etude de L'Electrode a Oxygene sur Platine en Milieu Alcalin," *Comp. Rend. Acad. Sc., Paris*, **280** 551 (1975).
37. R. J. Bowen and H. B. Urbach "Dynamic Behavior of the Oxygen-Peroxide Couple on Platinum," *J. Chem. Phys.* **49**, 1206 (1968).
38. S. M. Park, S. Ho, S. Aruliah, M. Weber, C. Ward, R. Venter, and S. Srinivasen, "Electrochemical Reduction of Oxygen at Platinum Electrodes in KOH Solutions, Temperature and Concentration Effects," *J. Electrochem. Soc.* **133**, 1641 (1986).
39. M. R. Tarasevich and V. A. Bogdanovskaya, "Influence of the State of Platinum Electrode Surface on Electroreduction of Molecular Oxygen, I. Oxidation of Electrode by Anodic

- Polarization," *Elektrokhim.* **7**, 1072 (1971).
40. V. S. Bagotskii, V. I. Luk'yanycheva and S. H. Leites, "Effect of Solution pH on the Kinetic Parameters of Molecular Oxygen Reduction at Smooth Platinum Electrodes with Different Surface States," *Elektrokhim.* **14**, 159 (1978).
 41. V. I. Luk'yanycheva, A. V. Yuzhanina, M. R. Tarasevich, N. A. Shumilova and V. S. Bagotskii, "Molecular Oxygen Reduction Kinetics at Preoxidized Platinum Electrodes in Alkaline Solutions," *Elektrokhim.* **13**, 506 (1977).
 42. V. I. Luk'yanycheva, A. V. Yuzhanina, N. A. Shumilova and V. S. Bagotskii, "Influence of Chemisorption Processes on the Kinetics of the Reduction of Molecular Oxygen and Other Reactions on Platinum, I. Effect of Chemisorbed Oxygen on the Kinetic Parameters of the Reduction of Molecular Oxygen at the Platinum Electrode in Alkaline Solution," *Elektrokhim.* **12**, 952 (1976).
 43. A. J. Appleby, "Oxygen Reduction on Active Platinum in 85% Orthophosphoric Acid," *J. Electrochem. Soc.* **117**, 641 (1970).
 44. J. C. Huang, R. K. Sen and E. Yeager, "Oxygen Reduction on Platinum in 85% Orthophosphoric Acid," *J. Electrochem. Soc.* **126**, 786 (1979).
 45. B. E. Conway and D. J. MacKinnon, "Interpretation and Significance of Heats of Adsorption for Electrochemical Reactions Exhibiting Anomalous Tafel Slopes," *J. Electrochem. Soc.* **116**, 1665 (1969).
 46. D. B. Sepa, M. J. Vojnovic, M. Stojanovic and A. Damjanovic, "Anomalous Transfer Coefficients for Oxygen Reduction at Iridium," *J. Electrochem. Soc.* **134**, 845 (1987).
 47. B. E. Conway, D. J. MacKinnon, and B. V. Tilak, "Significance of Electrochemical Bronsted Factors, Kinetic Studies over a Wide Temperature Range," *Trans. Farad. Soc.* **66**, 1203 (1970).

48. E. Yeager, "Dioxygen Electrocatalysis: Mechanisms in Relation to Catalyst Structure," *J. Mol. Cat.* **38**, 5 (1986).
49. D. B. Sepa, M. J. Vojnovic, Lj. M. Vracar and A. Damjanovic, "Apparent Enthalpies of Activation of Electrode Oxygen Reduction at Pt in Different Current Density Regions-I. Acid Solution," *Electrochim. Acta* **31**, 91 (1986).
50. D. B. Sepa, M. J. Vojnovic, Lj. M. Vracar and A. Damjanovic, "Apparent Enthalpies of Activation of Electrode Oxygen Reduction at Pt in Different Current Density Regions-II. Alkaline Solution," *Electrochim. Acta* **31**, 97 (1986).
51. M. Paucirova, D. M. Drazic, and A. Damjanovic, "The Effect of Surface Coverage by Adsorbed Oxygen on the Kinetics of Oxygen Reduction at Oxide Free Platinum," *Electrochim. Acta* **18**, 945 (1973).
52. K. F. Blurton and E. McMullin, "A Comparison of Fuel Cell Performance in Acid and Alkaline Electrolyte," *Energy Conversion* **9**, 141 (1969).
53. K. F. Blurton and E. McMullin, "The Cathodic Reduction of Oxygen on Platinum in Alkaline Solution," *J. Electrochem. Soc.* **116**, 1476 (1969).
54. A. J. Appleby, *Proc. Renewable Fuels and Advanced Power Sources for Transportation Workshop*, 55 (1982).
55. B. Baker, *Final Technical Report*, U.S. Army Mobility Equipment Research and Development Command, Contract No. DAAK02-73-C-0084, 1984.
56. P. N. Ross, "Evaluation of Tetrafluoroethane-1,2-Disulfonic Acid as a Fuel Cell Electrolyte," *J. Electrochem. Soc.* **130**, 882 (1983).
57. A. Damjanovic and V. Brusic, "Electrode Kinetics of Oxygen Reduction on Oxide-Free Platinum Electrodes," *Electrochim. Acta* **212**, 615 (1967).
58. A. J. Appleby, "Oxygen Reduction on Oxide-Free Platinum in 85% Orthophosphoric Acid: Temperature and Impurity Dependence," *J. Electrochem. Soc.* **117**, 328 (1970).

59. Y. Ya. Shepelev, M. R. Tarasevich and R. L. Burshstein, "Influence of Pressure on O Ionization at a Platinum Electrode, I. Reduction of Oxygen at Oxidized and Reduced Electrodes in Acid and Alkaline Solutions," *Elektrokhim.* **27**, 999 (1971).
60. J. Giner, "A Practical Reference Electrode," *J. Electrochem. Soc.* **111**, 376 (1964).
61. P. N. Ross and P. C. Andricacos, "The Effect of H_2PO_4^- Anion on the Kinetics of Oxygen Reduction on Pt," *J. Electroanal. Chem.* **154**, 205 (1983).
62. E. F. G. Herington, *Zone Melting of Organic Compounds*, Wiley, New York, 1963.
63. P. C. Andricacos and P. N. Ross, E.P.R.I. Report No. 1676-02, June 1982.
64. A. J. Appleby and B. S. Baker, "Oxygen Reduction on Pt in Trifluoromethane Sulfonic Acid," *J. Electrochem. Soc.* **125**, 404 (1978).
65. W. E. O'Grady, S. Srinivasan, and R. F. Dudley, *The Electrocatalysis of Fuel Cell Reactions*, in The Electrochemical Society Symposium Proceeding Series, The Electrochemical Society, Princeton, New Jersey (1978).
66. J. C. Huang, W. E. O'Grady and E. Yeager, "The Effect of Cations and Anions on Hydrogen Chemisorption on Pt," *J. Electrochem. Soc.* **124**, 1732 (1977).
67. H. Angerstein-Kozłowska, B. E. Conway B. Barnett and J. Mozota, "The Role of Ion Adsorption in Surface Oxide Formation and Reduction at Noble Metals: General Features of the Surface Process," *J. Electroanal. Chem.*, **100**, 417 (1973).
68. N. V. Osetrova, Y. B. Vasil'ev and V. S. Bagotskii, "Effect of pH on CO_2 Adsorption on Smooth Platinum Electrodes," *Elektrokhim.* **13**, 512 (1977).
69. J. Giner, "Electrochemical Reduction of Carbon Dioxide with Hydrogen Chemisorbed on a Platinum Electrode," *Electrochim. Acta* **8**, 857 (1963).
70. J. O'M. Bockris and A. K. N. Reddy, *Modern Electrochemistry*, Plenum Press, New York, 1970, p.730.

71. J. P. Hoare and R. Thacker, "Sorption of Oxygen from Solution by Noble Metals, I. Bright Platinum," *J. Electroanal. Chem.* **30**, 1 (1971).
72. J. Albery and S. Bruckenstein, "Ring-Disk Electrodes Part 2: Theoretical and Experimental Collection Efficiencies," *Trans. Farad. Soc.* **62**, 1920 (1966).
73. A. Schumpe, I. Adler, and W.-D. Deckwer, "Solubility of Oxygen in Electrolyte Solutions," *Biotech. Bioengr.* **20**, 145 (1978).
74. R. A. Robinson and R. H. Stokes, *Electrolyte Solutions*, Academic Press Inc., New York, 1959.
75. B. Pound, B. Sandararaj, R. P. Singh, and D. Macdonald, "Thermodynamic Framework for Estimating the Efficiency of Alkaline Batteries," Final Report, LBL Report #LBL-16806, October 1983.
76. R. N. Roy, J. J. Gibbons, R. Williams, L. Goodwin, G. Baker, J. Simonsin and K. Pitzer, "The Thermodynamics of Aqueous Carbonate Solutions, II. Mixtures of Potassium Carbonate, Bicarbonate and Chloride," *J. Chem. Thermod.* **16**, 303 (1984).
77. M. Watanabe, private communication, 1985.
78. S. U. Falk and A. J. Salkind *Alkaline Storage Batteries* Wiley, New York, 1969, Chapter 8.
79. K. E. Gubbins and R. D. Walker, "The Solubility and Diffusivity of Oxygen in Electrolytic Solutions," *J. Electrochem. Soc.* **112**, 469 (1965).
80. K. Kordesch, S. Jahangir, and M. Schautz, "Engineering Concepts and Technical Performance of Oxygen-Reducing Electrodes for Batteries and Electrochemical Processes," *Electrochim. Acta* **29**, 1589 (1984).
81. R. Holze and A. Maas, "On the Microstructure of Teflon-Bonded Platinum-Carbon Electrodes," *J. Applied Electrochem.* **13**, 549 (1983).
82. R. Holze and W. Vielstich, "Double-Layer Capacity Measurements as a Method to Characterize Porous Fuel Cell Electrodes," *Electrochim. Acta* **29**, 607 (1984).

83. T. Kenjo and K. Kawatsu, "Current-Limiting Factors and the Location of the Reaction Area in PTFE-Bonded Double-Layered Electrodes," *Electrochim. Acta* **30**, 229 (1985).
84. T. Kenjo and N. Nakajima, "The Polarization Characteristics and Thickness of the Catalyst Layers in Fuel Cell Electrodes," *Bull. Chem. Soc. Jpn.* **56**, 1 (1983).
85. U. Olender, J. McBreen, W. E. O'Grady, and S. Srinivasan, "Design of a Cell for Electrode Kinetic Investigations of Fuel Cell Reactions," *J. Electrochem. Soc.* **129**, 135 (1982).
86. J. Singer and V. Srinivasan, "Evaluation Parameters for the Alkaline Fuel Cell Oxygen Electrode," NASA Tech. Memo 87155, Nov. 1985.
87. M. Watanabe, K. Makita, H. Usami and S. Motoo "New Preparation Method of a High Performance Gas Diffusion Electrode Working at 100% Utilization of Catalyst Clusters and Analysis of Reaction Layer," *J. Electroanal. Chem.* **197**, 195 (1986).
88. M. Watanabe, M. Tomikawa and S. Motoo "Experimental Analysis of the Reaction Layer Structure in a Gas Diffusion Electrode," *J. Electroanal. Chem.* **195**, 81 (1985).
89. H. R. Kunz and G. A. Gruver, "The Catalytic Activity of Platinum Supported on Carbon for Electrochemical Oxygen Reduction in Phosphoric Acid," *J. Electrochem. Soc.* **122**, 1279 (1975).
90. P. N. Ross, "Anomalous Current Ratios in Phosphoric Acid Fuel Cell Cathodes," LBL Report #LBL-13955, March 1986.
91. J. T. Lundquist and P. Stonehart, "Platinum Crystallite Size Effects on Oxide Formation and Reduction Parameters," *Electrochim. Acta* **18**, 349 (1973).
92. M. Peuckert, T. Yoneda, R. A. Dalla Betta and M. Boudart, "Oxygen Reduction on Small Supported Platinum Particles," *J. Electrochem. Soc.* **133**, 944 (1986).
93. J. Bett, J. T. Lundquist, E. Washington and P. Stonehart, "Platinum Crystallite Size Considerations for Electrocatalytic Oxygen Reduction," *Electrochim. Acta* **18**, 343 (1973).

94. W. M. Vogel and J. T. Lundquist "Reduction of Oxygen on Teflon-Bonded Platinum Electrodes," *J. Electrochem. Soc.* **117**, 1512 (1970).
95. W. M. Vogel, J. T. Lundquist and A. Bradford, "Reduction of Oxygen on Teflon-Backed Platinum Black Electrodes," *Electrochim. Acta* **17**, 1735 (1972).
96. K. F. Blurton, P. Greenberg, H. G. Oswin and D. R. Rutt, "The Electrochemical Activity of Dispersed Platinum," *J. Electrochem. Soc.* **119**, 559 (1972).
97. L. J. Bregoli, "The Influence of Platinum Crystallite Size on the Electrochemical Reduction of Oxygen in Phosphoric Acid," *Electrochim. Acta* **23**, 489 (1978).
98. D. Luss, "The Effect of Crystallite Size Distribution on the Specific Activity of Supported Catalysts," *J. Catal.* **23**, 119 (1971).
99. A. J. Appleby and J. Marie, "Kinetics of Oxygen Reduction on Carbon Materials in Alkaline Solution," *Electrochim. Acta* **24**, 195 (1979).
100. J. C. Peiper and K. S. Pitzer, "Thermodynamics of Aqueous Carbonate Solutions Including Mixtures of Sodium Carbonate, Bicarbonate and Chloride," *J. Chem. Thermod.* **14**, 613 (1982).
101. H. Petrow and R. Allen, "Colloidal Platinum Catalyst for Fuel Cells," Belg. Patent 831,297, Prototech Co. assignee, Nov. 1975.
102. M. Watanabe, S. Motoo and M. Furiya "Gas Diffusion Electrode of High Performance," *J. Electroanal. Chem.* **160**, 351 (1984).
103. K. A. Klinedinst, W. M. Vogel and P. Stonehart, "Rheological Characterization and Thermal Degradation of PTFE, Part 2. The Interaction Between PTFE and Carbon Black," *J. Mat. Sci.* **11**, 794 (1976).
104. M. B. Cutlip, S. Yang and P. Stonehart, "Model Development for Porous Gas-Diffusion Electrodes and Application to the Phosphoric Acid Fuel Cell Cathode," *Electrochemical and Thermal Modeling of Battery, Fuel Cell, and Photoenergy Conversion Systems, in The*

- Electrochemical Society Symposium Proceeding Series, vol. 86-12, The Electrochemical Society, Princeton, New Jersey (1978).
105. Handbook of Chemistry and Physics, Chemical Rubber Co., 46th Ed., Cleveland, Ohio, 1964, p. F-106.
 106. J. Randin and E. B. Yeager, "Differential Capacitance Study on the Edge Orientation of Pyrolytic Graphite and Glassy Carbon Electrodes," *J. Electroanal. Chem.* **58**, 313 (1975).
 107. M. Hossain, "Oxygen Reduction on Carbon and Modified Carbon Surfaces," Dissertation, Case Western Res. Univ., May 1986.
 108. D. M. Kern, "The Hydration of Carbon Dioxide," *J. Chem. Educ.* **37**, 14 (1960).
 109. K. A. Striebel, F. R. McLarnon and E. J. Cairns, "The Effect of Carbonate Anions on the Reduction of Oxygen at Platinum Electrodes in Dilute Alkaline Electrolytes," Abstract No. 658, 167th Meeting of the Electrochem. Soc., Toronto, Canada, May 1985.
 110. E. A. Grens, R. M. Turner and T. Katan, "A Model for the Analysis of Porous Gas Electrodes," *Adv. En. Conv.* **4**, 109 (1964).
 111. J. O'M. Bockris and B. D. Cahan, "Effect of Finite-Contact-Angle Meniscus on Kinetics in Porous Electrode Systems," *J. Chem. Phys.* **50**, 1307 (1969).
 112. R. Darby, "A Comparison of Several Models for Porous Gas-Diffusion Electrodes," *Adv. En. Conv.* **5**, 43 (1965).
 113. D. N. Bennion and C. W. Tobias, "Current Distribution at a Gas-Electrode-Electrolyte Interface, II. Theoretical Treatment," *J. Electrochem. Soc.* **113**, 593 (1966).
 114. J. Giner and C. Hunter, "The Mechanism of Operation of the Teflon-Bonded Gas Diffusion Electrode: A Mathematical Approach," *J. Electrochem. Soc.* **116**, 1124 (1969).
 115. R. P. Iczkowski and M. B. Cutlip, "Voltage Losses in Fuel Cell Cathodes," *J. Electrochem. Soc.* **127**, 1433 (1980).

116. M. B. Cutlip, S. Yang and P. Stonehart, "Model Development for Porous Gas-Diffusion Electrodes and Application to the Phosphoric Acid Fuel Cell Cathode," *Electrochemical and Thermal Modeling of Battery, Fuel Cell, and Photoenergy Conversion Systems*, in The Electrochemical Society Symposium Proceeding Series, vol. 86-12, The Electrochemical Society, Princeton, New Jersey (1986).
117. L. Hsueh and J. Newman, "The Role of Bisulfate Ions in Ionic Migration Effects," *Ind. Eng. Chem. Fund.* **10**, 615 (1971).
118. C. H. Lin and J. Winnick, "An Electrochemical Device for Carbon Dioxide Concentration, II. Steady-State Analysis. CO₂ Transfer," *Ind. Eng. Chem. Process Des. Develop.* **13**, 63 (1974).
119. G. Kortüm, *Treatise on Electrochemistry*, Elsevier, Amsterdam, The Netherlands, 1965.
120. J. Newman, "Numerical Solution of Coupled, Ordinary Differential Equations," *Ind. Eng. Chem. Fund.* **7**, 514 (1968).

Appendix A

Thermodynamic Properties of KOH and K_2CO_3

There are many sources of thermodynamic data for aqueous KOH over a wide range of temperatures and concentrations (74,75). The only source of thermodynamic data for K_2CO_3 which takes into account the dissociation of this electrolyte into carbonate and bicarbonate ions is the recent work of Pitzer's group (76,100). They report calculated values for the molalities, mean molal activity coefficients of KOH, $KHCO_3$, and K_2CO_3 and water activities for a wide range of nominal salt concentrations of K_2CO_3 and $KHCO_3$. These calculations are based on Pitzer's mixed electrolyte theory and potential measurements on the cell



The pH values reported in Figure 5-1 were calculated with the following expressions and the assumption that $K_w = 10^{-14}$ mole²/liter²

$$\text{pH} = -\log_{10} a_{\text{H}^+} \quad (\text{A-2})$$

and

$$a_{\text{H}^+} = \frac{K_w a_w}{m_{\text{OH}^-} \gamma_{\text{KOH}}} \quad (\text{A-3})$$

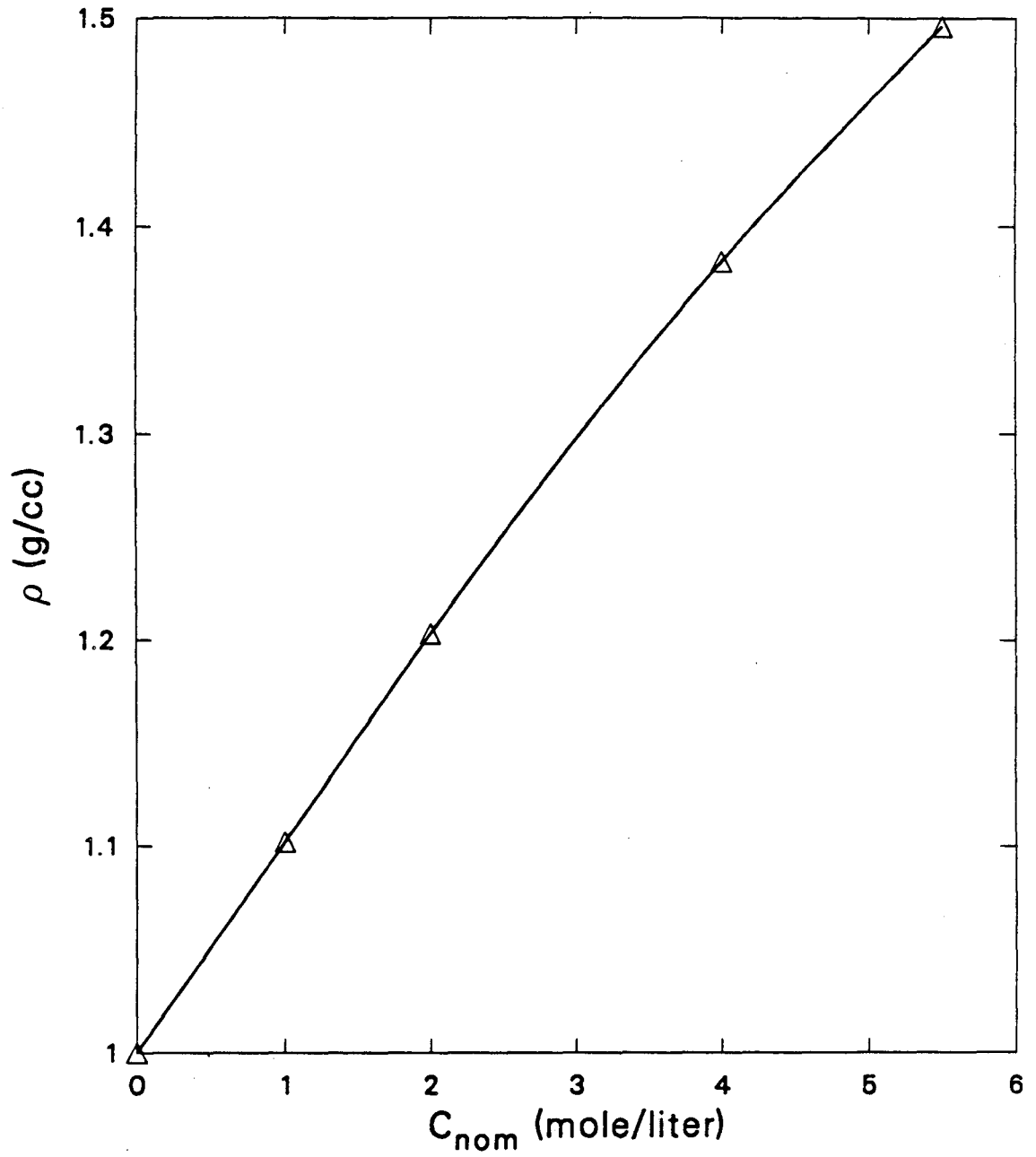
The apparent dissociation constant for the dissociation of carbonate into bicarbonate and hydroxide (Equation 6-33) is defined in terms of concentrations:

$$K_{\text{II}}^{\text{app}} = \frac{C_{\text{CO}_3^{2-}}}{C_{\text{OH}^-} C_{\text{HCO}_3^-}} = \frac{K_{\text{II}} f_{\text{KOH}} f_{\text{KHCO}_3}}{K_w f_{\text{K}_2\text{CO}_3}} \quad (\text{A-4})$$

where K_{II} is the literature value for the dissociation of HCO_3^- into H^+ and CO_3^{2-} ($K_{\text{II}} = 4.69 \times 10^{-11}$ lit/mol), and f_i are the mean molar activity coefficients. The terms f_i and γ_i are related by

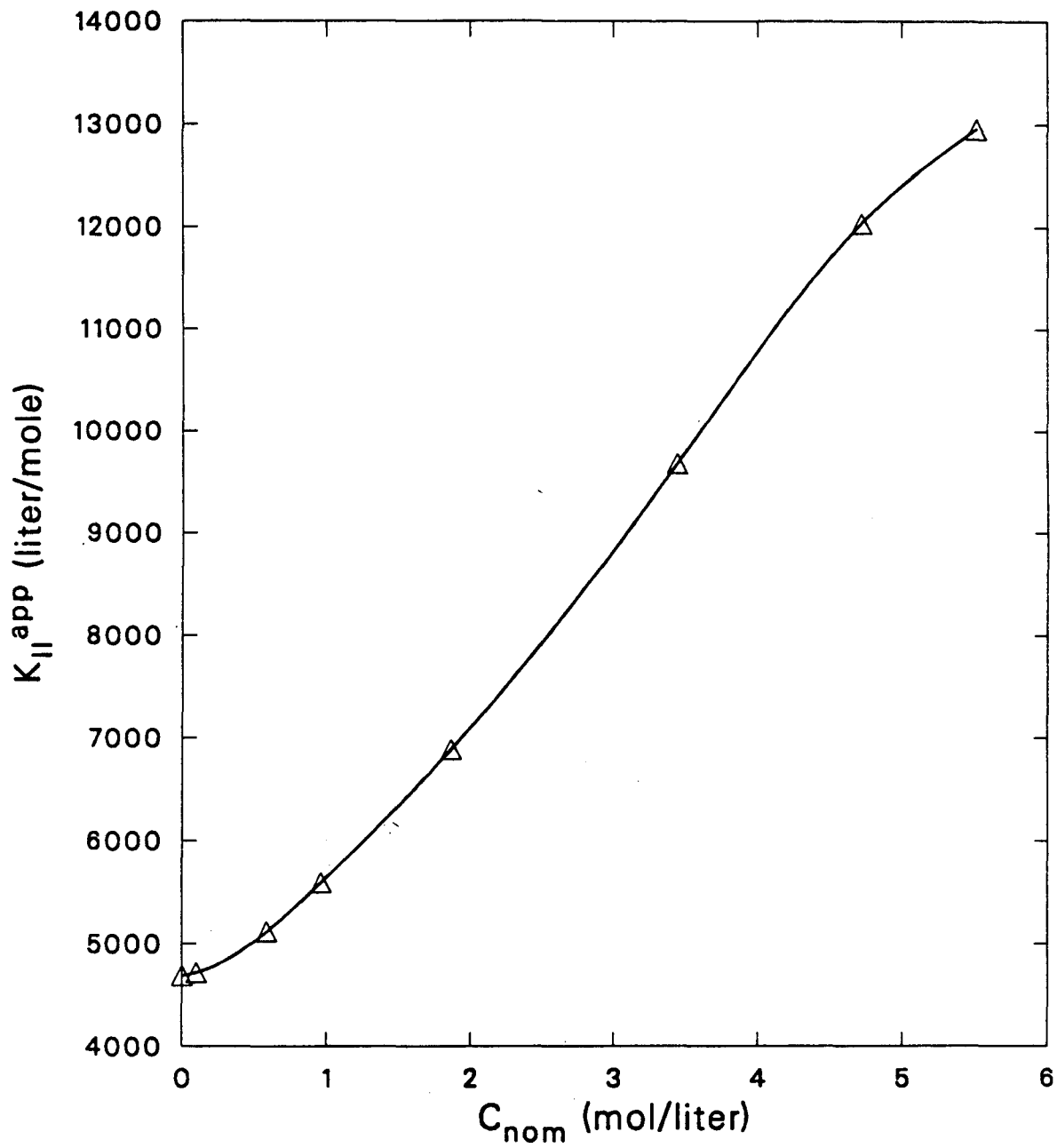
$$f_{\pm} = \gamma_{\pm} \left(1 + 0.001 \sum_{\text{solutes}} m_i M_i \right) \frac{\rho_{\text{solvent}}}{\rho_{\text{mix}}} \quad (\text{A-5})$$

for a multicomponent electrolyte (119) where M_i are the molecular weights of the solute species and ρ is the density. We measured carbonate solution densities at room temperature in order to make this conversion. These are shown in Figure A-1. Figure A-2 shows the calculated values for $K_{\text{II}}^{\text{app}}$.



- XBL 8711-4715 -

Figure A-1: Measured densities for K_2CO_3 solutions at 23 °C.



- XBL 8711-4716 -

Figure A-2: Calculated apparent dissociation constants for K_2CO_3 solutions at 23 °C.

Appendix B

Steady-State Flooded Agglomerate Model for the Gas-Diffusion Electrode in KOH and K_2CO_3

B.1 Introduction

The numerical solution of the equations developed in Chapter 6, which describe steady-state O_2 cathode behavior in KOH and K_2CO_3 electrolytes, will be discussed in this appendix. Section B.2 describes the non-dimensionalization of the equations developed in Sections 6.2 and 6.3 and presents the solution technique used to solve the mathematically similar problems. In Section B.3, the general behavior of the carbonate model is investigated by varying the magnitude of the dimensionless parameters. The calculated results for various O_2 partial pressures and non-perfect mixing at the electrode/electrolyte interface are also calculated. Section B.4 contains the Fortran code used to compute the numerical solutions to the equations.

B.2 Dimensionless Equations and Solution Technique

Model Equations were developed and discussed in Section 6.2.1 for the O_2 cathode with KOH electrolyte and in Section 6.3.1 for the K_2CO_3 electrolyte. For ease of solution and analysis of the results, the equations were put into dimensionless form with the definitions listed in Table B-1. The reaction coefficient, k' , defined in Equation 6-18 is eliminated through the identity which results for pure kinetic control:

$$\delta k' = i_0 a_0 \delta^2 \quad (B-1)$$

As mentioned in the text, the available information regarding ionic mobilities and diffusivities in concentrated KOH and K_2CO_3 solutions is limited. To understand the influence of electrolyte transport, therefore, we made use of the Nernst-Einstein equation,

Table B-1 Definitions

Part 1: KOH Problem

Dimensionless Variables	Dimensionless Groups
$x^* = \frac{x}{\delta}$	$\lambda = \frac{(D_- - D_+)u_+}{D_{\pm}(u_+ + u_-)}$
$C^* = \frac{C_{OH^-}}{C_{OH^-}^{\infty}} = \frac{C_{K^+}}{C_{K^+}^{\infty}}$	$Z_1 = \frac{i_o a_o \delta F \tau_a}{\epsilon_a \kappa RT}$
$\Psi^* = \frac{\Psi F}{RT} = \frac{(\Phi_S - \Phi_L)F}{RT}$	$Z_s = \frac{i_o a_o \delta F}{\sigma RT}$
$\phi^{*2} = \zeta^{*2} e^{-\alpha \Psi^*}$	$\zeta^{*2} = \frac{i_o a_o \tau_a R_p^2}{n F C_{O_2}^{\infty} D_{O_2} \epsilon_a (1 - \epsilon_e)}$
$\Gamma^* = \frac{I}{i_o a_o}$	

Part 2: K₂CO₃ Problem

Dimensionless Variables	Dimensionless Groups
$C_i^* = \frac{C_i}{C_i^{\infty}}$	$d_3 = \frac{2D_3}{D_6}, d_4 = \frac{2D_4}{D_6}, d_7 = \frac{2D_7}{D_6}$
for $i = 3, 4, 6, 7^{\dagger}$	$e_3 = \frac{C_3^{\infty}}{2C_6^{\infty}}, e_4 = \frac{C_4^{\infty}}{2C_6^{\infty}}, e_7 = \frac{C_7^{\infty}}{2C_6^{\infty}}$
$x^* = \frac{x}{\delta}$	$t_6 = \frac{4u_6 C_6^{\infty} F^2}{\kappa}$
$\Psi^* = \frac{\Psi F}{RT} = \frac{(\Phi_S - \Phi_L)F}{RT}$	$Z_s = \frac{i_o a_o \delta F}{\sigma RT}$
$\Gamma^* = \frac{I}{i_o a_o}$	$Z_1 = \frac{i_o a_o \delta F \tau_a}{\epsilon_a \kappa RT}$
$\phi^{*2} = \zeta^{*2} e^{-\alpha \Psi^*} (C_3^*)^{-\alpha}$	$\zeta^{*2} = \frac{i_o a_o \tau_a R_p^2}{n F C_{O_2}^{\infty} D_{O_2} \epsilon_a (1 - \epsilon_e)}$

 $\dagger 3 = OH^-, 4 = HCO_3^-, 6 = CO_3^{2-}$ and $7 = K^+$

$$D_i = RTu_i \quad (\text{B-2})$$

This reduces necessary transport parameters to N-1 ionic mobility (or diffusivity) ratios, where N is the number of ions, and the electrolyte conductivity, which is more readily available.

The two coupled non-linear differential equations, which describe the KOH problem (Equations 6-22 and 6-25), and the corresponding boundary conditions (Equations 6-26 and 6-27), are shown in dimensionless form in Table B-2.

The carbonate problem is described by three coupled ordinary non-linear differential equations (Equations 6-34, 6-35 and 6-37), and the algebraic expressions for the equilibrium between the anions (Equation 6-39) and electroneutrality (Equation 6-39). These equations and the two sets of boundary conditions are shown in dimensionless form in Table B-3.

Table B-2 Dimensionless Equations for KOH Problem

Dimensionless Equations	
$\nabla^2 C^* + (1 - \lambda)Z_1 \frac{(\phi^* \coth \phi^* - 1)}{(\zeta^{*2}/3)} = 0$	(B-8)
$\nabla^2 \Psi^* + Z_2 \frac{(\phi^* \coth \phi^* - 1)}{(\zeta^{*2}/3)} - \nabla^2 \ln C^* = 0$	(B-9)
Dimensionless Boundary Conditions	
at $x^* = 0$, electrode/electrolyte interface	
$C^* = 1$	(B-10)
$\nabla \Psi^* + \frac{\lambda}{1 - \lambda} \nabla C^* = Z_1 I^*$	(B-11)
at $x^* = 1$, electrode/gas-supply interface	
$\nabla C^* = 0$	(B-12)
$\nabla \Psi^* = -Z_2 I^*$	(B-12)

Table B-3 K_2CO_3 Problem in Dimensionless Form

Equations	
$d_3 e_3 [\nabla(C_3^* \nabla \ln C_7^*) + \nabla^2 C_3^*] + 2 \nabla(C_6^* \nabla \ln C_7^*) + \nabla^2 C_6^* + \frac{4Z_1}{t_6} \frac{(\phi^* \coth \phi^* - 1)}{(\zeta^{*2}/3)} = 0$	(B-22)
$d_4 e_4 [\nabla(C_4^* \nabla \ln C_7^*) + \nabla^2 C_4^*] + 2 \nabla(C_6^* \nabla \ln C_7^*) + \nabla^2 C_6^* = 0$	(B-23)
$\nabla^2 \Psi^* + Z_6 \frac{(\phi^* \coth \phi^* - 1)}{(\zeta^{*2}/3)} - \nabla^2 \ln C_7^* = 0$	(B-24)
$C_6^* = C_3^* C_4^*$	(B-25)
$e_3 C_3^* + e_4 C_4^* + C_6^* - e_7 C_7^* = 0$	(B-26)
Boundary Conditions	
@ $x^* = 0$, electrode/electrolyte interface:	
$\nabla \Psi^* + \frac{t_6}{4} (e_3 d_3 \nabla C_3^* + e_4 d_4 \nabla C_4^* + 2 \nabla C_6^* - e_7 d_7 \nabla C_7^*) = Z_1 I^*$	(B-27)
$\text{for perfect mixing: } C_i^* = 1$	(B-28a)
$\text{for a finite rate of mass transfer: } h_{mt}^* (C_i^* - 1) = d_i \nabla C_i^*$	(B-29)
@ $x^* = 1$, electrode/gas-supply interface:	
$\nabla \Psi^* = -Z_5 I^*$	(B-29)
$\nabla C_i^* = 0$	(B-30)

$$h_{mt}^* = \frac{h_{mt} \delta}{2D_6}$$

Solution Technique

Both problems consist of coupled non-linear differential equations. The non-linear terms were linearized using a Taylor expansion about a trial solution, y_{i0}

$$f(y_1, y_2, \text{etc}) = f_o + \sum_i (y_i - y_{io}) \left(\frac{\partial f}{\partial y_i} \right) \Big|_{y_{io}} \quad (\text{B-31})$$

This process results in the following approximations:

$$\phi^* \coth \phi^* - 1 = (\phi_o^* \coth \phi_o^* - 1) + (\Psi^* - \Psi_o^*) \left(-\frac{\alpha}{2} \right) L(\phi_o^*) \quad (\text{B-32})$$

for the KOH problem and

$$\phi^* \coth \phi^* - 1 = (\phi_o^* \coth \phi_o^* - 1) + (\Psi^* - \Psi_o^*) \left(-\frac{\alpha}{2} \right) L(\phi_o^*) + (C_3^* - C_{3o}^*) \left(-\frac{\alpha}{2C_{3o}^*} \right) L(\phi_o^*) \quad (\text{B-33})$$

for the K_2CO_3 problem, where

$$L(y) = y [\coth(y) + y - y \coth^2(y)] \quad (\text{B-34})$$

The other non-linear terms which appear in both problems are approximated as follows:

$$\nabla^2 \ln y = \nabla^2 \ln y_o + \left(\frac{1}{y_o} \right) \nabla^2 y - \left(\frac{2\nabla y_o}{y_o^2} \right) \nabla y + \left[\frac{2\nabla y_o^2}{y_o^3} - \frac{\nabla^2 y_o}{y_o^2} \right] \quad (\text{B-35})$$

and

$$z \nabla \ln y = \left(\frac{\nabla y_o}{y_o} \right) z - \left(\frac{z_o \nabla y_o}{y_o^2} \right) y + \left(\frac{z_o}{y_o} \right) \nabla y \quad (\text{B-36})$$

The linearized equations are solved by casting them into finite-difference form using central differences to approximate the space derivatives. For a mesh distance h ,

$$\nabla y^* = \frac{dy^*}{dx^*} = \frac{y^*(x_j^* + h) - y^*(x_j^* - h)}{2h} + O(h^2) \quad (\text{B-37})$$

$$\nabla^2 y^* = \frac{d^2 y^*}{dx^{*2}} = \frac{y^*(x_j^* + h) + y^*(x_j^* - h) - 2y^*(x_j^*)}{h^2} + O(h^2) \quad (\text{B-38})$$

The first trial solution is determined from the predicted result for pure kinetic control with uniform electrolyte concentration:

$$\Psi_o^* = -\left(\frac{1}{\alpha} \right) \ln \Gamma^* \quad \text{and} \quad C_i^* = 1 \quad (\text{B-39})$$

The BAND routine, developed by Newman (120), was used to compute the exact solution to the

set of approximate algebraic equations resulting from these operations. The new solution was used for the next trial, and computations were continued until the difference between successive iterations was less than 10^{-6} . No change in the computed results occurred when the number of mesh points was increased above 200.

B.3 General Model Behavior

The programs listed in the next section were written to solve the equations in dimensionless form. The user may input either dimensional or non-dimensional quantities. Computed voltage vs. current density curves are compared with experimental results in Chapter 6. General model behavior will be examined by varying the dimensionless parameters from the base-case values calculated with the parameters shown in Table 6-1. Table B-4 lists the base-case values of the dimensionless groups along with the range examined in this section.

Figure B-1 shows the sensitivity of performance predictions to order of magnitude changes in the three dimensionless groups, Z_s , Z_l , and ζ^* (defined in Table B-1). The maximum current in most of these plots is limited by the large increase in hydroxide concentration which causes the dimensionless potential difference variable, Ψ^* , to get very large. The program terminates when this variable is greater than 100. The only significant improvement in performance (without adjusting the kinetic parameters of the area, a_o) is gained by an increase in Z_l . This could most easily be achieved by increasing agglomerate porosity. This might be achieved with a different fabrication technique.

Table B-4: Dimensionless Parameters for GDE Model in K_2CO_3

Parameter	Base Case Value	Range Investigated	Figure
Z_s	1.126×10^{-7}	$1.126 \times 10^{-6} - 10^{-8}$	B-1a
Z_l	5.635×10^{-7}	$5.635 \times 10^{-6} - 10^{-8}$	B-1b
ζ^*	6.843×10^{-5}	$6.843 \times 10^{-4} - 10^{-6}$	B-1c
h_{mt}	∞	0.1 - 10	B-2
p_{O_2} (atm.)	1.0	0.04 - 1.0	B-3

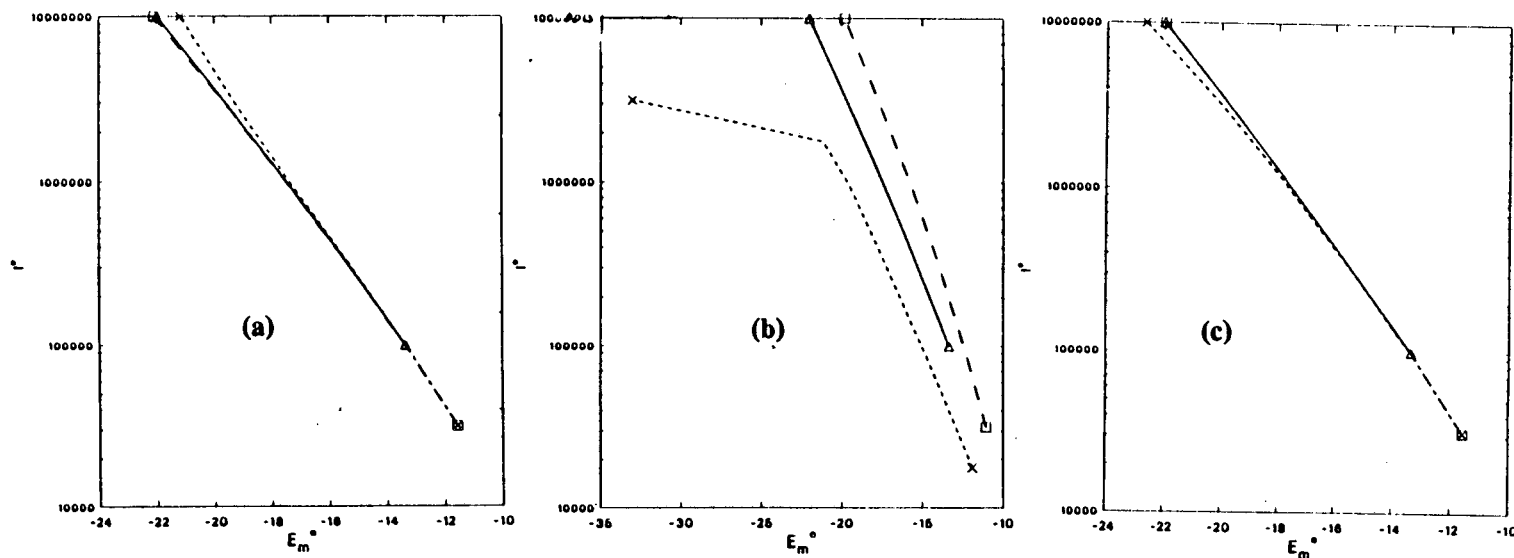


Figure B-1: Calculated performance curves for 2M K_2CO_3 .
 Table B-4 for base case values).
 (a) Vary Z_s , (b) Vary Z_l , (c) Vary ζ .
 — Δ , Base Case value,
 - - - \times , Base Case value $\times 10$,
 - . - \square , Base Case value $\times 0.1$.

Model dependence on dimensionless parameters (see

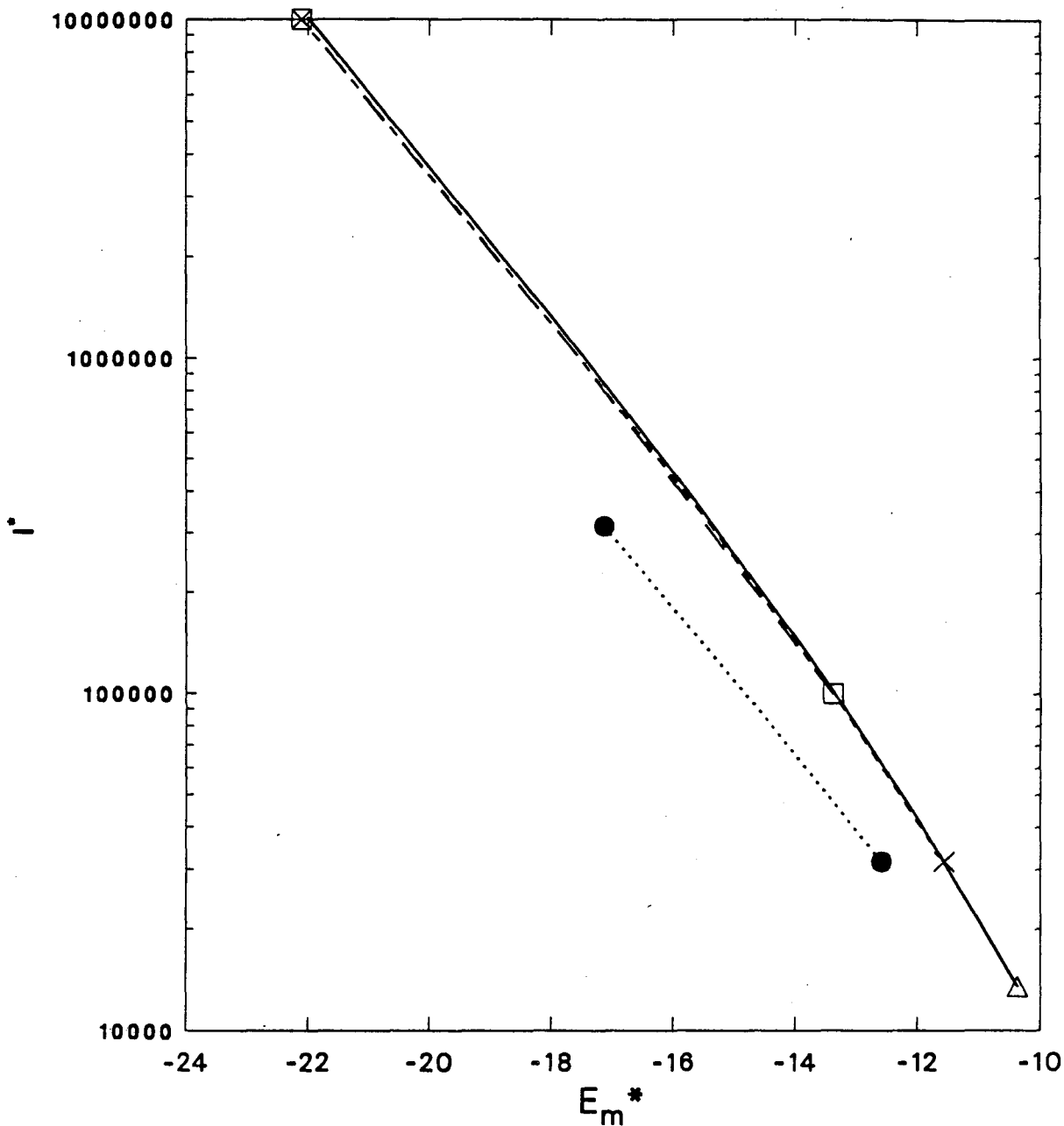


Figure B-2: Calculated dimensionless performance curves for 2M K_2CO_3 . Model results for finite mass-transfer rate boundary condition (see Table B-4 for base case values).

— Δ , Base Case (perfect stirring),
 - - - \times , $h_{mt}^* = 10$,
 - . - . \square , $h_{mt}^* = 1$,
 \bullet , $h_{mt}^* = 0.1$.

The inclusion of the finite mass-transfer boundary condition predicts a premature limiting current, as is shown in Figure B-2.

Figure B-3 was calculated using dimensional quantities to predict the dependence of performance on O_2 partial pressure. This involves adjusting the input values of $C_{O_2}^\infty$ and i_o , since $i_o = nFk_c C_{O_2}^\infty$. The dependence of current on p_{O_2} at a constant potential shifts from first-order at very low currents (kinetic Tafel slope regime) to half-order, in the double-Tafel-slope region. This result is consistent with the observations of Chapter 5.

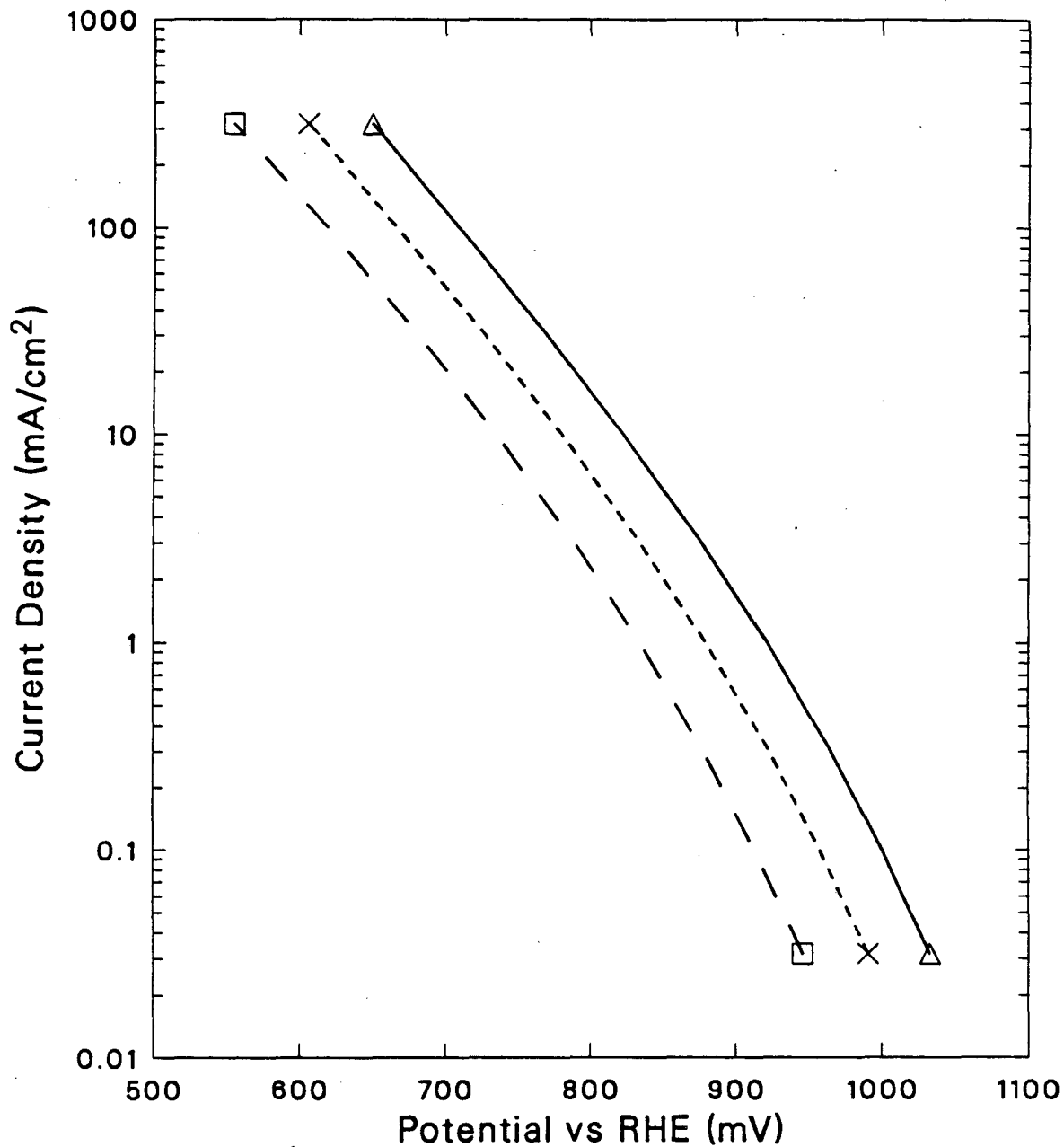


Figure B-3: Calculated performance curves for 2M K₂CO₃. Model results for variable oxygen pressure (see Table B-4 for base case values).
—Δ, Base Case, p_{O₂} = 1.0 atm.,
—X, p_{O₂} = 0.21 atm.,
—□, p_{O₂} = 0.04 atm.

B.4 Computer Code

KOH Problem

```

C
C   PROGRAM FOR THE NUMERICAL SOLUTION
C   FOR THE POTENTIAL VS CURRENT AND CONCENTRATION
C   PROFILES FOR AN OXYGEN ELECTRODE WITH HYDROXIDE ELECTROLYTE
C
C   PROGRAM KOHSIM
C
C   DIMENSIONLESS POTENTIAL DIFF. PSI*: C(1,j)
C   DIMENSIONLESS KOH CONCENTRATION: C(2,j)
C
C   Real*8 C(2,203)
C   Real*8 Cn(2,203)
C
C   CURRENT AND POTENTIAL VARIABLES
C
C   Real*8 im,imstar,fstcur,lstcur,curstp
C   Real*8 e0,psik,psikstar
C   Real*8 cursave(50),curstarsave(50)
C   Real*8 evsrhe,erhesave(50),estar, estarsave(50)
C   Real*8 potsav,deltaphis,deltaphisstar,psi0,psi0star
C   Real*8 slope(50),isolstar(202),jbarstar,cdist(202)
C
C   ELECTROLYTE PARAMETERS
C
C   Real*8 cnom,kappa
C   Real*8 c1b,dc1,Atc,ts,i0,T,nelec
C
C   ELECTRODE PARAMETERS
C
C   Real*8 sigma,delta,a0,Rp
C   Real*8 aporous,eporous,lvol,atau
C
C   DIMENSIONLESS PARAMETERS
C
C   Real*8 zetap,lamda,Zs,Zl
C
C   BAND COEFFICIENTS
C
C   Real*8 A(2,2),B(2,2),D(2,5)
C   Real*8 G(2),X(2,2),Y(2,2)
C
C   CONSTANTS AND PROGRAM CONTROL VARIABLES
C
C   Integer count,N,NJ,itnum,itmax,pcode
C   Integer check,ncur,curnum,icnt,i1,i2,n2
C   Real*8 h,tol
C   Real*8 alphan,aQalphan,k1,k3
C   Real*8 temp,cn3,dcn3,ddcn3,Anot,Bnot
C   Real*8 sum1,sum2,sum3,sum4,alph
C

```

```

Character*3  pcstring
Character*13 ansfile,paramfile,cdistkoh
Character*10 cohprofile
Real*8      dsqrt,dlog,dlog10
COMMON /BLK1/ A,B,C,D
COMMON /BLK2/ G,X,Y,N,NJ
Data  R,PI,F /8.314,3.1416,96487/
C
C  Read Input Data From: "kohinput.par"
C
C  Open (Unit=7,File='kohinput.par',Status='Old')

Read(7,*) pcode
Read(7,*) tol
Read(7,*) fstcur
Read(7,*) lstcur
Read(7,*) curstp
Read(7,*) NJ
Read(7,*) itmax
Read(7,*) cnom
Read(7,*) ts
Read(7,*) lamda
if(pcode .ge. 100) then
    Read(7,*) nelec
    Read(7,*) i0
    Read(7,*) e0
    Read(7,*) c1b
    Read(7,*) dc1
    Read(7,*) kappa
    Read(7,*) a0
    Read(7,*) delta
    Read(7,*) Rp
    Read(7,*) aporous
    Read(7,*) sigma
    Read(7,*) atau
    Read(7,*) lvlol
endif
if(pcode .lt. 100) then
    Read(7,*) Zs
    Read(7,*) Zl
    Read(7,*) zetap
endif
C
C  Create Filenames and Open Output Files
C
C  encode(3,22,pcstring) pcode
22 format(i3)
paramfile = 'kohres'//pcstring//'.txt'
ansfile = 'kohans'//pcstring//'.dat'
cohprofile = 'coh'//pcstring//'.pro'
cdistkoh = 'cddkoh'//pcstring//'.pro'
C
C  Open (Unit=8,File=paramfile,Status='New')

```

```

Open (Unit=9,File=ansfile,Status='New')
Open (Unit=11,File=cohprofile,Status='New')
Open (Unit=12,File=cdistkoh,Status='New')
C
C
C
CALCULATE OR SPECIFY CONSTANT PARAMETERS
C
N = 2
T = 298.0
h = 1.0/(NJ-2)
count = (NJ-2)/50
Atc = 2303 * R * T / ts / F
C
if(pcode .lt. 100) goto 20
C
C
CALCULATE THE DIMENSIONLESS GROUPS
C
eporous = 1.0 - (lvol / delta / (1.0 - aporous))
if(eporous .ge. 1.0) eporous = 0.5
zetap = Rp*dsqrt(a0*i0*atau/aporous/nelec/F/dcl/c1b/delta/(1-eporous))
Zs = i0 * a0 * delta * F / sigma / R / T
Zl = i0 * a0 * delta * F * atau / aporous / kappa / R / T
C
20 continue
C
k1 = 3.0 * Zs / zetap**2
k3 = 3.0 * (1.0 - lamda) * Zl / zetap**2
C
write(8,30)
write(8,32) NJ,h
write(8,34) cnom,T,ts,lamda
C
C
Write input and dimensionless parameters to result files
C
30 format('***Results for hydroxide cathode**SIM16')
32 format('***Mesh points = ',i4,
1      /' Step size = ',e10.3)
34 format(' KOH Added: ',e9.3,
1      /' . Temperature = ',f6.1,' K',
2      /' Tafel slope = ',f10.3,' mV/dec',
3      /' <m7)l<mx) = ',e10.3)
C
if(pcode .ge. 100) then
write(8,35)
write(8,40) delta,Rp,a0,sigma
write(8,45)
write(8,50) i0,e0,nelec,c1b,dcl
endif
C
35 format(/'***Electrode parameters**')
40 format(' Thickness = ',e10.3,' cm',
1      /' Agglomerate Radius = ',e10.3,' cm',
2      /' Platinum area/cm**3 = ',e10.3,' cm**-1',
3      /' Matrix Conductivity = ',e10.3,' (ohm-cm)**-1')

```

```

45         format(/'***Oxygen Parameters**')
50         format(' Exchange Current Dens = ',e10.3,' A/cm**2',
1           /' Equilibrium Pot = ',f6.3,
2           /' Stoichiometric # = ',f3.0,
3           /' Oxygen Conc.(mol/cc) : ',e11.4,
4           /' Oxygen Diff.(cm**2/sec) : ',e11.4)
C
        write(8,60)
        write(8,65) Zs,Zl,zetap
C
60         format(/'***Dimensionless parameters**')
65         format(/' Zs = ',e10.4,
1           /' Zl = ',e10.4,
2           /' zetap = ',e10.3)
C
C         write header data for TAG files
C
        write(9,70)
        write(11,70)
        write(12,70)
        write(11,75)
        write(12,77)
        write(9,80) pcode,ts,lamda,Zs,Zl,zetap
        write(11,80) pcode,ts,lamda,Zs,Zl,zetap
        write(12,80) pcode,ts,lamda,Zs,Zl,zetap
        write(9,85)
        write(11,85)
        write(12,85)
C
70         format(' title text " Hydroxide Cathode, SIMKOH" .',
1           /' every curve interp smooth,no color,delta 0,',
2           'symbol count 0.',
3           /' page border no. ')
75         format(' x axis label "Dimensionless Position" .',
1           /' y axis label "C<1.5h.8)3<lxhx) - 1" .')
77         format(' x axis label "Dimensionless Position" .',
1           /' y axis label ',
2           ' "Current Distribution" .')
80         format(' mes 1 units inches,line space ratio 2,',
1           /' x 7.75,y 4,text ',
2           /' " pcode : ',i5,' " ',
3           /' " Tafel Slope: ',f6.2,' mV/dec" ',
4           /' " <m7)l<mx) : ',e10.4,' " ',
5           /' " Zs : ',e10.4,' " ',
6           /' " Zl : ',e10.4,' " ',
7           /' " zetap : ',e10.4,' " .')
85         format(' INPUT DATA. ')
C
C         *****
C         * LOOP OVER CURRENT RANGE
C         *****
C
        icnt = 1

```

```

ncur = int(dlog10(lstcur/fstcur)/curstp)
C
do 400 curnum=1,ncur
C
  itnum = 0
  check = 0
  icurflg = 0
  im = 10**(dlog10(dabs(fstcur)) + (curnum*curstp))
  if(pcode .ge. 100) imstar = im / i0 / a0
  if(pcode .lt. 100) imstar = im
  rdec = dlog10(dabs(im))
  idec = int(rdec)
  if(abs(rdec-idec) .lt. 0.1) icurflg = 1
C
C   CALCULATE AND SET INITIAL GUESS FOR THIS CURRENT
C
  psikstar = -(1.0/Atc)*dlog(imstar)
  psik = psikstar*R*T*1000/F + 1230
C
  do 100 i2=1,NJ
    Cn(1,i2) = psikstar
    Cn(2,i2) = 1.0
100  continue
C
C   ***** COME HERE IF SOL'N HASN'T CONVERGED *****
C
200  continue
C
C   ZERO CONCENTRATION ARRAY FOR BAND
C
  do 210 i1=1,N
    do 209 i2=1,NJ
      C(i1,i2) = 0.0
209    continue
210  continue
C
C   Calculate first mesh point, j = 1
C
C   Zero Coefficients
C
  do 230 i1=1,N
    do 220 i2 = 1,N
      B(i1,i2) = 0.0
      X(i1,i2) = 0.0
      D(i1,i2) = 0.0
220    continue
      G(i1) = 0.0
230  continue
C
  j = 1
C
  B(1,1) = -0.5
  D(1,1) = 0.0

```



```

X(1,1) = 0.5
B(1,2) = - lamda / (1.0 - lamda) / 2.0
X(1,2) = -B(1,2)
G(1) = h * imstar * Z1
C
B(2,1) = 0.0
B(2,2) = 1.0
G(2) = 1.0
C
call BAND(1)
C
do 250 j = 2,NJ-1
C
Zero Coefficients
C
do 240 i1=1,N
do 235 i2 = 1,N
A(i1,i2) = 0.0
B(i1,i2) = 0.0
D(i1,i2) = 0.0
235 continue
G(i1) = 0.0
240 continue
C
cn3 = Cn(2,j)
dcn3 = (Cn(2,j+1)-Cn(2,j-1))/2.0/h
ddcn3 = (Cn(2,j+1)+Cn(2,j-1)-2.0*cn3)/h**2
alphan = zetap*dexp(-Atc*Cn(1,j)/2.0)
hypcot = 1.0/dtanh(alphan)
temp = alphan*hypcot - 1.0
aQalphan = alphan*(hypcot + alphan - (alphan*hypcot**2))
Anot = ddcn3/cn3 - (dcn3/cn3)**2
Bnot = 2.0*dcn3**2/cn3**3 - ddcn3/cn3**2
C
A(1,1) = 1.0
D(1,1) = 1.0
B(1,1) = -2.0 - (h**2)*(k1*Atc*aQalphan/2.0)
A(1,2) = -1.0/cn3 - h*dcn3/cn3**2
D(1,2) = -1.0/cn3 + h*dcn3/cn3**2
B(1,2) = 2.0/cn3 - (h**2)*(Bnot)
C
G(1) = (h**2)*(Anot - k1*(temp + Atc*Cn(1,j)*aQalphan/2.0))
C
A(2,1) = 0.0
D(2,1) = 0.0
B(2,1) = -(h**2)*(k3*Atc*aQalphan/2.0)
A(2,2) = 1.0
D(2,2) = 1.0
B(2,2) = -2.0
C
G(2) = -(h**2)*k3*(temp + Atc*Cn(1,j)*aQalphan/2.0)
C
call BAND(j)

```

```

C
250 continue
C
C Calculate last mesh point, j = NJ
C
do 260 i1=1,N
    do 255 i2 = 1,N
        A(i1,i2) = 0.0
        B(i1,i2) = 0.0
        Y(i1,i2) = 0.0
255     continue
        G(i1) = 0.0
260 continue
C
Y(1,1) = -0.5
B(1,1) = 0.5
A(1,1) = 0.0
G(1) = -h * imstar * Zs
Y(2,2) = -0.5
B(2,2) = 0.5
G(2) = 0.0
C
call BAND(NJ)
C
C *****
C CHECK FOR CONVERGENCE
C *****
C
do 280 i1=1,N
do 279 i2=1,NJ
C
conv = dabs((C(i1,i2)-Cn(i1,i2))/C(i1,i2))
if(conv .gt. tol) then
    itnum = itnum + 1
C
    if(itnum .ge. itmax) then
        write(8,270)
        format(' max iteration count exceeded')
        goto 300
    endif
270
C
C Save old try in Cn and check for blowup and neg conc.
C
do 272 n2= 1,NJ
    if(dabs(C(1,n2)).gt.100) check = 99
    if(C(2,n2) .lt. 0.0) check = 100
    Cn(1,n2) = C(1,n2)
    Cn(2,n2) = C(2,n2)
272 continue
C
C Go to next iteration unless check > 0
C
if(check .gt. 0) then

```

```

                if(check .eq. 99) write(8,274)
                if(check .eq. 100) write(8,276)
274             format(/' potential blow-up, goto next current!')
276             format(/' negative concentration, goto next current!')
                goto 300
            endif
C
                goto 200
C
            endif
279         continue
280         continue
C
C         IF WE CONVERGED or if itmax is exceeded, WE ARRIVE HERE
C         NOW WE CALCULATE THE RESULTS WE NEED AND WRITE THEM
C         TO THE APPROPRIATE FILES
C
300         continue
C
C         If there was a problem skip the answer calculations
C
            if(check .gt. 0) then
                icnt = icnt + 1
                check = 0
                goto 400
            endif
C
C         Write paramfile headings
C
            write(8,310) im,psikstar,alphan,itnum,check
            write(8,315)
C
310         format(/' CURRENT = ',e10.4,' A/cm**2',
2             /' Dimensionless initial guess: ',e10.3,
3             /' alphan = ',e10.3,
1             /' # iterations: ',i5,
4             /' check = ',i5)
315         format(/' Dimensionless Profiles',
1             /,t5,'y',t14,'psistar',t28,'c_',t42,'Cur.Dist.',t58,'alpha')
C
            sum1 = 0.0
            sum3 = 0.0
            sum4 = 0.0
C
            do 320 i2=1,NJ-1
C
C         First Integration to find i-s
C
                alph = zetap*dexp(-C(1,i2)*Atc/2.0)
                temp = (alph/dtanh(alph)) - 1.0
                jbarstar = 3.0*temp/(zetap**2)
                cdist(i2) = jbarstar / imstar
                sum1 = sum1 + h*jbarstar

```

```

        isolstar(i2) = sum1
C
C   Check for uniformity
C
        sum3 = sum3 + dabs(cdist(i2)-1.0)
        sum4 = sum4 + dabs(C(2,i2)-1.0)
C
C   Write profile results at each decade
C
        if(mod(i2,count).eq.0) write(8,325) i2,C(1,i2),
1          C(2,i2),cdist(i2),isolstar(i2)
320    continue
C
325    format(i7,4e14.4)
C
C   Second integration to calculate delta Phi_s
C
        sum2 = 0
        do 330 i1 = 1,NJ-1
            sum2 = sum2 + h*isolstar(i1)
330    continue
        deltaphisstar = - Zs * sum2
        deltaphis = R*T*deltaphisstar/F
C
C   PSI(0)
C
        psi0star = C(1,1)
        psi0 = R*T*C(1,2)/F
C
C   FINAL ANSWER
C
        estar = deltaphisstar + psi0star
        evsrhe = deltaphis + psi0 + e0
        erhesave(curnum) = evsrhe * 1000.0
        if(pcode .ge. 100) cursave(curnum) = im * 1000.0
        curstarsave(curnum) = imstar
        estarsave(curnum) = estar
        write(8,335) evsrhe,deltaphis,psi0
335    format(/' E_m vs RHE = ',f8.4,' volts',
1        /' Phi_s(1)-Phi_s(0) = ',e10.4,
2        /' Phi_s(0)-Phi_l(0) = ',e10.4)
C
C   Compute Tafel slope
C
        if(curnum.ne.0) then
            slope(curnum) = -1000.0*R*T*(estar-potsav)/((curstp*icnt)/F
            icnt = 1
        endif
        potsav = estar
340    format(e14.5,2x,e14.5)
C
C   Write individual profile files if non-uniform
C

```

```

        if(icurflg .eq. 1) then
            if(sum3 .gt. 0.1) write(12,355) imstar
            if(sum4 .gt. 0.1) write(11,355) imstar
            do 350 il = 1,NJ-1,count
                if(sum3.gt.0.1) write(12,360) ((i1-1)*h),cdist(i1)
                if(sum4.gt.0.1) write(11,360) ((i1-1)*h),C(2,i1)
350         continue
        endif
355     format(' "I-m* = ',e10.3,' " ')
360     format(f6.3,2x,e14.5)
C
C     END OF THIS CURRENT CALCULATION
C
400     continue
C
C     FINISH OFF PROFILE FILES
C
        write(11,510)
        write(12,510)
C
C     WRITE FINAL RESULT FILES
C
        if(pcode .lt. 100) goto 430
C     DIMENSIONAL FILE
C
        write(9,520)
        do 420 il=1,curnum-1
            write(9,340) erhesave(il),cursave(il)
420     continue

        write(9,525)
        do 425 il=1,curnum-1
            write(9,340) erhesave(il),slope(il)
425     continue
C
C     DIMENSIONLESS FILE
C
430     write(9,540)
        do 435 il=1,curnum-1
            write(9,340) estarsave(il),curstarsave(il)
435     continue
C
        write(9,510)
C
510     format(' END OF DATA.')
520     format(' "Current Density" ')
525     format(' "slope" ')
540     format(' "imstar" ')
C
        stop
        end

```

K₂CO₃ Problem

```

C
C PROGRAM FOR THE NUMERICAL SOLUTION
C FOR THE POTENTIAL VS CURRENT AND CONCENTRATION
C PROFILES FOR AN OXYGEN ELECTRODE WITH CARBONATE ELECTROLYTE
C
C PROGRAM SIMKC
C
C CONCENTRATION: C(1,j) = C3 (OH-)
C CONCENTRATION: C(2,j) = C4 (HCO3-)
C DIMENSIONLESS POTENTIAL DIFFERENCE: C(3,J)
C CONCENTRATION: C(4,j) = C6 (CO3=)
C CONCENTRATION: C(5,j) = C7 (K+)
C
C Real*8 C(5,203)
C Real*8 Cn(5,203)
C
C CURRENT AND POTENTIAL VARIABLES AND STORAGE
C
C Real*8 im,imstar,fstcur,lstcur,curstp
C Real*8 cursave(50),curstarsave(50)
C Real*8 evsrhe,estar
C Real*8 erhesave(50),estarsave(50),Tslope(50)
C Real*8 deltaphis,psi0,psik
C Real*8 deltaphisstar,psi0star,psikstar
C
C INPUT ELECTROLYTE PARAMETERS
C
C Real*8 cnom,kiiapp,T,c1b,dc1,kappa,kappathstar
C Real*8 i0,alpha,nelec,ts,e0,kmtc
C Real*8 p6,p7,d3,d4,d6,d7
C
C INPUT ELECTRODE PARAMETERS
C
C Real*8 sigma,delta,a0
C Real*8 Rp,atau,lvol,eporous,aporous
C
C CALCULATED ELECTROLYTE PARAMETERS
C
C Real*8 c3b,c4b,c6b,c7b
C Real*8 e3,e4,e6,e7,dc6
C Real*8 Atc
C
C DIMENSIONLESS PARAMETERS
C
C Real*8 Zs,Zl,t6,zetap,mtc
C
C NUMERICAL SOLUTION PARAMETERS
C
C BAND Coefficients
C
C Real*8 A(5,5),B(5,5),D(5,11)
C Real*8 G(5),X(5,5),Y(5,5)
C

```

```

C   Other
C
Real*8 tol,h
Integer N,NJ,pcode,check,itnum,itmax,icnt
Integer icurflg,ncur,curnum,i1,i2,n1,n2,pcount,count
C
C   Misc. Storage
C
Real*8 isolstar(202),jbarstar,cdist(202),alphapro(202)
Real*8 alphavg(50),cohavg(50)
Real*8 alph,potsav
Real*8 sum1,sum2,sum3,sum4,sum5,sum6,temp
C
C
Real*8 dsqrt,dlog,dlog10
Character*25 infile
Character*12 cdistfile,ansfile,paramfile
Character*10 c3profile,c4profile,c6profile,c7profile
Character*3 pcstring
C
COMMON /BLK1/ A,B,C,D
COMMON /BLK2/ G,X,Y,N,NJ
COMMON /BLK3/ Cn,imstar,h,Atc,t6,Zs,Zl,zetap,mtc
COMMON /BLK4/ e3,e4,e7,d3,d4,d7
C
Data R,PI,F /8.314,3.1416,96487/
C
C   Open Data Input File
C
infile = 'kcinput'
C
Open (Unit=7,File=infile//'.par',Status='Old')
C
Read(7,*) pcode
C
PCODE < 100 computes results from dimensionless parameters
PCODE >= 100 computes results from dimensional parameters
C   individual parameters listed by code#
C
Read(7,*) tol
Read(7,*) fstcur
Read(7,*) lstcur
Read(7,*) curstp
Read(7,*) NJ
Read(7,*) itmax
Read(7,*) cnom
Read(7,*) kiiapp
Read(7,*) ts
Read(7,*) d3
Read(7,*) d4
Read(7,*) d7
if(pcode .ge. 100) then
    Read(7,*) kmtc

```

```

        Read(7,*) nelec
        Read(7,*) i0
        Read(7,*) c1b
        Read(7,*) dc1
        Read(7,*) kappa
        Read(7,*) a0
        Read(7,*) delta
        Read(7,*) Rp
        Read(7,*) aporous
        Read(7,*) sigma
        Read(7,*) atau
        Read(7,*) lvol
    endif
    if(pcode .lt. 100) then
        Read(7,*) Zs
        Read(7,*) Zl
        Read(7,*) zetap
        Read(7,*) mtc
    endif
endif
C
C  CALCULATE OR SPECIFY CONSTANT PARAMETERS
C
N = 5
e0 = 1.23
T = 298.0
h = 1.0/(NJ-2)
count = (NJ-2)/50
pcount = 2 * count
Atc = 2303 * R * T / ts / F
C
C  Calculate bulk ionic compositions and concentration ratios
C
c4b = (dsqrt(1.0+(4.0*cnom*kiiapp))-1.0)/2.0/kiiapp
c6b = cnom - c4b
c3b = c6b / kiiapp / c4b
c7b = 2 * cnom
e3 = c3b/c6b/2.0
e4 = c4b/c6b/2.0
e6 = 1.0
e7 = c7b/c6b/2.0
d6 = 1.0
p6 = 1.0
t6 = 4.0 / (4.0 + e3*d3 + e4*d4 + e7*d7)
C
C
    if(pcode .lt. 100) goto 20
    If pcode >= 100 Calculate dimensionless parameters
C
C
    eporous = 1.0 - (lvol / delta / (1.0 - aporous))
    zetap = Rp*dsqrt(a0*i0*atau/aporous/nelec/F/dc1/c1b/delta/(1-eporous))
    Zl = i0 * a0 * delta * F * atau / aporous / kappa / R / T
    Zs = i0 * a0 * delta * F / (sigma * R * T)
    dc6 = t6 * kappa * R * T / c6b / (F**2) / 4.0

```



```

mtc = kmtc * delta / dc6 / 2.0
C
20 continue
C
C
C Write input and dimensionless parameters to result files
encode(3,22,pcstring) pcode
22 format(i3)
   paramfile = 'param'//pcstring//'.txt'
   ansfile = 'final'//pcstring//'.dat'
   c3profile = 'c3s'//pcstring//'.pro'
   c4profile = 'c4s'//pcstring//'.pro'
   c6profile = 'c6s'//pcstring//'.pro'
   c7profile = 'c7s'//pcstring//'.pro'
   cdistfile = 'cdist'//pcstring//'.pro'
C
C Open (Unit=8,File=paramfile,Status='New')
C
   write(8,30)
   write(8,31) NJ,h,tol ,pcode
   write(8,32) cnom,ts
   write(8,52)
   write(8,55) c3b,c4b,c6b,c7b
   write(8,60) e3,e4,e6,e7
   write(8,75) d3,d4,d6,d7
C
30 format(' **Results for carbonate cathode-SIM2**')
31 format(' **Mesh points = 'i4,5x,
   1      /' Step size = ',e10.3,
   2      /' tolerance = ',e10.3,
   3      /' pcode   = ',i5)
32 format(' Nominal Carbonate Concentration: ',e9.3,
   1      /' Tafel slope = ',f7.2,' mv/dec')
52 format(/' **Solution parameters**')
   1      T31,'OH-',T42,'HCO3-',T53,'CO3=',T64,'K+')
55 format(' Bulk Conc.(mol/cc)',T27,4e11.3)
60 format(' Ionic Conc. Ratios (ei)',T27,4e11.3)
75 format(' 2Di/D6',T27,4e11.3)
C
   if(pcode .ge. 100) then
       write(8,45)
       write(8,50) i0,nelec
       write(8,65) c1b,dc1
       write(8,33)
       write(8,40) delta,a0,Rp,sigma,aporous,eporous,atau,lvol
C
45 format(/' **Kinetic and Oxygen Parameters**')
50 format(/' rate constant = ',e10.3,' A/cm**3',
   3      /' Stoichiometric # = ',f3.0)
65 format(/' O2 conc.(mol/cc): ',e11.4,
   1      /' O2 diff.(cm**2/sec): ',e11.4)
33 format(/' **Electrode parameters**')
40 format(' Thickness = ',e10.3,' cm',

```

```

1          /' Platinum area/cm**3 = ,e10.3,' cm**-1',
2          /' Agglomerate Radius = ,e10.3,' cm',
3          /' Matrix Conductivity = ,e10.3,' (ohm-cm)**-1',
4          /' Agglomerate porosity = ,f6.3,
5          /' Electrode porosity = ,f6.3,
6          /' Agglomerate tortuosity = ,f6.2,
7          /' Electrode load vol. = ,f6.2)
C
      endif
C
      write(8,85)
      write(8,90) Zs,Zl,t6,zetap,mtc
C
85     format(/' **Dimensionless parameters**')
90     format(' Zs = ,e10.4,' kinetics/matrix cond.',
1      /' Zl = ,e10.4,' kinetics/soln cond.',
2      /' t6 = ,e10.4,' kappath/kappa',
3      /' zetap = ,e10.4,' kinetics/O2 diff',
4      /' mtc = ,e10.4,' dim.less mass-trans.coeff.')
```

C
C
C

```

      Open (Unit=9,File=ansfile,Status='New')
      Open (Unit=10,File=c3profile,Status='New')
      Open (Unit=11,File=c4profile,Status='New')
      Open (Unit=12,File=cdistfile,Status='New')
      Open (Unit=13,File=c6profile,Status='New')
      Open (Unit=14,File=c7profile,Status='New')
```

C
C
C

```

      title info

      write(9,91) cnom
      write(10,91) cnom
      write(11,91) cnom
      write(12,91) cnom
      write(13,91) cnom
      write(14,91) cnom
```

C
C
C

```

      axis labels

      write(10,93) 'C_OH-/C_OH-o'
      write(11,93) 'C_HCO3-/C_HCO3-o'
      write(12,93) 'C. Dist, J*/I'
      write(13,93) 'C_CO3=/C_CO3=o'
      write(14,93) 'C_K+/C_K+o'
```

C
C
C

```

      message

      write(9,89) pcode,Zs,Zl,zetap,mtc
      write(10,89) pcode,Zs,Zl,zetap,mtc
      write(11,89) pcode,Zs,Zl,zetap,mtc
      write(12,89) pcode,Zs,Zl,zetap,mtc
```

```

write(13,89) pcode,Zs,Zl,zetap,mtc
write(14,89) pcode,Zs,Zl,zetap,mtc
C
91  format('title text " ',e8.2,' mol/cc KC Cathode". ',
1    /' every curve no color,',
2    'symbol size 1.5, count 9999.')
```

92 format(' x axis label "Potential vs. RHE (V)"',
1 /' y axis label " Current Density (A/cm**2) "'')

C

93 format(' x axis label "x<e.5h.8)*<exhx"'',
1 /' y axis label "' ,A, "'')

C

89 format(' mes 1 units inches,line space ratio 2,'
1 /' x 7.75,y 5,text ',
2 /' " pcode : ',i5,'"',
3 /' " Zs : ',e10.4,'"',
4 /' " Zl : ',e10.4,'"',
5 /' " zetap : ',e10.4,'"',
6 /' " mtc : ',e10.4,'"'')

C

```

write(9,95)
write(10,95)
write(11,95)
write(12,95)
write(13,95)
write(14,95)
C
95  format(' INPUT DATA.')
```

C

C *****

C * MAIN LOOP OVER THE CURRENTS OF CHOICE

C *****

C

```

icnt = 1
ncur = int(dlog10(lstcur/fstcur)/curstp)
C
do 500 curnum=1,ncur
C
icurflg = 0
im = 10**(dlog10(dabs(fstcur)) + (curnum*curstp))
if(pcode .ge. 100) imstar = im / i0 / a0
if(pcode .lt. 100) imstar = im
rdec = dlog10(dabs(im))
idec = int(rdec)
if(abs(rdec - float(idec)) .lt. 0.1) icurflg = 1
if(pcode .ge. 100) cursave(curnum) = im * 1000.0
curstarsave(curnum) = imstar
C
psikstar = -(1.0/Atc)*dlog(imstar)
psik = (psikstar * R * T / F ) + 1.23
C
itnum = 0
check = 0
```

```

C
C   SET INITIAL GUESS FOR THIS CURRENT
C
  do 99 i2=1,NJ
      Cn(1,i2) = 1.0
      Cn(2,i2) = 1.0
      Cn(3,i2) = psikstar
      Cn(4,i2) = 1.0
      Cn(5,i2) = 1.0
99  continue
C
C   ***** COME HERE IF SOL'N HASN'T CONVERGED *****
C
200 continue
C
C   ZERO CONCENTRATION ARRAY FOR BAND
C
  do 210 i1=1,N
      do 209 i2=1,NJ
          C(i1,i2) = 0.0
209  continue
210 continue
C
C   Calculate first mesh point, j = 1
C
  j = 1
  call BCOEFFS(j)
  call BAND(j)
C
C   Calculate NJ-2 interior points
C
  do 250 j=2,NJ-1
      call JCOEFFS(j)
      call BAND(j)
C
250 continue
C
C   Calculate last mesh point, j = NJ
C
  call BCOEFFS(NJ)
  call BAND(NJ)
C
C   *****
C   CHECK FOR CONVERGENCE
C   *****
C
  do 280 i1=1,N
      do 279 i2=1,NJ
C
  if(dabs((C(i1,i2)-Cn(i1,i2))/Cn(i1,i2)) .gt. tol) then
      itnum = itnum + 1
C

```

```

        if(itnum .ge. itmax) then
            write(8,281)
281         format(' max iteration count exceeded')
            goto 399
        endif
C
C     Save old try in Cn
C
        do 355 n1=1,N
        do 350 n2= 1,NJ
            if(n1.eq.3) then
                if(dabs(C(3,n2)).gt.100) check = 99
            endif
            if(n1 .ne. 3) then
                if(C(n1,n2) .lt. 0.0) then
                    C(n1,n2) = 0.01
                    check = 100
                endif
            endif
            Cn(n1,n2) = C(n1,n2)
350         continue
355         continue
C
C     Time to go back for another round
C
C         unless check = 99
C
C             if(check .eq. 100) write(8,357)
C             if(check .eq. 99) then
C                 write(8,356)
C                 goto 399
C             endif
C
C             format(' **error** potential blowup, go on to next current')
356         format(' neg. HCO3- conc., ')
357         format(' check = ',i4)
358
C             check = 0
C             goto 200
C
C         endif
279     continue
280     continue
C
C     IF WE CONVERGED or if itmax is exceeded, WE ARRIVE HERE
C     NOW WE CALCULATE THE RESULTS WE NEED AND WRITE THEM
C     TO THE APPROPRIATE FILES
C
399     continue
C
        write(8,400) im,psikstar,itnum
400     format(/' CURRENT = ',e10.3,' A/cm**2',
2     /' pure kinetic overpotential : ',e10.3,

```

```

4  /' # of iterations required: ',i5)
   if(check .eq. 99) then
       icnt = icnt + 1
       goto 500
   endif
C
   write(8,405)
405  format(/' Dimensionless Concentration Profiles')
   write(8,410)
410  format(//,t5,'j',t14,'C-OH-',t26,
1    'PSI*',t40,'IS*',t54,'cd')
C
   sum1 = 0.0
   sum3 = 0.0
   sum4 = 0.0
C
   do 420 i2=1,NJ-1
C
C    First Integration to calculate i-s (x) from j-bar
C
       temp = -Atc * C(3,i2) / 2.0
       alph = zetap*dexp(temp)*(C(1,i2)**(-Atc/2.0))
       alphpro(i2) = alph
C
       temp = (zetap**2)*imstar
       jbarstar = 3.0*(alph/dtanh(alph) - 1.0)/temp
       isolstar(i2) = sum1 + h*jbarstar
       sum1 = isolstar(i2)
       cdist(i2) = jbarstar
C
C    determine whether profile is non-uniform enough to be interesting
C
       sum3 = sum3 + dabs(cdist(i2)-1.0)
       sum4 = sum4 + dabs(C(1,i2)-1.0)
C
C    print profile points once in a while
C
       if( mod(i2,pcount) .eq. 0) write(8,424) i2,
1       C(1,i2),C(3,i2),isolstar(i2),cdist(i2)
C
420  continue
424  format(i6,7e12.4)
C
C    Second integration to find (F/RT)[PHI-s(delta) - PHI-s(0)]
C
   sum2 = 0.0
   do 421 i2 = 1,NJ-1
       sum2 = sum2 + isolstar(i2)*h
421  continue
C
   deltaphistar = -sum2*Zs
   psi0star = C(3,2)
C

```

```

C      Calculate answers in dimensional and dimensionless form
C
C      The dimensionless overpotential
C
      estar = deltaphisstar + psi0star
      estarsave(curnum) = estar
C
C      potential vs. RHE
C
      evsrhe = R*T*estar/F + e0
      erhesave(curnum) = evsrhe * 1000.0
C
C      MISC. CALCULATIONS
C
C      Individual potential drops
C
      deltaphis = R*T*deltaphisstar/F
      psi0 = R*T*psi0star/F
C
C      Tafel Slope
C
      if(curnum.ne.0) then
          Tslope(curnum) = -R*T*(estar-potsav)/curstp/icnt/F
          icnt = 1
      endif
      potsav = estar
C
C      Average hydroxide conc.
C
      sum5 = 0.0
      sum6 = 0.0
      do 470 i2=1,NJ
          sum5 = sum5 + C(1,i2)
          sum6 = sum6 + alphapro(i2)
470      continue
      cohavg(curnum) = sum5 / (NJ - 2)
      alphavg(curnum) = sum6 / (NJ - 2)
C
C
C      Write dimensionless profiles at each current decade
C      if they are non-uniform enough
C
      if(icurflg .eq. 1) then
          if(sum3 .gt. 0.5) write(12,440) imstar
          if(sum4 .gt. 0.5) then
              write(10,440) imstar
              write(11,440) imstar
              write(13,440) imstar
              write(14,440) imstar
          endif
          do 451 i1 = 1,NJ-1,count
              if(sum3 .gt. 0.5) write(12,441) ((i1 - 1.0)*h),cdist(i1)

```

```

        if(sum4 .gt. 0.5) then
            write(10,441) ((i1 - 1.0)*h),C(1,i1)
            write(11,441) ((i1 - 1.0)*h),C(2,i1)
            write(13,441) ((i1 - 1.0)*h),C(4,i1)
            write(14,441) ((i1 - 1.0)*h),C(5,i1)
        endif
451      continue
    endif
C
441      format(f6.3,2x,e14.5)
440      format(' 'I-m* = ',e10.3,' ' ')
C
C
        write(8,422) evsrhe,psi0,deltaphis
422      format(' E_m: ',f10.4,' mV'
1      /' psi(0): ',f10.4,/' delphis: ',f10.4)
C
C      END OF CALCULATION FOR THIS CURRENT
C
500      continue
C
C      FINISH OFF PROFILE TAG FILES
C
        write(10,510)
        write(11,510)
        write(12,510)
        write(13,510)
        write(14,510)
C
C      WRITE FINAL RESULT FILE FOR THIS RUN
C
        if(pcode .lt. 100) goto 526
        DIMENSIONAL FILE
C
C
        write(9,520)
        do 521 i1=1,curnum-1
            write(9,550) erhesave(i1),cursave(i1)
521      continue

        write(9,525)
        do 528 i1=1,curnum-1
            write(9,550) erhesave(i1),Tslope(i1)
526      continue
C
        write(9,530)
        do 531 i1=1,curnum-1
            write(9,550) estarsave(i1),cohavg(i1)
531      continue
C
C      DIMENSIONLESS FILE
C
        write(9,540)

```



```

do 541 i1=1,curnum-1
    write(9,550) estarsave(i1),curstarsave(i1)
541 continue
C
    write(9,545)
do 546 i1=1,curnum-1
    write(9,550) estarsave(i1),alphavg(i1)
546 continue

    write(9,510)
C
510 format(' END OF DATA. ')
520 format(' "Current Density" ')
525 format(' "T slope" ')
530 format(' "C-OH* avg" ')
540 format(' "imstar" ')
545 format(' "<M7)a<MX)-avg" ')
550 format(e12.4,3x,e14.5)
C
C
551 stop
    end

SUBROUTINE JCOEFFS(j)
C
C This routine calculates BAND Coefficients for SIMKC
C at mesh points 1 < j < NJ
C
Real*8 A(5,5),B(5,5),C(5,203),D(5,11)
Real*8 G(5),X(5,5),Y(5,5)
Real*8 Cn(5,203)
Real*8 d3,d4,d7,e3,e4,e7
Real*8 imstar,h,t6,Zs,Zl,Atc,zetap,mtc
Real*8 k1,k3
Real*8 cn3,cn4,cn5,cn6,cn7
Real*8 dcn3,dcn4,dcn6,dcn7
Real*8 ddcn7,alphan,aQalphan,term1,term2
Integer N,NJ

C
Real*8 Anot,Bnot,Cnot,Dnot,q3,q4,q3prime,q4prime,hypcot
Real*8 dtanh,dexp

C
Common /BLK1/ A,B,C,D
Common /BLK2/ G,X,Y,N,NJ
COMMON /BLK3/ Cn,imstar,h,Atc,t6,Zs,Zl,zetap,mtc
COMMON /BLK4/ e3,e4,e7,d3,d4,d7

C
C Calculate new values for k1 and k3
C
k1 = 12.0 * Zl / t6 / (zetap**2)
k3 = 3.0 * Zs / (zetap**2)

C
C First recover the values of Cn[k,j] from memory with

```

```

C   the above note in mind.
C
cn3 = Cn(1,j)
cn4 = Cn(2,j)
cn5 = Cn(3,j)
cn6 = Cn(4,j)
cn7 = Cn(5,j)

C
C   Next we will compute the derivative quantities needed
C
den3 = ( Cn(1,j+1) - Cn(1,j-1) ) / 2.0 / h
den4 = ( Cn(2,j+1) - Cn(2,j-1) ) / 2.0 / h
den6 = ( Cn(4,j+1) - Cn(4,j-1) ) / 2.0 / h
den7 = ( Cn(5,j+1) - Cn(5,j-1) ) / 2.0 / h

C
ddcn7 = ( Cn(5,j+1) + Cn(5,j-1) - 2.0 * cn7 ) / h**2

C
C   Next the complex functions, alpha and alphaQ(alpha)
C
alphan = zetap * dexp(-cn5*Atc/2.0) * (cn3 **(-Atc/2.0))
hycpot = 1.0 / dtanh(alphan)
term1 = alphan*hycpot - 1.0

C
aQalphan = alphan*(hycpot + alphan - alphan * (hycpot**2))

C
C   First initialize all array values to zero
C
do 10 i=1,N
    do 5 k=1,N
        A(i,k) = 0.0
        B(i,k) = 0.0
        D(i,k) = 0.0
5        continue
        G(i) = 0.0
10    continue

C
C   Now we are ready to calculate coefficients
C       calculate some prelim. quantities
C
Bnot = dcn7 / cn7
Anot = ddcn7/cn7 - dcn7**2/cn7**2
Cnot = (2.0*dcn7**2/cn7**3) - (ddcn7/cn7**2)
Dnot = dcn7 / cn7**2

C
C   ***** Equation 1 terms *****
C
q3 = e3 * d3 * cn3 + 2.0 * cn6
q3prime = e3 * d3 * dcn3 + 2.0 * dcn6

C
A(1,1) = d3 * e3 * (1.0 - (h/2)*Bnot)
B(1,1) = -2.0*d3*e3 + (h**2)*(e3*d3*Anot - k1*aQalphan*Atc/cn3/2.0)
D(1,1) = e3 * d3 *(1.0 + (h/2)*Bnot)

C

```

$$\begin{aligned} A(1,4) &= 1.0 - (h/2)*(2.0*Bnot) \\ B(1,4) &= -2.0 + (h**2)*(2.0*Anot) \\ D(1,4) &= 1.0 + (h/2)*(2.0*Bnot) \end{aligned}$$

C

$$\begin{aligned} A(1,5) &= q3/cn7 - (h/2)*(q3prime/cn7 - 2.0*q3*Dnot) \\ B(1,5) &= -2.0*q3/cn7 + (h**2)*(q3*Cnot - q3prime*Dnot) \\ D(1,5) &= q3/cn7 + (h/2)*(q3prime/cn7 - 2.0*q3*Dnot) \end{aligned}$$

C

$$\begin{aligned} A(1,3) &= 0.0 \\ B(1,3) &= (h**2)*(-k1*Atc*aQalphan/2.0) \\ D(1,3) &= 0.0 \end{aligned}$$

C

C

C

***** Equation 2 terms *****

$$\begin{aligned} q4 &= e4 * d4 * cn4 + 2.0 * cn6 \\ q4prime &= e4 * d4 * dcn4 + 2.0 * dcn6 \end{aligned}$$

C

$$\begin{aligned} A(2,2) &= e4 * d4 * (1.0 - (h/2)*Bnot) \\ B(2,2) &= -2.0*e4*d4 + (h**2)*(e4*d4*Anot) \\ D(2,2) &= e4*d4 * (1.0 + (h/2)*Bnot) \end{aligned}$$

C

$$\begin{aligned} A(2,4) &= A(1,4) \\ B(2,4) &= B(1,4) \\ D(2,4) &= D(1,4) \end{aligned}$$

C

$$\begin{aligned} A(2,5) &= q4/cn7 - (h/2)*(q4prime/cn7 - 2.0*q4*Dnot) \\ B(2,5) &= -2.0*q4/cn7 + (h**2)*(q4*Cnot - q4prime*Dnot) \\ D(2,5) &= q4/cn7 + (h/2)*(q4prime/cn7 - 2.0*q4*Dnot) \end{aligned}$$

C

C

C

***** Equation 3 *****

continue

22

C

$$B(3,1) = (h**2)*(-k3*aQalphan*Atc/cn3/2.0)$$

C

$$\begin{aligned} A(3,3) &= 1.0 \\ B(3,3) &= -2.0 + (h**2)*(-k3*aQalphan*Atc/2.0) \\ D(3,3) &= 1.0 \end{aligned}$$

C

$$\begin{aligned} A(3,5) &= -1.0/cn7 - h*Dnot \\ B(3,5) &= 2.0/cn7 + (h**2)*(-Cnot) \\ D(3,5) &= -1.0/cn7 + h*Dnot \end{aligned}$$

C

$$\text{term2} = \text{term1} + (aQalphan/2.0)*(Atc*cn5 + Atc)$$

C

$$\begin{aligned} G(1) &= (h**2)*(-k1*term2) \\ G(2) &= 0 \\ G(3) &= (h**2)*(Anot - k3*term2) \end{aligned}$$

C

$$\begin{aligned} B(4,1) &= -cn4 * h**2 \\ B(4,2) &= -cn3 * h**2 \\ B(4,4) &= h**2 \end{aligned}$$

C

```

B(5,1) = -e3 * h**2
B(5,2) = -e4 * h**2
B(5,4) = - h**2
B(5,5) = +e7 * h**2
C
G(4) = -cn3 * cn4 * h**2
G(5) = 0
C
C
C   That's all
C   return
C   end
C   *****

Subroutine BCOEFFS(j)
C
C   Calculate BAND Coefficients at the Boundaries
C
C   Real*8 A(5,5),B(5,5),C(5,203),D(5,11)
C   Real*8 G(5),X(5,5),Y(5,5)
C   Real*8 Cn(5,203)
C   Real*8 imstar,h,t6,Zs,Zl,Atc,zetap,mtc
C   Real*8 e3,e4,e7,d3,d4,d7
C   Integer N,NJ,j,k
C
C   Common blocks
C
C   COMMON /BLK1/ A,B,C,D
C   COMMON /BLK2/ G,X,Y,N,NJ
C   COMMON /BLK3/ Cn,imstar,h,Atc,t6,Zs,Zl,zetap,mtc
C   COMMON /BLK4/ e3,e4,e7,d3,d4,d7
C
C   if(j .eq. NJ) goto 100
C
C   FOR j = 1
C
C   Zero the arrays
C
C   do 35 i=1,5
C       do 30 k=1,5
C           X(i,k) = 0.0
C           B(i,k) = 0.0
C           D(i,k) = 0.0
30       continue
C       G(i) = 0.0
35   continue
C
C   PERFECT MIXING BC
C
C   if (mtc .gt. 9999) then
C
C       B(1,1) = 1.0
C       B(2,2) = 1.0
C       B(4,4) = 1.0

```

```

        B(5,5) = 1.0
        G(1) = 1.0
        G(2) = 1.0
        G(4) = 1.0
        G(5) = 1.0
        goto 50
    endif

C
C   MASS-TRANSFER BC
C
    B(1,1) = -0.5
    B(2,2) = -0.5
    B(4,4) = -0.5
    B(5,5) = -0.5

C
    X(1,1) = 0.5
    X(2,2) = 0.5
    X(4,4) = 0.5
    X(5,5) = 0.5

C
    D(1,1) = -h * d3 * mtc
    D(2,2) = -h * d4 * mtc
    D(4,4) = -h * 2.0 * mtc
    D(5,5) = -h * d7 * mtc

C
    G(1) = -h * d3 * mtc
    G(2) = -h * d4 * mtc
    G(4) = -h * 2.0 * mtc
    G(5) = -h * d7 * mtc

C
C   CURRENT FLUX BC DOESN'T DEPEND ON MIXING
C
C   50   continue
C
    X(3,1) = e3 * d3 * t6 / 8.0
    X(3,2) = e4 * d4 * t6 / 8.0
    X(3,3) = 0.5
    X(3,4) = t6 / 4.0
    X(3,5) = -e7 * d7 * t6 / 8.0
    G(3) = h * imstar * Z1

C
    do 40 k=1,5
        B(3,k) = -X(3,k)
40   continue
C
    return

C
C   ***** COME HERE FOR J = NJ *****
100  continue
C
C   Zero appropriate arrays
C
    do 10 i=1,N

```

```
do 5 k=1,N
    A(i,k) = 0.0
    B(i,k) = 0.0
    Y(i,k) = 0.0
5    continue
    G(i) = 0.0
10   continue
C
do 20 i=1,5
    B(i,i) = 0.5
    Y(i,i) = -0.5
20   continue
C
G(3) = - h * imstar * Zs
C
return
end
```

*LAWRENCE BERKELEY LABORATORY
TECHNICAL INFORMATION DEPARTMENT
UNIVERSITY OF CALIFORNIA
BERKELEY, CALIFORNIA 94720*